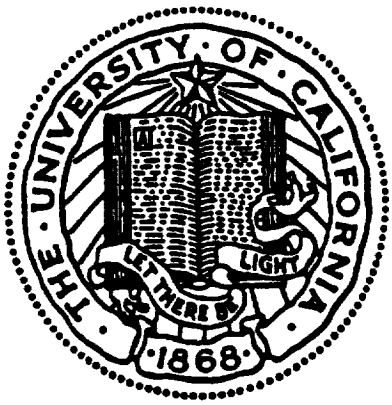

STRUCTURAL SYSTEMS
RESEARCH PROJECT

Report No.
SSRP - 93/10

THE EXPERIMENTAL BEHAVIOR OF SPINNING PRETWISTED LAMINATED COMPOSITE PLATES

by

J.B. Kosmatka
A.J. Lapid

Final Report on a Research Project Funded through NASA Research Grant Number NCC 3-173.

Period of Performance
5/1/90-9/30/93

Department of Applied Mechanics
and Engineering Sciences
University of California, San Diego
La Jolla, California

University of California, San Diego
Structural Systems Research Project

Report No. SSRP-93/10

THE EXPERIMENTAL BEHAVIOR OF SPINNING PRETWISTED LAMINATED COMPOSITE PLATES

by

J.B. Kosmatka and A.J. Lapid

Department of Applied Mechanics and Engineering Sciences
University of California, San Diego
La Jolla, California 92093-0411

Final Report on a Research Project Funded through
NASA Research Grant Number NCC 3-173

Period of Performance
May 1, 1990 through September 30, 1993

Forward

This final technical report was prepared by the Aerospace Structures Laboratory of the Applied Mechanics and Engineering Sciences Department, University of California, San Diego under contract number NCC 3-173 with the NASA-Lewis Research Center. This grant was monitored and administered by Oral Mehmed of the Structural Dynamics Branch of the NASA-Lewis Research Center.

This research program was developed and supervised by Professor John B. Kosmatka, Principal Investigator. Professor Kosmatka and Alex J. Lapid performed all of the experimental work and they were provided invaluable assistance with the work performed at the NASA-Lewis Research Center by O. Mehmed, E. Meyn, J. Quinones, C. Finlay, A. Kurkov, and K. Weiland. The test hardware components were manufactured at UCSD by G. Foreman, S. Porter, and B. Thomas. The composite plates were manufactured by J. Anton and G. Brinkman of General Dynamics- Convair Division.

Table of Contents

List of Symbols vi

List of Figures ix

List of Tables xvii

Abstract xxi

1 Introduction and Review of Present Research 1

1.1 Introduction 1

1.2 Review of Literature on the Experimental Behavior of Pre-Twisted Plates 5

1.3 Objectives of Present Research 7

2 Experimental Equipment and Procedures 10

2.1 Clamping Assembly 10

2.1.1 Clamp 1 13

2.1.2 Test Description and Results for Clamp 1 13

2.1.3 Clamp 2 14

2.1.4 Test Description and Results for Clamp 2 16

2.1.5 Clamp 3 17

2.1.6 Test Description and Results for Clamp 3 19

2.1.7 Clamp 4 21

2.1.8 Test Description and Results for Clamp 4 21

2.2 Plate Description 23

2.2.1 Plate Geometry, Material Properties, and Lay-up 23

2.2.2 Determining the Quality of the Plate Sets 29
2.2.3 Experimental Procedure 30
2.2.4 Geometry Measurements 32
2.2.5 The Strain Gage Circuit Equations 35

2.3 The Aerospace Structures Laboratory at the University of California San Diego 38
2.3.1 The Vibration Tests 39
2.3.2 The Static Displacement Tests 42

2.4 The NASA Lewis Research Center 44
2.4.1 The Laser Holography Laboratory 44
2.4.2 Theory of Holographic Vibration Analysis 45
2.4.3 Experimental Setup 47
2.4.4 The Dynamic Spin Rig Facility 48
2.4.5 Steady-State Strain and Deflections 52
2.4.6 Rotating Vibratory Natural Frequencies and Mode Shapes 55

3 Strain and Displacement Results and Discussion 56

3.1 Non-Rotating Static Displacements and Strain 56

3.2 Rotating Strain and Displacements 65
3.2.1 Flat and Pre-Twisted Plate about the Mid-Chord with $[\pm 22.5/0_2/-22.5/0_2/+22.5/0_2]_S$ Lay-Up 67
3.2.2 Pre-Twisted Plates about the Mid-Chord and Quarter-Chord with $[\pm 22.5/0_2/-22.5/0_2/+22.5/0_2]_S$ Lay-Up 70
3.2.3 Pre-Twisted Plates about the Quarter-Chord with $[\pm \theta/0_2/-\theta/0_2/+\theta/0_2]_S$ Lay-Up (θ = 22.5° and 45°) 73
3.2.4 The Asymmetric Lay-Ups 75
3.2.5 Plate 11 79
3.2.6 Plate 21 81
3.2.7 Plate 31 83
3.2.8 Plate 32 85
3.2.9 Plate 13 87

3.2.10 Plate 23* 89
3.2.11 Plates 11 and 21, Configuration A 91
3.2.12 Plates 11 and 21, Configuration B 93
3.2.13 Plates 11 and 21, Configuration C 95
3.2.14 Plates 21 and 31, Configuration A 97
3.2.15 Plates 21 and 31, Configuration B 100
3.2.16 Plates 21 and 31, Configuration C 101
3.2.17 Plates 31 and 32, Configuration A 103
3.2.18 Plates 31 and 32, Configuration B 105
3.2.19 Plates 31 and 32, Configuration C 107
3.2.20 Plates 11 and 13, Configuration A 108
3.2.21 Plates 21 and 23*, Configuration A 110
3.2.22 Plates 13 and 23*, Configuration A 112

4 Vibration Results and Discussion 115

4.1 Non-Rotating Vibrations 115

4.2 Rotating Vibrations 131

4.2.1 Flat Plate with $[\pm 22.5/0_2/-22.5/0_2/+22.5/0_2]_S$ Lay-Up 133

4.2.2 Pre-Twisted Plate about the Mid-Chord with $[\pm 22.5/0_2/-22.5/0_2/+22.5/0_2]_S$ Lay-Up 1 133

4.2.3 Pre-Twisted Plate about the Quarter-Chord with $[\pm 22.5/0_2/-22.5/0_2/+22.5/0_2]_S$ Lay-Up 134

4.2.4 Pre-Twisted Plate about the Quarter-Chord with $[\pm 45/0_2/-45/0_2/+45/0_2]_S$ Lay-Up 134

4.2.5 Flat Plate with $[+22.5_5/0_5]_A$ Lay-Up 135

4.2.6 Pre-Twisted Plate about the Mid-Chord with $[0_2/+22.5_2/0_2/+22.5_3/0]_A$ Lay-Up 135

4.2.7 Rotating Vibrations Comparisons and Discussions 147

5 Conclusions 155

5.1 Static Displacement and Strain 155

5.2 Rotating Displacement and Strain 156

5.3 Non-Rotating Vibrations 157

5.4 Rotating Vibrations 158

Appendices **160**

Appendix A: Geometry Measurements 160

Appendix B: Experimental Strain and Displacement Results 164

Appendix B.1: Error Analysis 166

Appendix B.2: Strain and Displacement Results 167

References **194**

List of Symbols

c	=	Chord length
c_{ITA}	=	Distance from the leading edge to the initial twist axis
D	=	Tip deflection
F_c	=	Centrifugal force
K_N	=	Non-Rotating plate stiffness
K_R	=	Rotating plate stiffness
l	=	Plate length
m	=	Mass of the plate
P	=	Tip load
r	=	Perpendicular distance from the spin axis to the plate centroid
S	=	Southwell coefficient
t	=	Plate thickness
x	=	x-displacement
y	=	y-displacement
z	=	z-displacement
c/t	=	Thickness ratio
l/c	=	Aspect ratio
$\|\alpha\|$	=	Magnitude of the frequency response function
β_S	=	Sweep angle
β_P	=	Pitch angle
ε_A	=	Axial strain
ε_B	=	Bending strain
ϕ	=	Pre-Twist angle
θ	=	Ply angle
ω_a, ω_b	=	Half-power point frequencies

ω_n = Plate natural frequency

Ω = Rotational speed

ψ = Tip rotation

ζ = Damping

Material Properties

E_{11} = Apparent Young's modulus in the direction of the fibers

E_{22}, E_{33} = Apparent Young's modulus in the direction transverse to the fibers

E_f = Young's modulus of the fiber

E_m = Young's modulus of the fiber,

G_{12}, G_{13} = In-plane shear modulus of a lamina

G_f = Shear modulus of the fiber

G_m = Shear modulus of the matrix

V_f = Fiber volume fraction

V_m = Matrix volume fraction

ν_{12}, ν_{13}, and ν_{23} = Poisson's ratio

ν_f = Poisson's ratio of the fiber,

ν_m = Poisson's ratio of the fiber,

Strain Gage Circuit Equations

$1\text{-}n$ = Nonlinearity factor

a = Bridge ratio

G_F = Gage factor

R = Resistance

V, V_{out}, and V_{in} = Voltage, output voltage, and input voltage

Laser Holography

E = Laser Source Point

F = Arbitrary Point on a Stationary Beam

F', F'' = Arbitrary Extreme Points on a Vibrating Beam

G = Peak-to-Peak Amplitude between F' and F''

η = Angle between the Surface Normal and the Laser

λ = Wavelength of the Laser

τ = Viewing Angle

List of Figures

Figure 1.1: Propeller system from a C-130 Hercules. 2

Figure 1.2: Propeller system from the Advance Turboprop Program. 3

Figure 1.3: Implementation of the counter-rotating prop-fan. 3

Figure 1.4: A pre-twisted, cantilevered plate. 4

Figure 1.5: Capturing the effects of sweep. 5

Figure 1.6: Plate geometries. 7

Figure 2.1: The clamping assembly used during the spin tests. 11

Figure 2.2: The centrifugal force on a10x3 inch and 11x3 inch aluminum plate with a thickness of 0.125 inch. 12

Figure 2.3: Clamp 1 features a 1x3 in^2 clamping area and is constructed out of 4340 Steel. 13

Figure 2.4: Description of aluminum specimens used to test the first clamping assembly. 14

Figure 2.5: Clamp 2 features a 1x3 in^2 serrated surface that greatly enhances the gripping ability of the clamp. 15

Figure 2.6: Plate clamping assembly for the Tensile-Compression Machine. The plate jaws for the Tensile-Compression Machine feature a serrated surface at ±30°. 16

Figure 2.7: Plate specimen design used to test Clamp 2. 16

Figure 2.8: Clamp 3 utilizing a wedge design. 18

Figure 2.9: The centrifugal force on the heaviest graphite/epoxy plate (weight = 0.196 lbf). 19

Figure 2.10: A typical graphite/epoxy tensile-compression sample. 20

Figure 2.11: Main assembly configuration for Clamp 4. 21

Figure 2.12: Graphite/Epoxy test specimen for the tensile tests on Clamp 4. Two flat plate specimens were prepared with $[\pm\theta/0_2/-\theta/0_2/+\theta/0_2]_S$ with θ = 22.5° and 45°. 22

Figure 2.13: The dimensions and geometry of the graphite/epoxy plate specimens.....24
Figure 2.14: The manufacturing process of a pair of graphite/epoxy plates. 27
Figure 2.15: The magnitude diagram of a frequency response function. The peaks on the plot are the natural frequencies of the system. 31
Figure 2.16: The phase diagram of a frequency response function. 31
Figure 2.17: Calculating the damping using the half power point method.....31
Figure 2.18: A description of the setup used to measure the geometry of the pre-twisted plates. The milling table is capable of moving in three orthogonal directions. The table is moved so that the pin points to the desired position on the plate. The xy-measurements are recorded using dial indicators on the milling machine. The height gage is used to measure the z-coordinates. 33
Figure 2.19: A graphite/epoxy plate instrumented with strain gages.....35
Figure 2.20: A Wheatstone Bridge with a single strain gage in a quarter bridge. 36
Figure 2.21: A quarter bridge with two lead wires from the strain gage. 38
Figure 2.22: The experimental modal analysis setup at the Aerospace Structures Lab at the University of California San Diego. The PC based software package, The Star System, allows easy data processing and visualization of mode shapes. 40
Figure 2.23: The real and imaginary portions of the frequency response function and the coherence. 41
Figure 2.24: The natural frequencies and mode shapes of a 30° pre-twisted plate about the mid-chord the with a $[\pm 22.5/0_2/\ 22.5/0_2/22.5/0_2]_S$ lay-up.....42
Figure 2.25: The plate coordinates used for the static deflection tests. The xyz-deflections are measured at points A and B, and the load, P, is applied at point A. The strain is recorded from strain gage 2.....43
Figure 2.26: Definitions of (a) deflection with no twist, and (b) twist with no deflection. 44
Figure 2.27: A cantilevered beam vibrating at its first fundamental mode is illuminated by a laser at point A. The camera records the phase difference and amplitude of the scattered laser.....45
Figure 2.28: A hologram of the 1st Bending, 1st Torsion, and 2nd Bending modes for one of the graphite/epoxy plates.....46
Figure 2.29: Laser holography setup at the NASA Lewis Research Center. 47
Figure 2.30: The Dynamic Spin Rig Facility at the NASA Lewis Research Center. 49

Figure 2.31: Available sweep and pitch angles at the Dynamic Spin Rig Facility at the NASA Lewis Research Center. 50
Figure 2.32: Photograph of the plate setup within the spin chamber at the NASA Lewis Research Center. 51
Figure 2.33: Block diagram description to record the rotating steady-state strains. 52
Figure 2.34: Laser deflection measurement system. 53
Figure 2.35: (a) The once-per-revolution pulse and (b) the blade pulse. 54
Figure 3.1: The experimental plate setup for the static strain and displacement tests..... 57
Figure 3.2: The finite element mesh used for the analytical modeling on I DEAS. 58
Figure 3.3: Load case descriptions for the I-DEAS models. 59
Figure 3.4: Analytical deflections due to a 1 lb. transverse load at the tip center..... 62
Figure 3.5: Analytical twist due to a 1 lb. transverse load at the tip center..... 62
Figure 3.6: Analytical deflections due to a 1 lb. axial load at the tip center. 63
Figure 3.7: Analytical twist due to a 1 lb. axial load at the tip center. 63
Figure 3.8: Analytical deflections due to a 1 lb-in right-hand moment in the positive x-direction at the tip center. 64
Figure 3.9: Analytical twist due to a 1 lb-in right-hand moment in the positive x-direction at the tip center. 64
Figure 3.10 Orientation of the pre-twisted plate about the quarter-chord within the spin rig, the positive pitch direction, and the sweep angle..... 66
Figure 3.11: Strain gage labels and locations. 67
Figure 3.12: Axial and bending strains of Plate 11 for Configurations A, B, and C. 79
Figure 3.13: Deflections of Plate 11 for Configurations A, B, and C. 79
Figure 3.14 Torsion strains of Plate 11 for Configurations A, B, and C..... 80
Figure 3.15: Twist of Plate 11 for Configurations A, B, and C..... 80
Figure 3.16: Axial and bending strains of Plate 21 for Configurations A, B, and C. 81
Figure 3.17: Deflections of Plate 21 for Configurations A, B, and C. 81
Figure 3.18: Torsion strains of Plate 21 for Configurations A, B, and C..... 82
Figure 3.19: Twist of Plate 21 for Configurations A, B, and C..... 82
Figure 3.20: Axial and bending strains of Plate 31 for Configurations A, B, and C. 83
Figure 3.21: Strains from Gages 1 and 2 of Plate 31 for Configurations A, B, and C... 83
Figure 3.22: Deflections of Plate 31 for Configurations A, B, and C. 84

Figure 3.23: Torsion strains of Plate 31 for Configurations A, B, and C. 84
Figure 3.24: Twist of Plate 31 for Configurations A, B, and C. 85
Figure 3.25: Axial and bending strains of Plate 32 for Configuration A....85
Figure 3.26: Deflections of Plate 32 for Configurations A, B, and C....86
Figure 3.27: Torsion strains of Plate 32 for Configurations A, B, and C. 86
Figure 3.28: Twist of Plate 32 for Configurations A, B, and C. 87
Figure 3.29: Strain from Gage 2 of Plate 13 for Configuration A....87
Figure 3.30: Deflections of Plate 13 for Configuration A....88
Figure 3.31: Torsion strains of Plate 13 for Configuration A. 88
Figure 3.32: Twist of Plate 13 for Configuration A. 89
Figure 3.33: Axial and bending strains of Plate 23* for Configuration A....89
Figure 3.34: Deflections of Plate 23* for Configuration A....90
Figure 3.35: Torsion strains of Plate 23* for Configuration A. 90
Figure 3.36: Twist of Plate 23* for Configuration A. 91
Figure 3.37: Axial and bending strain comparisons between Plates 11 and 21 for Configuration A. 91
Figure 3.38: Deflection comparisons between Plates 11 and 21 for Configuration A....92
Figure 3.39: Torsion strain comparisons between Plates 11 and 21 for Configuration A. 92
Figure 3.40: Twist comparisons between Plates 11 and 21 for Configuration A....93
Figure 3.41: Axial and bending strain comparisons between Plates 11 and 21 for Configuration B. 93
Figure 3.42: Deflection comparisons between Plates 11 and 21 for Configuration B....94
Figure 3.43: Torsion strain comparisons between Plates 11 and 21 for Configuration B. 94
Figure 3.44: Twist comparisons between Plates 11 and 21 for Configuration B. 95
Figure 3.45: Axial and bending strain comparisons between Plates 11 and 21 for Configuration C. 95
Figure 3.46: Deflection comparisons between Plates 11 and Plate 21 for Configuration C. 96
Figure 3.47: Torsion strain comparisons between Plates 11 and 21 for Configuration C. 96
Figure 3.48: Twist comparisons between Plates 11 and 21 for Configuration C. 97

Figure 3.49: Axial and bending strain comparisons between Plates 21 and 31 for Configuration A 97
Figure 3.50: Strain gage comparisons between Plates 21 and 31 for Configuration A 98
Figure 3.51: Deflection comparisons between Plates 21 and 31 for Configuration A. .. 98
Figure 3.52: Torsion strain comparisons between Plates 21 and 31 for Configuration A 99
Figure 3.53: Twist comparisons between Plates 21 and 31 for Configuration A. 99
Figure 3.54: Deflection comparisons between Plates 21 and 31 for Configuration B. 100
Figure 3.55: Torsion strain comparisons between Plates 21 and 31 for Configuration B 100
Figure 3.56: Twist comparisons between Plates 21 and 31 for Configuration B. 101
Figure 3.57: Axial and bending strain comparisons between Plates 21 and 31 for Configuration C 101
Figure 3.58: Deflection comparisons between Plates 21 and 31 for Configuration C. 102
Figure 3.59: Torsion strain comparisons between Plates 21 and 31 for Configuration C 102
Figure 3.60: Twist comparisons between Plates 21 and 31 for Configuration C. 103
Figure 3.61: Axial and bending strain comparisons between Plates 31 and 32 for Configuration A 103
Figure 3.62: Deflection comparisons between Plates 31 and 32 for Configuration A. 104
Figure 3.63: Torsion strain comparisons between Plates 31 and 32 for Configuration A 104
Figure 3.64: Twist comparisons between Plates 31 and 32 for Configuration A. 105
Figure 3.65: Deflection comparisons between Plates 31 and 32 for Configuration B. 105
Figure 3.66: Torsion strain comparisons between Plates 31 and 32 for Configuration B 106
Figure 3.67: Twist comparisons between Plates 31 and 32 for Configuration B. 106
Figure 3.68: Deflection comparisons between Plates 31 and 32 for Configuration C. 107
Figure 3.69: Torsion strain comparisons between Plates 31 and 32 for Configuration C 107
Figure 3.70: Twist comparisons between Plates 31 and 32 for Configuration C. 108
Figure 3.71: Strain comparisons between Plates 11 and 13 for Configuration A. 108
Figure 3.72: Deflection comparisons between Plates 11 and 13 for Configuration A. 109

Figure 3.73: Torsion strain comparisons between Plates 11 and 13 for Configuration A. 109
Figure 3.74: Twist comparisons between Plates 11 and 13 for Configuration A. 110
Figure 3.75: Axial and bending strain comparisons between Plates 21 and 23* for Configuration A. 110
Figure 3.76: Deflection comparisons between Plates 21 and 23* for Configuration A. 111
Figure 3.77: Torsion strain comparisons between Plates 21 and 23* for Configuration A. 111
Figure 3.78: Twist comparisons between Plates 21 and 23* for Configuration A. 112
Figure 3.79: Strain comparisons between Plates 13 and 23* for Configuration A. 112
Figure 3.80: Deflection comparisons between Plates 13 and 23* for Configuration A. 113
Figure 3.81: Torsion strain comparisons between Plates 13 and 23* for Configuration A. 113
Figure 3.82: Twist comparisons between Plates 13 and 23* for Configuration A. 114
Figure 4.1: Mode shapes of a cantilevered plate. The nodal lines are represented by the dashed curves. 116
Figure 4.2: The first bending natural frequency for lay-ups 1 and 2. 118
Figure 4.3: The second bending and first torsion natural frequencies for lay-ups 1 and 2. 120
Figure 4.4: The third bending and second torsion natural frequencies for lay-ups 1 and 2. 124
Figure 4.5: The first chordwise natural frequency for lay-ups 1 and 2. 126
Figure 4.6: Photographs of the first six mode shapes for Plate 11. 128
Figure 4.7: Photographs of the first six mode shapes for Plate 31. 129
Figure 4.8: Photographs of the first six mode shapes for Plate 13. 130
Figure 4.9: The measured natural frequencies vs. the rotational speed for Plate 11. . 141
Figure 4.10: Least squares fit of the square of the natural frequency vs. the square of the rotational speed for Plate 11. 141
Figure 4.11: The measured natural frequencies vs. the rotational speed for Plate 21. . 142
Figure 4.12: Least squares fit of the square of the natural frequency vs. the square of the rotational speed for Plate 21. 142
Figure 4.13: The measured natural frequencies vs. rotational speed for Plate 31. 143

Figure 4.14: Least squares fit of the square of the natural frequency vs. the square of the rotational speed for Plate 31. 143
Figure 4.15: The natural frequency vs. the rotational speed for Plate 32..... 144
Figure 4.16: Least squares fit of the square of the natural frequency vs. the square of the rotational speed for Plate 32. 144
Figure 4.17: The natural frequency vs. the rotational speed for Plate 13..... 145
Figure 4.18: Least squares fit of the square of the natural frequency vs. the square of the rotational speed for Plate 13. 145
Figure 4.19: The natural frequency vs. the rotational speed for Plate 23*..... 146
Figure 4.20: Least squares fit of the square of the natural frequency vs. the square of the rotational speed for Plate 23*..... 146
Figure 4.21: Geometry comparisons of the rotating vibration modes between Plates 11 and 21. 152
Figure 4.22: Geometry comparisons of the rotating vibration modes between Plates 21 and 31. 152
Figure 4.23: Lay-up comparisons of the rotating vibration modes between Plates 31 and 32. 153
Figure 4.24: Lay-up comparisons of the rotating vibration modes between Plates 11 and 13. 153
Figure 4.25: Lay-up comparison of the rotating vibration modes between Plates 21 and 23*. 154
Figure A.1: Pre-twist geometry and strain gage locations. 160
Figure B.1: The experimental plate setup for the static strain and displacement tests..... 165
Figure B.2: The finite element mesh used for the analytical modeling on I DEAS. ... 165
Figure B.3: Experimental and analytical strain results for Plate 11. 177
Figure B.4: Experimental and analytical deflection results for Plate 11..... 177
Figure B.5: Experimental and analytical twist results for Plate 11. 178
Figure B.6: Experimental and analytical strain results for Plate 21. 179
Figure B.7: Experimental and analytical deflection results for Plate 21..... 179
Figure B.8: Experimental and analytical twist results for Plate 21. 180
Figure B.9: Experimental and analytical strain results for Plate 31. 181
Figure B.10: Experimental and analytical deflection results for Plate 31..... 181

Figure B.11: Experimental and analytical twist results for Plate 31.....182
Figure B.12: Experimental and analytical deflection results for Plate 41.....183
Figure B.13: Experimental and analytical twist results for Plate 41.....183
Figure B.14: Experimental and analytical deflection results for Plate 22.....184
Figure B.15: Experimental and analytical twist results for Plate 22.....184
Figure B.16: Experimental and analytical strain results for Plate 32.....185
Figure B.17: Experimental and analytical deflection results for Plate 32.....185
Figure B.18: Experimental and analytical twist results for Plate 32.....186
Figure B.19: Experimental and analytical deflection results for Plate 42.....187
Figure B.20: Experimental and analytical twist results for Plate 42.....187
Figure B.21: Experimental strain results for Plate 13.....188
Figure B.22: Experimental and analytical deflection results for Plate 13.....188
Figure B.23: Experimental and analytical twist results for Plate 13.....189
Figure B.24: Experimental strain results for Plate 23*.....190
Figure B.25 : Experimental and analytical strain results for Plate 23*.....190
Figure B.26: Experimental and analytical twist results for Plate 23*.....191
Figure B.27: Experimental and analytical deflection results for Plate 33*.....192
Figure B.28: Experimental and analytical twist results for Plate 33*.....192
Figure B.29: Experimental and analytical deflection results for Plate 43*.....193
Figure B.30: Experimental and analytical twist results for Plate 43*.....193

List of Tables

Table 2.1: Summary of the test results for the first clamping assembly. Aluminum plates (6061 T6) were used to test the first clamp. 14

Table 2.2: Tensile test results and plate descriptions for Clamp 2. 17

Table 2.3: Tensile test results for the plate specimen with $[\pm 22.5/0_2/-22.5/0_2/+22.5/0_2]_S$. 23

Table 2.4: Tensile test results for the plate specimen with $[\pm 45/0_2/-45/0_2/+45/0_2]_S$. 23

Table 2.5: Material properties of the graphite/epoxy plates. 26

Table 2.6: Plate serial numbers. The first digit refers to the geometry and the second is the lay-up. 29

Table 2.7: List of equipment used to perform the first modal analysis on the graphite/epoxy plates. 29

Table 2.8: A list of the plates chosen to be spin tested at the Dynamic Spin Rig Facility at the NASA Lewis Research Center. 34

Table 2.9: List of modal analysis equipment at the Aerospace Structures Laboratory. 39

Table 2.10: Equipment list at the Laser Holography Laboratory. 48

Table 2.11: Pitch and sweep settings for the graphite/epoxy plates. 50

Table 3.1: Plate Serial Numbers. The first digit refers to the geometry and the second is the lay up. 57

Table 3.2: Pitch and sweep configurations for the steady-state strain and displacement tests. 66

Table 3.3: Laser locations for Plate 11. Locations are measured from the tip of the plate. 77

Table 3.4: Laser locations for Plate 21. Locations are measured from the tip of the plate. 77

Table 3.5: Laser locations for Plate 31. Locations are measured from the tip of the plate. 78

Table 3.6: Laser locations for Plate 32. Locations are measured from the tip of the plate. 78

Table 3.7: Laser locations for Plate 13. Locations are measured from the tip of the plate. 78

Table 3.8: Laser locations for Plate 23*. Locations are measured from the tip of the plate. 78

Table 4.1: Ply lay-up and geometry effects on the 1st Bending natural frequency. 118

Table 4.2: Ply lay-up and geometry effects on the 2nd Bending natural frequency. 119

Table 4.3: Ply lay-up and geometry effects on the 1st Torsion natural frequency. 119

Table 4.4: Ply lay-up and geometry effects on the 3rd Bending natural frequency. 123

Table 4.5: Ply lay-up and geometry effects on the 2nd Torsion natural frequency. 123

Table 4.6: Ply lay-up and geometry effects on the 1st Chordwise natural frequency. 125

Table 4.7: Comparison of the natural frequency results from the ASL and Laser Holography Laboratory to the Dynamic Spin Rig Facility at 0 rpm for Plate 11. 136

Table 4.8: Measured experimental natural frequencies from 0 to 8000 rpm for Plate 11. 136

Table 4.9: Comparison of the natural frequency results from the ASL and Laser Holography Laboratory to the Dynamic Spin Rig Facility at 0 rpm for Plate 21. 137

Table 4.10: Measured experimental natural frequencies from 0 to 8000 rpm for Plate 21. 137

Table 4.11: Comparison of the natural frequency results from the ASL and Laser Holography Laboratory to the Dynamic Spin Rig Facility at 0 rpm for Plate 31. 137

Table 4.12: Measured experimental natural frequencies from 0 to 8000 rpm for Plate 31. 138

Table 4.13: Comparison of the natural frequency results from the ASL and Laser Holography Laboratory to the Dynamic Spin Rig Facility at 0 rpm for Plate 32. 138

Table 4.14: Measured experimental natural frequencies from 0 to 7000 rpm for Plate 32. 138

Table 4.15: Comparison of the natural frequency results from the ASL and Laser Holography Laboratory to the Dynamic Spin Rig Facility at 0 rpm for Plate 13. 139

Table 4.16: Measured experimental natural frequencies from 0 to 8000 rpm for Plate 13. 139

Table 4.17: Comparison of the natural frequency results from the ASL and Laser Holography Laboratory to the Dynamic Spin Rig Facility at 0 rpm for Plate 23*. 139

Table 4.18: Measured experimental natural frequencies from 0 to 8000 rpm for Plate 23*. 140

Table 4.19: The experimentally measured Southwell coefficients (S), ... 151

Table 4.20: The linear correlation coefficients, r^2 151

Table A.1: Geometry measurements for plates with $[\pm 22.5/0_2/-22.5/0_2/+22.5/0_2]_S$. 161

Table A.2: Geometry measurements for plates with $[\pm 45/0_2/-45/0_2/+45/0_2]_S$. 161

Table A.3: Geometry measurements for plates with $[\pm 22.5_5/0_5]_A$. 162

Table A.4: Strain gage locations for Plates 11, 21, and 31. 162

Table A.5: Strain gage locations for Plates 32, 13, and 23*. 163

Table B.1: Plate Serial Numbers. The first digit refers to the geometry and the second is the lay-up. 164

Table B.2: Experimental and analytical strain results for Plate 11 168

Table B.3: Experimental and analytical deflection results for Plate 11. 168

Table B.4: Experimental and analytical twist results for Plate 11. 168

Table B.5: Experimental and analytical strain results for Plate 21 169

Table B.6: Experimental and analytical deflection results for Plate 21. 169

Table B.7: Experimental and analytical twist results for Plate 21. 169

Table B.8: Experimental and analytical strain results for Plate 31 170

Table B.9: Experimental and analytical deflection results for Plate 31. 170

Table B.10: Experimental and analytical twist results for Plate 31. 170

Table B.11: Experimental and analytical deflection results for Plate 41. 171

Table B.12: Experimental and analytical twist results for Plate 41. 171

Table B.13: Experimental and analytical deflection results for Plate 22. 171

Table B.14: Experimental and analytical twist results for Plate 22. 172

Table B.15: Experimental and analytical strain results for Plate 32 172

Table B.16: Experimental and analytical deflection results for Plate 32. 172

Table B.17: Experimental and analytical twist results for Plate 32. 172
Table B.18: Experimental and analytical deflection results for Plate 42. 173
Table B.19: Experimental and analytical twist results for Plate 42. 173
Table B.20: Experimental and analytical strain results for Plate 13. 173
Table B.21: Experimental and analytical deflection results for Plate 13. 173
Table B.22: Experimental and analytical twist results for Plate 13. 174
Table B.23: Experimental and analytical strain results for Plate 23*. 174
Table B.24: Experimental and analytical deflection results for Plate 23* 174
Table B.25: Experimental and analytical twist results for Plate 23*. 175
Table B.26: Experimental and analytical deflection results for Plate 33* 175
Table B.27: Experimental and analytical twist results for Plate 33*. 175
Table B.28: Experimental and analytical deflection results for Plate 43* 176
Table B.29: Experimental and analytical twist results for Plate 43*. 176

Abstract

The purpose of the research is to gain an understanding of the material and geometric couplings present in advanced composite turbo-propellers. Twelve pre-twisted laminated composite plates are tested. Three different ply lay-ups (2 symmetric and 1 asymmetric) and four different geometries (flat and 30° pre-twist about the mid-chord, quarter-chord, and leading edge) distinguish each plate from one another.

Four rotating and non-rotating tests are employed to isolate the material and geometric couplings of in an advanced turbo-propeller. The first series of tests consist of non-rotating static displacement, strain, and vibrations. These tests examine the effects of ply lay-up and geometry. The second series of tests consist of rotating displacement, strain, and vibrations with various pitch and sweep settings. These tests utilize the Dynamic Spin Rig Facility at the NASA Lewis Research Center. The rig allows the spin testing of the plates in a near vacuum environment. The tests examine how the material and plate geometry interact with the pitch and sweep geometry of an advanced turbo-propellers.

Chapter 1

Introduction and Review of Present Research

1.1 Introduction

The purpose of this research is understand the material and geometric couplings that are present in advanced composite turbo-propellers. The advanced turbo-propeller offers performance gains over conventional turbo-propellers, such as the one found on the C–130 Hercules (Figure 1.1). The turbo-propeller system on the C–130 has an installed propulsion efficiency of about 80%, which is 30% greater than a typical high bypass turbofan engine found on a large passenger plane [1]. The C–130 Hercules, however, has a top speed of about Mach 0.65 and at higher velocities there is a significant drop in the efficiency due to the compressibility effects at the blade tip. Researchers at NASA have shown that it is possible to increase the cruising speed of the turbo-propeller to the Mach 0.85 regime and maintain its propulsion efficiency over the turbofan engine [1]. This is accomplished by utilizing the advanced turbo-propeller or prop-fan design (Figures 1.2 and 1.3). The prop-fan incorporates thin, highly swept blades to reduce the effects of compressibility and noise at high speed cruise. Successful implementation of the prop-fan would make it a viable candidate for the commercial airline market that would lead to lower direct operating costs for the airlines and significant savings in the fuel consumption of the United States.

The shape and thinness of the advanced turbo-propeller blade, however, creates its own set of problems with vibrations, deflections, and noise. Any slight imbalance in the spinning propellers and turbofans introduces vibratory behavior that will affect not only

the individual blades but all of the existing structures that surround it. At worst these vibrations lead to catastrophic failure at a resonant frequency or, at the very least, a shorter life span for the structure due to fatigue. The sweep and thinness of the blade also make the structure especially sensitive to centrifugal forces. These forces cause the bowed shape of the advanced turbo-propeller to flex towards the leading edge, which creates compressive forces on the hump of the blade (Figure 1.2). Finally, another design obstacle facing engineers is the noise of propeller driven systems. High bypass turbofan engines have their rotor assemblies enclosed in a duct that insulates the outside environment from the noise. All of these problems have lead engineers to implement the use of advanced composite materials into the propeller blade design. The composite blades are quieter and lighter than their aluminum counterparts [2]; and because of the fibrous nature of composites, the engineer has some control over the dynamic behavior of the plate. Furthermore, since the composite blades are manufactured in a mold, they are cheaper and easier to produce than their aluminum counterparts, which require computer controlled machining processes for each individual blade.

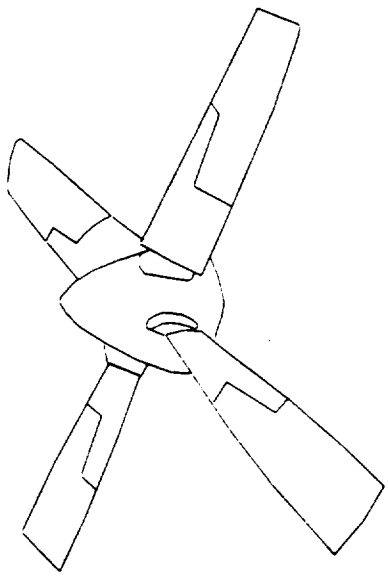

Figure 1.1: Propeller system from a C-130 Hercules.

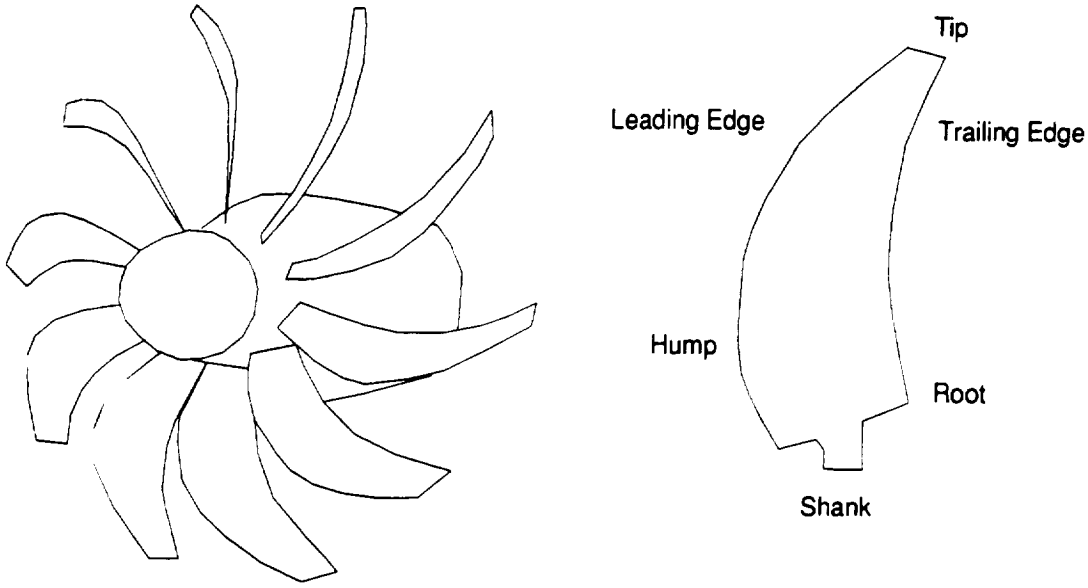

Figure 1.2: Propeller system from the Advance Turboprop Program.

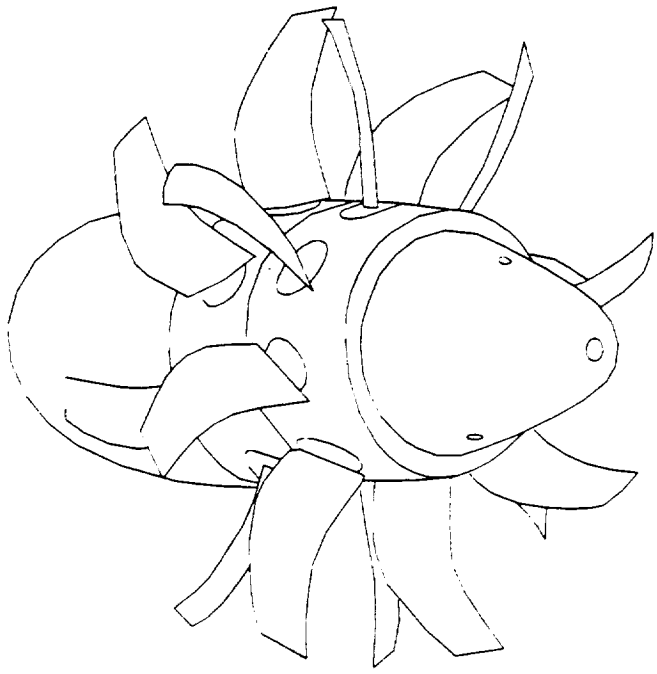

Figure 1.3: Implementation of the counter-rotating prop-fan.

The problem for the scientists and engineers in the design of advanced turbo-propellers is to accurately predict the deflections and natural frequencies of the spinning and non-spinning blades. In order to better understand the physics, each element that

affects the behavior of the advanced composite turbo-propeller–pitch, sweep, geometry, and material coupling–will be examined independently and in various combinations together. This is done by utilizing cantilevered, pre-twisted, composite plates (Figure 1.4). The pre-twisted plate shown in Figure 1.4 has a length (l), width or chord length (c), thickness (t), and a constant linear pre-twist (ϕ) through the length. The plate is spun about a vector parallel to the y-axis. The effects of pitch are examined by rotating the plate about the x-axis, and sweep is implemented by rotating the plate in the plane of the spin axis about some point (Figure 1.5). The focus of this research is to gain a physical understanding on behavior of the turbo-propellers and to develop a comprehensive set of experimental data on the behavior of spinning and non-spinning pre-twisted, composite plates. The database will be used to correlate new analytical codes developed by researchers and engineers.

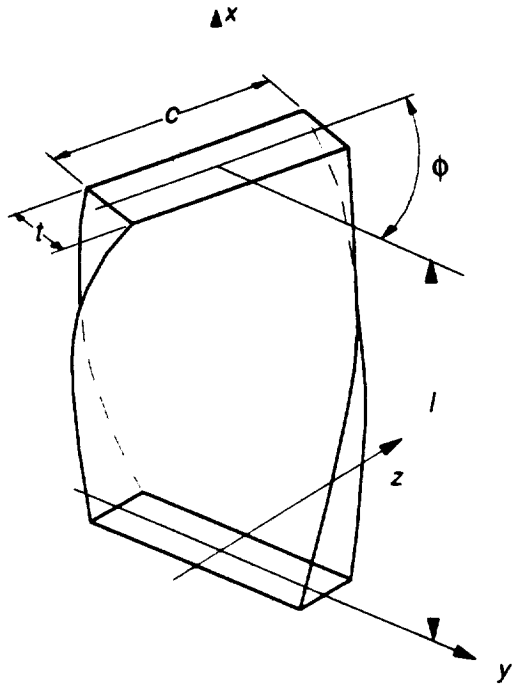

Figure 1.4: A pre-twisted, cantilevered plate.

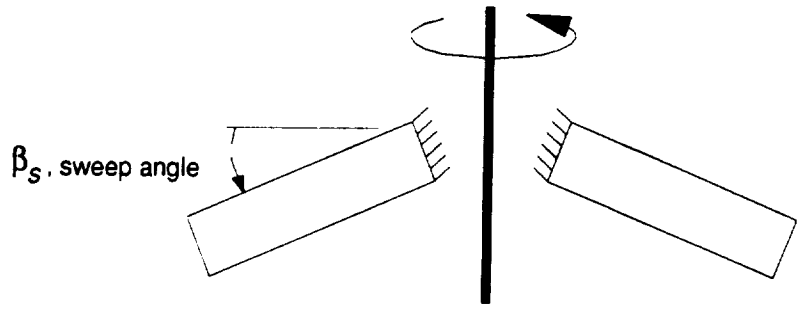

Figure 1.5: Capturing the effects of sweep.

1.2 Review of Literature on the Experimental Behavior of Pre-Twisted Plates

This section presents a review of the experimental database on the natural frequencies of cantilevered isotropic and composite plates. There exists a large amount of experimental data on the non-spinning vibrations of pre-twisted, cantilevered, isotropic plates and only a limited amount on the spinning natural frequencies. The literature on composite plates is restricted to the non-spinning results of the flat plate geometry.

Carnegie [3] measured the first six bending and first four torsion frequencies of six plates with an aspect ratio ($l/c = 6$), thickness ratio ($c/t = 14.7$), and pre-twist angles of $\phi = 0°$, 15°, . . ., 90°. Dawson, Ghosh, and Carnegie [4] measured the first five non-spinning natural frequencies of 24 blades with two aspect ratios (l/c = 3 and 6), with all the combinations of three thickness ratios (c/t = 8, 4, and 2) and four pre-twist angles (ϕ = 0, 30, 60, and 90 degrees). They found the bending frequencies, with the exception of the first mode, to decrease with the pre-twist angle and the first torsion mode to increase. There was a slight increase in the first bending mode, but for the most part the 1st Bending frequency was largely insensitive to the twist. For the second torsion mode the frequencies initially decreased upon pre-twist, but then rose again for pre-twist angles greater than 90°.

MacBain [5] investigated pre-twisted plates with an aspect ratio ($l/c = 2.33$), a thickness ratio ($c/t = 33.3$), and with $\phi = 0°$, 12°, 17°, 23.5°, 30°, and 38°. The first 10 non-spinning natural frequencies and mode shapes were determined using holographic interferometry. Leissa, MacBain, and Kielb [7] presented a summary of analytical and experimental studies on the vibrations of pre-twisted cantilevered plates, and in a follow-up paper, MacBain, Kielb, and Leissa [8] conducted non-spinning vibration tests on thirty aluminum plates with the following geometric parameters: aspect ratios, $l/c = 1$, 2, and 3; thickness ratios, $c/t = 5$, 20; and pre-twist angles, $\phi = 0°$, 15°, 30°, 45°, and 60°. They measured as many as 12 natural frequencies and mode shapes for the plates with aspect ratios ($l/c = 2$ and 3), and up to 6 modes for the plate with $l/c = 1$ and $c/t = 5$. Kielb, Leissa, and MacBain [9] concluded the study by making comparisons among 19 different analytical models and the experimental results; a complete list of the results is given in Kielb, Leissa, MacBain, and Carney [10]. They found a large increase in the torsion frequencies as the tip twist increased from 0°. The bending modes decreased with the twist but the rate of decrease was not as great as the rate of increase in the torsion modes. Finally, the support compliance became significant for the plates with lower aspect ratios and length to thickness ratios (l/t).

Nagamatsu and Michimura [6] investigated the spinning and non-spinning behavior of a flat plate with $l/c = 2.37$ and $c/t = 15$, and a pre-twisted plate with $l/c = 2.18$, $c/t = 20$, and $\phi = 90°$. They measured the first 5 spinning and non-spinning natural frequencies and mode shapes for the flat plate and the first 4 for the pre-twisted one. All of the frequencies for both plates were shown to increase with the rotational speed. Brown, Kielb, Meyn, Morris, and Posta [11] presented results for a flat, steel plate with an aspect ratio ($l/c = 3$) and a thickness ratio ($c/t = 20$). The first 5 spinning and non-spinning natural frequencies and mode shapes were measured. They also showed the first five natural frequencies to increase with the rotational speed.

Crawley [12] presented the first three non-spinning natural frequencies and mode shapes for six flat, cantilevered composite plates. The six plates had aspect ratios (l/c = 1 and 2), a thickness ratio (c/t = 71.1), and the following three lay-ups: $[0_2/\pm30]_S$, $[0/\pm45/90]_S$, and $[\pm45/\mp45]_S$. For an aspect ratio of 2 and $[\pm45/\mp45]_S$ lay-up, there was a switching of the second and third natural frequencies from what was observed for all the other plates including an isotropic aluminum plate. That is, for all the other plates in his study, the second and third natural frequencies were 1st Torsion and 2nd Bending modes, respectively. For the $[\pm45/\mp45]_S$ lay-up (l/c = 2), the second and third natural frequencies were the 2nd Bending and 1st Torsion modes, respectively. Jensen, Crawley, and Dugundji [13] also presented the first three natural frequencies for the same material for an aspect ratio (l/c = 4), a thickness ratio (c/t = 94.8), and the following seven lay-ups: $[0_2/90]_S$ and $[\theta/0]_S$ where θ = 15°, 30°,. . ., 90°. The two bending frequencies decreased as θ was increased from 0° to 90° while the 1st Torsion mode reached a maximum at θ = 30°.

1.3 Objectives of Present Research

The purpose of the present research is to understand the linear and nonlinear material and geometric couplings in spinning and non-spinning blades, and to continue to expand the experimental database on the behavior of pre-twisted laminated composite plates. The five main goals of this research are to: (1) design and fabricate the graphite/epoxy plates and the test fixtures ; (2) perform static displacement and strain tests; (3) steady-state rotating displacement and strain tests; (4) non-rotating vibratory tests; and (5) rotating vibratory tests.

The plates in this study are unique from other studies because the effects of the pre-twist axis location and both symmetric and asymmetric stacking sequences are investigated. For the plate in Figure 1.4, the pre-twist axis or x-axis divides the width of the plate into two equal sections, that is the distance from one edge of the plate to the pre-

twist axis is $\frac{c}{2}$. The plates in this research have their pre-twist axis defined along the mid-chord $\left(\frac{c}{2}\right)$, quarter-chord $\left(\frac{c}{4}\right)$, and the leading edge (Figure 1.6). The mid-chord geometry is typical of ducted turbofan blades, the quarter-chord geometry for aviation propellers, tiltrotors, helicopter, and wind turbine blades. The rectangular plates have a length ($l = 9$ inch), chord ($c = 3$ inch), a thickness ($t = 0.1$ inch), and pre-twist angles ($\phi = 0°$ and 30°). The composite plates have three stacking sequences–2 symmetric and 1 asymmetric, which with the four different geometries gives a total of 12 plate sets.

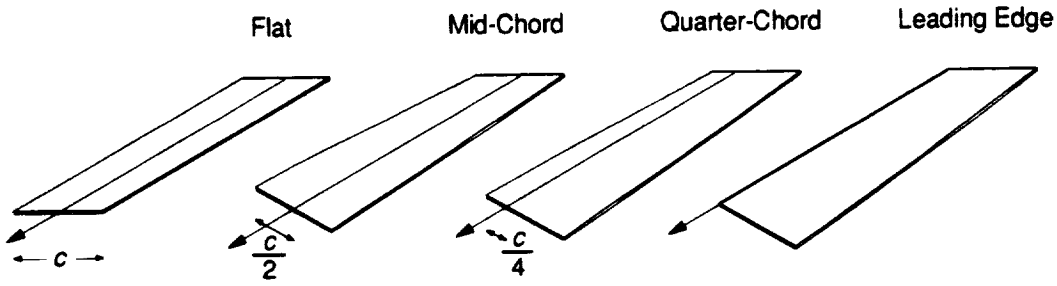

Figure 1.6: Plate geometries.

The four experimental tests are outlined as follows:

1. Non-rotating static strain and displacement tests. A point load is placed at one of the free tip corners of the cantilevered plate. The deflections and twist are measured at the tip and the strains are measured at the root.
2. Steady-state rotating displacement and strain tests. The plate's deflection, twist, and strain are measured versus the rotational speed. The plates are spun in a vacuum to eliminate any aerodynamic forces.
3. Non-rotating vibratory tests. Six natural frequencies and mode shapes are measured and characterized using two methods: (1) an impact hammer technique and (2) holographic interferometry.

4. **Rotating vibratory tests**. The natural frequencies and mode shapes of the plates are measured as a function of the rotational speed. The plates are spin tested in vacuum for these tests.

Chapter 2

Experimental Equipment and Procedures

This chapter describes the equipment and procedures used for this research project. The first section begins with a description and history of the unique clamping fixture used to hold the plates during all the tests. Second, a description of the graphite/epoxy plates is given. The third section describes the non-rotating modal and static displacement tests at the Aerospace Structures Laboratory at the University of California San Diego. The fourth and final section describes tests conducted at the Laser Holography Laboratory and the Dynamic Spin Rig Facility at the NASA Lewis Research Center. Non-spinning vibration tests are conducted at the Laser Holography Laboratory and all the rotating tests are performed at the Dynamic Spin Rig Facility.

2.1 Clamping Assembly

The first series of experiments called for the spin testing of a number of different plate sets where each set embodied a combination of pre-twist, pre-twist axis location, and lay-up. Because of the large number of plates involved it was worthwhile to design a clamping fixture that would keep the plate design as simple as possible. The clamping design used to hold the plates needed to accomplish two things: (1) securely hold the plates within the test assembly at large rotational speeds and (2) facilitate the changing of different plate sets. There was a total of four design iterations that finally ended with a satisfactory clamping assembly (Figure 2.1). The torque setting for the four vertical screws that go through the plate is 110 in-lb. For the four horizontal screws, the top two screws and bottom two screws are torqued to 110 in-lb. and 65 in-lb. respectively.

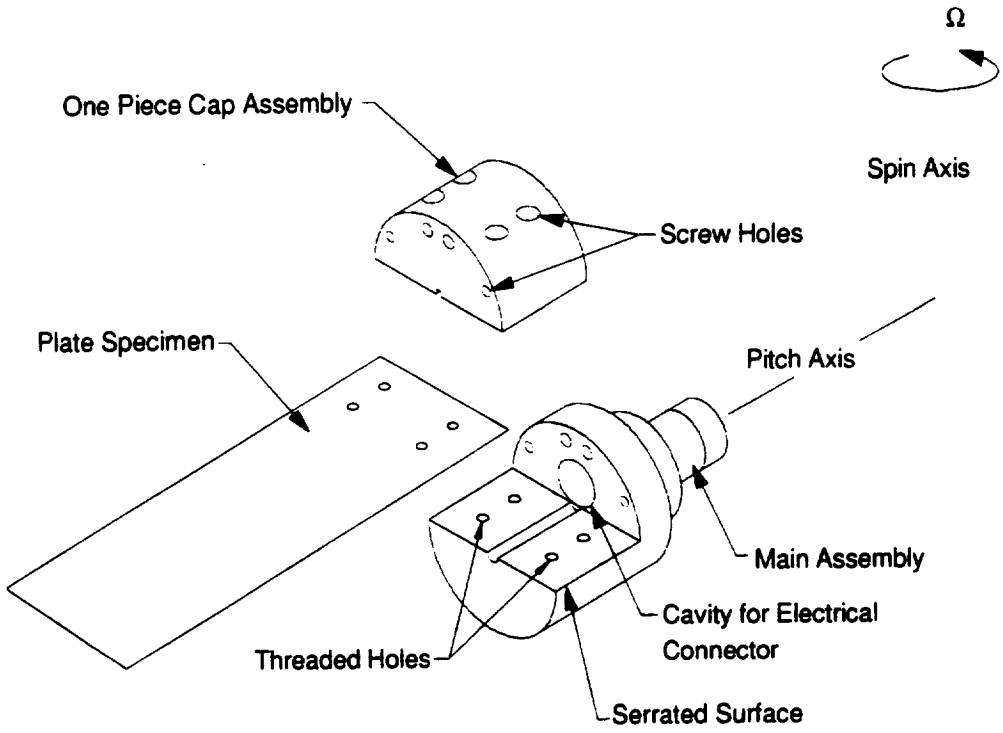

Figure 2.1: The clamping assembly used during the spin tests.

The clamping force is provided by socket head cap screws that squeeze the clamping jaws together. Holes are drilled into the plates to accommodate the screws. If the plates begin to slip out of the jaws then they would load up the screws transversely. If the plates begin to butt up against the screws then a stress concentration would form at the plate holes and would tear out at the screw holes. The intent is to have the centrifugal forces flow through the plate, through the entire clamping area, and then through the rest of the spin rig assembly. An 0.875 inch diameter cavity is drilled into the front of the clamping assembly to house an electrical connector.

Because the level of the friction forces generated by the clamping assembly was unknown, a series of tests was ongoing during the design. An American Chain and Cable Company (ACCO) Tensile-Compression Machine manufactured by the Wilson Instrument Division of ACCO (Model No. 2612) was used to simulate the centrifugal forces on the plates and to test the soundness of the clamping design.

No graphite/epoxy samples were available during the initial designs. Aluminum was used to model the composite plates and to test the clamping assemblies on the Tensile-Compression Machine. At this stage of the project the final dimensions of the plates had not yet been decided. It was known that the cantilevered area of the plate would have a width and length of 3 inches and 9 inches, respectively, with either a 3x1 or 3x2 in^2 clamping area and a thickness of about 0.1 inch.

Using a lumped mass approach, the centrifugal force on an aluminum plate can be expressed by

$$F_c = m\Omega r^2 \tag{2.1}$$

where m is the mass, Ω is the rotational velocity and r is the perpendicular distance of the lumped mass to the spin axis. The specific weight of aluminum is 0.098 lb/in^3 and $r = 9.882$ inches and 10.882 inches for a plate with a length of 10 inches and 11 inches, respectively. The thickness of the aluminum plate is a standard thickness of 0.125 inch. The maximum rotational speed of the spin rig facility is 20,000 rpm. Figure 2.2 shows a graph of the centrifugal forces on an aluminum plate as a function of rotational speed.

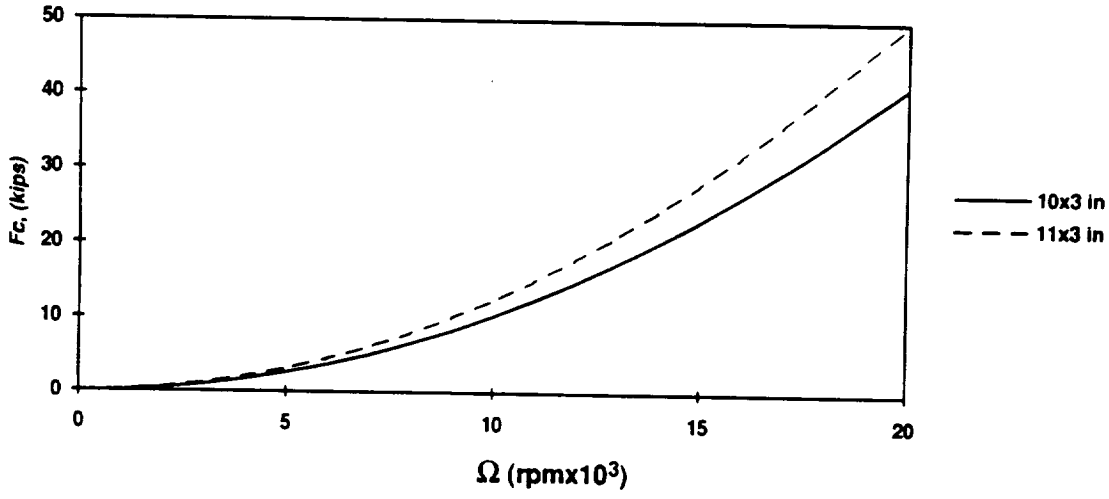

Figure 2.2: The centrifugal force on a10x3 inch and 11x3 inch aluminum plate with a thickness of 0.125 inch.

2.1.1 Clamp 1

The first design of the clamping fixture had a 1x3 in^2 clamping area for the plate (Figure 2.3). This clamp was constructed out of 4340 steel and had two socket head cap screws to squeeze down onto the plate; the plate had two holes drilled into it for the screws.

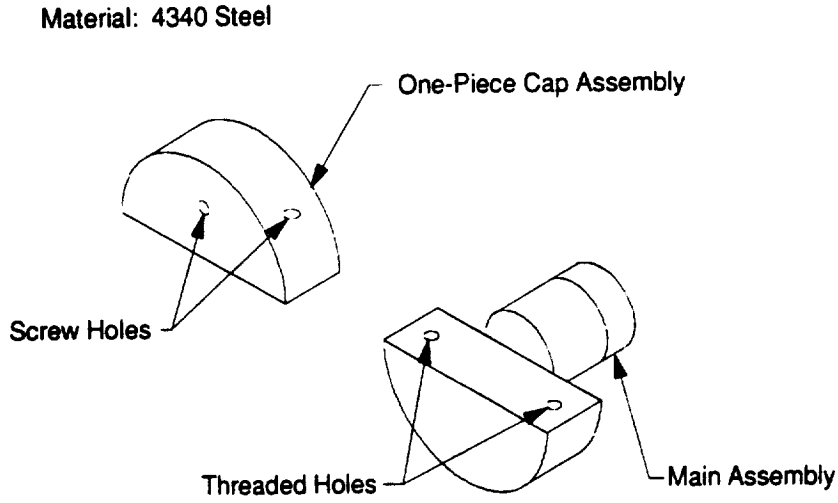

Figure 2.3: Clamp 1 features a 1x3 in^2 clamping area and is constructed out of 4340 Steel.

2.1.2 Test Description and Results for Clamp 1

A special adapter was machined so that the clamping assembly could be set up on the Tensile-Compression Machine. Five aluminum plate specimens (6061-T4) were prepared for this initial test (Figure 2.4). Each plate had a 1x3 in^2 clamping area to accommodate Clamp 1. The plates had an overall length of 12 inches and a thickness of 0.0625 inch. Rectangular cutouts were made at the other end of the plate for the Tensile-Compression Machine.

Table 2.1 gives a summary of the results of the five plate specimens for this test where the strain rate is the rate at which the tensile force is being applied on the Tensile-

Compression Machine. It is evident from Table 2.1 that Clamp 1 is not providing any frictional force to hold the plate under tension. The plate slips out of the clamp at very low tensile forces and rips out at the screw holes.

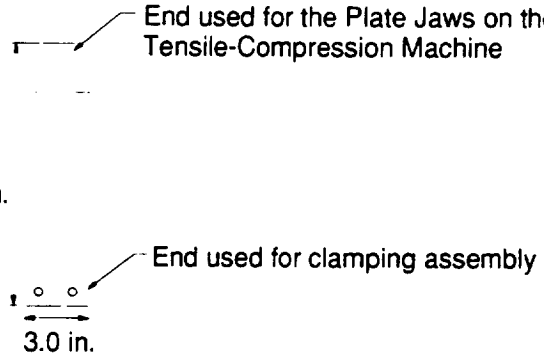

Figure 2.4: Description of aluminum specimens used to test the first clamping assembly.

Table 2.1: Summary of the test results for the first clamping assembly. Aluminum plates (6061-T6) were used to test the first clamp.

Plate	Measured Failure Force, (lbf)	Description of Failure
1	2346	Plate ripped out at the screw holes
2	2330	Plate ripped out at the screw holes
3	2350	Plate ripped out at the screw holes
4	2271	Plate ripped out at the screw holes
5	2224	Plate ripped out at the screw holes
Strain Rate = 0.03 strains/sec		

2.1.3 Clamp 2

Several changes were incorporated into the design of Clamp 2 (Figure 2.5). To reduce the weight, the material for Clamp 2 was changed from 4340 steel to 7075-T6 aluminum. Geometry changes had also occurred so that this second clamp could mate with the setup at the Dynamic Spin Rig Facility at the NASA Lewis Research Center. The clamp still utilized a 1x3 in^2 clamping area to retain the plate. Holes and grooves were

incorporated into the design so that the clamping assembly could house the instrumentation of the composite plates.

A more fundamental change consisted of serrating the surface of the clamp that contacted the plate. This design feature was inspired by the equipment used during the initial tensile tests with Clamp 1. The plate jaws for the Tensile-Compression Machine were specifically designed to hold plates under tensile forces as high as 30,000 lbf. The jaws on this clamping assembly for the Tensile-Compression Machine featured a surface of teeth that dig into the plate specimen and retain the plate specimen just using frictional forces (Figure 2.6). The serrations on the plate jaws for the Tensile-Compression Machine ran at ±30° from the front. The serrations on the Clamp 2, however, only ran in a direction parallel to the front of the clamping assembly. Lastly, tapered pins were added to the design to help set the pitch angle at the Dynamic Spin Rig Facility.

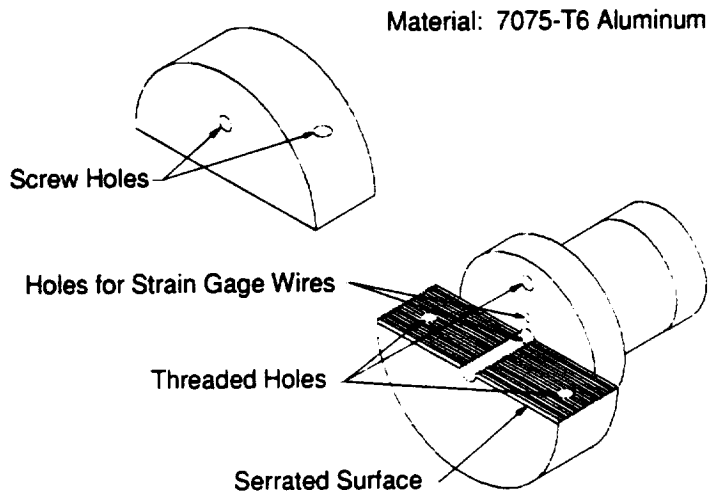

Figure 2.5: Clamp 2 features a 1x3 in^2 serrated surface that greatly enhances the gripping ability of the clamp.

2.1.4 Test Description and Results for Clamp 2

The next series of pull tests on Clamp 2 checked the gripping enhancements of the serrated surface. The aluminum (6061-T4) plate specimens to be tested in Clamp 2 also differed from the first series of tests on Clamp 1. The first three plates to be tested had triangular cutouts in them (Figure 2.7); this was done to force the plates to fail at a specified load.

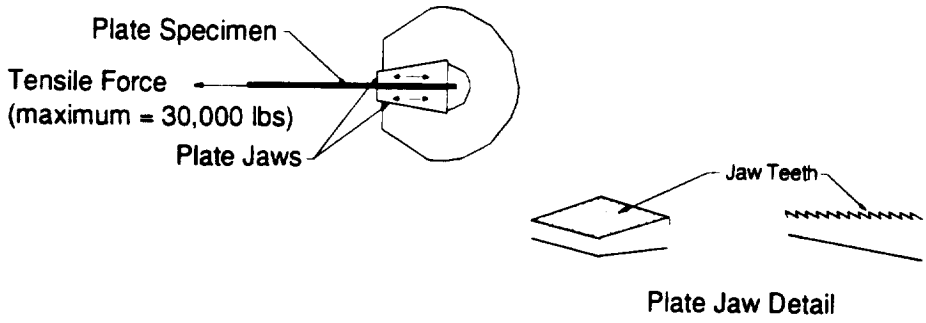

Figure 2.6: Plate clamping assembly for the Tensile-Compression Machine. The plate jaws for the Tensile-Compression Machine feature a serrated surface at ±30°.

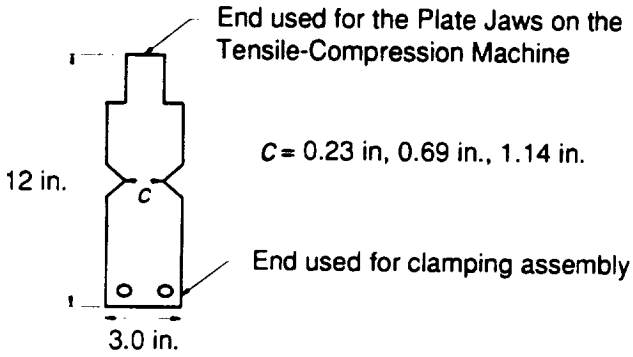

Figure 2.7: Plate specimen design used to test Clamp 2

Table 2.2 summarizes the results of the tests on Clamp 2. As Table 2.2 indicates, the serrated surface greatly enhances the gripping mechanism. The test results show that the plates are not slipping and are securely held in place by the new clamping design. The

tests also show, however, that the screws and the 1x3 in^2 clamping area are inadequate at holding the plates at high tensile forces. For an aluminum plate with 10x3x0.125 inch dimensions, the highest rotational speed the Clamp 2 can achieve without a factor of safety is 9000 rpm (Figure 2.2).

Table 2.2: Tensile test results and plate descriptions for clamp 2.

Plate	Width, a (in)	Predicted Failure Force (lbf)	Experimental Failure Force (lbf)
1	0.23	1000	1090
2	0.69	3000	3280
3	1.14	5000	5470
4	3.00	13,000	Screws on the clamping assembly failed at ~8,300 lbf

Plate Thickness = 0.125 in
Strain Rate = 0.03 strains/s

Material Properties for Aluminum 6061-T4
Yield Strength, S_y = 21 ksi
Ultimate Strength, S_u = 35 ksi.

2.1.5 Clamp 3

The third design of the clamping assembly was constructed out of 7075-T6 Aluminum (Figure 2.8). The clamping area of Clamp 3 had been doubled to 2x3 in^2 and the serrated surface introduced in the design of Clamp 2 was still present. Four screws squeezed the plate specimen between the main assembly and the cap assembly, and four additional screws held the clamping assembly axially (Figure 2.1). Two cap assemblies were machined, a regular one-piece cap assembly as in Figure 2.1 and a wedge design similar to the plate jaws on the Tensile-Compression Machine (Figure 2.6). It was hoped that this wedge assembly would further enhance the frictional forces on the plate specimen. The angle on the wedge was 30°; a shallower angle was not possible because the vertical component of the centrifugal force would have been too high and would load

the four vertical screws. The tensile tests determined which of the cap assemblies were used; the one-piece cap assembly was the preferred choice because of its simplicity.

Because of the relative softness of aluminum all the screw holes in Clamp 3 were replaced with Helicoils; this extended the life of the screw holes during the plate changes. At this point during the project graphite/epoxy plates were available and were used to test the gripping ability of the clamping assemblies. The connectors that would be used for the strain gages were ordered and a hole was drilled into the main assembly of Clamp 3 to house the connector.

Recall that the main gripping mechanism of the clamping assembly was friction. If, however, the plate did begin to slip and load up against the screws, then the plate holes should butt up against a smooth surface and not a threaded one. Contact with a threaded surface would create more of a stress concentration and would accelerate catastrophic failure. The screws were modified so that if the plate did begin to slip, it would butt up against a smooth surface.

Material: 7075-T6 Aluminum

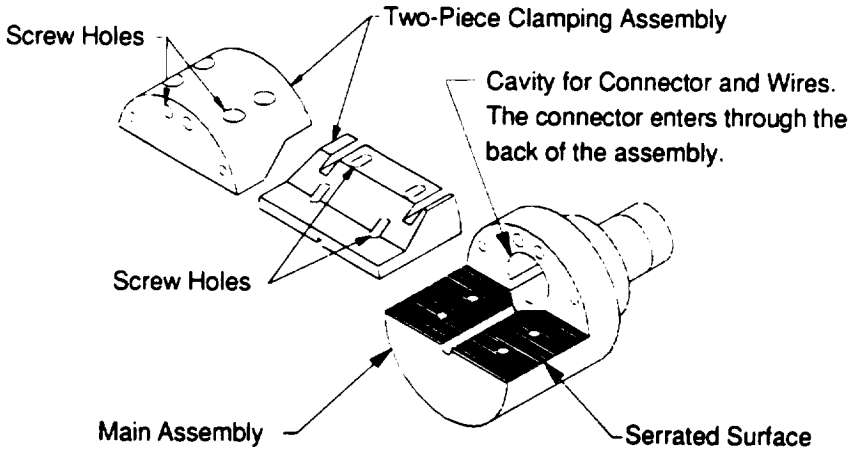

Figure 2.8: Clamp 3 utilizing a wedge design.

2.1.6 Test Description and Results for Clamp 3

Graphite/Epoxy test specimens were available for the tests for Clamp 3 tests. The heaviest of the plates weighed in at 0.196 lbf. Using a lumped mass approach, Equation (2.1), a plot of the centrifugal force as a function of rotational speed for this composite plate was calculated (Figure 2.9). The maximum speed at which the plates were to be tested was determined analytically at 10,000 rpm. The centrifugal force on the heaviest plate at this speed was 6.04 kips. With a factor of safety of 2, the minimum tensile force Clamp 3 needed was 12.1 kips (Figure 2.9).

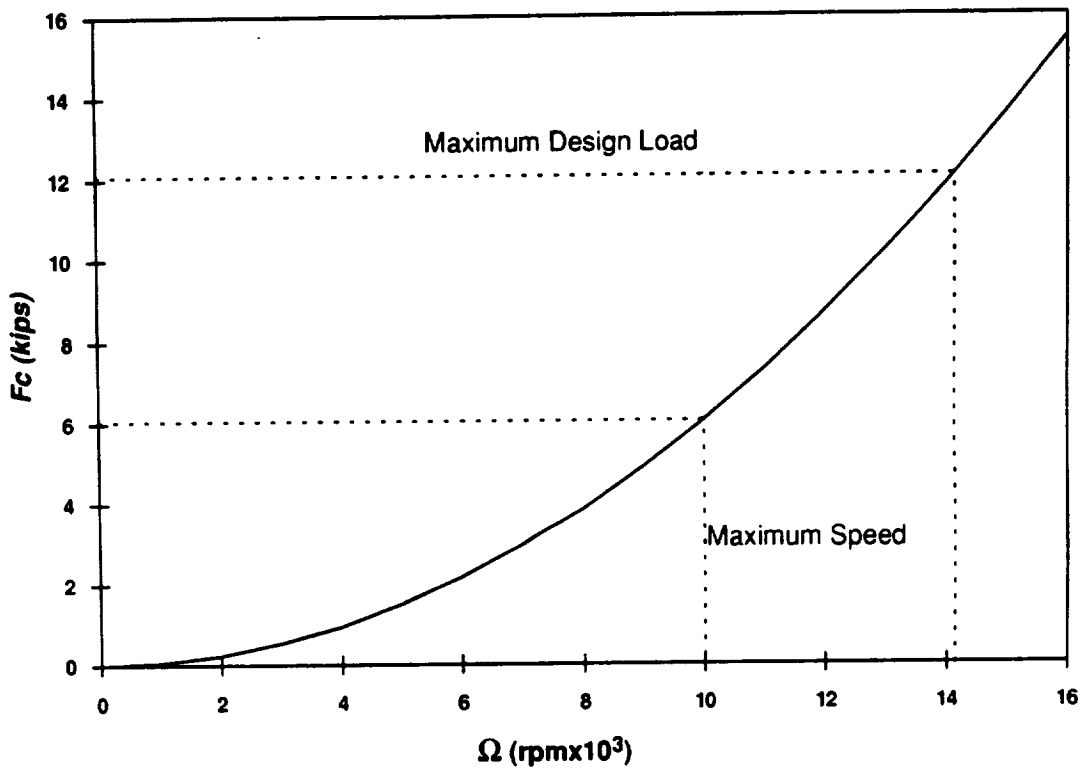

Figure 2.9: The centrifugal force on the heaviest graphite/epoxy plate (weight = 0.196 lbf).

The first and second tensile tests for Clamp 3 were with aluminum plates (6061-T4) with a thickness of 0.125 inch with the one-piece cap assembly (Figure 2.1) and then

the two-piece (Figure 2.8). Clamp 3 was able to hold the aluminum plates at tensile forces of up to 10,000 lbf with both cap assemblies. The plate was not tested to failure; the predicted failure for this plate was 13,000 lbf. Subsequent tests for Clamp 3 involved using the available extra flat graphite/epoxy test specimens. Problems arose immediately when the graphite/epoxy test specimens were placed in the plate jaws for the Tensile-Compression Machine. The graphite/epoxy plates were not as ductile as the softer aluminum plates and the teeth of the plate jaws would not dig into the composite material. The graphite/epoxy plates and Clamp 3 were unable to be tested in the Tensile-Compression Machine because the composite plates would slip out of the plate jaws of the Tensile-Compression Machine.

On the basis of discussions with engineers from Composite-Optics Incorporated, soft 1/32-inch fiberglass doublers are bonded onto the end regions of the graphite/epoxy test specimens to provide a better grip surface for the plate jaws. This preparation is standard for composites engineers whenever they perform tensile and compression tests on composite materials. Figure 2.10 shows a typical graphite/epoxy test sample with the fiberglass doublers. A shallow angle of about 10° or 15° is machined onto the doubler to eliminate the stress concentration at the interface between the doubler and the test specimen. Optimal failure occurs at the middle of the sample.

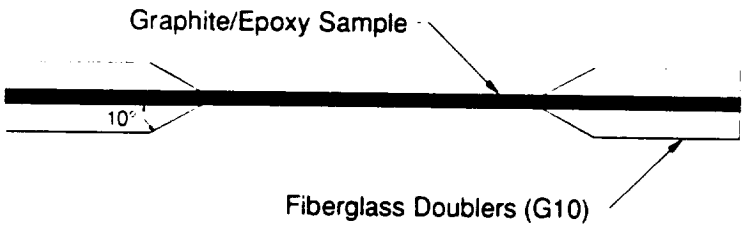

Figure 2.10: A typical graphite/epoxy tensile-compression sample.

2.1.7 Clamp 4

There were three minor changes made in the fourth clamp design. First, the serrated surface of the clamping assemblies was cut at 0° and 90°; this was done to increase the surface area contact on the composite plate. Second, the recessed region for the electrical connector was moved from the hollowed out assembly back (Figure 2.8) to a cavity machined adjacent to the clamping surface. This modification was done to move the connector closer to the test plates and to strengthen the rear of the main assembly by reducing the hole from 0.875 inch to 0.25 inch diameter. Third, all sharp edges of the clamping assembly were rounded.

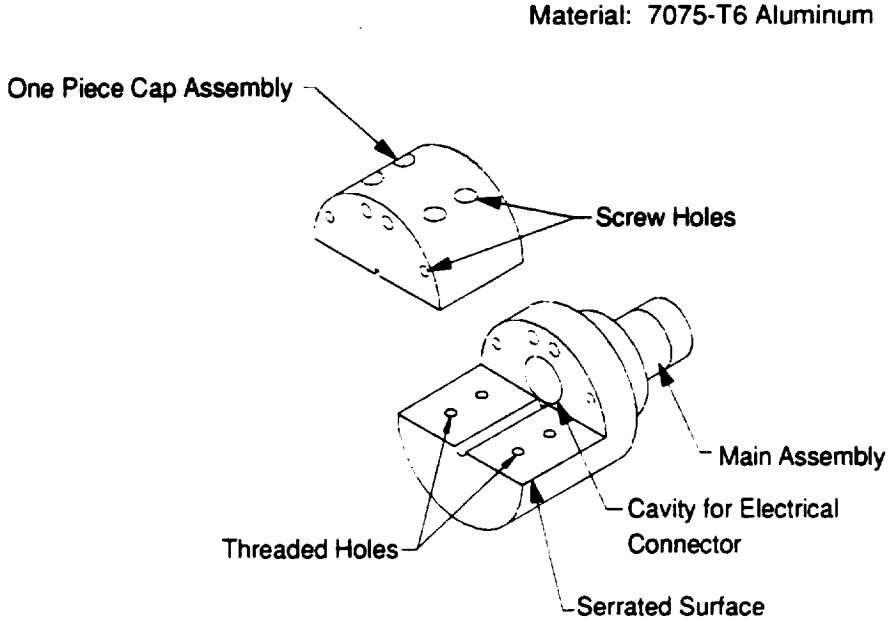

Figure 2.11: Main assembly configuration for Clamp 4.

2.1.8 Test Description and Results for Clamp 4

Two 3x6x0.10 inch graphite/epoxy plates with fiberglass doublers were prepared for the testing of Clamp 4. The stacking sequences of the two laminates were $[\pm 22.5/0_2/-22.5/0_2/+22.5/0_2]_S$ and $[\pm 45/0_2/-45/0_2/+45/0_2]_S$. Fiberglass doublers (G10,

2x3x$^{1}/_{32}$ inch) were epoxied (Scotch-Weld 3M 2216 A/B epoxy) onto each test specimen. Tapered doublers were not used.

Two complete assemblies of Clamp 4 and a graphite/epoxy test specimen were placed in the Tensile-Compression Machine. The upper Clamp 4 assembly had a one-piece cap assembly (Figure 2.11) and the lower clamp had the two-piece cap assembly (Figure 2.8). The two cap designs were assessed up to the maximum design load of 13,000 lbf.

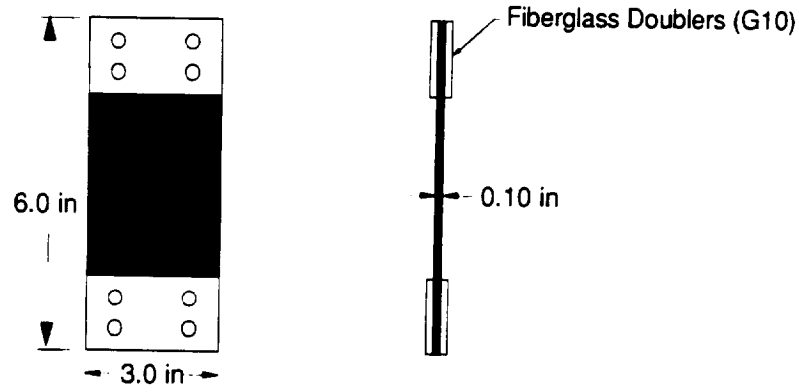

Figure 2.12: Graphite/Epoxy test specimen for the tensile tests on Clamp 4. Two flat plate specimens were prepared with $[\pm\theta/0_2/-\theta/0_2/+\theta/0_2]_S$ with θ = 22.5° and 45°.

Tables 2.3 and 2.4 present the results of the two tests conducted on Clamp 4. Visual and acoustic methods were used to check the clamp assembly for slippage and laminate failure.

It was determined from the tests on Clamp 4 that the one-piece cap assembly worked equally as well as the two-piece one at tensile forces up to 14,000 lbf. More importantly, the results from Tables 2.3 and 2.4 show that the combination of the 2x3 in^2 clamping area, the serrated surface of the clamping assemblies, and the G10 fiberglass doublers on the graphite/epoxy test specimens work together to hold the plates at forces as high as 14,000 lbf thus exceeding the 13,000 lbf goal. The fourth design iteration of the

clamping assembly with the one-piece cap assembly has successfully passed the tensile tests and was used for all the spinning tests at the NASA Lewis Research Center.

Table 2.3: Tensile test results for the plate specimen with $[\pm 22.5/0_2/-22.5/0_2/+22.5/0_2]_S$.

Tensile Force, (lbf)	Strain Rate, (strains/sec)	Visual/Acoustic Check of the Plate
$0 \rightarrow 3000$	0.03	OK, no slipping or cracking
$3000 \rightarrow 14{,}000$	0.02	OK, no slipping or cracking. Plate has reached maximum desired tensile force.

Table 2.4: Tensile test results for the plate specimen with $[\pm 45/0_2/-45/0_2/+45/0_2]_S$.

Tensile Force, (lbf)	Strain Rate, (strains/sec)	Visual/Acoustic Check of the Plate
$0 \rightarrow 14{,}000$	0.02	OK, no slipping or cracking. Plate has reached maximum desired tensile force.

2.2 Plate Description

This section gives a physical description of the graphite/epoxy plates used for the research project. It starts with a description of the geometries and the material properties of the composite plates. It also discusses the lay-up process, the stacking sequences, and the problems with the asymmetric laminates. The second part lists the experimental procedure used to determine the quality of plates. The third subsection is a description of the method to measure the geometry. The final section describes the strain gages that are bonded to the plates and the circuit equations used for the tests.

2.2.1 Plate Geometry, Material Properties, and Lay-up

The thin, swept, twisted shape of an advanced turbopropeller is modeled as a thin, twisted rectangular plate. The dimensions of the plates in this experiment are 3x9x0.10 inch with a twist that varies linearly with the length. The twist level is 3.333°/in (0.05818 rad/in) or 30° over the entire length. Four different plate geometries are investigated: a flat plate; a 30° pre-twisted plate about the mid-chord; a 30° pre-twisted plate about the

quarter-chord; and a 30° pre-twist about the leading edge. Figure 2.13 gives a physical description of the four plate geometries as well as the positive ply orientation angle.

The flat plate serves as a base point for the study while the other geometries investigate the effects of adding pre-twist. Previous studies [3–14] only examine the mid-chord geometry. The 3 different pre-twist axis locations (mid-chord, quarter-chord, and leading edge-chord) investigate the effects of placing the pre-twist axis at different locations. The quarter-chord and leading edge-chord geometries introduce a geometric asymmetry which under rotating conditions would investigate an extension-bend-twist coupling. The pre-twist axis locations are chosen based on existing advanced turbopropeller designs and are typical of the wide variety of spinning structures in use today, from turbofans and advanced turbopropellers to helicopter and tiltrotor blades. The mid-chord geometry will produce large levels of extension-twist coupling. The quarter-chord geometry will exhibit extension-bend-twist behavior as it rotates, and the leading edge-chord geometry will exhibit larger levels of extension-bend coupling and less extension-twist coupling.

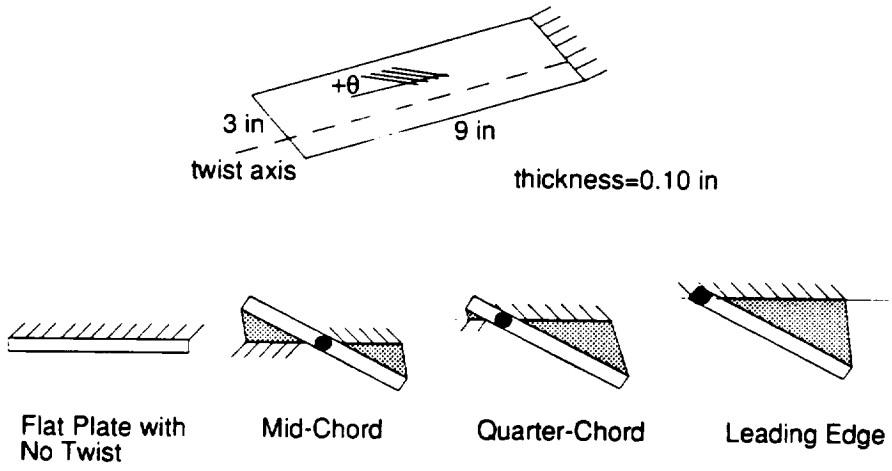

Figure 2.13: The dimensions and geometry of the graphite/epoxy plate specimens.

The plates are constructed of high-strength unidirectional graphite/epoxy material. The material property list from the manufacturer is incomplete; furthermore, the values for the composite plates may differ because of the curing process. Using the manufacturer's material properties, the rule of mixtures [15], and scaling the experimental first bending and first torsion natural frequencies, the material properties are calculated and listed in Table 2.5. The formulas to calculate the material properties of a fiber/matrix system are given by

$$E_{11} = E_f V_f + E_m V_m,$$

$$E_{22} = E_{33} = \frac{E_m}{V_m E_f + V_f E_m},$$

$$G_{12} = G_{13} = \frac{G_m G_f}{V_m G_f + V_f G_m},$$

$$G_{23} = \frac{E_{22}}{2(1+\nu_{23})}$$

and

$$\nu_{12} = \nu_{13} = V_m \nu_m + V_f \nu_f$$

where

E_{11} = the apparent Young's modulus in the direction of the fibers,

E_{22} = the apparent Young's modulus in the direction transverse to the fibers,

G_{12} and G_{13} = the in-plane shear modulus of a lamina,

ν_{12} and ν_{13} = the major Poisson's ratio,

E_f = the Young's modulus of the fiber,

ν_f = the Poisson's ratio of the fiber,

E_m = the Young's modulus of the fiber,

ν_m= the Poisson's ratio of the fiber,

$$V_f = \frac{\text{Volume of Fibers}}{\text{Total volume of composite}},$$

$$V_m = 1 - V_f,$$

and the Poisson's ratio, ν_{23}, is assumed a value of 0.40.

Table 2.5: Material properties of the graphite/epoxy plates.

Material Property	Graphite/Epoxy Plates
E_{11}	22.43 Msi
$E_{22}=E_{33}$	1.45 Msi
$G_{12}=G_{13}$	917 ksi
G_{23}	518 ksi
$\upsilon_{12}=\upsilon_{13}$	0.25
υ_{23}	0.40

The plates are fabricated by laying up by hand the graphite/epoxy prepreg onto aluminum molds (Figure 2.14). Three aluminum molds are constructed for each of the three pre-twisted plate geometries; no special molds are needed for the flat plates. The aluminum molds are machined using a Bridgeport Numerically Controlled (NC) Mill at the Department of Engineering Machine Shop at the University of California San Diego. The program MasterCam version 3.21 by CNC Software Inc. is used to control the NC Mill. The prepreg plies are laid over the area indicated in Figure 2.14. The dimensions of this area encompass the final shape of the plate plus a 1.5 inch border around it. The plate is cured this way in order to insure a uniform ratio of fibers-to-matrix. After the curing process, the laminate is cut to its final dimensions with a router. The plate is then cut down the middle that results in a pair of plates (Figure 2.14). Finally, four holes are drilled into the flat area of each plate so that each plate can be placed into the clamping assembly.

General Dynamics-Convair performed the lay-up process of all the plates as well as the final trimming of the pre-twisted plates. Prototype Model and Mold performed the final machining of the flat plates as well as drilling the four holes in all the plates.

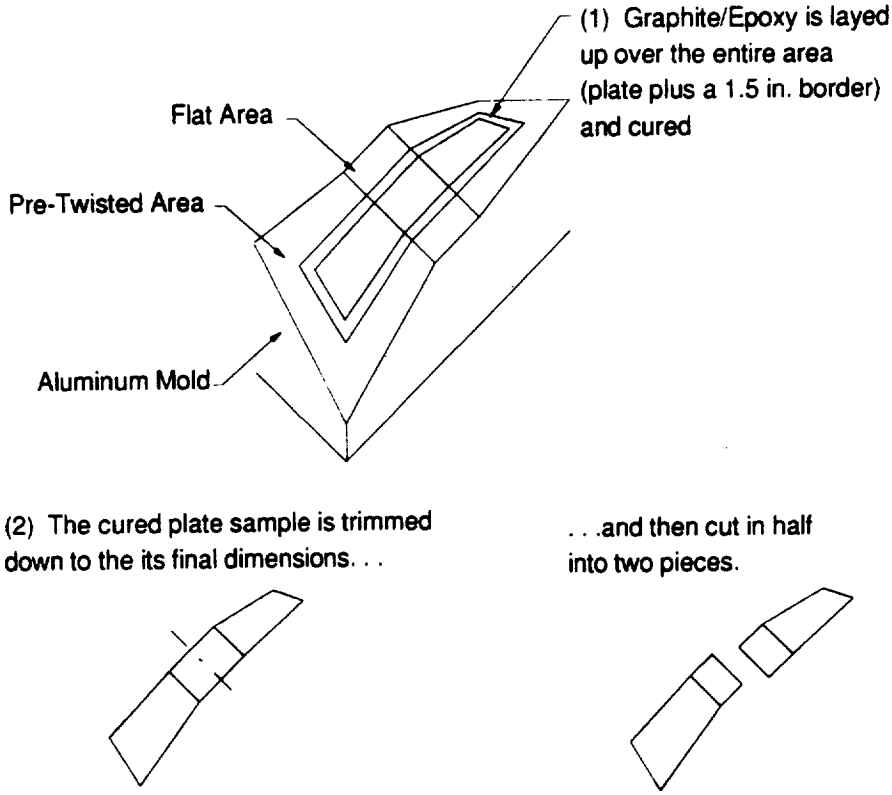

Figure 2.14: The manufacturing process of a pair of graphite/epoxy plates.

There are three different ply lay-ups for the plates–2 symmetric and 1 asymmetric. The two symmetric lay-ups are $[\pm\theta/0_2/-\theta/0_2/+\theta/0_2]_S$ where θ = 22.5° and 45° for each respective lay-up and the one asymmetric lay-up is $[(+22.5)_5/0_2]_A$. The purpose of the two symmetric lay-ups is to investigate how the ply lay-up affects the dynamic and static behavior of the plate. The zero angle plies are used to give the plates strength under high centrifugal loads. The asymmetric lay-up introduces extension-twist coupling which gives the designer further ability to control the shape of the plates. There is, however, a problem that exists for all asymmetric lay-ups. The plate is cured at an elevated

temperature (350°F), as the plate cools down there exist residual forces within the fibers of the material. If this plate has a symmetric lay-up the residual forces would counteract each other, but because the lay-up is asymmetric the forces reinforce one another and cause the plate to twist as it comes down to room temperature. The plate would untwist if the temperature of the plate is increased up to its cure temperature.

Because of this twisting problem with the asymmetric lay-up, the engineers and technicians at General Dynamics-Convair tried alternate curing techniques in an attempt to prevent unwanted twisting of the plates. They first tried to cure two plates at the same time one on top of each other and upside down and separated by a Teflon film so that it would simulate a symmetric laminate, $\left[[(+22.5)_5/0_2]_A/\text{Teflon Film}\right]_S$. They would then separate the two asymmetric laminates at the Teflon film interface. The entire plate assembly was flat as it cooled down to room temperature, but as soon as the plates were separated they began to twist. A final attempt was to change the stacking sequence to $[0_2/(+22.5)_2/0_2/(+22.5)_3/0]_A$ thereby putting more zero angle plies on the outer surface; this would lessen the effect of the residual forces caused by the off angle plies and make the plate less resistant to twisting. This alternative stacking sequence, however, failed to prevent the laminate from twisting upon final curing. The results of General Dynamics' efforts were two sets of plates with two different asymmetric stacking sequences.

Table 2.6 summarizes the different geometries and lay-ups of the plates. There are 12 different combinations of plate pairs; two sets of each plate pair are manufactured giving a total of 48 individual plates. Each individual plate within each plate set is then given a letter A, B, C, or D where plates A and B are the "best" plate pair, and plates C and D are the backup set.

Table 2.6: Plate serial numbers. The first digit refers to the geometry and the second is the lay-up.

Geometry \ Lay-up	1. $\theta = 22.5°$	2. $\theta = 45°$	3. $[(+22.5)_5/0_5]_A$
1. Flat	11	12	13
2. 30° Pre-Twist about the Mid-Chord	21	22	23*
3. 30° Pre-Twist about the Quarter-Chord	31	32	33*
4. 30° Pre-Twist about the Leading Edge	41	42	43*
For the first two lay-ups the stacking sequence is $[\pm\theta/0_2/-\theta/0_2/+\theta/0_2]_S$			
*The lay-up for this plate is $[0_2/+22.5_2/0_2/+22.5_3/0]_A$			

2.2.2 Determining the Quality of the Plate Sets

Modal tests were conducted on all plates to determine which of the 24 plates were to be designated as the best set. The initial vibration tests were conducted at the University of California San Diego with the equipment listed in Table 2.7. The first step in determining the better plate set was to check how much the natural frequencies differed between each plate within a set. If this failed to distinguish the quality of the plates then the plate set with the least amount of damping would decide which of the pairs is the better set. Any imperfections such as delaminations or voids would cause the damping to increase. The vibration results are presented in the next chapter.

Table 2.7: List of equipment used to perform the first modal analysis on the graphite/epoxy plates.

Kistler Impact Hammer (Model 972A500)
2 Kistler Accelerometers (Model 8616A500)
Length = 0.235 inch
Diameter = 0.200 inch
Mass = 0.5 grams
Acceleration Range = ±500 g
Hewlett Packard 3582A Two Channel Spectrum Analyzer

2.2.3 Experimental Procedure

The graphite/epoxy plate is placed into the Clamping Assembly. The two accelerometers are placed on the two free corners of the cantilevered plate and their signals are fed into the two channels of the spectrum analyzer. The accelerometers are mounted to the plates with wax, which is a suitable adhesive for measurements up to 5 kHz [16]. The natural frequencies are measured by lightly tapping the plate with the hammer near the root. The signal analyzer digitizes the time signals of the accelerometers and calculates the Fast Fourier Transform (FFT). Figures 2.15 and 2.16 give a typical example of a frequency response spectrum where the frequency response function is defined as the ratio of the response of the system to the input.

The natural frequencies of the plate are determined by noting the magnitude peaks on the power spectra. An estimate of the mode shape is determined by examining the phase difference between the two accelerometers at resonance. A phase difference of ~0° between the two accelerometers would indicate a bending mode whereas a difference of ~180° would indicate a torsion mode. A more detailed determination of the mode shapes is not necessary at this point because only the frequency variation amongst each plate set and the damping at each mode are being measured. The damping is calculated by using the half power point method from the frequency response function between the hammer and one of the accelerometers [16]. If the magnitude of the structure at a natural frequency is given by $|\alpha|$, then the equation for damping can be expressed by

$$\zeta_n = \frac{2(\omega_a^2 - \omega_b^2)}{\omega_n^2} \tag{2.2}$$

where ω_n = the natural frequency of the structure, ω_a is the frequency above the natural frequency where the magnitude is equal to $\frac{|\alpha|}{\sqrt{2}}$, and ω_b is the frequency below the natural frequency where the magnitude is equal to $\frac{|\alpha|}{\sqrt{2}}$ (Figure 2.17).

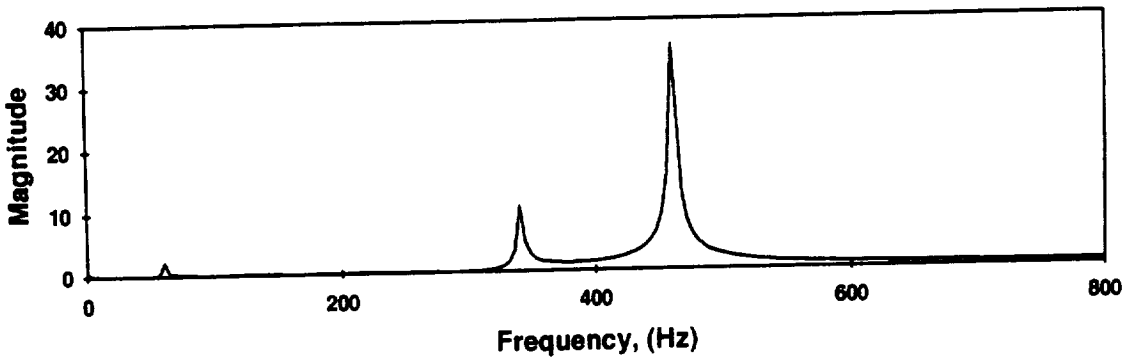

Figure 2.15: The magnitude diagram of a frequency response function. The peaks on the plot are the natural frequencies of the system.

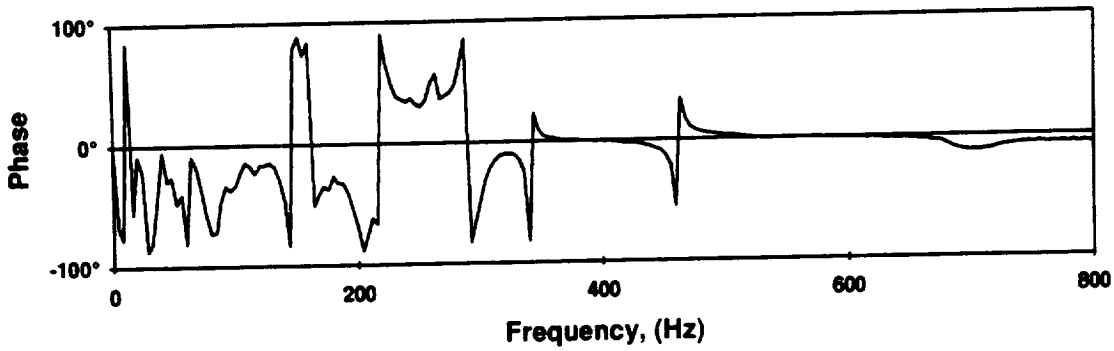

Figure 2.16: The phase diagram of a frequency response function.

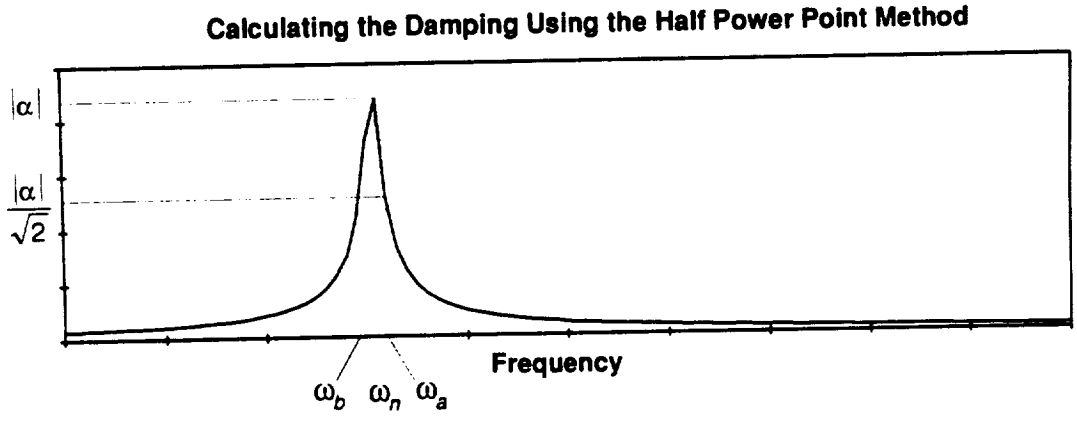

Figure 2.17: Calculating the damping using the half power point method.

2.2.4 Geometry Measurements

After the modal tests, detail geometry measurements of the 12 plate sets chosen were performed. The measurements were used for the analytical modeling[1]. An individual plate was first placed in the Clamping Assembly and this entire assembly was placed in the vise of a Bridgeport Mill (Figure 2.18). A thin tapered pin was placed within the collet of the mill; this pin would be used to point to various positions on the pre-twisted plate. The table of the mill could be moved in the x-, y-, and z-space. It was easier, however, to measure the z-coordinates using a height gage (Mitutoyo Digimatic Height Gage Series-1550-571) which rested on the milling table. The lower right corner of the plate at the cantilevered end was chosen as the origin, and the xy-coordinates of the plate were measured using the dial indicators on the mill. The four corners of the pre-twisted plates with the symmetric lay-ups were measured using this method. Four additional points, spaced equally along the x-axis and on both edges of the plate, were measured on the asymmetric plates. The flat plates with the symmetric lay-up were measured using vernier calipers and the flatness was checked by placing the plates on a marble stone.

All 12 combinations of geometry and ply lay-ups were not able to be tested at the Dynamic Spin Rig Facility at the NASA Lewis Research Center because of the time allotted to us for the tests. Half of the 12 plate sets were chosen to be tested and none of the Leading Edge plates were tested (Table 2.8). The plates were chosen based on the type of behavioral trends that could be examined. The remaining six plate sets were to be tested at a later time.

Referring to Table 2.8, the set of plates in the second column ($\theta = 22.5°$) investigates the geometry effects of a symmetric lay-up by first looking at a flat plate with a symmetric

---

[1]The results of the geometry measurements are listed in Appendix A.

lay-up, then a pre-twisted plate about the mid-chord, and finally a pre-twisted plate about the quarter-chord. A similar type of comparison study is accomplished with the asymmetric lay-up with plates listed in the fourth column. Likewise the first row of Table 2.8 investigates the behavioral effects of flat plates with first a symmetric lay-up and subsequently an asymmetric one. For the third row, the coupled effects of pre-twist and symmetric and asymmetric laminates are investigated. The fourth examines the effects of a torsionally stiffer lay-up on a pre-twisted plate.

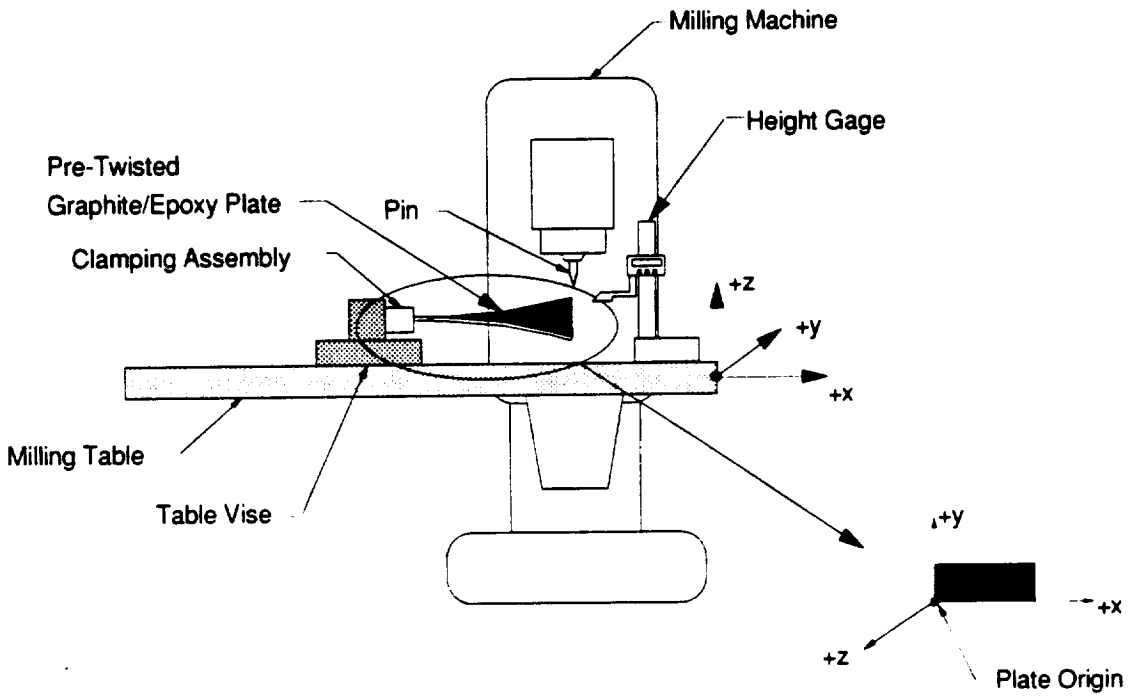

Figure 2.18: A description of the setup used to measure the geometry of the pre-twisted plates. The milling table is capable of moving in three orthogonal directions. The table is moved so that the pin points to the desired position on the plate. The xy-measurements are recorded using dial indicators on the milling machine. The height gage is used to measure the z-coordinates.

Table 2.8: A list of the plates chosen to be spin tested at the Dynamic Spin Rig Facility at the NASA Lewis Research Center.

Lay-up / Geometry	$\theta = 22.5°$	$\theta = 45°$	$[(+22.5)_5/0_5]_A$
Flat	Tested		Tested
30° Pre-Twist about the Mid-Chord	Tested		Tested
30° Pre-Twist about the Quarter-Chord	Tested	Tested	
30° Pre-Twist about the Leading Edge-Chord			
For the first two lay-ups the stacking sequence is $[\pm\theta/0_2/-\theta/0_2/+\theta/0_2]_S$			

The first step in preparing the six plate sets is epoxying fiberglass (G10) doublers onto the flat regions of the composite plates using Scotch-Weld 3M 2216 A/B epoxy. Four strain gages (Micro-Measurements: CEA-00-062UW-650) were epoxied onto the plates with Micro-Measurements AE-10 Epoxy. Two gages were placed mid-chord on opposite sides of each other near the root of the plate and were aligned parallel to the initial twist axis (Figure 2.19). These two gages were used to measure the bending and extensional strains of the plate. The two other gages were located mid-span and on the same side of the plate. These gages were aligned at 45° angles to the initial twist axis (Figure 2.19). The exact locations of all four gages on all the plates were measured at the NASA Lewis Research Center and this information is listed in Appendix A. Each of the gages has two bondable terminals; two wires (30 AWG) were soldered onto one terminal and a third wire (30 AWG) onto the other one. The wires were bonded onto the plate in a two step process: (1) the wires were first set into place with a cyanoacrylate adhesive and (2) epoxied and coated with Micro-Measurements AE10 Epoxy. Finally, the wires were assembled into an ITT Cannon 13-pin quick release connector (Model No.: KJ5E10B35PN).

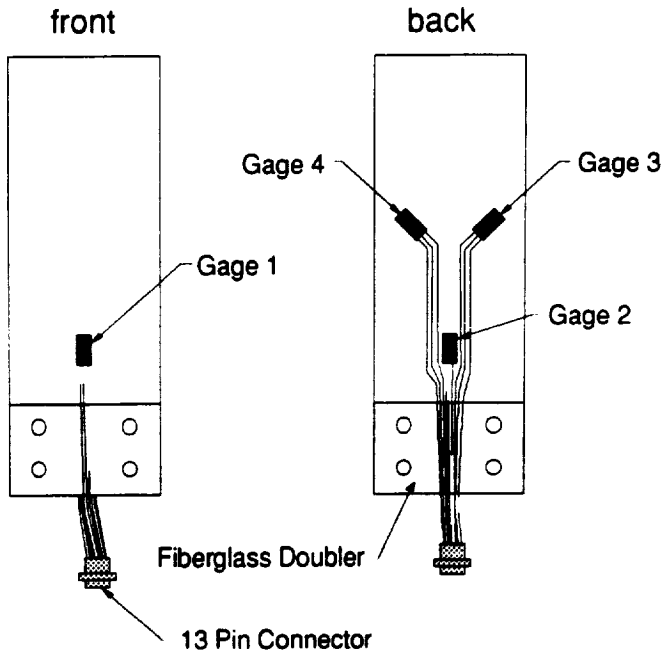

Figure 2.19: A graphite/epoxy plate instrumented with strain gages.

2.2.5 The Strain Gage Circuit Equations

This section describes the circuit and equations used to determine the experimental strains of each strain gage [17–18]. Each strain gage was wired into a quarter bridge of a Wheatstone Bridge (Figure 2.20) where R_i is a resistor, R_G is the resistance of the strain gage, and V is the voltage [17]. The voltage, V_{out}, can be expressed as

$$V_{out} = V_{in} \frac{R_1 R_G - R_2 R_3}{(R_1 + R_2)(R_G + R_3)}. \tag{2.3}$$

If the strain gage undergoes a change in resistance from R_G to $R_G+\Delta R_G$, then the output voltage will change from V_{out} to $V_{out}+\Delta V_{out}$ and Equation (2.3) can be rewritten as

$$V_{out} + \Delta V_{out} = V_{in} \frac{R_1 (R_G + \Delta R_G) - R_2 R_3}{(R_1 + R_2)(R_G + R_3)}. \tag{2.4}$$

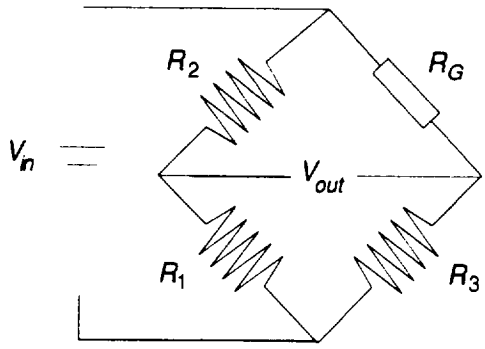

Figure 2.20: A Wheatstone Bridge with a single strain gage in a quarter bridge.

Substituting Equation (2.3) into Equation (2.4) and solving for ΔV_{out} results in

$$\Delta V_{out} = V_{in}\frac{R_1(R_G+\Delta R_G)-R_2R_3}{(R_1+R_2)(R_G+R_3)} - V_{in}\frac{R_1R_G-R_2R_3}{(R_1+R_2)(R_G+R_3)} \tag{2.5}$$

which is the general expression for the change in the bridge output from the initial state.

For an initially balanced bridge $V_{out} = 0$ for $V_{in} \neq 0$ which implies

$$R_1R_G - R_2R_3 = 0, \tag{2.6}$$

so that Equation (2.5) becomes

$$\Delta V_{out} = V_{in}\frac{R_1(R_G+\Delta R_G)-R_2R_3}{(R_1+R_2)(R_G+\Delta R_G+R_3)}. \tag{2.7}$$

Multiplying Equation (2.7) by $\frac{1}{R_1R_G}$ gives

$$\Delta V_{out} = V_{in}\frac{\left(1+\frac{\Delta R_G}{R_G}\right)-\frac{R_2R_3}{R_1R_G}}{\left(1+\frac{R_2}{R_1}\right)\left(1+\frac{\Delta R_G}{R_G}+\frac{R_3}{R_G}\right)}. \tag{2.8}$$

Since it is an initially balanced bridge, Equation (2.6) yields $\frac{R_2R_3}{R_1R_G} = 1$. Furthermore, the bridge ratio is defined as

$$a = \frac{R_2}{R_1} = \frac{R_G}{R_3}, \tag{2.9}$$

so that Equation (2.8) becomes

$$\Delta V_{out} = V_{in} \frac{\dfrac{\Delta R_G}{R_G}}{(1+a)\left(1+\dfrac{1}{a}+\dfrac{\Delta R_G}{R_G}\right)}. \tag{2.10}$$

Multiplying the numerator and denominator of Equation (2.10) by a and then factoring out $(1 + a)$ from the denominator yields

$$\Delta V_{out} = V_{in} \frac{a}{(1+a)^2} \frac{\Delta R_G}{R_G}(1-n) \tag{2.11}$$

where the term, $(1 - n)$, is the nonlinearity factor given by

$$1-n = \frac{1}{\left[1+\left(\dfrac{a}{1+a}\right)\dfrac{\Delta R_G}{R_G}\right]}. \tag{2.12}$$

For strains below 10,000 με the error due to nonlinearity is less than 1%.

The strain from the gage is determined from the relation

$$\varepsilon_G = \frac{\Delta R_G / R_G}{G_F} \tag{2.13}$$

where G_F is the manufacturer's gage factor. Ignoring the nonlinearity factor and substituting $\Delta R_G / R_G$ from Equation (2.13) into Equation (2.11) yields

$$\varepsilon = \frac{a}{G_F(1+a)^2} \frac{\Delta V_{out}}{V_{in}}. \tag{2.14}$$

The strain in Equation (2.14) is given as $\varepsilon \times 10^{-6}$ in/in.

Temperature compensation of the strain gage is needed because of two factors [19]. The first is because the resistance of most wires changes with temperature. Temperature variations within the circuit naturally arise because the energy dissipated from a resistor is in the form of heat. The second factor is the difference in the thermal coefficient of expansion between the strain gage and the structure to which it is bonded. To get around this problem a strain gage whose thermal coefficient of expansion closely matched the one on the composite plates is chosen. Second, a self-temperature-compensated strain gage and a stable precision resistor in the adjacent arm in a three-wire, quarter bridge circuit (Figure 2.21) is used.

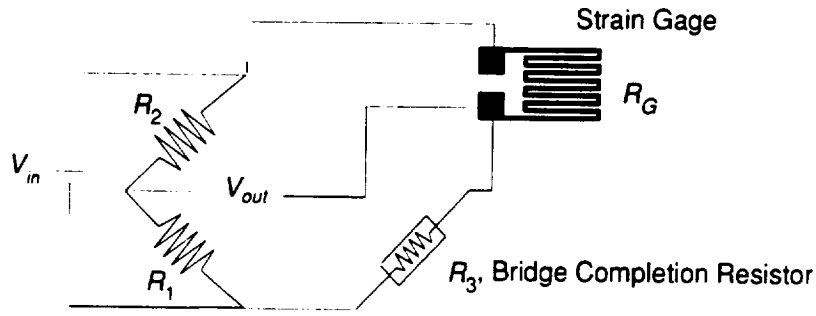

Figure 2.21: A quarter bridge with two lead wires from the strain gage.

The derivation of the equations relating the output voltage, V_{out}, and the strain for the circuit in Figure 2.21 is the same as in Equations (2.3-2.14). If the structure is tested at temperatures away from the room temperature then corrections must be made to the indicated strain of the gage. The graphite/epoxy plates in this research project are tested at room temperature.

2.3 The Aerospace Structures Laboratory at the University of California San Diego

This section describes the procedures and equipment used to perform the modal and static displacement tests at the Aerospace Structures Laboratory. For the vibration

tests the plate's natural frequencies, mode shapes, and damping are determined. The static displacement tests consist of determining the strain, deflection, and twist of the cantilevered plate due to a point load at one of the free corners.

2.3.1 The Vibration Tests

The equipment used to perform the modal analysis is listed in Table 2.9 and a diagram of the setup is given in Figure 2.22. A roving hammer technique was used to determine the plate's natural frequencies, damping, and mode shapes. The dynamic signal analyzer was used to capture the time signals of the accelerometer and impact hammer and to calculate the frequency response functions of the data. The STAR System, a PC based software program, was used to process the frequency data and to animate the mode shapes of the cantilevered plate. The results of the vibration tests are presented in Chapter 4.

Table 2.9: List of modal analysis equipment at the Aerospace Structures Laboratory.

Hewlett Packard 35665A Dynamic Signal Analyzer
AST 386SX Bravo Personal Computer
The STAR System for Windows version 3.01D by Structural Measurement Systems
Kistler Impact Hammer (Model 972A500)
Kistler Accelerometer (Model 8616A500)

Nine points on the composite plate are marked and used to model the mode shapes of the plate. The composite plate is placed in the Clamping Assembly and an accelerometer is attached to a free corner of the plate with a wax adhesive. Each of the nine points is lightly tapped with the impact hammer. The signal analyzer calculates the average frequency response function and the coherence. The coherence is a measure of how much noise is in the system; its value ranges from 0 to 1 where a value of 1 indicates an absence of noise. The data is acceptable if the coherence is at least 0.95 at a resonant frequency. Figure 2.23 shows examples of the real and imaginary portions of the

frequency response function and the coherence for one of the graphite/epoxy plates. The frequency response function, the cross power spectrum, the auto-power spectrum, and the coherence spectrum data from all 9 points on the plate are transferred to the PC and saved to the hard disk.

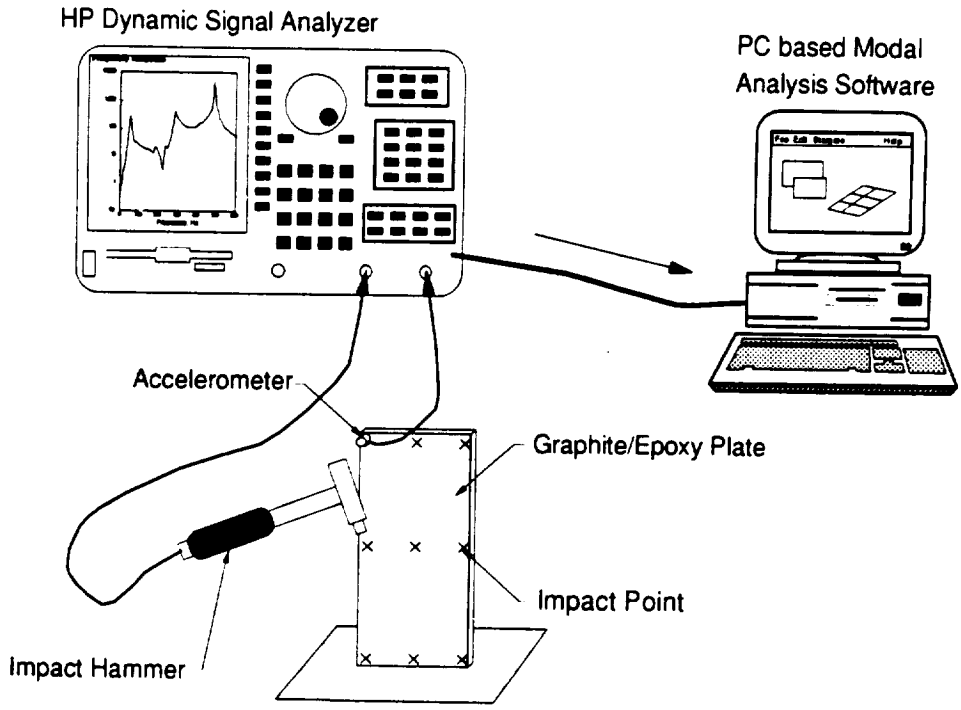

Figure 2.22: The experimental modal analysis setup at the Aerospace Structures Lab at the University of California San Diego. The PC based software package, The Star System, allows easy data processing and visualization of mode shapes.

Using the STAR System the natural frequencies, mode shapes and damping of the plates are determined by first curve fitting the frequency data using a polynomial fit. The curve fitted data is then processed and used to calculate the natural frequencies and damping, and to animate the mode shapes. The natural frequencies are visually determined from the peaks of the magnitude plot of the frequency response function. The mode shapes are determined from the imaginary portion of the frequency response functions (Figure 2.23) where the mode shape is directly proportional to the value of the

imaginary portion of the frequency response function. The damping is expressed by Equation (2.2) and is calculated from the curve fitted data. Figure 2.24 depicts examples of the mode shapes and frequencies of one of the pre-twisted composite plates from the STAR system.

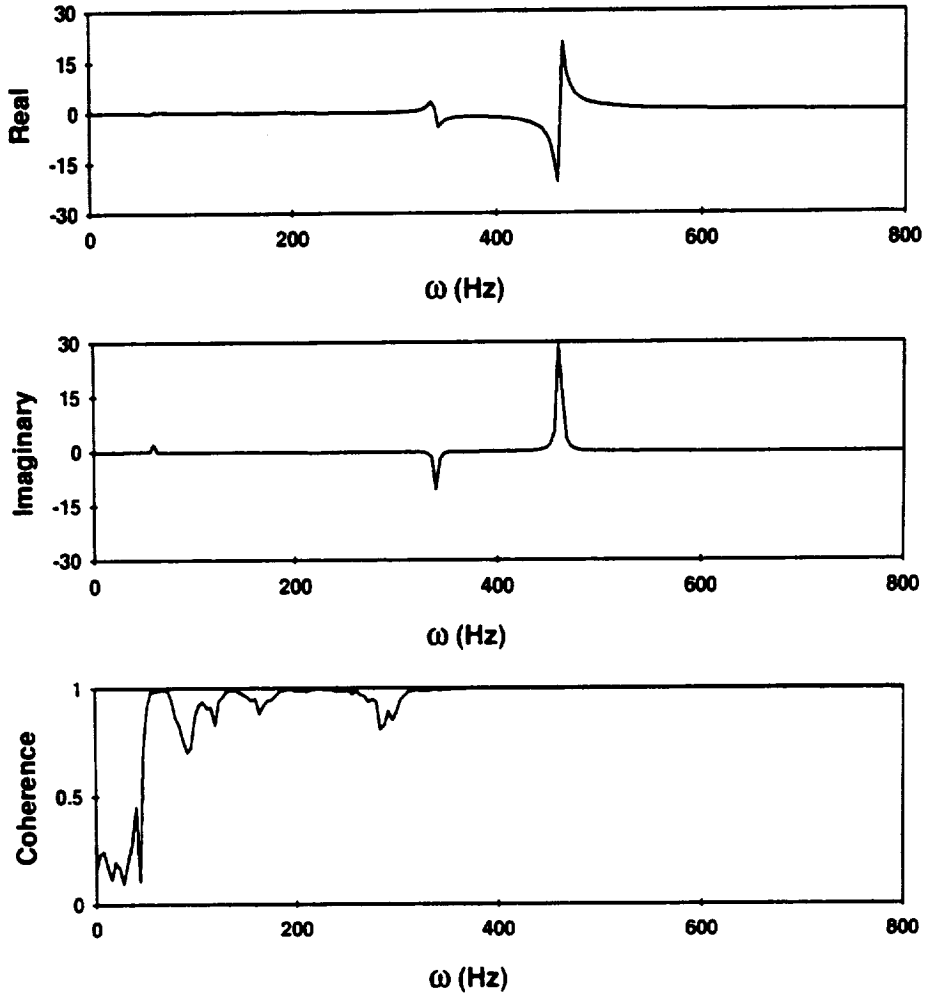

Figure 2.23: The real and imaginary portions of the frequency response function and the coherence.

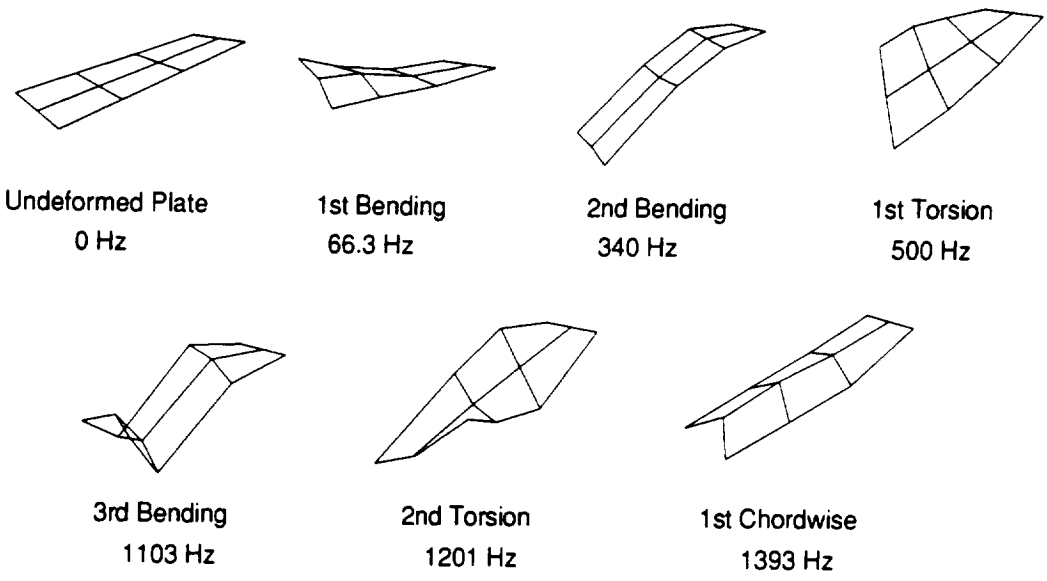

Figure 2.24: The natural frequencies and mode shapes of a 30° pre-twisted plate about the mid-chord the with a $[\pm 22.5/0_2/-22.5/0_2/22.5/0_2]_S$ lay-up.

2.3.2 The Static Displacement Tests

This section describes the experimental setup and procedure of the static displacement tests of the graphite/epoxy plates. The strains and displacements of the cantilevered plate due to a load at one of the corners are measured. Figure 2.25 describes the plate setup and coordinate system for the tests. A point load is applied at Point A and the xyz-displacements of Points A and B and the strains at gage 2 are measured.

The purpose of the static displacement tests is to determine the twist and deflection of the plate. Consider the plate in Figure 2.26(a) that undergoes a deflection with no twist and another plate in Figure 2.26(b) that twists with no deflection. The tip deflection is defined as the average displacement of points A and B, that is

$$D = \frac{z_A + z_B}{2}. \tag{2.15}$$

The tip twist, ψ, is defined as the arcsine of the ratio of the sum of the displacements to the chord length, c. From Figure 2.26(b),

$$\psi = \arcsin\left(\frac{z_A + z_B}{c}\right). \tag{2.16}$$

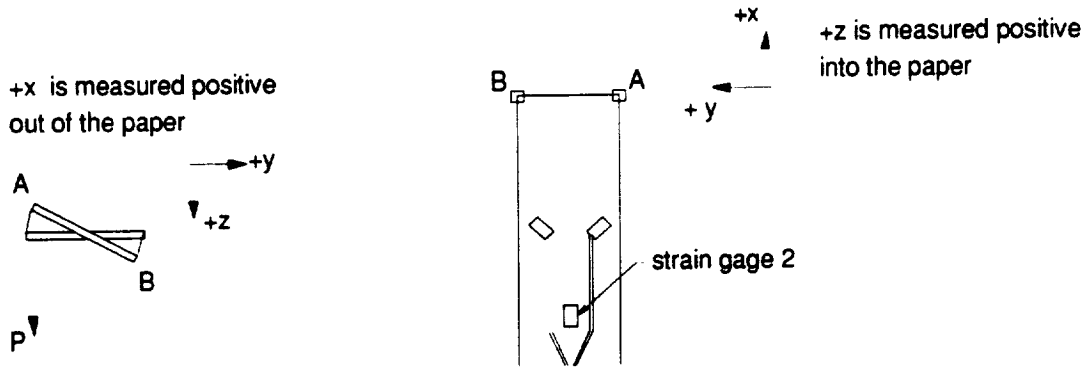

Figure 2.25: The plate coordinates used for the static deflection tests. The xyz-deflections are measured at points A and B, and the load, P, is applied at point A. The strain is recorded from strain gage 2.

The static displacement tests of the cantilevered composite plates were performed on a Bridgeport Series I Mill located at the Division of Engineering Machine Shop at the University of California San Diego. The experimental setup used for the tests was very similar to one used for the geometry measurements (Figure 2.18). A graphite/epoxy plate was set up on the table of the mill that could move in three orthogonal directions. Six of the 12 composite plates (Chapter 2.2.2) were instrumented with strain gages (Micro-Measurements, Model CEA-00-062UW-350) and these gages were connected to a Micro-Measurements Digital Strain Indicator (Model P-3500) in a quarter bridge circuit (Figure 2.21). A narrow, tapered pin was used as a pointer and was placed in the collet of the mill. The table of the mill was moved so that the pointer tip was located at one of the corners of the plate. Weights up to 28 lbf in approximately 5 lbf increments were used to load the plates at Point A (Figure 2.25). The dial indicators on the mill were used to measure the xyz-displacements of Points A and B.

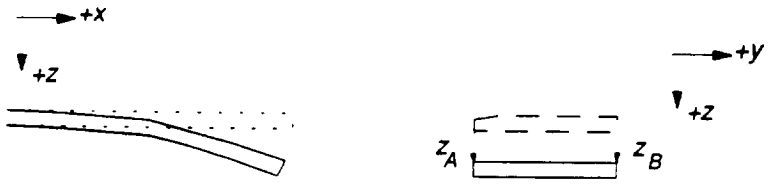

(a) Deflection with no twist.

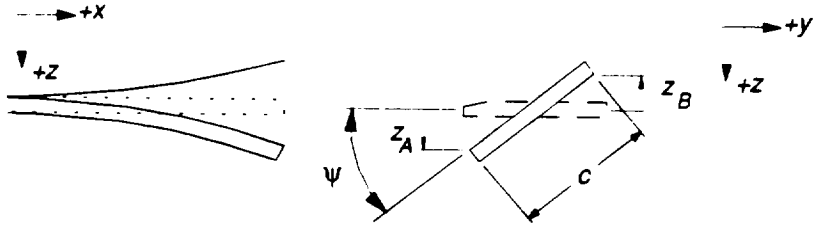

(b) Twist with no deflection.

Figure 2.26: Definitions of (a) deflection with no twist, and (b) twist with no deflection.

2.4 The NASA Lewis Research Center

The equipment and hardware of two laboratories at the NASA Lewis Research Center were used to test the plates. Non-spinning natural frequencies and their mode shapes were measured and identified at the Laser Holography Laboratory. The steady-state strain and deflections of the rotating plates were recorded at the Dynamic Spin Rig Facility. The rotating vibration frequencies and corresponding mode shapes were also measured and identified at the Dynamic Spin Rig Facility.

2.4.1 The Laser Holography Laboratory

Holographic interferometry is a non-obtrusive method to determine the natural frequencies and the entire mode shapes of structures. The following sections discuss the theory of identifying mode shapes with the holographic method and describe the equipment and setup of the Laser Holography Laboratory at the NASA Lewis Research Center.

2.4.2 Theory of Holographic Vibration Analysis

The following discussion is a simplified model of the holographic technique used for vibration analysis; a more detailed description is given in [20–22]. Figure 2.27 depicts a cantilevered beam vibrating at its first mode; τ is the viewing angle and η is the angle between the surface normal and the ray from the laser source at point E to a point F on the stationary beam. A camera records both the phase difference and amplitude of the scattered laser source. Points F' and F'' represent point F at the extremes of the vibrating beam. The distance G is the peak-to-peak amplitude between points F' and F''.

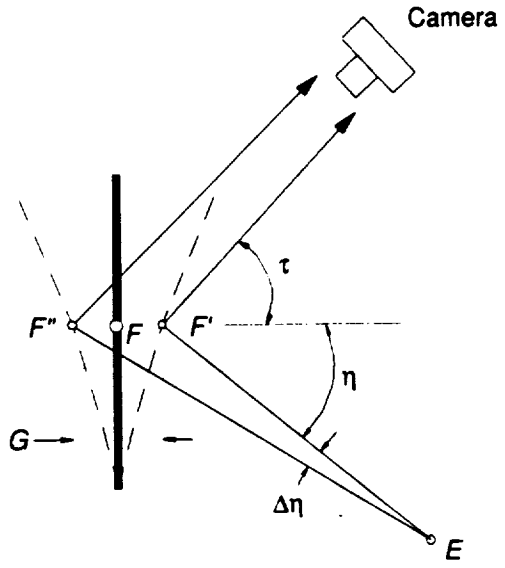

Figure 2.27: A cantilevered beam vibrating at its first fundamental mode is illuminated by a laser at point A. The camera records the phase difference and amplitude of the scattered laser.

If G is assumed to be very small, then the angular difference $\Delta\eta$ is assumed to be small, and the phase difference between the two rays originating from F' and F'' is $\frac{2\pi G(\cos\tau+\sin\eta)}{\lambda}$ where λ is the wavelength of the ray. At the clamped edge the phase difference is zero since $G = 0$. The phase difference and G increase continuously as one moves along the beam. Since G varies along the length of the vibrating beam and the

phase difference is a function of G, the interference patterns or fringes between the two rays will be recorded onto the camera. The dark fringes or areas of destructive interference have phase differences of π for the darkest fringe nearest the root of the beam, 3π for the next dark fringe, 5π for the next one and so on. The bright fringes are areas of constructive interference and have a phase difference of 0 at the root, 2π for the next bright fringe, 4π for the next and so on. The fringe pattern can then be expressed by

$$\frac{2\pi G(\cos\tau + \sin\eta)}{\lambda} = n\pi \quad (n = 0 \rightarrow \infty),$$

where n increases continuously from the root of the beam to the tip. It must be noted that n is a real number and when n is equal to an integer either a dark or bright fringe will occur; a gray fringe will occur for any non-integer n. Figure 2.28 shows holograms of the first bending, second bending, and first torsion modes for one of the graphite/epoxy plates.

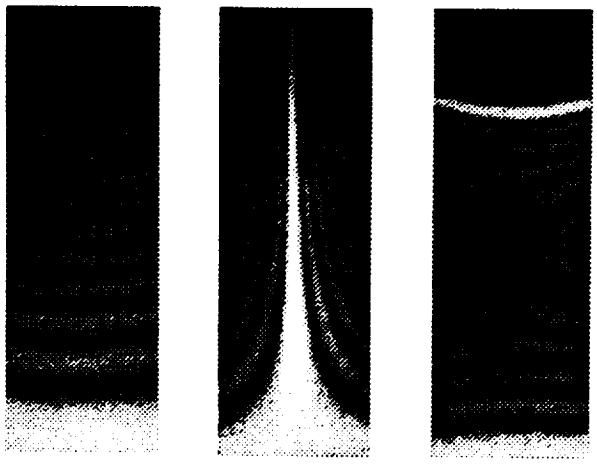

Figure 2.28: A hologram of the 1st Bending, 1st Torsion, and 2nd Bending modes for one of the graphite/epoxy plates.

2.4.3 Experimental Setup

The equipment at the Laser Holography Laboratory is listed in Table 2.10 and is depicted in Figure 2.29. The laser beam is split into two rays and illuminates the cantilevered plate. The plate is acoustically excited by a speaker. The resonant frequencies of the plate are found by performing a manual sine sweep and observing the fringe patterns through the holocamera. At a natural frequency, the speaker is set to dwell at that frequency and a time-averaged hologram is taken of the vibrating plate. An IBM-AT PC with a Matrox Frame Grabber Board (Model PIP-512B) is used to capture the mode shape image onto the computer. The mode shapes are processed on a Silicon Graphics 4D/35 Personal Iris Workstation using the program ENHANCE and are printed out to a laser printer.

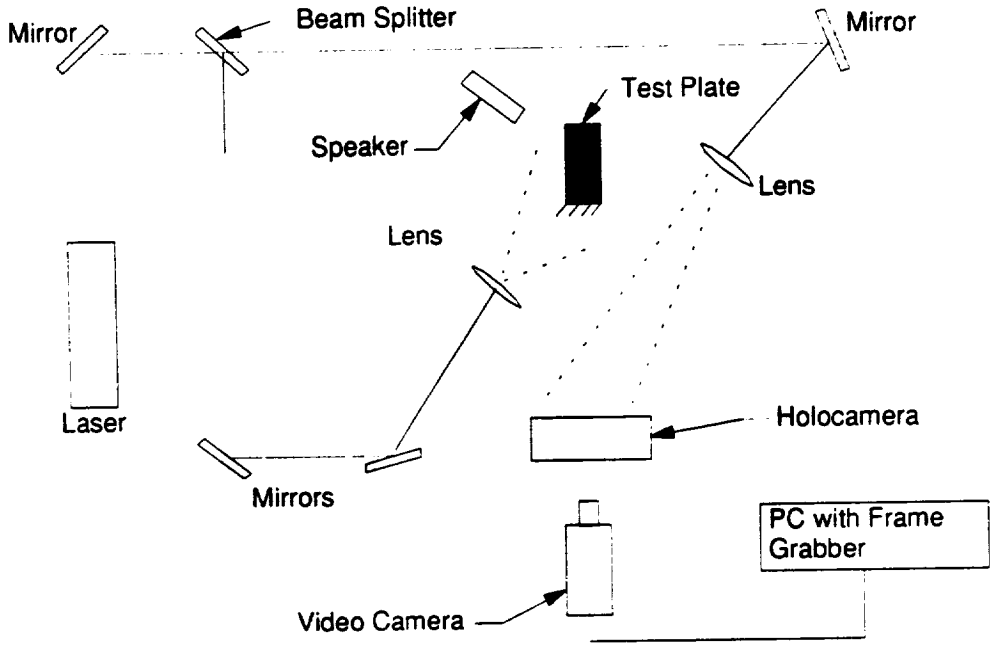

Figure 2.29: Laser holography setup at the NASA Lewis Research Center.

Table 2.10: Equipment list at the Laser Holography Laboratory.

2 Newport Research Corporation 8'x16' Vibration Isolation Tables
Coherent INNOVA-90 Argon-Ion Laser (set at 514.5 nm. wavelength)
IBM-AT Personal Computer with Matrox Frame Grabber Board, Model PIP-512B
Laser Technology Inc. (LTI) "Holomatic 6000" Holocamera with LTI's Lasertest Film for Argon
University Sound Model ID-40T 40 watt Multi-Impedance Driver Unit (speaker)
California Instruments AC Power Source, Model 251T
Precision Oscillator series 800T (20 – 20 kHz)
Fluke 1953A Counter-Timer
Jodan VBA-Beam splitter
Oriel Microscope objective holders
Oriel 2" mirror holders
Oriel 20X microscope objectives
Newport Research Corporation (NRC) BD-1 Mirrors 2" diameter (broad band)

2.4.4 The Dynamic Spin Rig Facility

The following sections describe the equipment and procedures for the spinning steady-state strain and deflection tests and the spinning vibration studies at the Dynamic Spin Rig Facility at the NASA Lewis Research Center. The purpose of the Dynamic Spin Rig (Figure 2.30) is to provide a chamber to spin test rotors in the absence of aerodynamic forces [11].

The spin rig can spin rotors with diameters up to 28 inch to speeds as high as 20,000 rpm; the speed is monitored by a magnetic speed sensor at the turbine. The spin rig is powered by a Barbour Stockwell 2775 bi-directional air turbine and the 48 ft^3 cylindrical steel tank can be evacuated to a pressure less than 0.15% of 1 atm. A 100-channel PolyScientific slip ring assembly is located at the bottom of the spin rig and is used to route the strain signals to the tape recorders in the control room. For performing the spinning vibration tests the main shaft can be excited by two 50 lbf electromagnetic shakers that transfer the load through the yoke shown in Figure 2.30. The two main

bearings of the rotating shaft rest on two soft rubber springs that allows the system some freedom of motion to vibrate. The shakers can vibrate in phase with each other thus exciting the system up and down or 180° out-of-phase with each other thereby providing a vibratory moment on the shaft.

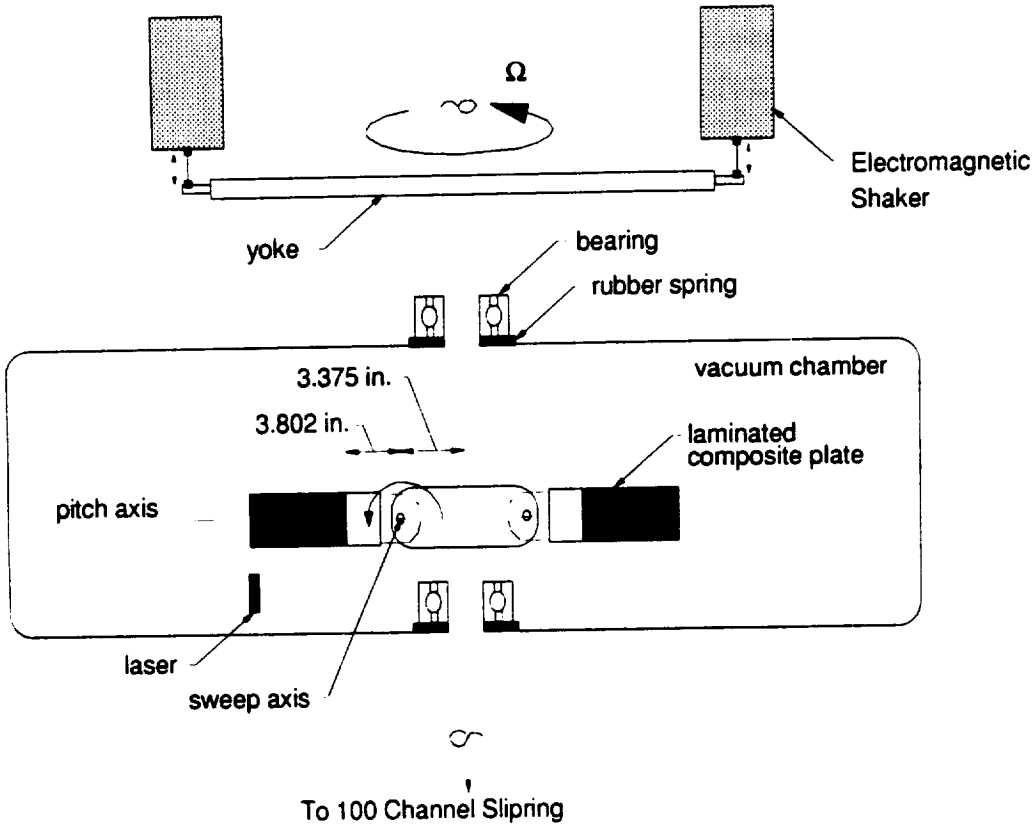

Figure 2.30: The Dynamic Spin Rig Facility at the NASA Lewis Research Center.

The existing equipment from previous experiments at the Dynamic Spin Rig Facility is composed of hardware designed specifically to test rotating cantilevered plates [11]. This equipment allows pitch settings of 0°, 30°, 60°, and 90° and sweep settings of 0°, 22.5°, and 45°. The sweep angle, β_s, is defined as the angle between the blade centerline (initial twist axis) with the spin plane (Figure 2.31). A positive sweep angle is defined where the blade is swept below the horizontal plane. The pitch angle, β_p, is defined as the angle the blade root plane makes with the axis of rotation (Figure 2.31). In

Figure 2.30 the perpendicular distance from the spin axis to the sweep axis is 3.375 inch and the perpendicular distance from the sweep axis to the root of the plate is 3.802 inch. The plates are tested in the four different configurations listed in Table 2.11. Figure 2.32 shows a photograph of one of the graphite/epoxy plates set up within the test chamber of the Dynamic Spin Rig.

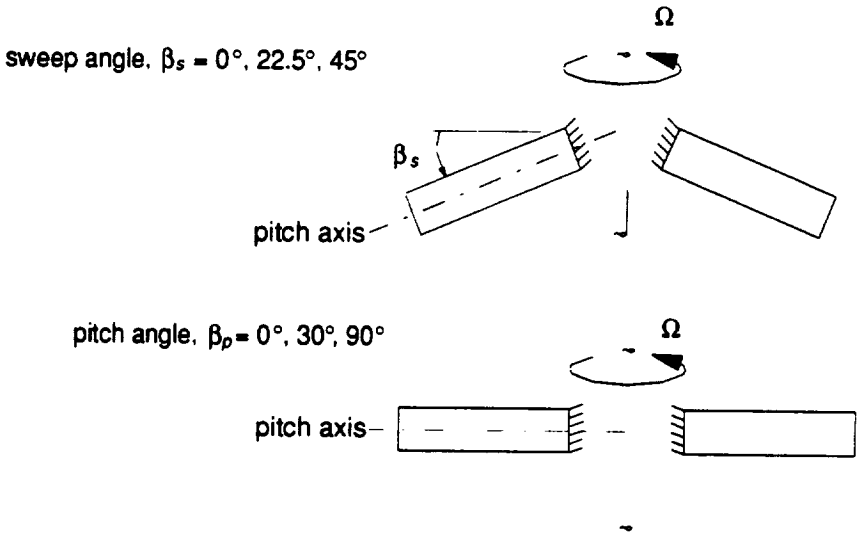

Figure 2.31: Available sweep and pitch angles at the Dynamic Spin Rig Facility at the NASA Lewis Research Center.

Table 2.11: Pitch and sweep settings for the graphite/epoxy plates.

Configuration	A	B	C	D
Pitch	0°	30°	0°	90°
Sweep	0°	0°	22.5°	0°

Data for the strain and deflection tests was collected for configurations A, B, and C. Data for the vibratory tests was collected for configuration D. The tests were run at constant speeds as low as 500 rpm and as high as 8000 rpm in increments of 1000-2000 rpm. Data was recorded onto magnetic tapes at each speed for 30 seconds using two Honeywell 101 magnetic tape recorders.

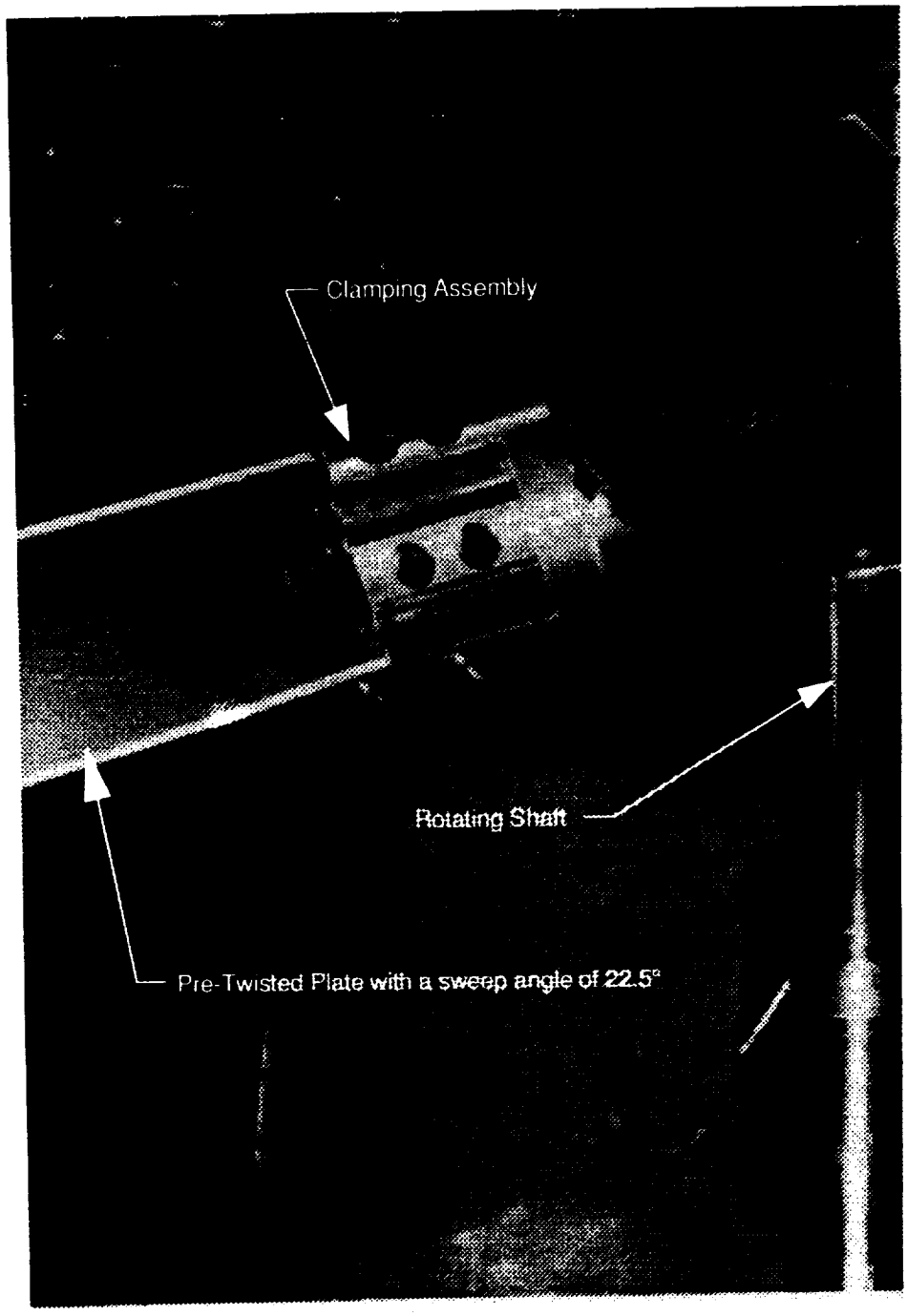

Figure 2.32: Photograph of the plate setup within the spin chamber at the NASA Lewis Research Center.

2.4.5 Steady-State Strain and Deflections

The four strain gages on each plate are used to measure the rotating steady-state strains. The block diagram for the experimental setup is shown in Figure 2.33. The wires from the gages are routed into the slip ring, and into a bank of signal conditioners and amplifiers located in the control room of the Dynamic Spin Rig Facility. The strain gage is arranged in a quarter bridge circuit (Figure 2.21). The analog signals are recorded onto tape and are later digitized and stored on a computer.

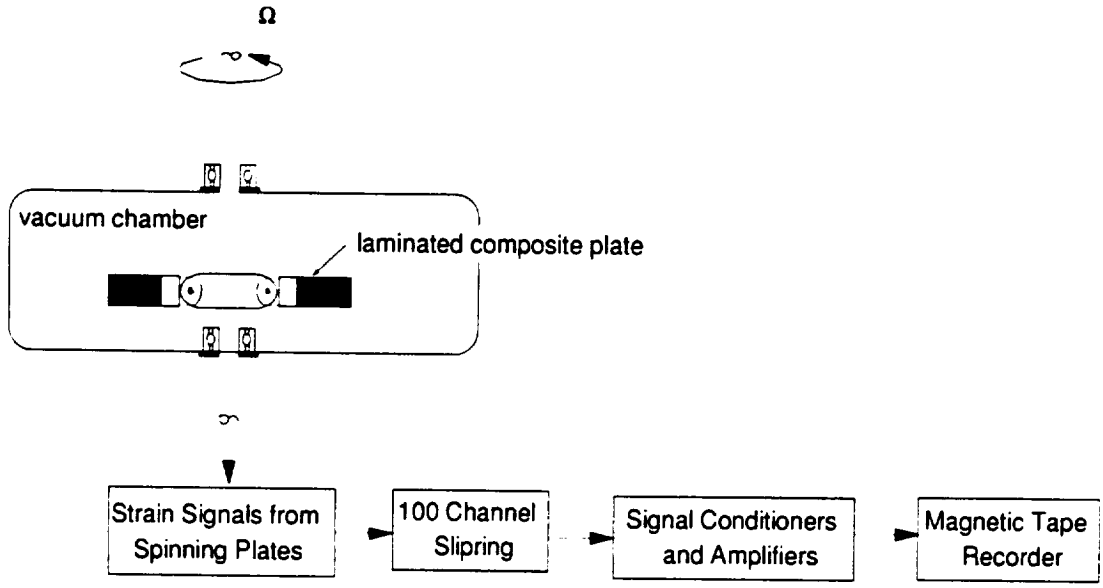

Figure 2.33: Block diagram description to record the rotating steady-state strains.

The deflections of the plate are measured using a laser deflection system developed at the NASA Lewis Research Center [23–24]. This system is composed of three Aerotech 0.5 mW randomly polarized helium-neon lasers, power supplies, United Detector Technology (UDT) large-area silicon photo-diodes, UDT 201A amplifiers, and a magnetic tape recorder (Figure 2.34). The lasers are positioned within the vacuum spin chamber with magnetic stands. Two of the lasers are used to measure the deflections of the plate

tip and at a location mid-length of the plate; the third laser is used to measure the speed of the rotating shaft. The signals from all three gages are recorded onto a magnetic tape.

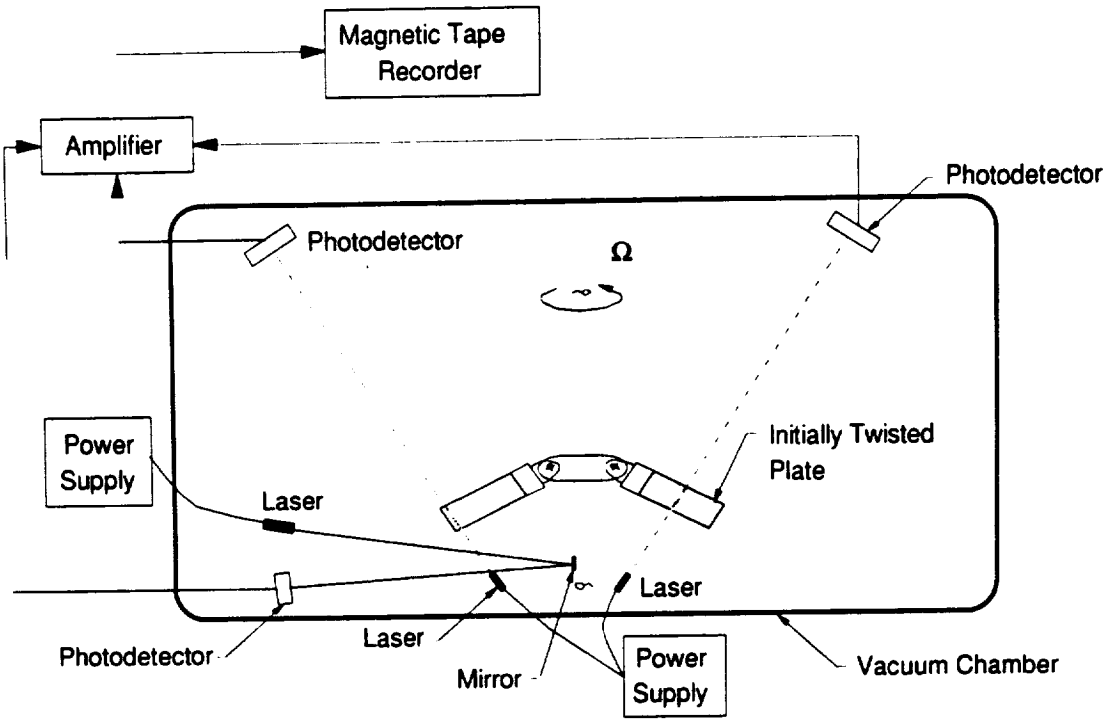

Figure 2.34: Laser deflection measurement system.

The two lasers used to measure the deflections are directed toward the plates in a plane perpendicular to the pitch axis. The incident light beam forms a small angle of about 10° relative to the chord. Photodetectors are placed in the path of the lasers and output a voltage between 1 and 2 volts when a beam shines on it. As the two plates rotate within the chamber, the leading and trailing edges of the plates intersect the light beam and shadow the photodetector from the laser. This results in a series of negative pulses (Figure 2.35). The third laser is directed towards a small mirror epoxied onto the rotating shaft. Its light beam bounces off the mirror and into the photodetector. As the shaft rotates a series of once-per-revolution (1P) positive pulses are generated (Figure 2.35).

The 1P signal is used to track the instantaneous blade positions for each revolution in a rotating frame of reference.

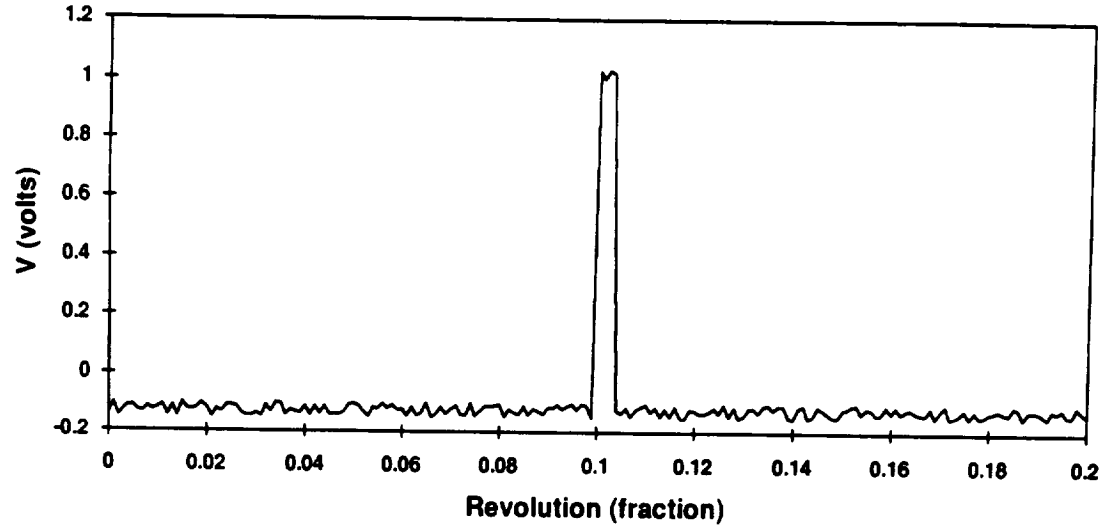

(a)

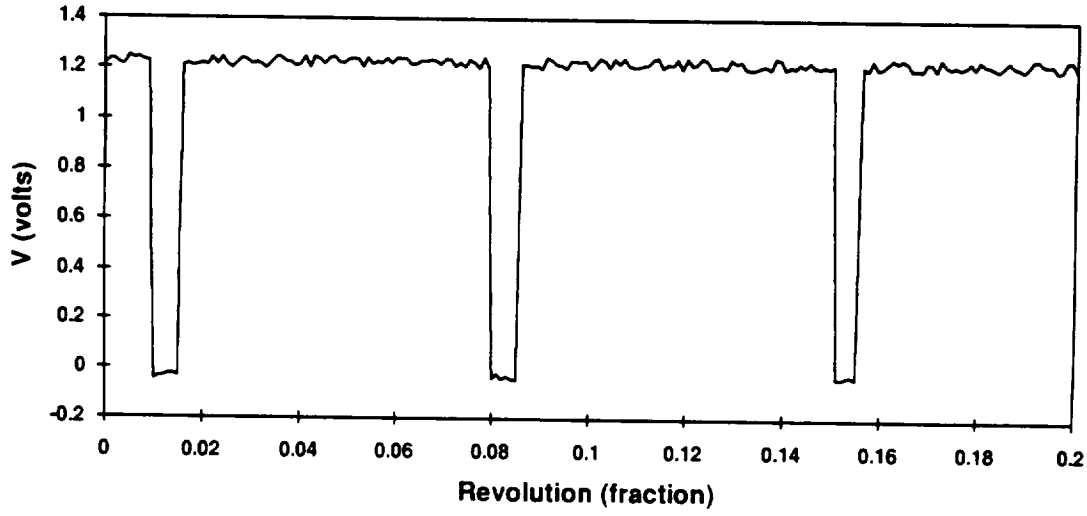

(b)

Figure 2.35: (a) The once-per-revolution pulse and (b) the blade pulse.

The plates are first spun at 500 rpm and data is recorded onto tape for 30 seconds. The plates are then spun at 1000 rpm and in increments of 1000 or 2000 rpm thereafter.

The recorded signals from the laser deflection system are digitized and processed on a minicomputer using a NASA developed code [23–25]. It is assumed that the deflections and twist at 500 rpm are zero. The deflections and twist of the two stations where the lasers are located along the plate are defined as in Equations (2.15) and (2.16). The blade pulse width is directly proportional to the twist of the plate and the time between the 1P pulse and the blade pulse determines the deflection of the plate.

2.4.6 Rotating Vibratory Natural Frequencies and Mode Shapes

The setup to record the spinning vibration modes is the same used to record the steady-state strains (Figure 2.33). The electromagnetic shakers are shaken 180° out-of-phase with each other while the plates are rotating at a constant speed. The Fast Fourier Transforms (FFT) of the strain signals are processed off the tape recorder using an eight channel, PC-based Hewlett Packard 3566A/67A Data Acquisition System. The mode shapes are determined from data at 0 rpm. The mode shapes are then tracked and identified at the different speed increments.

Chapter 3

Strain and Displacement Results and Discussion

This chapter presents and discusses the experimentally measured strain and displacement results. The first section presents data from the non-rotating static displacement and strain tests and the second section contains experimental data from the rotating steady-state strain and displacement tests. The purpose of these experiments is to investigate the static and dynamic properties of the spinning, pre-twisted, laminated composite plates. The coupled effects of the stacking sequence and geometry are examined, and for the rotating tests the effects of pitch and sweep are investigated. Table 3.1 lists a summary of the plate descriptions and serial numbers from Chapter 2. The serial number is a two digit number followed by a letter where the first digit refers to the geometry type, the second is the lay-up, and the letter is unique to each plate.

3.1 Non-Rotating Static Displacements and Strain

This section presents data from the static displacements and strain tests conducted at the University of California. Figure 3.1 shows the plate setup for the experiment. The displacements of points A and B due to a transverse tip load at point A are measured. The deflection, D, and twist, ψ, are defined by equations 2.15 and 2.16 (Section 2.3.2). The strains are measured from strain gage 2 as shown in Figure 3.1.

Analytical results were performed using the graphical finite element package I-DEAS. The mesh used for these plates has 49 nodes along the x-direction and 17 nodes along the y-direction. Three node linear, triangular elements were used with a total of

1536 elements used to model the plates (Figure 3.2). A linear static analysis was used to solve for the strains and deflections; the results converged to less than 1% from the previous mesh.

Table 3.1: Plate Serial Numbers. The first digit refers to the geometry and the second is the lay-up.

Lay-up / Geometry	1. $\theta = 22.5°$	2. $\theta = 45°$	3. $[(+22.5)_5/0_5]_A$
1. Flat	11	12	13
2. 30° Pre-Twist about the Mid-Chord	21	22	23*
3. 30° Pre-Twist about the Quarter-Chord	31	32	33*
4. 30° Pre-Twist about the Leading Edge	41	42	43*
For the first two lay-ups the stacking sequence is $[\pm\theta/0_2/-\theta/0_2/+\theta/0_2]_S$ *The lay-up for this plate is $[0_2/+22.5_2/0_2/+22.5_3/0]_A$ Aspect Ratio, $c/l = 3$ Thickness Ratio, $c/t = 30$			

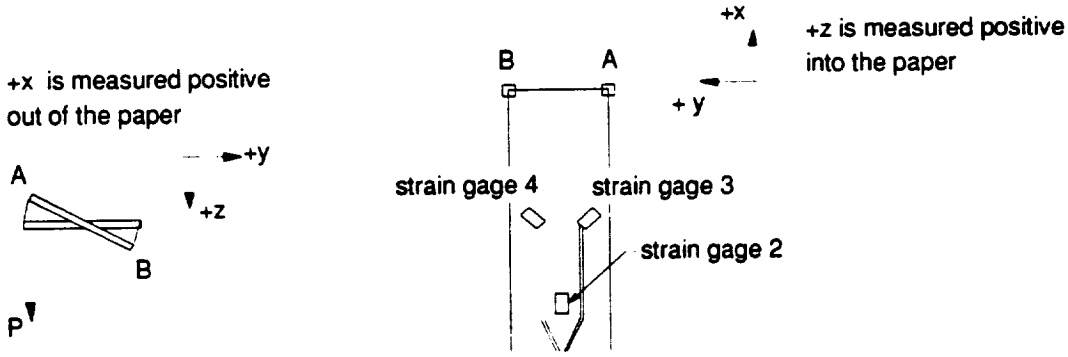

1. xyz-Deflections are measured at points A and B
2. The load, P, is applied at point A
3. The strain is recoreded from strain gage 2.

Figure 3.1: The experimental plate setup for the static strain and displacement tests.

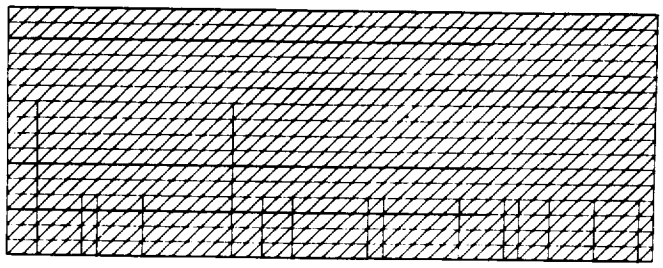

Figure 3.2: The finite element mesh used for the analytical modeling on I-DEAS.

The results from the tests were difficult to analyze because the data did not follow any discernible trends. It was thought that the analytical results from I-DEAS might be of help but this data proved just as perplexing as the experimental ones. The geometry that was used for the I–DEAS models was the exact experimentally measured geometries of the plates. This meant that the length of the plate, for example, could have been anywhere from 8.90 inch to 9.10 inch and the pre-twist anywhere from 29° to 31°. These dimensional differences became important when trying to assess the effects on the location of the pre-twist axis because the differences between each plate were very small. The I–DEAS models were modified so that all of the plates had a 9x3 inch geometry and a 30° pre-twist. Three separate load cases were run: (1) a 1 lb. transverse tip load; (2) a 1 lb. axial load in the positive x-direction; and (3) a 1 lb.-in right-hand moment in the positive x-direction, all of the loads were applied at the center tip node of the plate. For the first load case another plate graphite/epoxy plate with $[\mp 22.5/0_2/+22.5/0_2/-22.5/0_2]_S$ was modeled because the material bend-twist coupling of lay-up 1 proved interesting. Since a linear, static analysis was being used, any other transverse load case could be calculated from a linear superposition of the first and third load cases. Furthermore, three material combinations were modeled: (1) aluminum; (2) graphite/epoxy with lay-up 1; and (3) graphite/epoxy with lay-up 3. The aluminum plates eliminated any material coupling introduced by the graphite/epoxy and the third lay-up is an asymmetric one, which

introduces extension-twist coupling. The modified I–DEAS models proved to be helpful in isolating the effects of the pre-twist axis location.

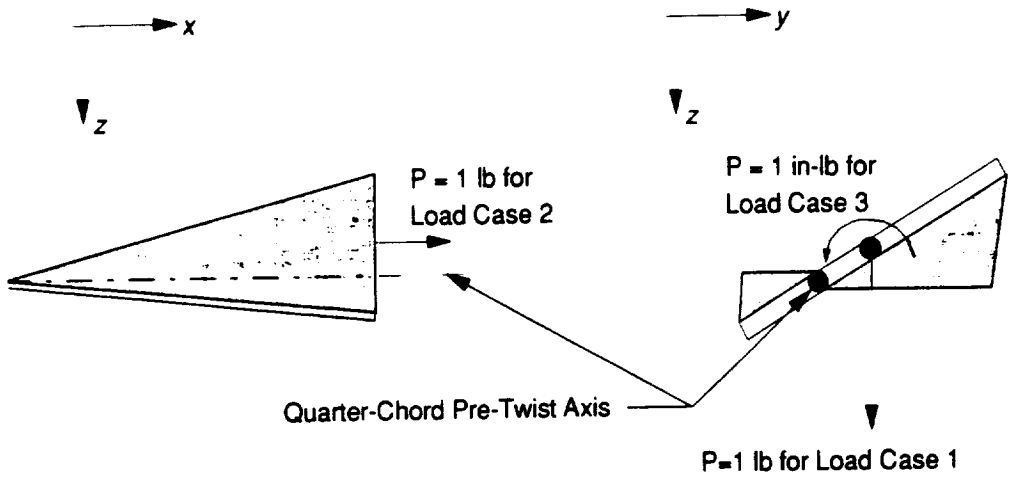

Figure 3.3: Load case descriptions for the I–DEAS models.

The following discussion is on the results from the static, analytical displacement results from I–DEAS. Figures 3.4–3.9 show the deflections and twist for the three loading configurations in Figure 3.3. Tables and graphs of the experimental results are presented in Appendix B and are compared with I–DEAS models using the measured plate geometry.

Figures 3.4 and 3.5 show the deflections and twist due to a transverse load at the tip center. Lay-up 3 is shown to have the largest deflections out of the three material combinations with lay-ups 1 and 1* being the stiffest. Lay-up 1*, which has the stacking sequence $[\mp 22.5/0_2/+22.5/0_2/-22.5/0_2]_S$, takes the off angle plies of lay-up 1 and reverses them. Lay-ups 1 and 1* are symmetric laminates with bend-twist coupling, which explains why these lay-ups are the only plates with non-zero twist for the flat plate geometry (Figure 3.5). Lay-up 1* twists in the opposite direction of lay-up 1 because of its stacking sequence. The pre-twisted plates deflect less than the flat ones because of the geometric coupling that also causes the plates to twist. The twist in Figure 3.5 shows an increase in

the twist from a flat plate to a 30° pre-twisted plate about the mid-chord for the aluminum plate and the graphite/epoxy plates with lay-ups 1* and 3, and a decrease for lay-up 1. For lay-ups 1 and 1*, the twist converges as the plate goes to a pre-twisted plate from a flat one, which suggests that the geometric coupling plays a larger role in the twist than the lay-up. As the pre-twist axis moves from the mid-chord to the leading edge, the deflections for all three materials increase and the twist decreases. The twist decrease is easily explained by the location of the load relative to the pre-twist axis; the transverse load in Figure 3.3 causes the plate to untwist clockwise. The largest untwist occurs for the leading edge plate because the transverse load is furthest away from pre-twist axis. The deflection data shows a 0.3% increase in the deflections from the mid-chord geometry to the leading edge.

Figures 3.6 and 3.7 show the deflections and twist due to an axial load at the tip center. For the flat and mid-chord geometries there are no out-of-plane deflections due to the axial load because of the geometric symmetry about the load. For the quarter-chord and leading edge geometries, however, the deflections increase as the pre-twist axis is moved away from the mid-chord. The deflections are caused by the geometric extension-twist-bend coupling. The geometric asymmetry of the load relative to the quarter-chord and leading edge pre-twist axes causes the plate not only to untwist but to also deflect. Figure 3.7 shows all of the pre-twisted plates to untwist due to the axial load. Only the flat plate with lay-up 3 has a non-zero twist caused by the extension-twist coupling of the asymmetric lay-up. The twist in the aluminum plate increases from the mid-chord geometry to the leading edge, while for the pre-twisted composite plates the untwist is at a minimum for the quarter-chord plate geometry. This behavior is caused by a combination of the geometry and material coupling. The quarter-chord and leading edge plates are undergoing extensional as well as transverse deflections due to the load, and the coupling causes the graphite/epoxy plates to exhibit extension-bend-twist coupling. The aluminum

plate has no material coupling and is shown to have a steady decrease in its absolute twist as the pre-twist axis moves from the mid-chord to the leading edge.

Figures 3.8 and 3.9 show the deflections and twist due to a 1 in-lb right hand moment in the positive x-direction. For the flat plate, only lay-up 1 is shown to have any deflections due to the moment, which is caused by the bend-twist coupling of the laminate. The absolute deflections of the plates increase as the pre-twist axis moves from the mid-chord to the leading edge, which is caused by the distance from the applied moment to the pre-twist axis. There is a large decrease in the twist as the plate goes from a flat to a pre-twisted plate, which is due to the geometric coupling that makes the pre-twisted plate torsionally stiffer. Once the plate is pre-twisted, there is very little effect on the twist due to the location of the pre-twist axis.

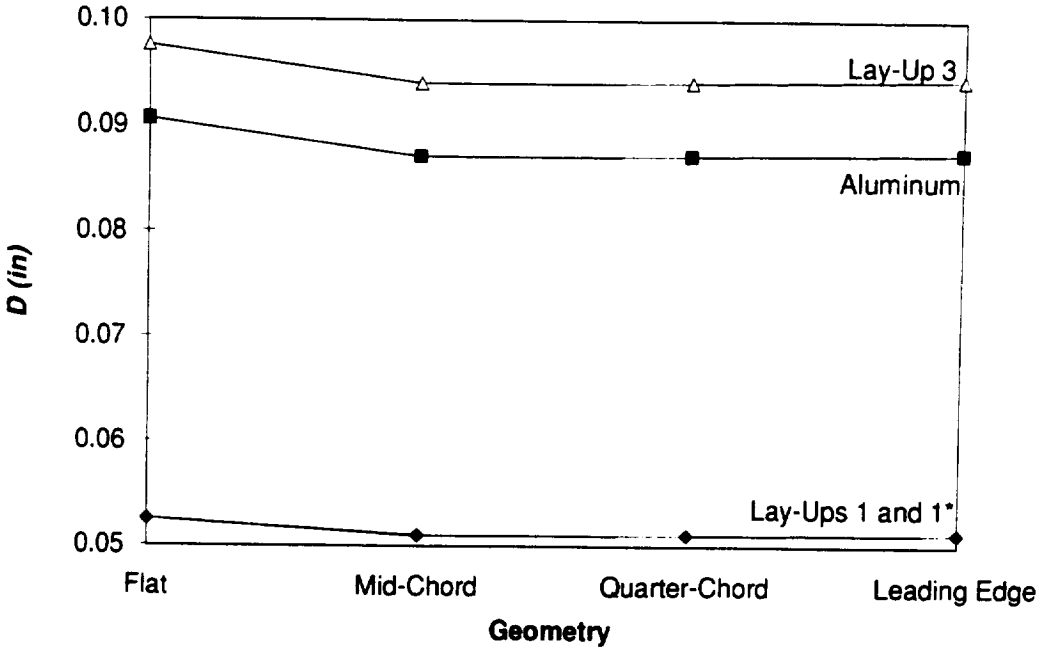

Figure 3.4: Analytical deflections due to a 1 lb. transverse load at the tip center.

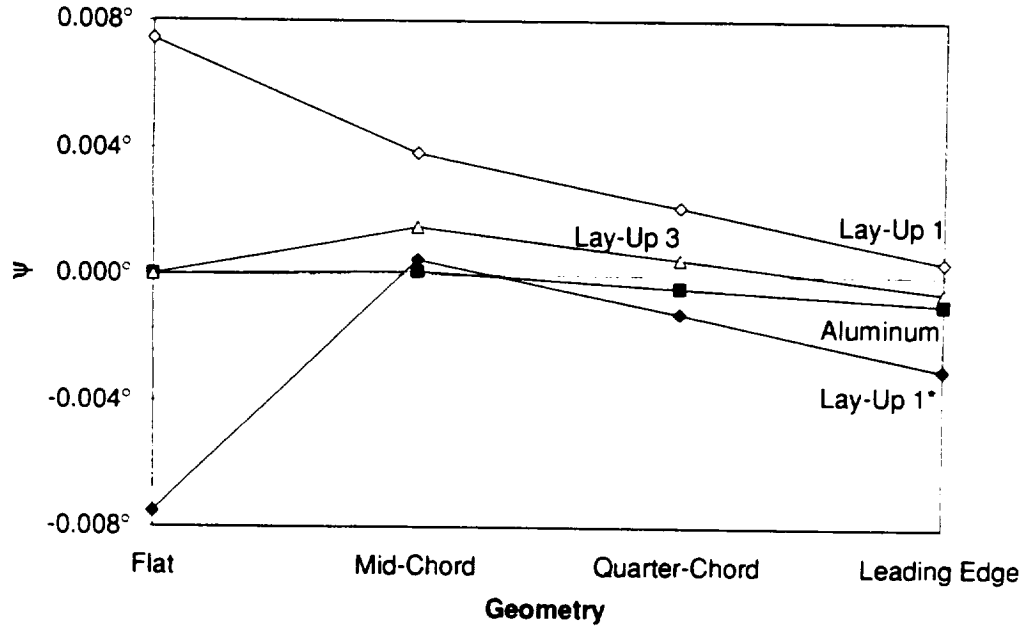

Figure 3.5: Analytical twist due to a 1 lb. transverse load at the tip center.

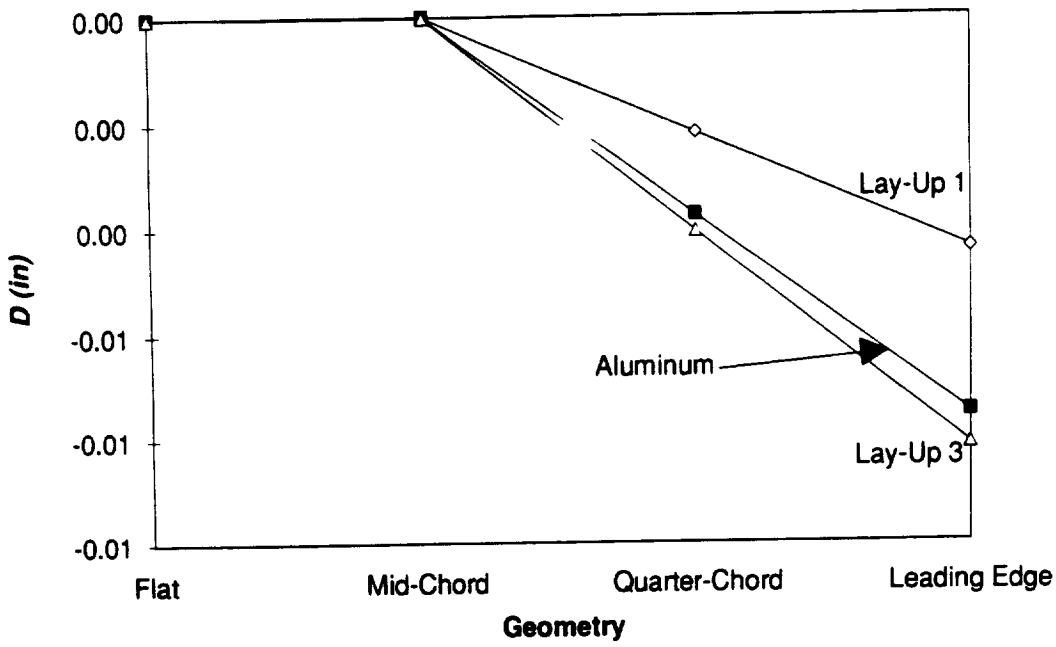

Figure 3.6: Analytical deflections due to a 1 lb. axial load at the tip center.

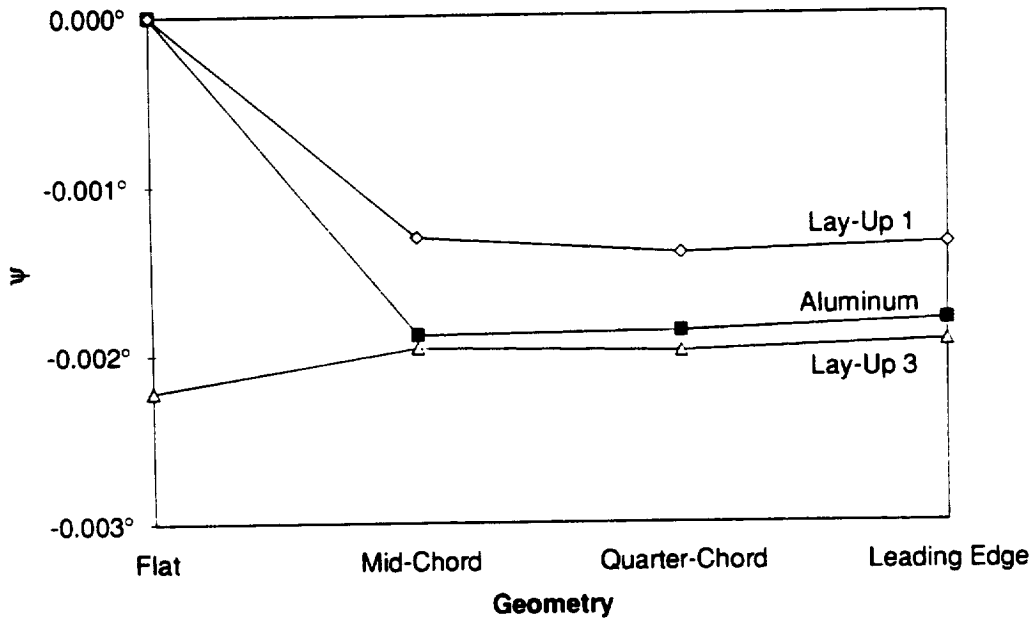

Figure 3.7: Analytical twist due to a 1 lb. axial load at the tip center.

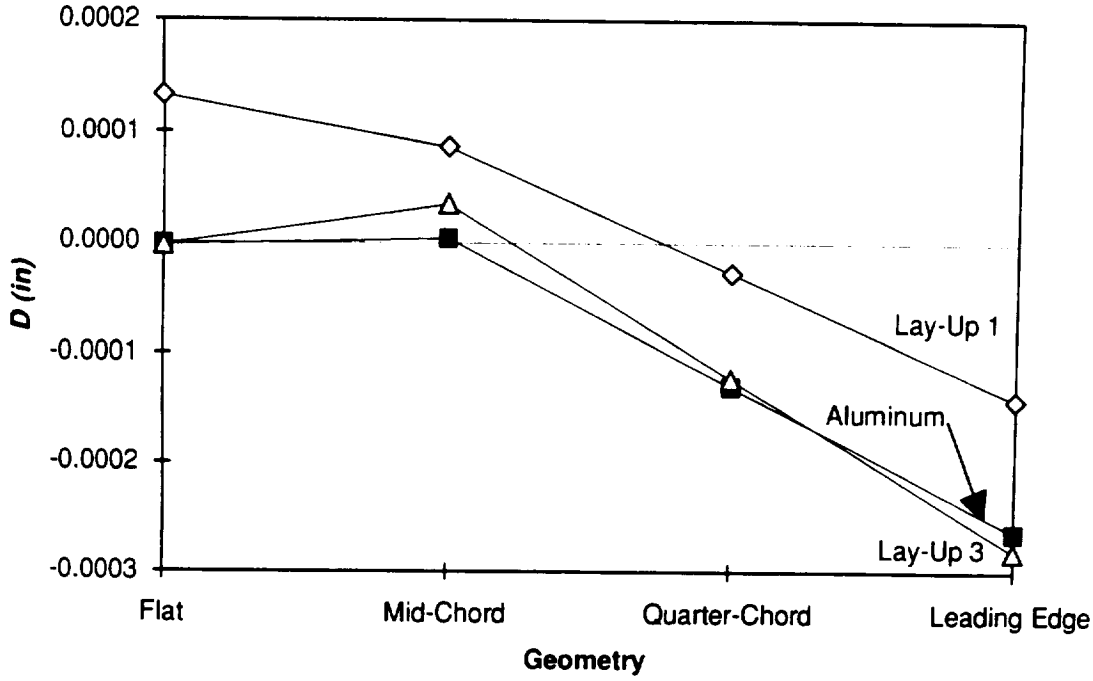

Figure 3.8: Analytical deflections due to a 1 lb-in right-hand moment in the positive x-direction at the tip center.

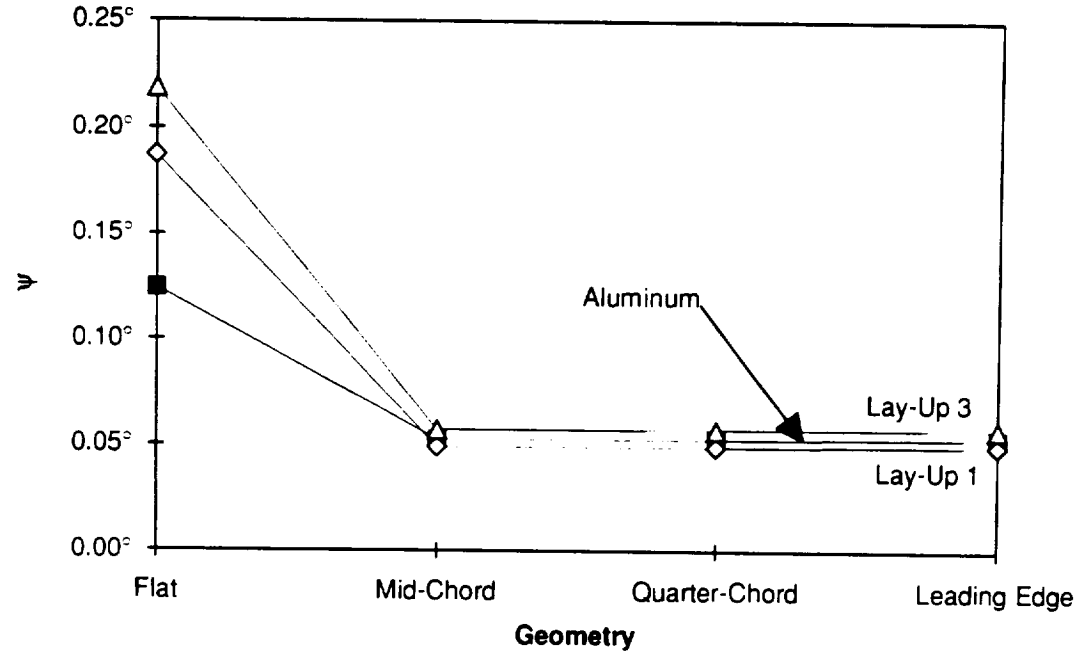

Figure 3.9: Analytical twist due to a 1 lb-in right-hand moment in the positive x-direction at the tip center.

3.2 Rotating Strain and Displacements

This section presents results from the steady-state, rotating strain tests conducted at the Dynamic Spin Rig Facility at the NASA Lewis Research Center. Only six of the twelve plate sets are tested because of the time limitations–Plates 11, 21, 31, 32, 13, and 23* (Table 3.1). These specific six plate sets were selected so that all possible geometric and material parameters could be investigated. For example, the introduction of the mid-chord pre-twist can be studied by comparing Plate 21 with Plate 11 and by comparing Plate 23 with Plate 13. To study the effect of moving the pre-twist axis location from the mid-chord $\left(\frac{c}{2}\right)$ to the quarter-chord $\left(\frac{c}{4}\right)$, one compares the results of Plate 31 with Plate 21. The effect of ply orientation on a symmetric pre-twisted plate can be studied by comparing Plates 32 and 31. Finally, the effect of the asymmetric stacking sequence on flat and pre-twisted plates can be investigated by comparing Plate 11 with Plate 13, and Plate 21 with Plate 23, respectively. The plates are tested in the three different configurations listed in Table 3.2. Configuration A is the baseline case and Configurations B and C examine the effects of pitch and sweep, respectively.

Figure 3.10 is a sketch of a pre-twisted plate about the quarter-chord with a pitch setting of 0° (Configuration A). It shows the direction of a positive pitch change, β_p, as well as the location of the pre-twist axis with respect to the spin axis.

For the strain measurements there are four gages instrumented on each plate and are labeled as in Figure 3.11. Gages 1 and 2 are used to measure the axial and bending strains and Gages 3 and 4 are for the torsion strains. The displacements are measured at two locations, one near the tip and another mid span of the plate; the exact location is given for each of the measurements. Some of the strain gage data is incomplete because of short circuits at higher speeds. Plates 13 and 23* were not able to be tested in Configuration C because the pin that sets the sweep angle on the clamping fixture was damaged during testing.

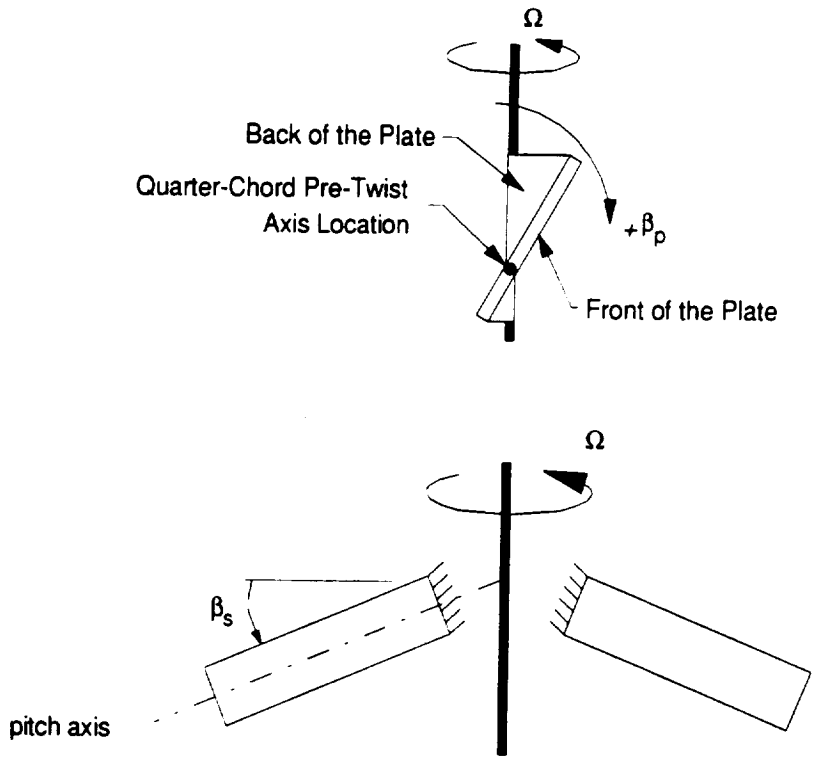

Figure 3.10 Orientation of the pre-twisted plate about the quarter-chord within the spin rig, the positive pitch direction, and the sweep angle.

Table 3.2: Pitch and sweep configurations for the steady-state strain and displacement tests.

Configuration	A	B	C
Pitch, β_p	0°	30°	0°
Sweep, β_s	0°	0°	22.5°

The raw data from Gages 1 and 2 are processed in such a way to calculate the bending and axial strains of the plate. The axial strain is calculated as

$$\varepsilon_A = \frac{\varepsilon_{Gage\ 1} + \varepsilon_{Gage\ 2}}{2}, \tag{3.1}$$

and the bending strain is

$$\varepsilon_B = \frac{\varepsilon_{Gage\ 1} - \varepsilon_{Gage\ 2}}{2}. \tag{3.2}$$

The orientation of Gages 3 and 4 makes them sensitive to any twisting of the plate, and the strains from these gages are referred to as the torsion strains. For the displacement data the deflections and twist are defined as in Equations 2.15 and 2.16.

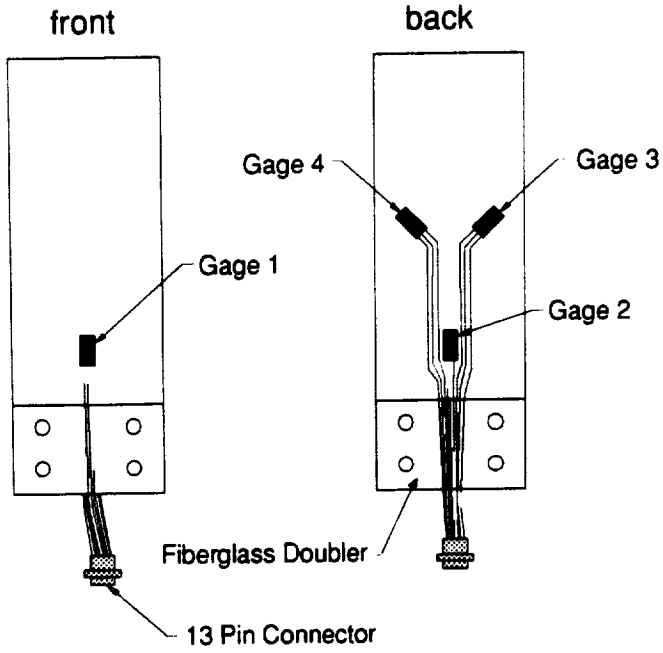

Figure 3.11: Strain gage labels and locations.

There are a total of 71 graphs presented at the end of this section, and each set of graphs is presented in its own subsection for easier reference. The first six sets of graphs present data for each individual plate set in all of the configurations, and the next six sets make comparisons between the different plate sets. The comparisons examine the effects of pre-twist, pre-twist axis location, and lay-up. Preceding the first set of graphs are six tables (pp. 77-78) listing the locations of the mid-span and tip lasers used to measure the deflections and twist for each of the six plate sets.

3.2.1 Flat and Pre-Twisted Plate about the Mid-Chord with $[\pm 22.5/0_2/-22.5/0_2/+22.5/0_2]_S$ Lay-Up

This section discusses the steady-state strain and displacement results for the flat plate and the pre-twisted plate about the mid-chord with lay-up 1 (Plates 11 and 21). Figures 3.12–3.19 (pp. 79–82) compare the results of the two plates for each of the three

test configurations. Figures 3.37–3.48 (pp. 91–97) make direct comparisons between the two plates for the three configurations. Tables 3.3 and 3.4 list the laser locations of the tip and mid-span laser where the deflections and twist are measured.

Plate 11. Figures 3.12 and 3.13 show that for Configurations A and B, Plate 11 only axially extends, with no out-of-plane deflections or twisting. The plate deflections and bending strains are 0.028 inch at 8000 rpm and less than 1 $\mu\varepsilon$ at 7500 rpm, respectively. The torsion and twist data in Figures 3.14 and 3.15 shows very little twisting by the plate in Configurations A and B. The torsion gages show the plate to be twisting, but the indicated strain is due to the axial extension of the plate.

For Configuration C ($\beta_S = 22.5°$), the centrifugal forces cause the plate to swing upward producing compressive strains along the top edge and tensile strains on the bottom one. Therefore, the bending strains, deflections, and twist for Configuration C should be zero. Figures 3.12–3.15, however, show that the plate is bending and twisting in Configuration C. This is because the pitch setting for this configuration ($\beta_P = 0°$) is critically stable, and any slight offset from this angle causes the plate to bend and twist out of plane rather than deflect in-plane.

Plate 21. Results from the rotating strains and displacements for the pre-twisted plate about the mid-chord with lay-up 1 are presented in Figures 3.16–3.19 (pp. 81–82). The displacement data for the mid-span laser for Plate 21 is not available and only the tip deflections and twist will be presented.

There is little or no bending of the plate in Configurations A and B (Figures 3.16 and 3.17). The torsion gages and twist data show Gage 3 to be increasing and Gage 4 to be decreasing with the rotational speed (Figures 3.18 and 3.19) which means the plate is untwisting as it spins. The data also shows the plate to be untwisting more in Configuration B than in A.

For Configuration C, the centrifugal forces force the plate to swing upwards. Because the plate is pre-twisted, the plate bends and twists with increasing speed, which explains the rise in the bending strains and deflections in Configuration C (Figures 3.16 and 3.17). The rise in the axial strain for Configuration C is not as great as in Configuration A because of the extension-twist-bend coupling of the pre-twisted geometry. The bending strains level off at the higher rotational speeds while the axial strains continue to increase. The twisting of the plate in Configuration C is opposite of the twist that occurs in Configurations A and B (Figures 3.18 and 3.19). In configurations A and B the extension-twist coupling causes the plate to untwist while the orientation of the plate in Configuration C ($\beta_p = 0°$, $\beta_s = 22.5°$) causes the lower edge of the plate to swing upwards (see Figure 3.10). Because the axial strains continually increase with speed the plate will resist twisting. This explains why the absolute twist of the plate in Configuration C isn't as large as the absolute untwist in the other configurations (Figure 3.19).

Plates 11 and 21. Figures 3.37–3.48 (pp. 91–97) compare the steady-state data from a flat and pre-twisted plate about the mid-chord with lay-up 1. Figures 3.37–3.40 compare the strains and displacement data for Configuration A, Figures 3.41–3.44 compare data from Configuration B, and Figures 3.45–3.48 compare data from Configuration C.

Figures 3.37 and 3.41 show that neither of the two plates are bending in Configurations A and B. The absolute deflections for the two plates in both configurations are small and have a maximum value of about 0.07 inch and average at about 0.03 inch at 8000 rpm. The axial strains for the pre-twisted plate (Plate 21) are larger than the strains for the flat plate (Plate 11), 650 $\mu\varepsilon$ versus 400 $\mu\varepsilon$ at 7500 rpm for Configuration A, respectively. This is caused by the extension-twist geometry coupling which makes the pre-twisted plate extensionally softer.

The torsion strains and twist data for Configuration A show the flat plate to have little or no twisting while the pre-twisted plate about the mid-chord is untwisting (Figures 3.39 and 3.40). For Configuration B, both plates are twisting; Plate 21 is untwisting counter-clockwise while the flat plate (Plate 11) twists counter-clockwise.

For Configuration C, both plates are bending as well as axially extending (Figures 3.45 and 3.46). Plate 21 has an absolute deflection that is 200% more than the flat plate. The torsion and twist data also show both plates to be twisting in opposite directions with the pre-twisted plate twisting clockwise. The twist increase for Plate 21 is due to the bend-twist coupling of the sweep angle.

3.2.2 Pre-Twisted Plates about the Mid-Chord and Quarter-Chord with $[\pm 22.5/0_2/-22.5/0_2/+22.5/0_2]_S$ Lay-Up

This section presents steady-state data for the pre-twisted plate about the quarter-chord with lay-up 1 (Plate 31) and compares this with data from Plate 21 from the previous section. Table 3.5 lists the spanwise locations where the rotating deflections and twists are measured. Figures 3.20–3.24 (pp. 83–85) show the steady-state strains, deflections, and twist for Plate 31 for all three configurations, and Figures 3.49–3.60 (pp. 97–103) compare the pre-twisted plates about mid-chord and quarter-chord (Plates 21 and 31).

Plate 31. Figures 3.20–3.24 (pp. 83–85) show the strains and displacement results for the pre-twisted plate about the quarter-chord with lay-up 1. Figure 3.20 shows the axial and bending strains for Configurations A and C; the strains for Configuration B are not found because of strain gage short circuits during testing. Both the axial and bending strains for Plate 31 increase with the rotational speed. To better understand which direction the plate is bending the individual strains from Gages 1 and 2 are shown in Figure 3.21. Gage 2 in Configuration A goes into compression at the lower speeds, reaches a local minimum at 4000 rpm (-200 $\mu\varepsilon$), and increases to 20 $\mu\varepsilon$ at 7000 rpm; Gage 1, meanwhile, continually

increases to 1200 με at 7000 rpm. This means the plate is bending to the left in Figure 3.10 and is caused by the geometric asymmetry of the plate. The bending levels off at the higher speeds while the axial straining continues to increase. Figure 3.22 corroborates this bending strain behavior and shows the plate to be deflecting about 0.25 inch at 6500 rpm. The figure also shows the deflections to level off and that there is not much difference between the behavior in Configurations A and B.

Figures 3.23 and 3.24 show the torsion strains from Gages 3 and 4 and the twist data. For Configurations A and B the plate is untwisting. The strain data, however, contains some of the effect of the plate bending because strain data is not centered about 0 με line. The plate bending causes both gages to go negative and the untwisting causes Gage 3 to rise again. The torsion strain and twist data also show the plates to be twisting more in Configuration B than in A.

For Configuration C, the bending strains and deflections are larger than the strains and deflections in Configurations A and B (Figures 3.20 and 3.22), and the torsion strain and twist data show the plate to be twisting clockwise (Figures 3.23 and 3.24). The sweep angle and the geometric asymmetry work together to cause the plate to deflect to the left and twist, which explains the increased deflections and bending strains. The torsion strain data is affected by the plate bending, which causes Gages 3 and 4 to go into compression at the higher speeds. The twist of the plate is limited by the axial extension that causes the plate to untwist.

Plates 21 and 31. The most obvious effect of moving the pre-twist axis from the mid-chord to the quarter-chord is the rise in the bending strains and deflections (Figures 3.49 and 3.51) for the quarter-chord plate for Configuration A. The axial strains for both plates in Configuration A, however, are very nearly equal. Figure 3.50 shows the individual strains of Gages 1 and 2 for the two plates in Configuration A. The gages for the mid-chord plate are composed almost entirely of axial straining with little or no

bending, while the strains for Gages 1 and 2 on the quarter-chord plate are comprised of both axial and bending strains. Gage 1 for both plates experiences tension strains throughout the entire speed range while Gage 2 initially goes into compression due to the plate bending. The strain for Gage 1 on the quarter-chord plate is higher because of the combined axial and bending strains. As the speed increases, the bending strains begin to level off while the axial straining continues to increase.

The plate deflections for Configurations A and B show Plate 31 to have greater deflections than Plate 21, about -0.25 inch vs. -0.02 inch at 6500 rpm (Figures 3.51 and 3.54). The shape of the deflection curves also indicates the plate bending to level off at the higher speeds due to the steady increase in the axial extension.

The torsion strain and twist data for Configurations A and B show that both plates are untwisting (Figures 3.52–3.53 and 3.55–56). For Configuration A the torsion strains for the mid-chord plate are centered about the 0 με line; the quarter-chord strains, however, are influenced by the plate bending (Figure 3.52). Plate 31 is untwisting and bending with the rotational speed, which initially makes Gage 3 go into compression. After the deflections level off the axial straining begins to dominate. the plate continues to untwist, and Gage 3 rises. The twist data in Figures 3.53 and 3.56 shows the plates to be untwisting at about the same rate.

For Configuration C, both plates deflect upwards and to the left because of the sweep angle. The quarter-chord plate has higher bending strains and deflects more because of its geometric asymmetry (Figures 3.57 and 3.58). Both plates experience comparable amounts of axial straining. If in Figure 3.10, the twist axis location for the quarter-chord plate was placed on the upper half of the plate, the deflection caused by the geometric asymmetry would counteract the deflection caused by the sweep angle.

Figure 3.60 shows both plates to be twisting as the rotational speed is increased with the quarter-chord plate twisting more than the mid-chord one. Gage 3 undergoes

compressive straining due to the bending and twisting of the plate with both plates having nearly equal strains (Figure 3.59). Gage 4 is strained in tension due to the twisting while the bending and the axial straining due to the centrifugal forces cause the strains in Gage 4 to decrease. The strains on Gage 4 for the quarter-chord plate (Plate 31) are lower than the one on the mid-chord plate because the quarter-chord plate deflects more causing the torsion gages on Plate 31 to go into compression at higher rotational speeds (Figure 3.59).

3.2.3 Pre-Twisted Plates about the Quarter-Chord with $[\pm\theta/0_2/-\theta/0_2/+\theta/0_2]_S$ Lay-Up (θ = 22.5° and 45°)

This section presents results for the pre-twisted plate about the quarter-chord with lay-up 2 (Plate 32) and makes comparisons between this plate and Plate 31 of the previous section. Table 3.6 lists the locations of the tip and mid-span lasers where the deflections and twist are measured. Figures 3.25–3.28 (pp. 85–87) depict the strain and displacement data for Plate 32 for all three configurations. Figure 3.25 shows the axial and bending strains for Plate 32 for Configuration A; similar data is unavailable for Configurations B and C because of the high centrifugal forces on the strain gage wires. Figure 3.26 is a graph of the plate deflections at the tip and mid-span locations of the plate for all three configurations. Figures 3.27 and 3.28 depicts the torsion strains and twist, respectively, for the all three configurations.

Plate 32. The axial and bending strains and deflections in Figures 3.25 and 3.26 show that Plate 32 is deflecting because of the geometric asymmetry. The deflections for Configurations A and B show that there is a negligible effect due to the pitch (Figure 3.26). For Configuration C, the plate twists and deflects upwards and to the left.

In Figures 3.27 and 3.28, the torsion strains and twist data shows that Plate 32 twists more in Configuration B than in A. The figures also show that for Configuration C the plate twists clockwise and bends upwards to the left. Gage 3 will always be in

compression due to the twisting and bending while Gage 4 goes into tension due to the twisting. The tension strains in Gage 4, however, level off due to the plate bending.

Plates 31 and 32. Figures 3.61–3.70 (pp. 103–108) are graphs comparing the data for the pre-twisted quarter-chord plates with lay-ups 1 and 2 for all configurations. Figure 3.61 compares the axial and bending strains for Configuration A. Both plates show axial and bending strains for Configuration A with Plate 32 exhibiting more axial straining than Plate 31. Lay-up 1 is axially stiffer because its fibers are aligned closer to the direction of the centrifugal forces. The geometric asymmetry of the plates causes them to deflect, and both plates have comparable values for the bending strains. The deflections in Figures 3.62, 3.65, 3.68 show Plate 31 to have smaller deflections for Configurations A, B, and C. This is because the lay-up for Plate 31 is stiffer in bending than Plate 32.

Figures 3.63 and 3.66 show Gage 3 for both plates going into compression due to the plate bending. Because this plate bending dominates the behavior at the lower speeds, Gage 3 on Plate 32 has higher compressive strains than Plate 31 because of its ply lay-up. The data for Gage 4 on the other hand suggests Plate 31 to be untwisting more than Plate 32 because the stacking sequence of Plate 32 is more resistant to untwisting than Plate 31.

For Configuration C, the plates are bending upwards and twisting. Figure 3.68 shows the plate deflections at the mid-span and tip locations and Plate 32 is deflecting more than Plate 31 because of its ply lay-up. The twist results in Figure 3.70 also show Plate 32 to be twisting more. This is supported by the torsion strain data in Figure 3.69 where Gages 3 and 4 of Plate 31 are affected by the plate bending. Both gages go into compression at the higher rotational speeds because of the deflections while the gages on Plate 32 are indicating smaller deflections because Gage 4 never goes into compression. It does, however, reach a local maximum and begin to decrease at the higher speeds because of the plate bending.

3.2.4 The Asymmetric Lay-Ups

This section presents the data for the flat plate with $[+22.5_5/0_5]_A$ (Plate 13) and the pre-twisted plate about the mid-chord with $[0_2/+22.5_2/0_2/+22.5_3/0]_A$ (Plate 23*) for Configuration A. The plates are not tested in Configurations B and C because problems with the mechanical hardware at the Dynamic Spin Rig Facility. Three plate comparisons are made in this section: (1) Plates 11 and 13; (2) Plates 21 and 23*; and (3) Plates 13 and 23*. The comparisons between Plates 11 and 13, and Plates 21 and 23* investigate the effect of the asymmetric lay-up on the flat and pre-twisted plate geometries, respectively. Plates 21 and 23* compare the effects of the pre-twist on the asymmetric laminates. Tables 3.7 and 3.8 lists the locations of the mid-span and tip laser for Plates 13 and 23* where the deflections and twist are measured. Figures 3.29–3.32 (pp. 87–89) and 3.33–3.36 (pp. 89–91) present the strain and displacement data for Plates 13 and 23*, respectively. Figures 3.71–3.74 (pp. 108–110) show the plate comparisons between Plates 11 and 13, Figures 3.75–3.78 (pp. 110–112) compare Plates 21 and 23*, and Figures 3.79–3.82 (pp. 112–114) compare Plates 13 and 23*.

Figure 3.29 is graph of the measured strains of Gage 2. The axial and bending strains are not presented because of complications with Gage 1. Because of the flat plate geometry, there are no out-of-plane deflections, 0.065 inch at 8000 rpm (Figure 3.30). The asymmetric laminate introduces geometric and material extension-twist coupling. A truly flat asymmetric plate is proven impossible to manufacture for this experiment. As a result, there is an initial 10° pre-twist in the "flat" plate in the same direction indicated in Figure 3.10. The asymmetric lay-up, $[+22.5_5/0_5]_A$, also introduces material coupling that causes the plate to twist counter-clockwise (Figure 3.10) with an applied tensile force. The torsion strains and twist data (Figures 3.31 and 3.32) show the plate to be untwisting. The geometric and material coupling of the plate work together to cause the plate to untwist. If the lay-up is reversed to $[-22.5_5/0_5]_A$ the initial pre-twist goes in the opposite

direction of Figure 3.10 and the material and geometric extension-twist coupling causes the plate to untwist clockwise.

Figure 3.33 shows the axial and bending strains of Plate 23*; the plate is axially extending with no bending because no geometric asymmetry exists for this plate. The deflections in Figure 3.34 show relatively small deflections, approximately 0.043 inch at 8000 rpm. Like the flat, asymmetric plate the extension-twist coupling of the lay-up and the geometry work together to cause the plate to untwist in the counter-clockwise direction (Figure 3.10). If, however, we put the initial pre-twist in the opposite direction the geometric coupling causes the plate to untwist in the clockwise direction while the material coupling of the lay-up makes the plate twist in the counter-clockwise direction. The torsion strain and twist data show the plate to be untwisting. The torsion data in Figure 3.35 shows Gage 3 going into tension (926 $\mu\varepsilon$ at 8000 rpm) and Gage 4 (–606 $\mu\varepsilon$ at 8000 rpm) going into compression. The twist data shows the plate to be untwisting about 0.2° at 8000 rpm.

Plates 11 and 13. Figures 3.71–3.74 compare the flat plates with the symmetric and asymmetric lay-ups. Because of the geometric symmetry, both plates are shown to have little or no deflections (Figure 3.72). Figure 3.71 compares the strains for Gages 1 and 2 for the two plates and shows the asymmetric plate (Plate 13) to have higher extensional strains than the symmetric one (Plate 11). This is due to the asymmetry of the lay-up that causes the extension-twist coupling that makes the plate strain more extensionally. The torsion strains and twist data also show that the flat asymmetric plate is twisting due to the geometric and material extension twist coupling, while the flat plate exhibits no twist for Configuration A (Figures 3.73 and 3.74).

Plates 21 and 23*. Figure 3.75 compares the axial and bending strains for the pre-twisted plates about the mid-chord with lay-ups 1 and 3*. Both plates have no bending strains or deflections due to the geometric symmetry about the mid-chord (Figure 3.76). Figure

3.75 shows Plate 23* to have larger axial straining, which is again due to the asymmetry of the laminate. The torsion strain and twist data also show Plate 23* to have larger torsion strains and twist because of the material coupling caused by the asymmetric lay-up (Figures 3.77 and 3.78).

Plates 13 and 23*. Figures 3.79–3.82 show plate comparisons between the flat plate with $[+22.5_5/0_5]_A$ (Plate 13) and the pre-twisted plate about the mid-chord with $[0_2/+22.5_2/0_2/+22.5_3/0]_A$ (Plate 23*). Comparing the flat and pre-twisted asymmetric plates, Figure 3.79 shows the pre-twisted plate to have more axial straining than the flat plate due to the enhanced extension-twist coupling of the pre-twisted geometry. The torsion strains also show Plate 23* to be straining more torsionally for Gage 3 while the strains for Gage 4 are approximately the same if the offset is taken into account (Figure 3.81). The twist data shows both plates to have about the same levels of twist at 8000 rpm (Figure 3.82).

Table 3.3: Laser locations for Plate 11. Locations are measured from the tip of the plate.

Configuration	Tip Laser (in)	Mid-Span Laser (in)
A	0.296	3.622
B	0.305	3.671
C	1.378	3.603

Table 3.4: Laser locations for Plate 21. Locations are measured from the tip of the plate.

Configuration	Tip Laser, (in)	Mid-Span Laser,(in)
A	0.532	3.632
B	0.345	3.603
C	0.965	3.613

Table 3.5: Laser locations for Plate 31. Locations are measured from the tip of the plate.

Configuration	Tip Laser, (in)	Mid-Span Laser,(in)
A	0.507	3.612
B	0.345	3.617
C	0.979	3.593

Table 3.6: Laser locations for Plate 32. Locations are measured from the tip of the plate.

Configuration	Tip Laser (in)	Mid-Span Laser (in)
A	0.502	3.622
B	0.335	3.603
C	0.989	3.583

Table 3.7: Laser locations for Plate 13. Locations are measured from the tip of the plate.

Configuration	Tip Laser, (in)	Mid-Span Laser, (in)
A	0.276	3.593
B	Not Tested in this Configuration	Not Tested in this Configuration
C	Not Tested in this Configuration	Not Tested in this Configuration

Table 3.8: Laser locations for Plate 23*. Locations are measured from the tip of the plate.

Configuration	Tip Laser, (in)	Mid-Span Laser, (in)
A	0.463	3.607
B	Not Tested in this Configuration	Not Tested in this Configuration
C	Not Tested in this Configuration	Not Tested in this Configuration

3.2.5 Plate 11

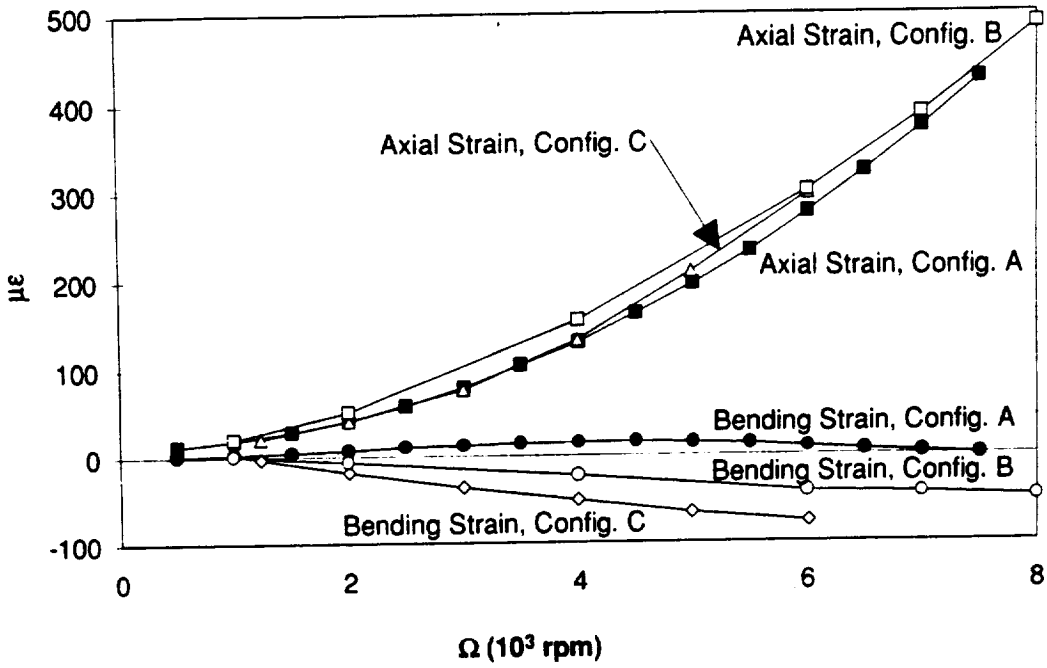

Figure 3.12: Axial and bending strains of Plate 11 for Configurations A, B, and C.

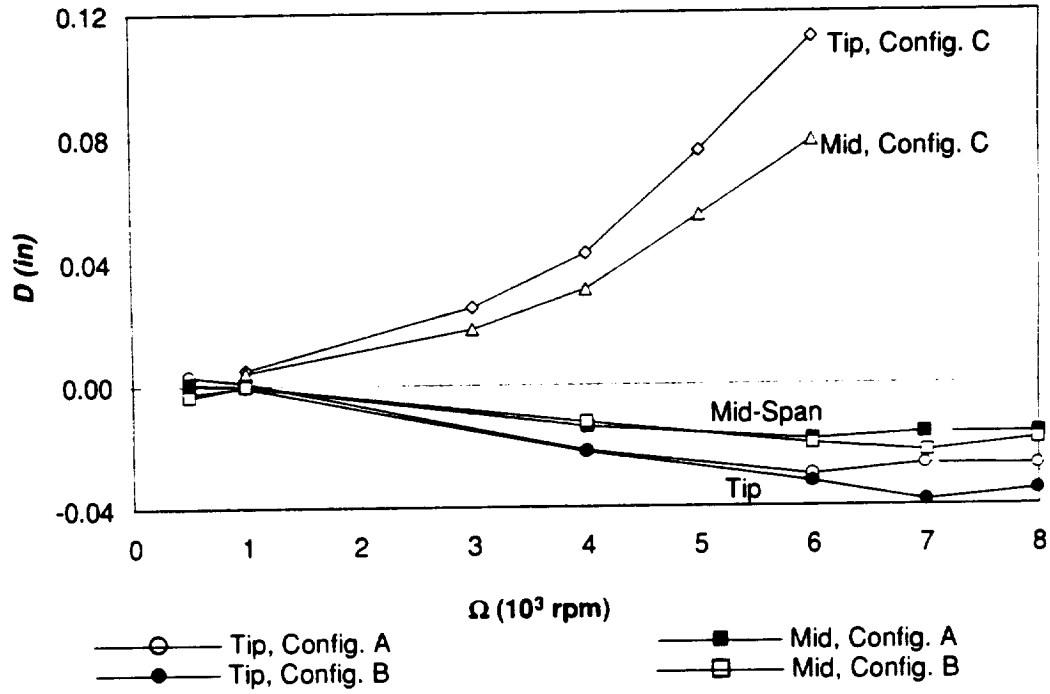

Figure 3.13: Deflections of Plate 11 for Configurations A, B, and C.

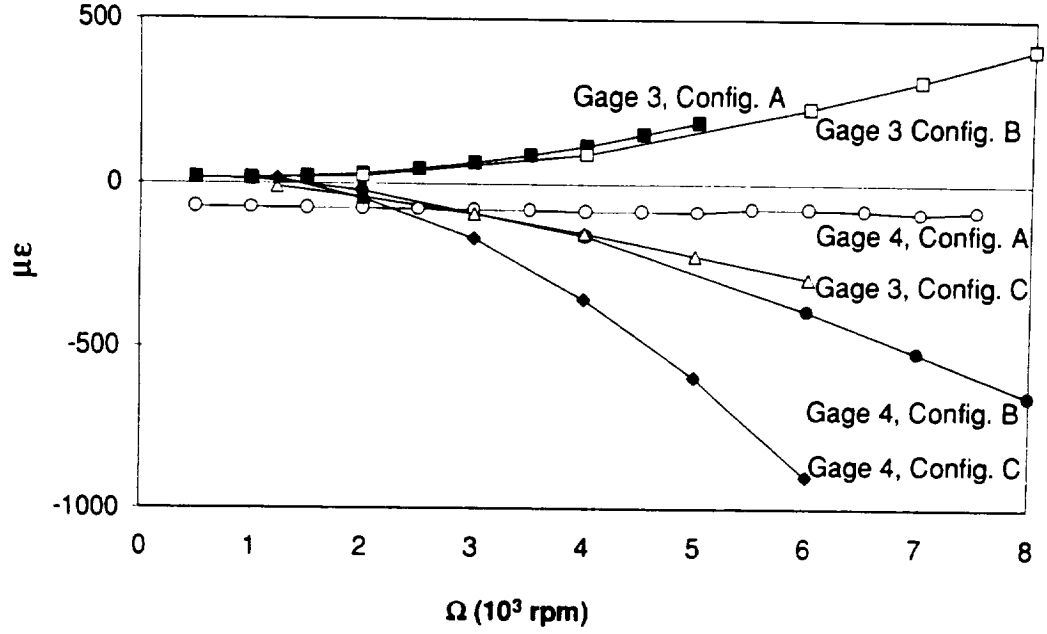

Figure 3.14 Torsion strains of Plate 11 for Configurations A, B, and C.

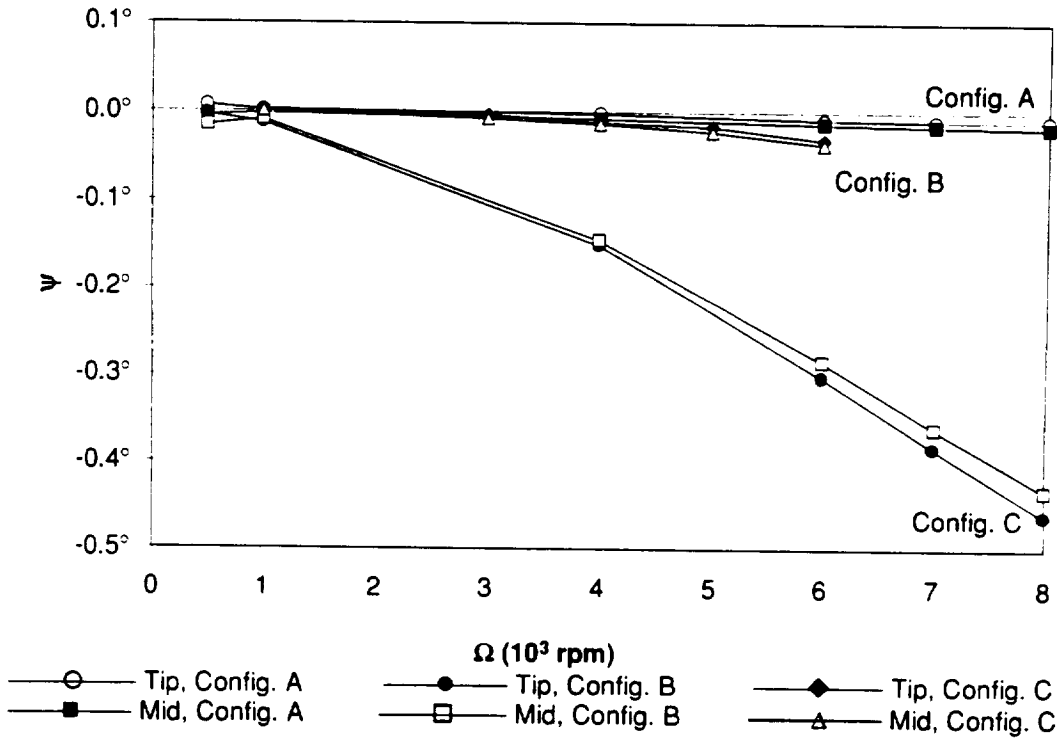

Figure 3.15: Twist of Plate 11 for Configurations A, B, and C.

3.2.6 Plate 21

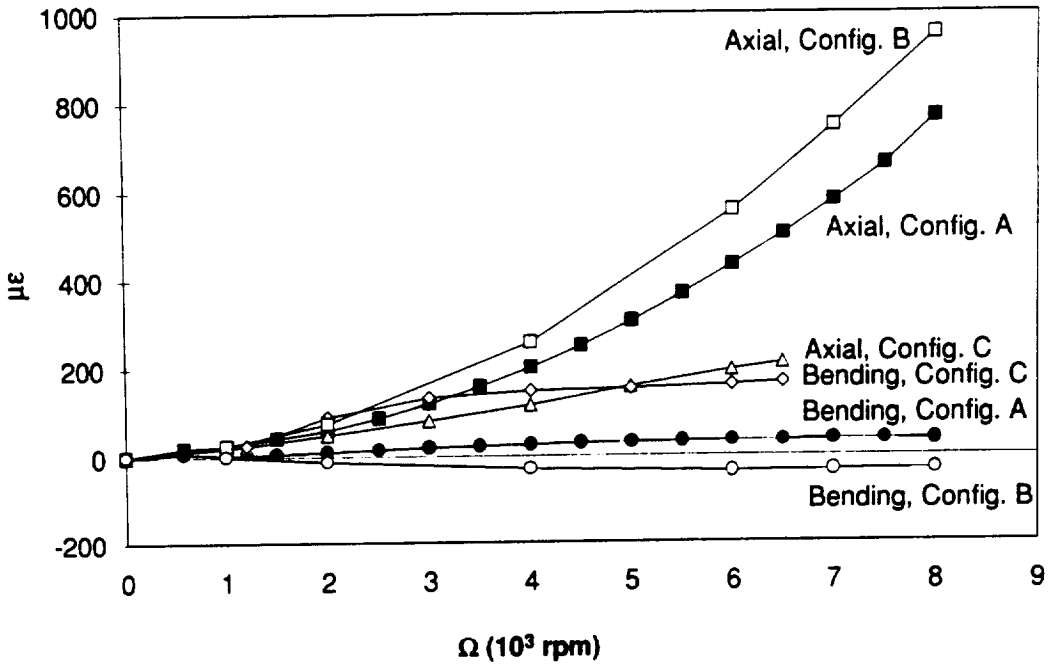

Figure 3.16: Axial and bending strains of Plate 21 for Configurations A, B, and C.

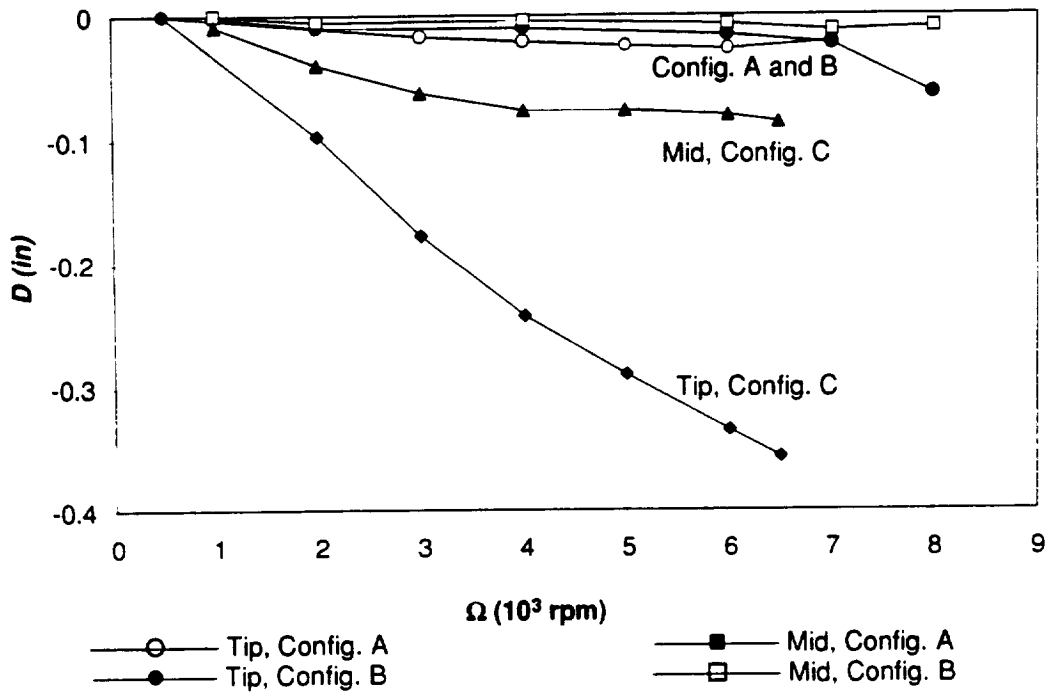

Figure 3.17: Deflections of Plate 21 for Configurations A, B, and C.

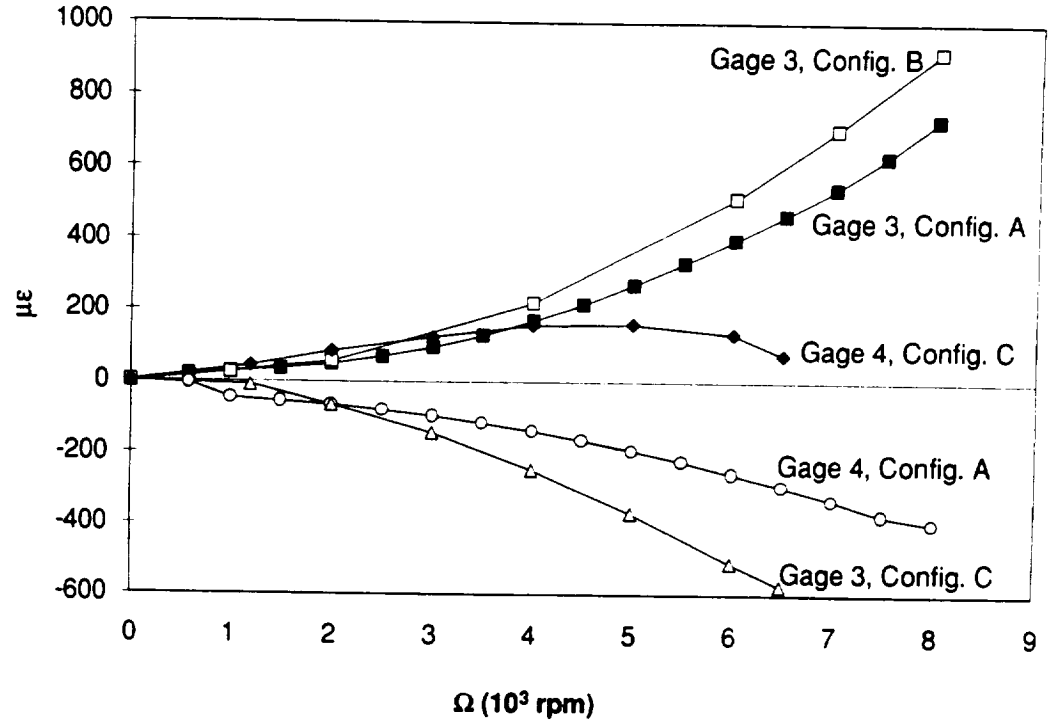

Figure 3.18: Torsion strains of Plate 21 for Configurations A, B, and C.

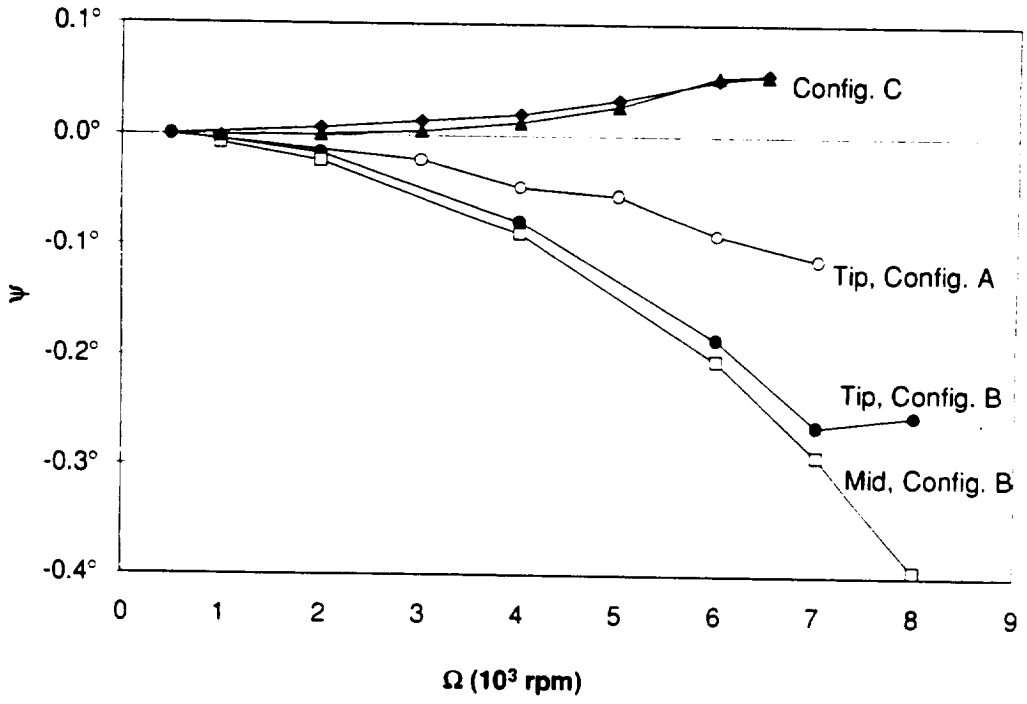

Figure 3.19: Twist of Plate 21 for Configurations A, B, and C.

3.2.7 Plate 31

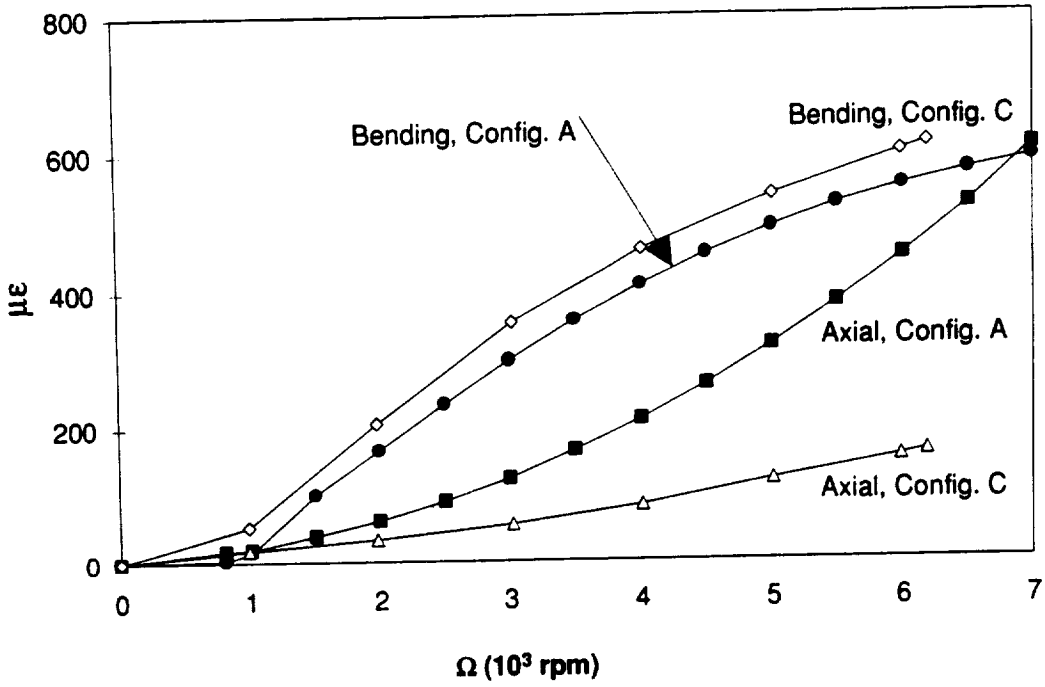

Figure 3.20: Axial and bending strains of Plate 31 for Configurations A, B, and C.

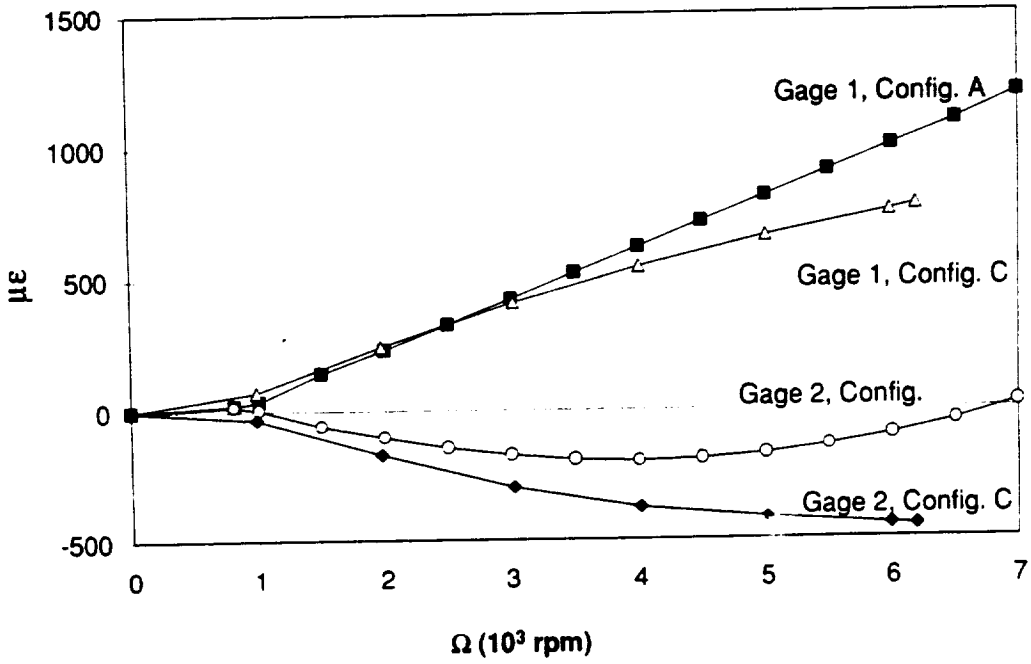

Figure 3.21: Strains from Gages 1 and 2 of Plate 31 for Configurations A, B, and C.

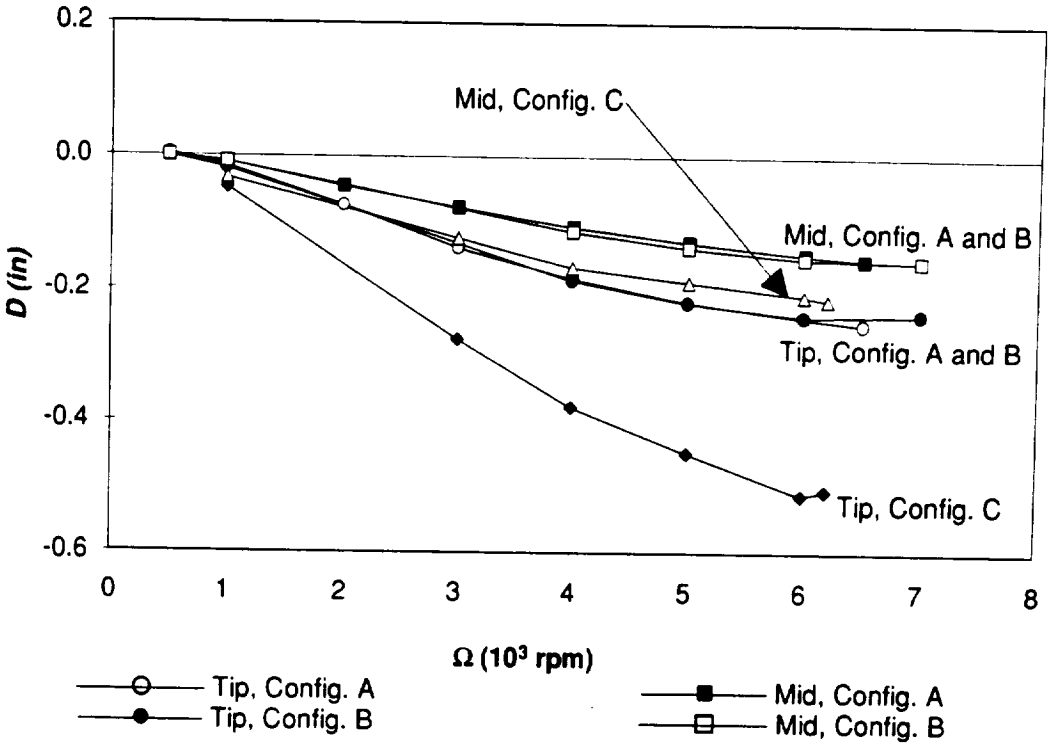

Figure 3.22: Deflections of Plate 31 for Configurations A, B, and C.

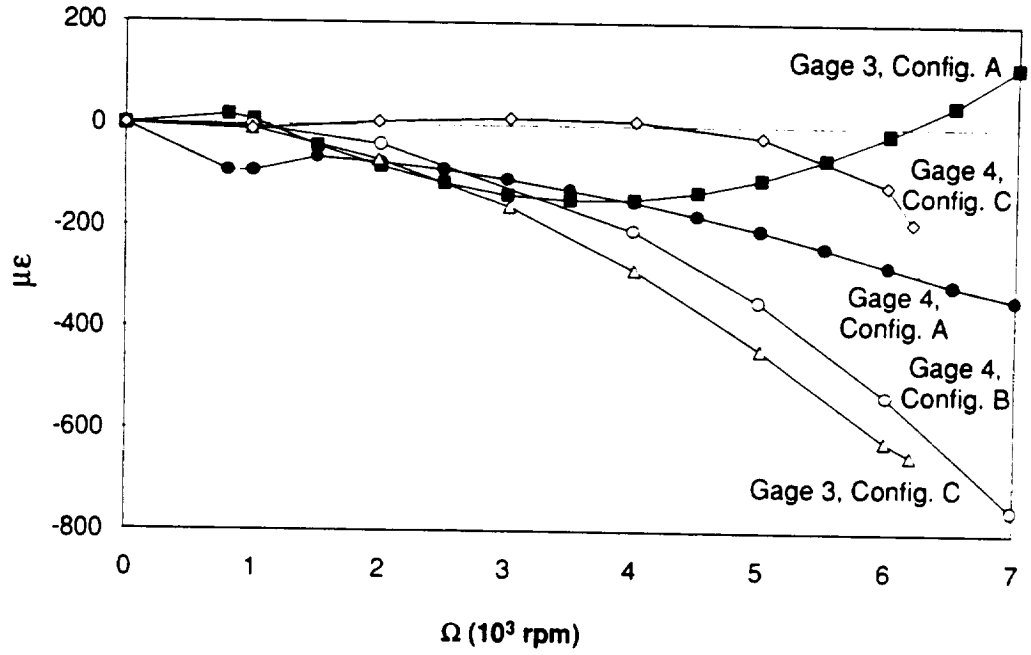

Figure 3.23: Torsion strains of Plate 31 for Configurations A, B, and C.

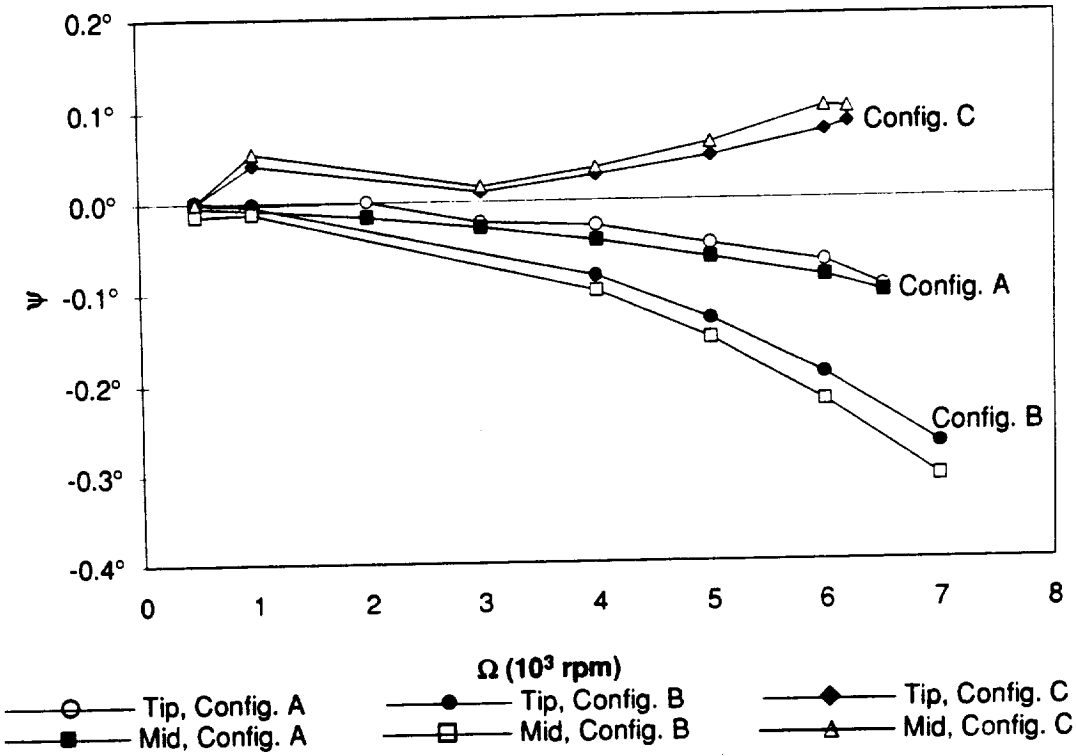

Figure 3.24: Twist of Plate 31 for Configurations A, B, and C.

3.2.8 Plate 32

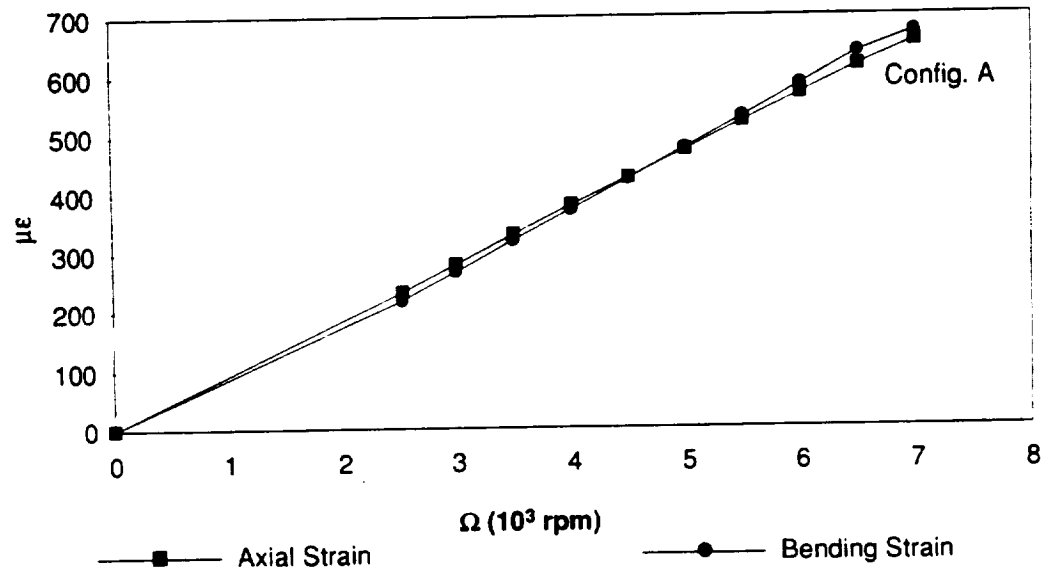

Figure 3.25: Axial and bending strains of Plate 32 for Configuration A.

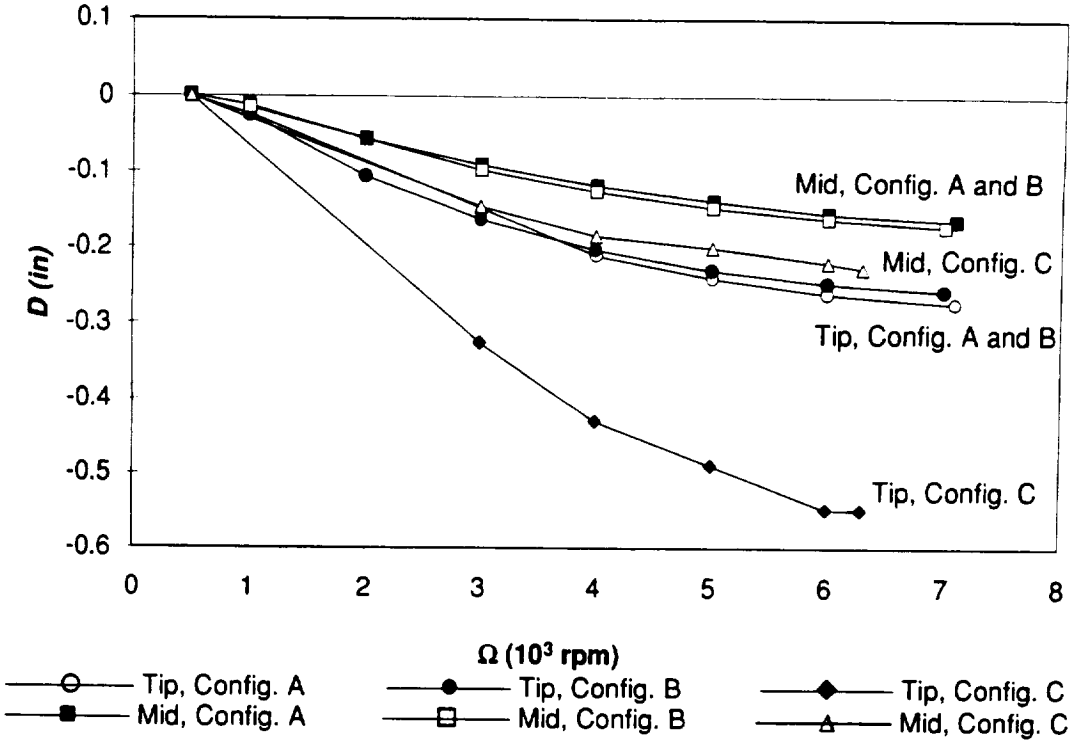

Figure 3.26: Deflections of Plate 32 for Configurations A, B, and C.

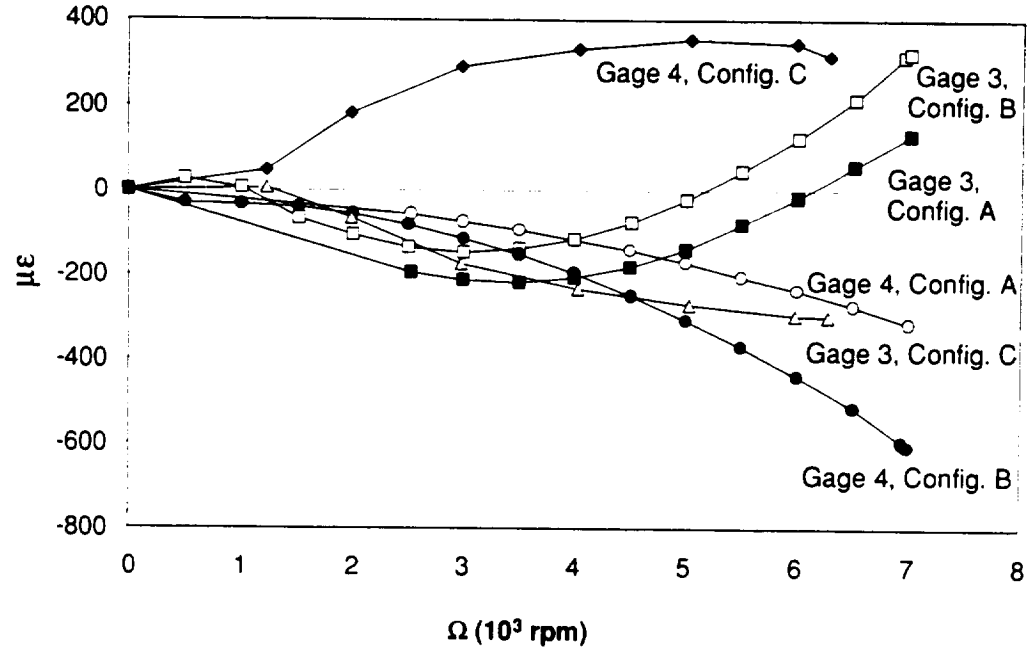

Figure 3.27: Torsion strains of Plate 32 for Configurations A, B, and C.

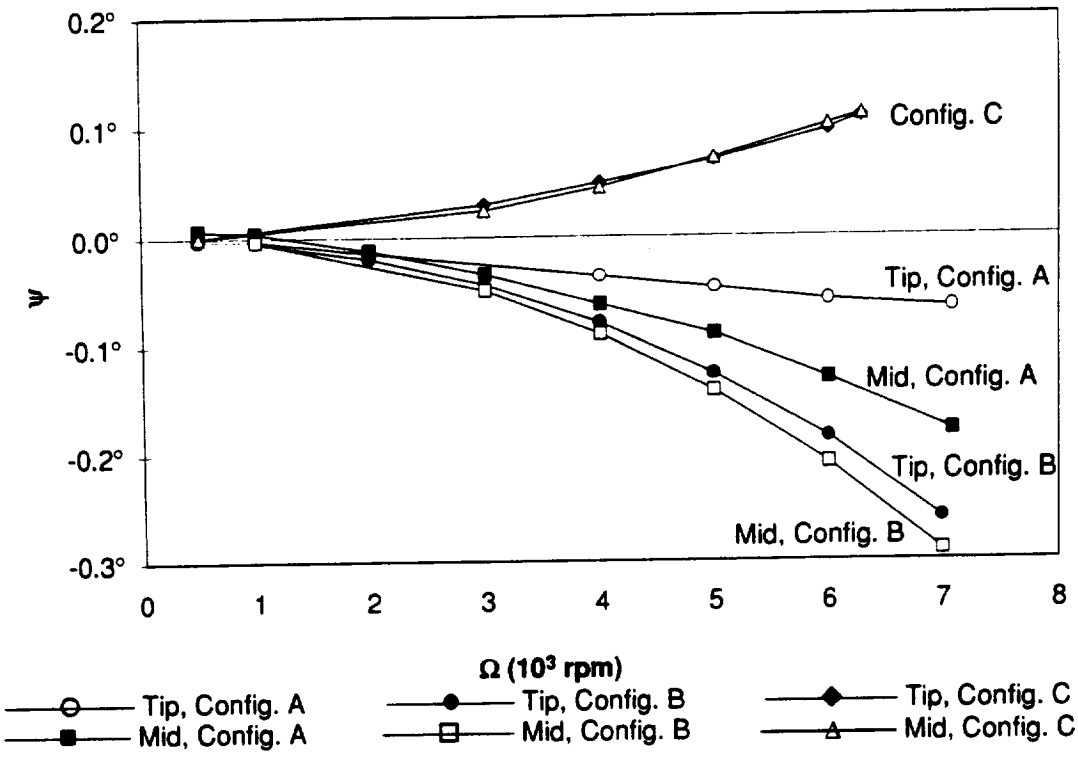

Figure 3.28: Twist of Plate 32 for Configurations A, B, and C.

3.2.9 Plate 13

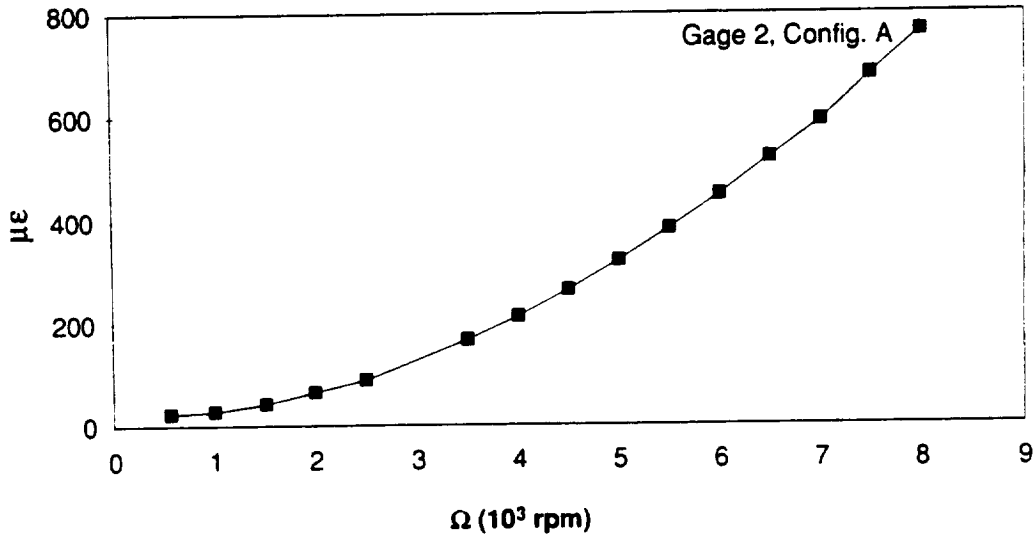

Figure 3.29: Strain from Gage 2 of Plate 13 for Configuration A.

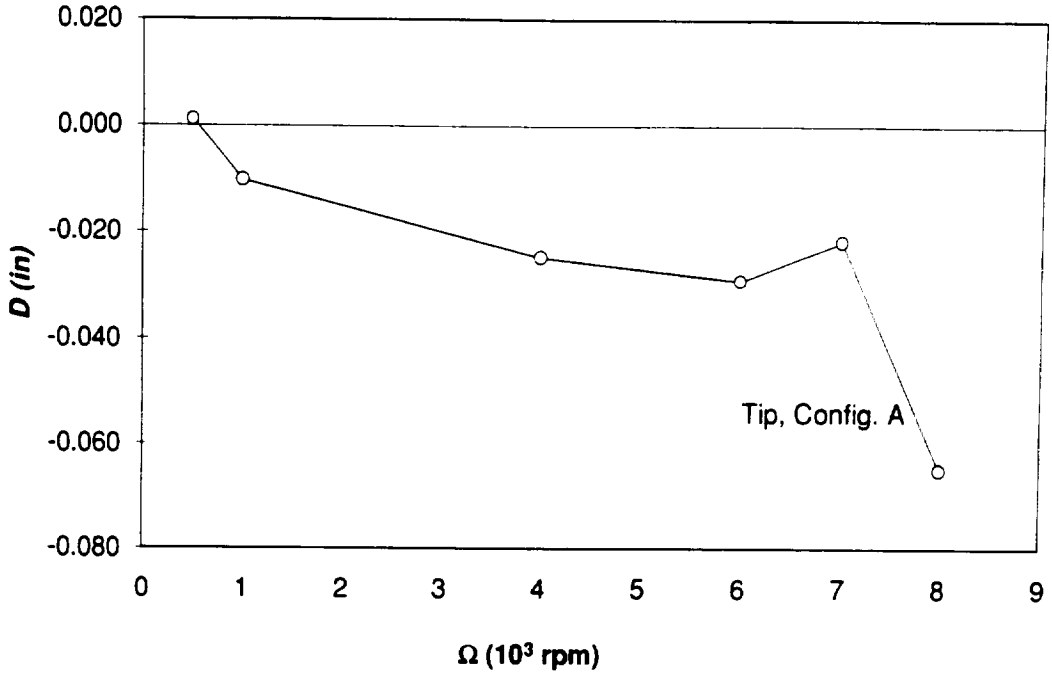

Figure 3.30: Deflections of Plate 13 for Configuration A.

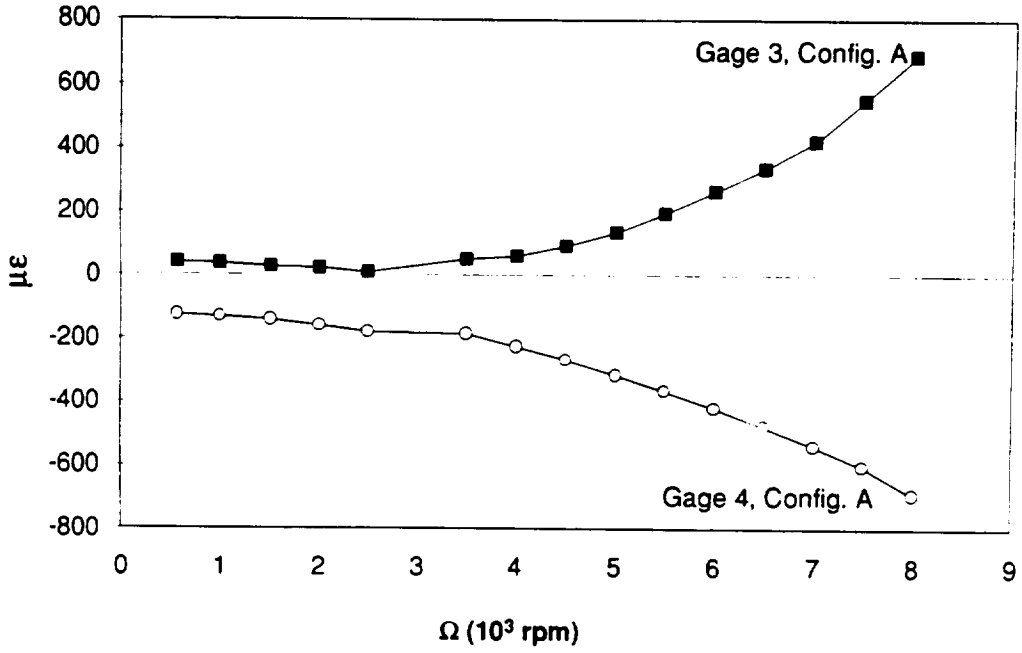

Figure 3.31: Torsion strains of Plate 13 for Configuration A.

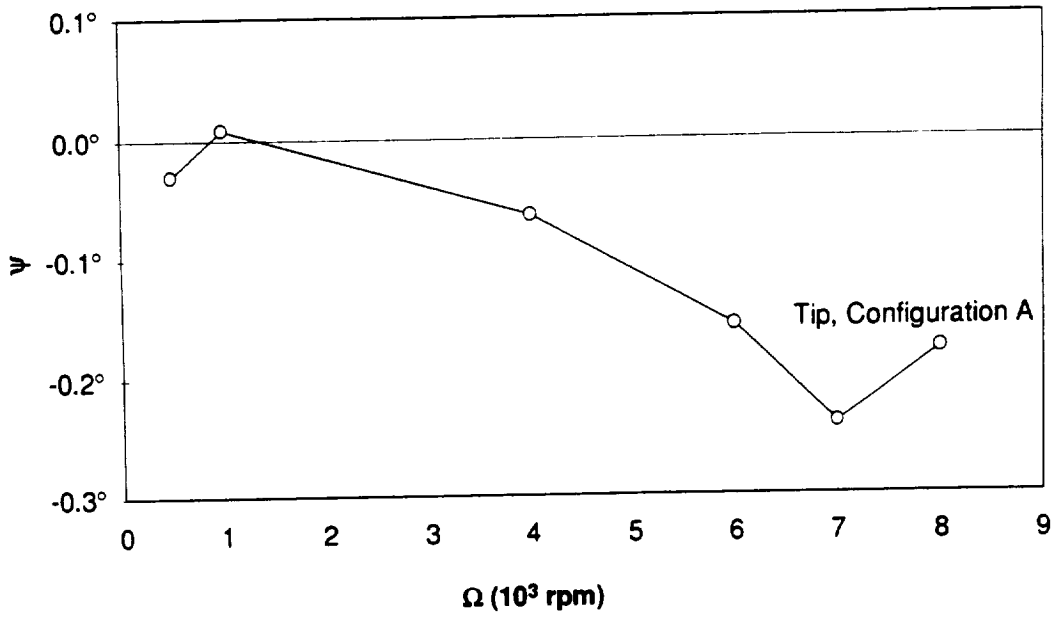

Figure 3.32: Twist of Plate 13 for Configuration A.

3.2.10 Plate 23*

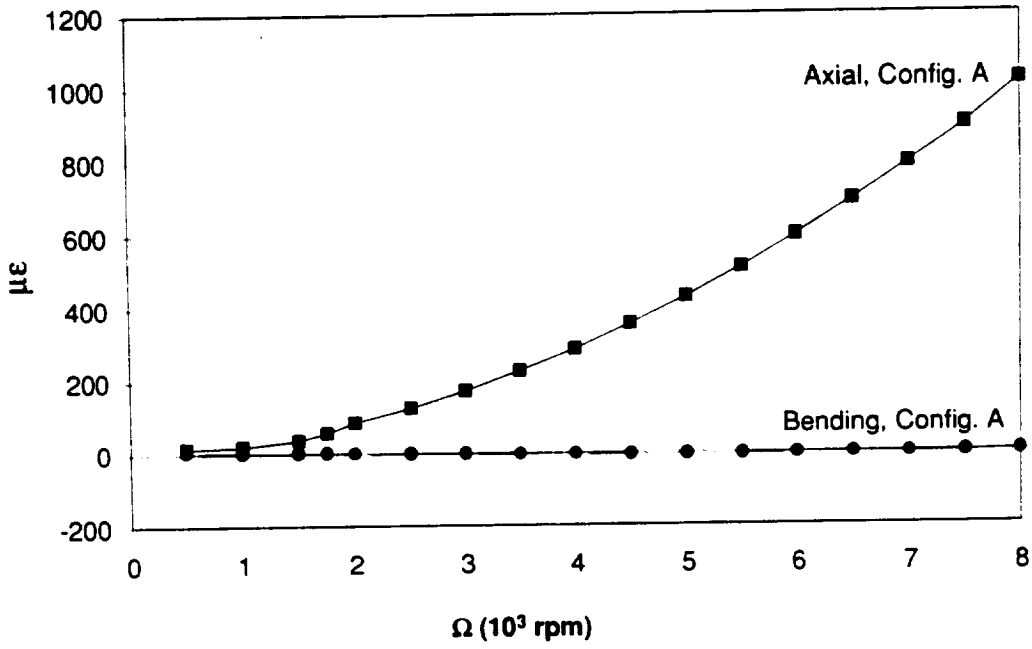

Figure 3.33: Axial and bending strains of Plate 23* for Configuration A.

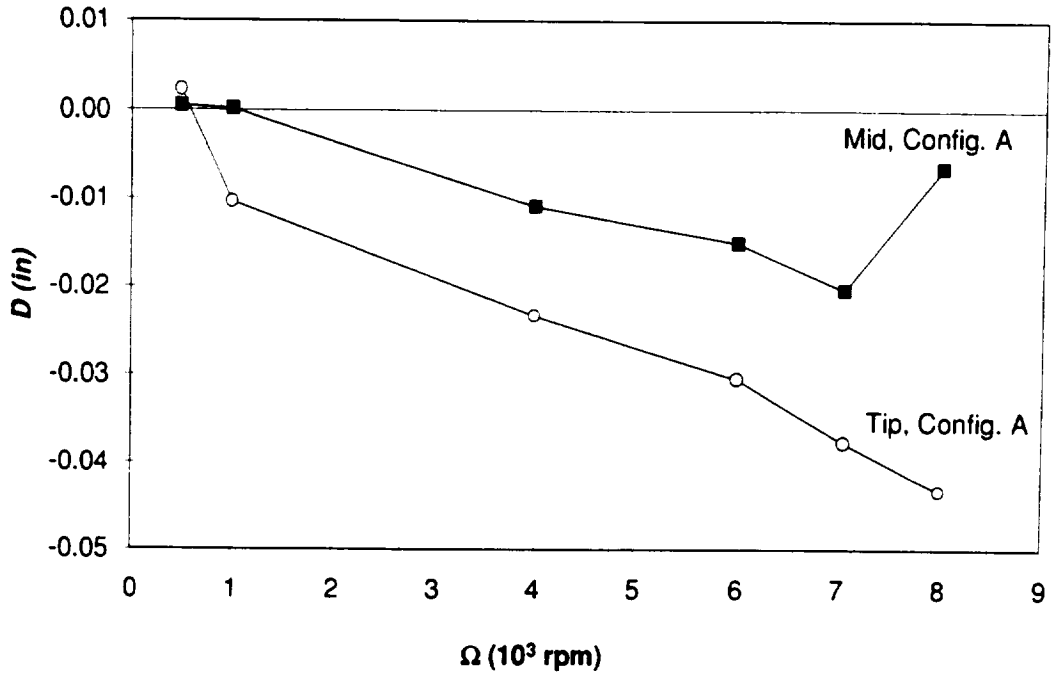

Figure 3.34: Deflections of Plate 23° for Configuration A.

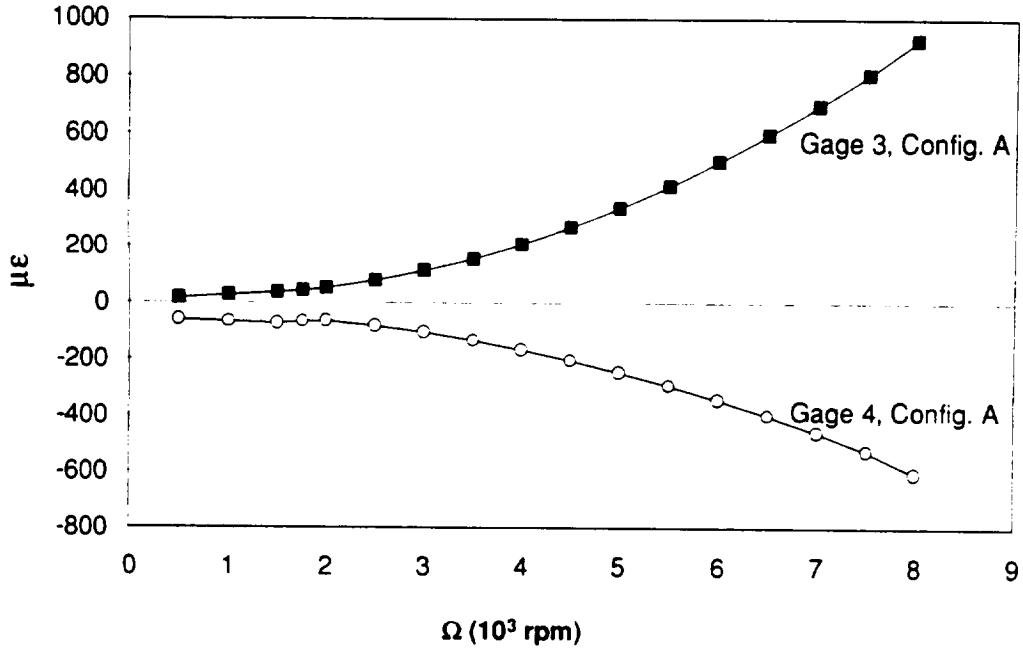

Figure 3.35: Torsion strains of Plate 23° for Configuration A.

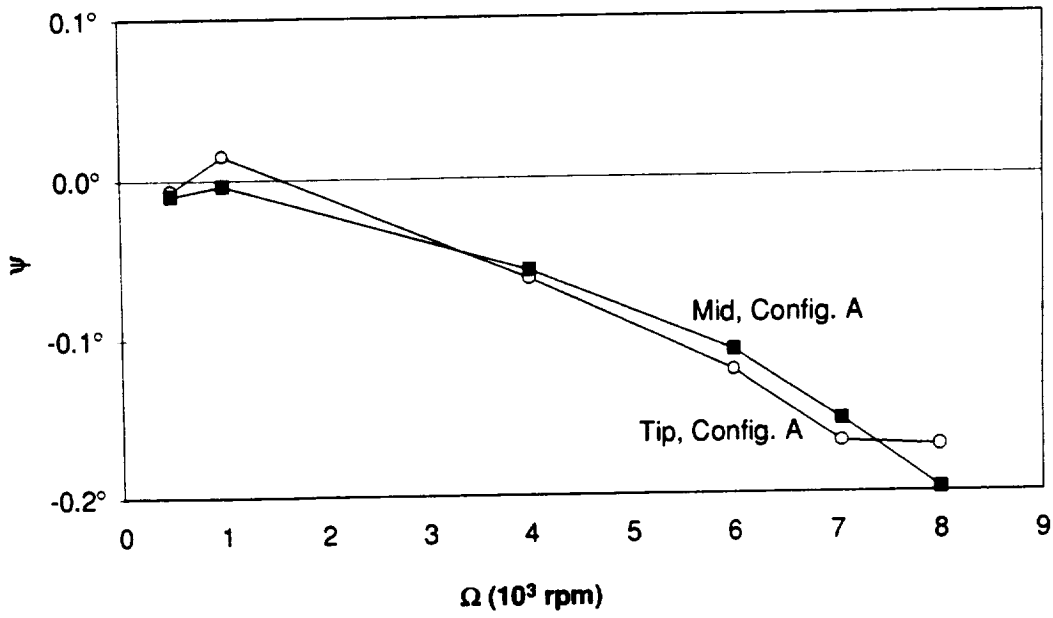

Figure 3.36: Twist of Plate 23* for Configuration A.

3.2.11 Plates 11 and 21, Configuration A

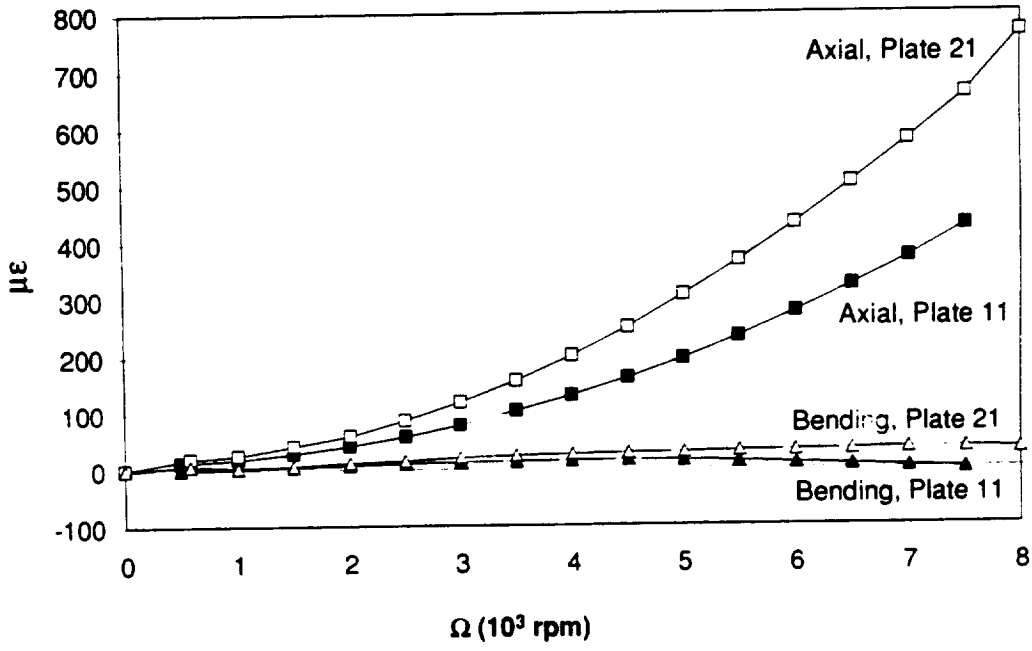

Figure 3.37: Axial and bending strain comparisons between Plates 11 and 21 for Configuration A.

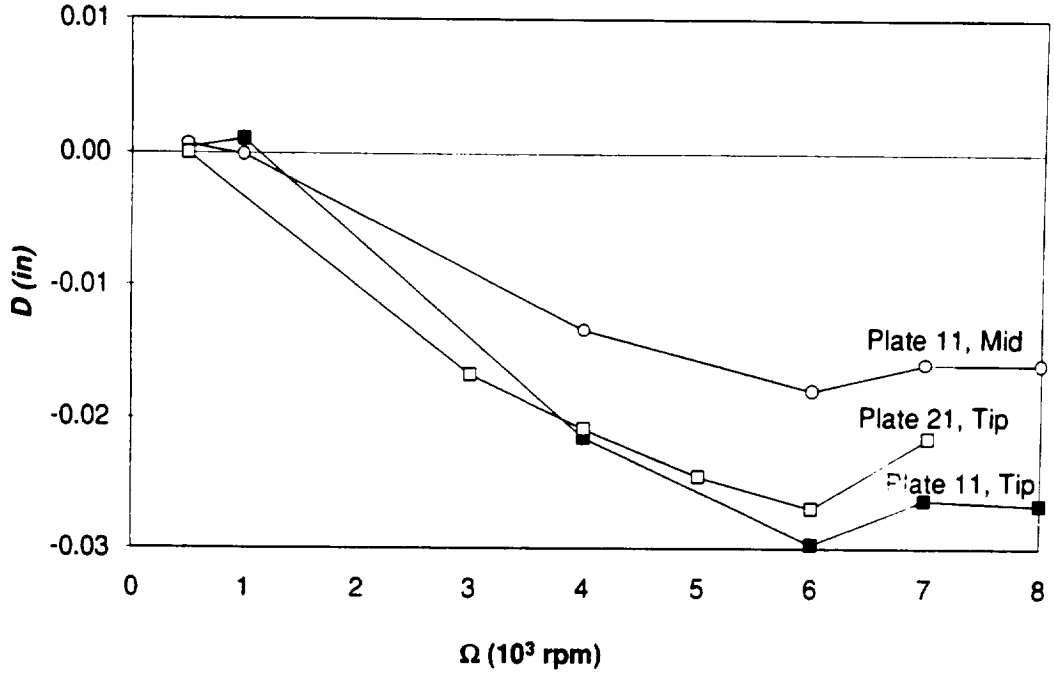

Figure 3.38: Deflection comparisons between Plates 11 and 21 for Configuration A.

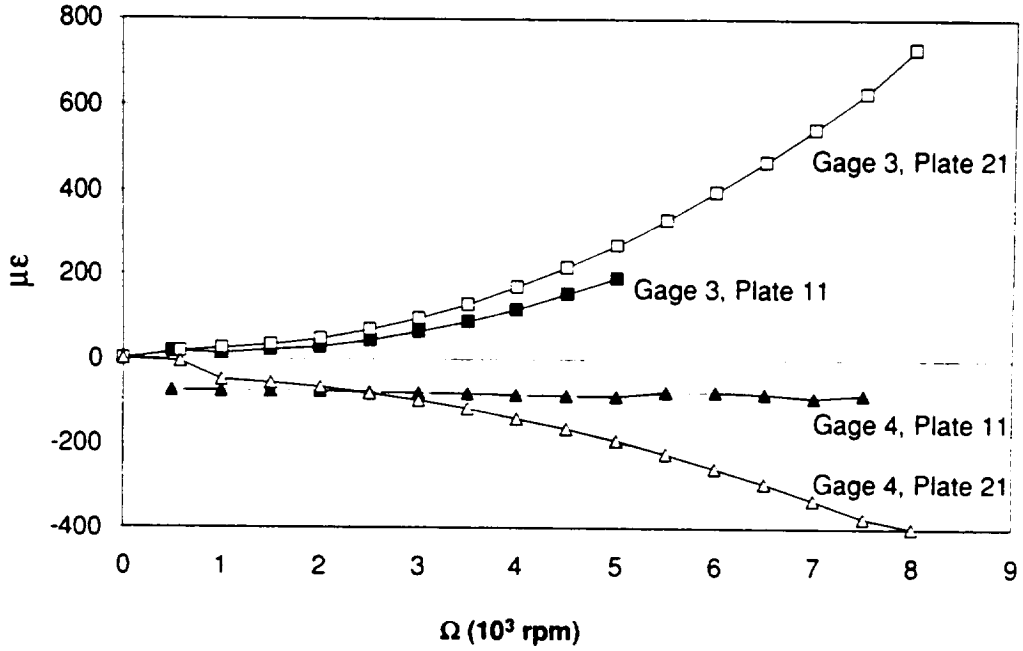

Figure 3.39: Torsion strain comparisons between Plates 11 and 21 for Configuration A.

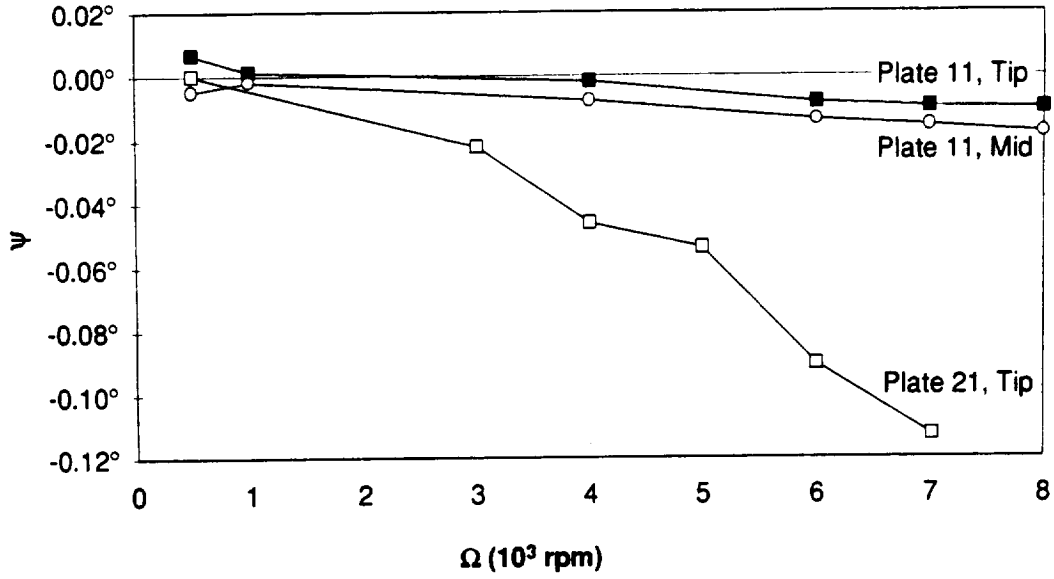

Figure 3.40: Twist comparisons between Plates 11 and 21 for Configuration A.

3.2.12 Plates 11 and 21, Configuration B

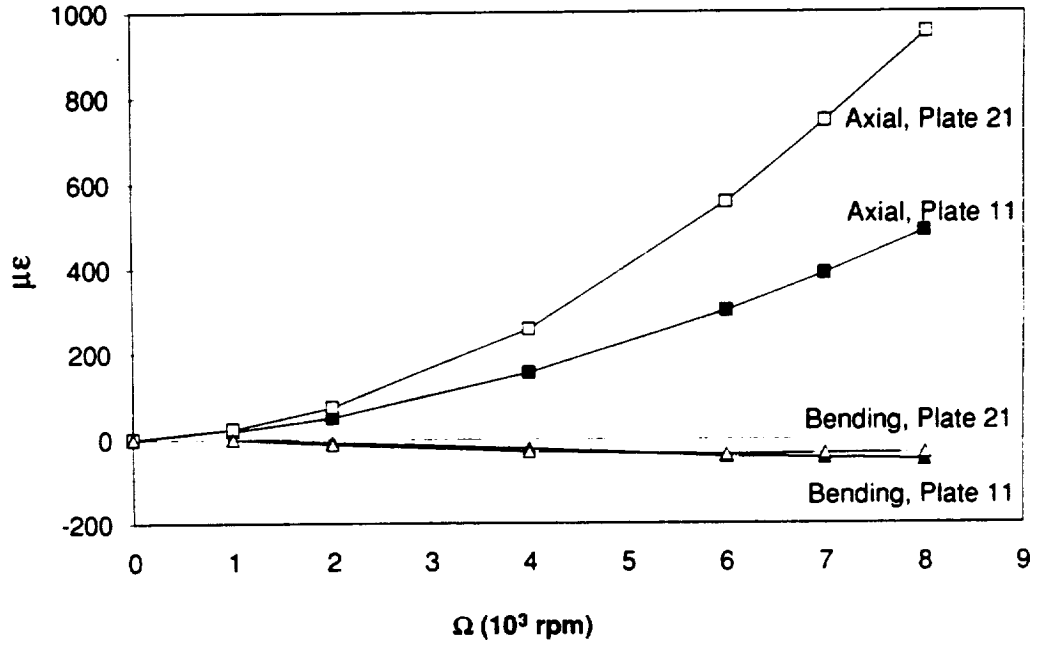

Figure 3.41: Axial and bending strain comparisons between Plates 11 and 21 for Configuration B.

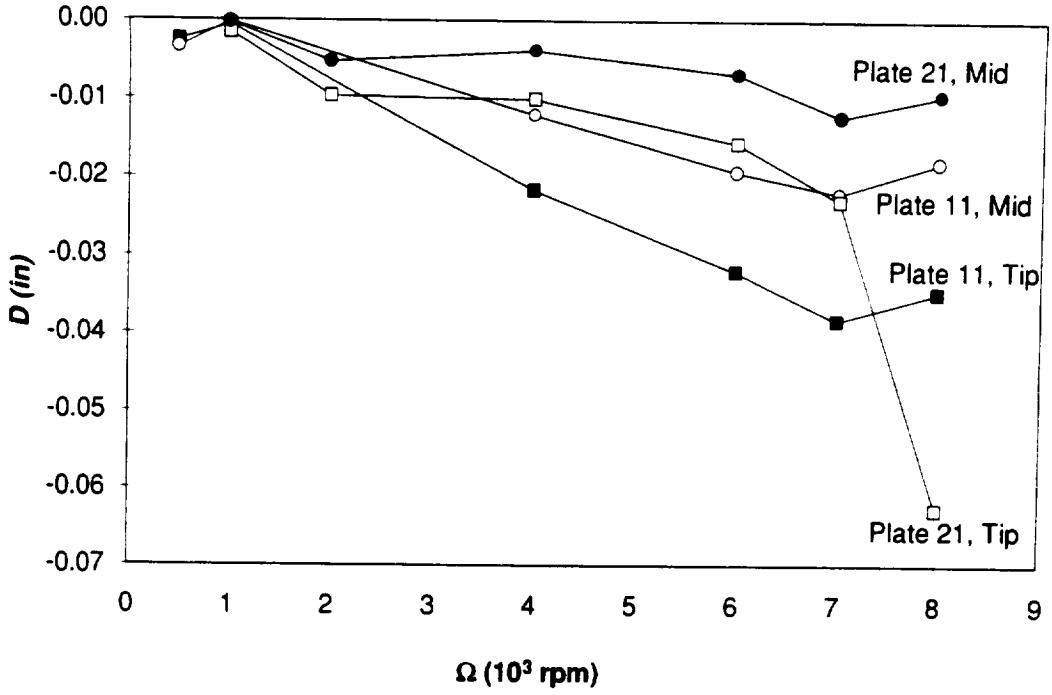

Figure 3.42: Deflection comparisons between Plates 11 and 21 for Configuration B.

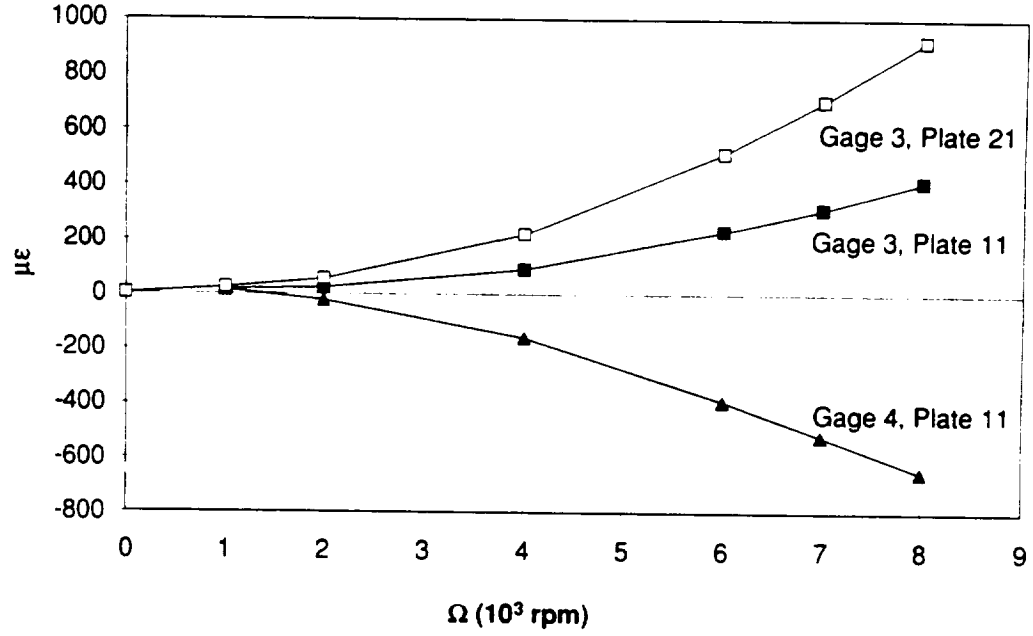

Figure 3.43: Torsion strain comparisons between Plates 11 and 21 for Configuration B.

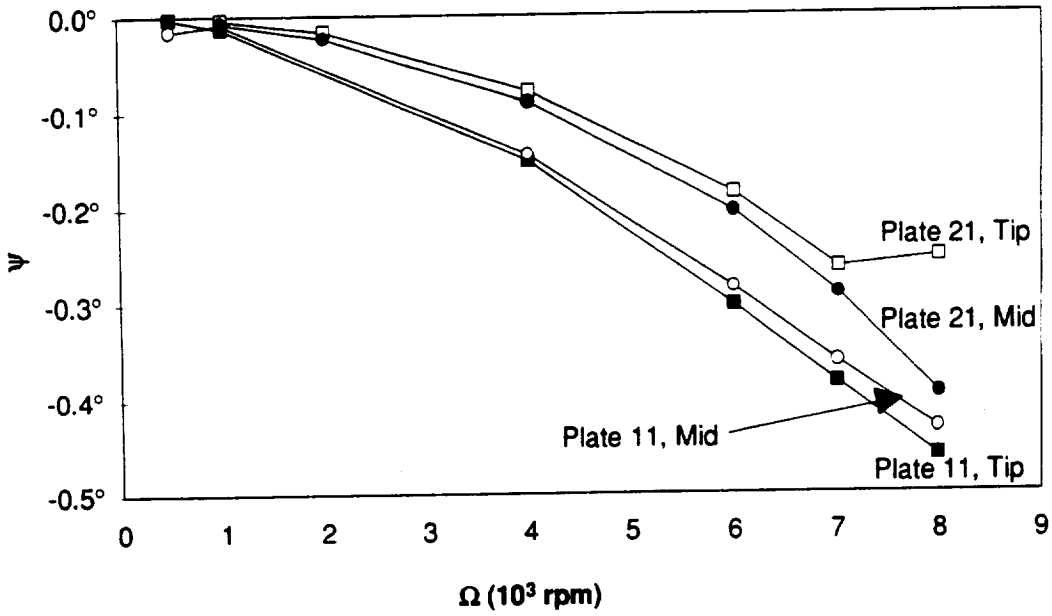

Figure 3.44: Twist comparisons between Plates 11 and 21 for Configuration B.

3.2.13 Plates 11 and 21, Configuration C

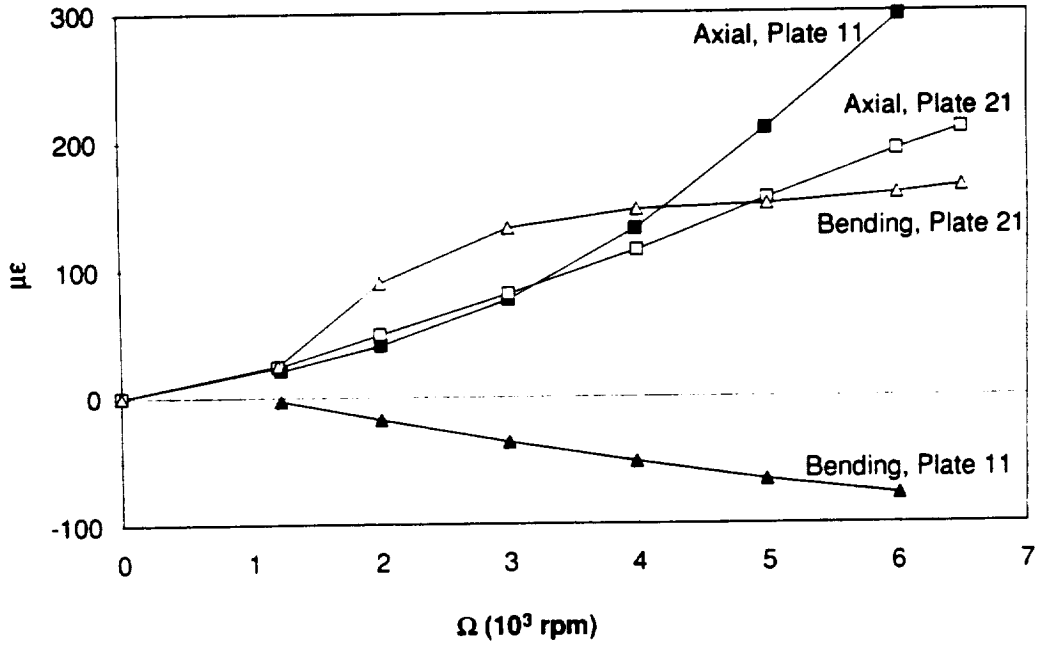

Figure 3.45: Axial and bending strain comparisons between Plates 11 and 21 for Configuration C.

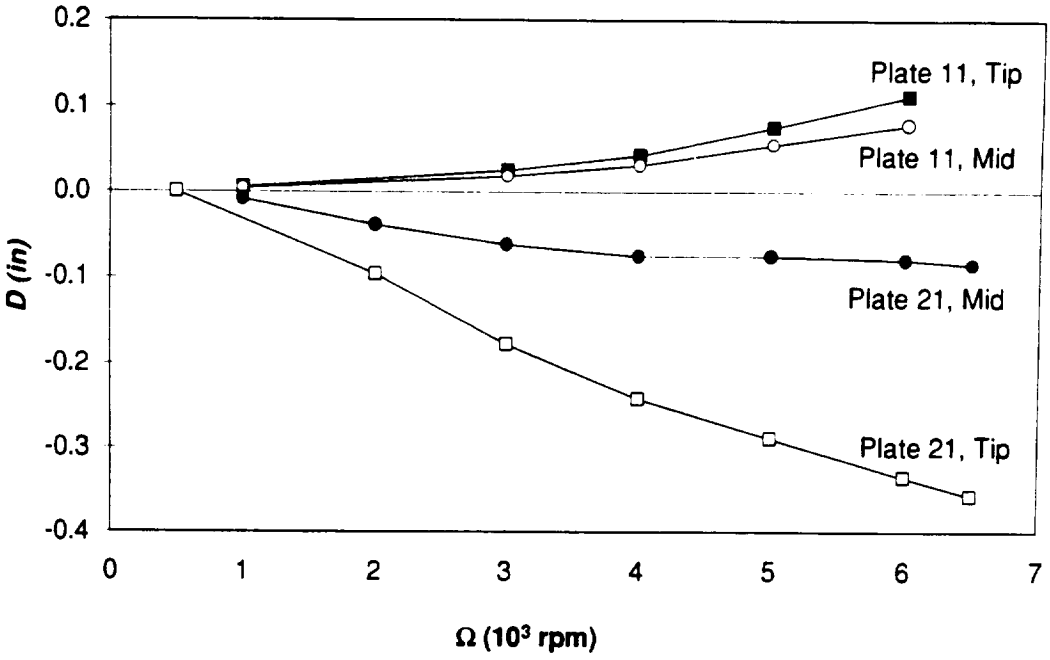

Figure 3.46: Deflection comparisons between Plates 11 and Plate 21 for Configuration C.

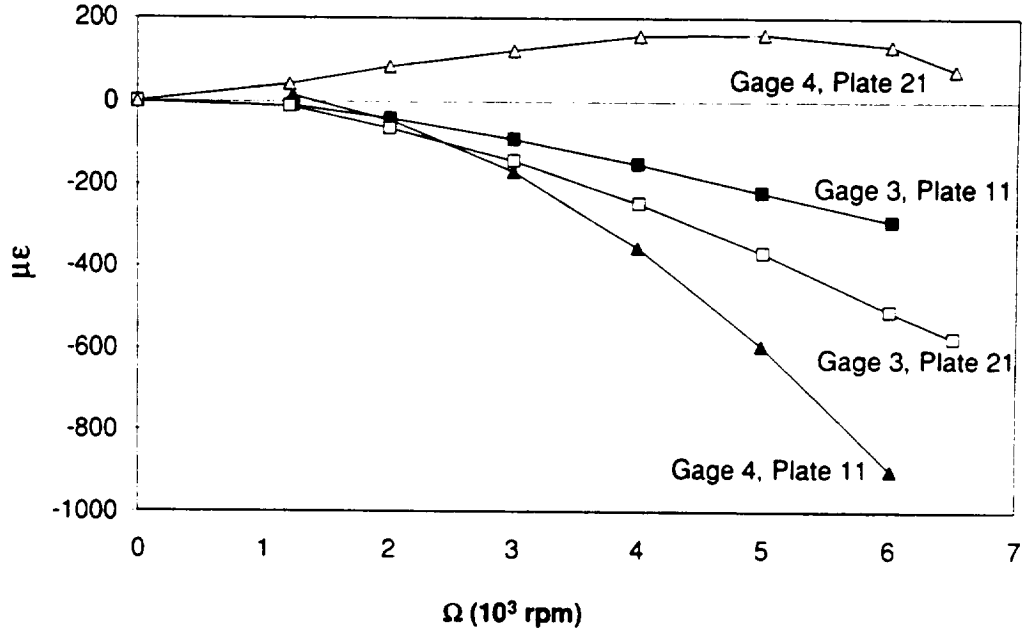

Figure 3.47: Torsion strain comparisons between Plates 11 and 21 for Configuration C.

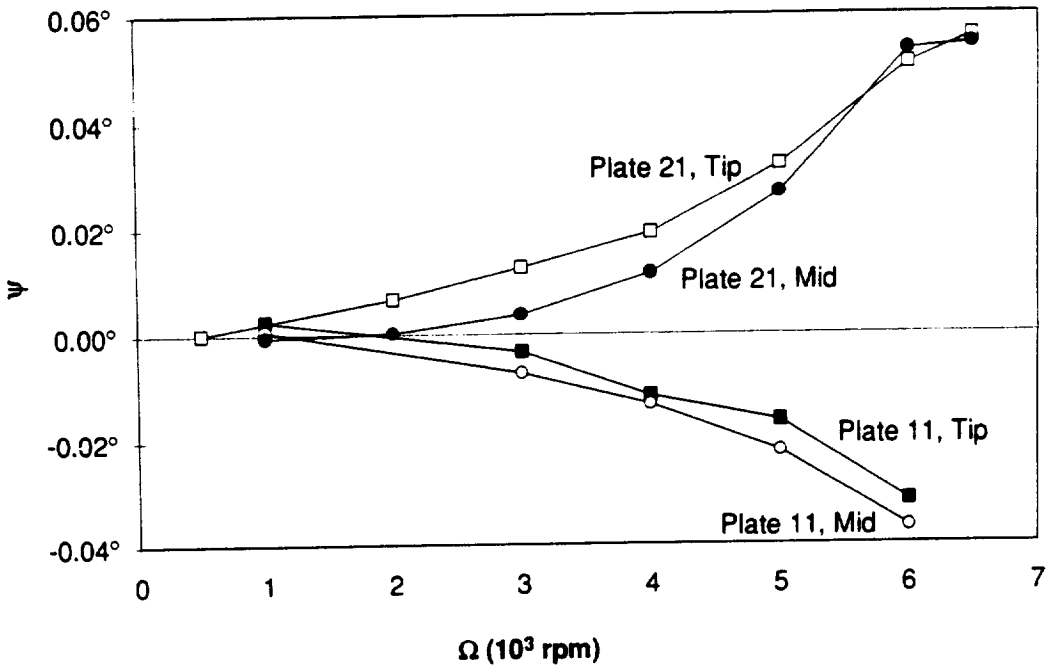

Figure 3.48: Twist comparisons between Plates 11 and 21 for Configuration C.

3.2.14 Plates 21 and 31, Configuration A

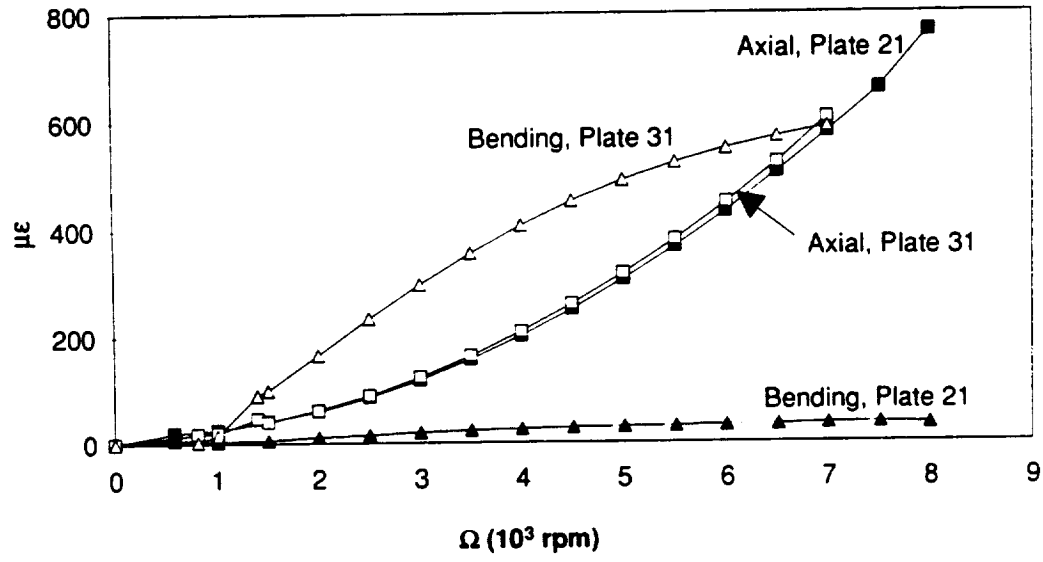

Figure 3.49: Axial and bending strain comparisons between Plates 21 and 31 for Configuration A.

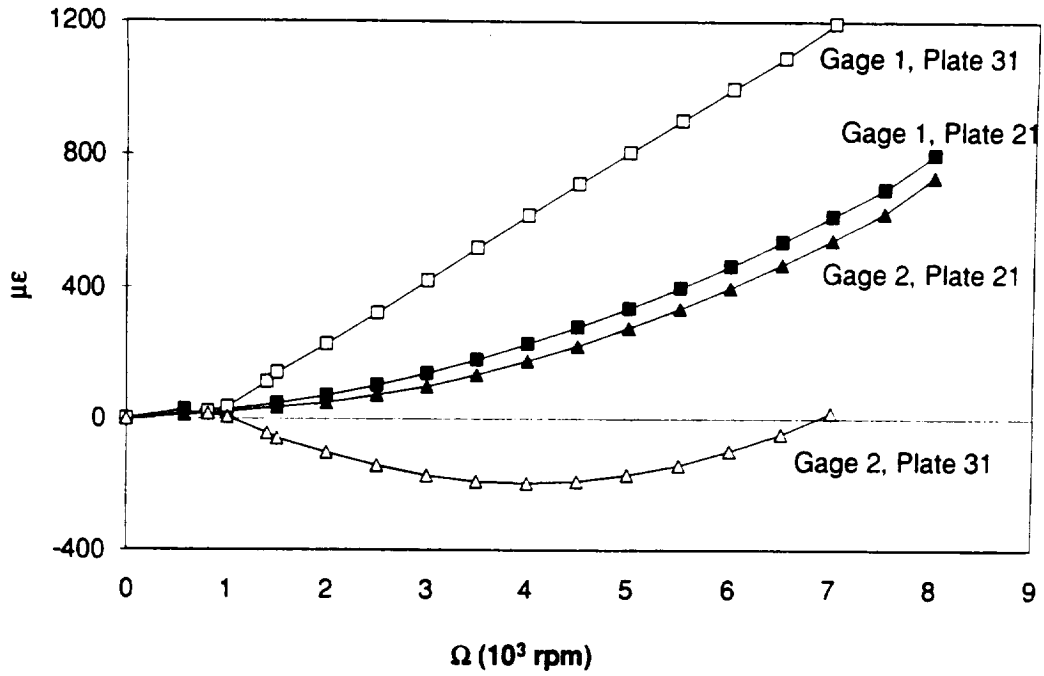

Figure 3.50: Strain gage comparisons between Plates 21 and 31 for Configuration A.

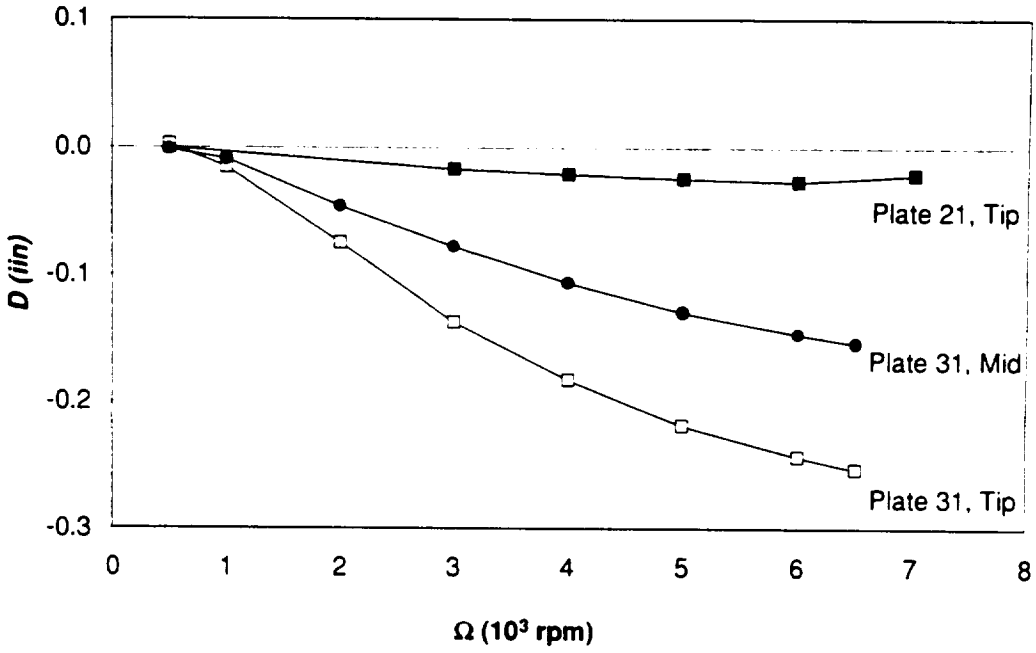

Figure 3.51: Deflection comparisons between Plates 21 and 31 for Configuration A.

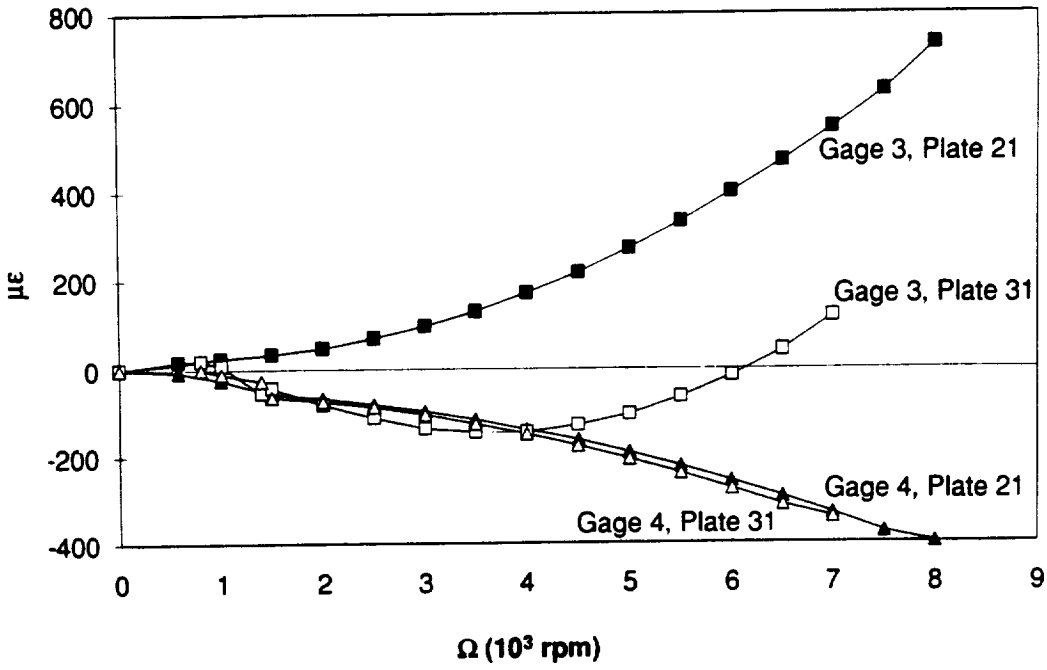

Figure 3.52: Torsion strain comparisons between Plates 21 and 31 for Configuration A.

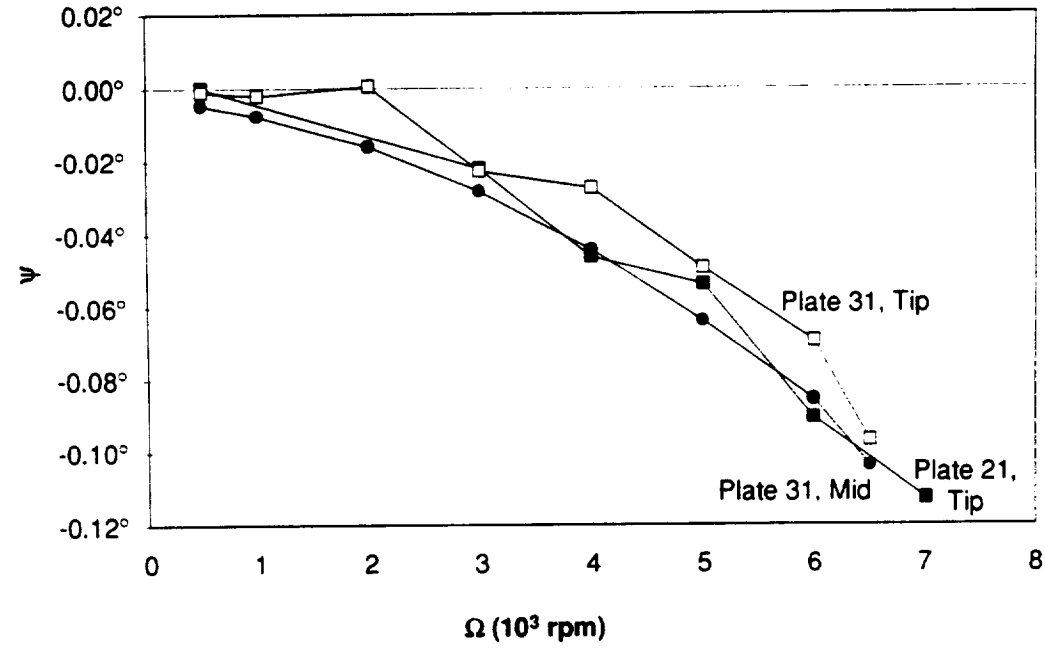

Figure 3.53: Twist comparisons between Plates 21 and 31 for Configuration A.

3.2.15 Plates 21 and 31, Configuration B

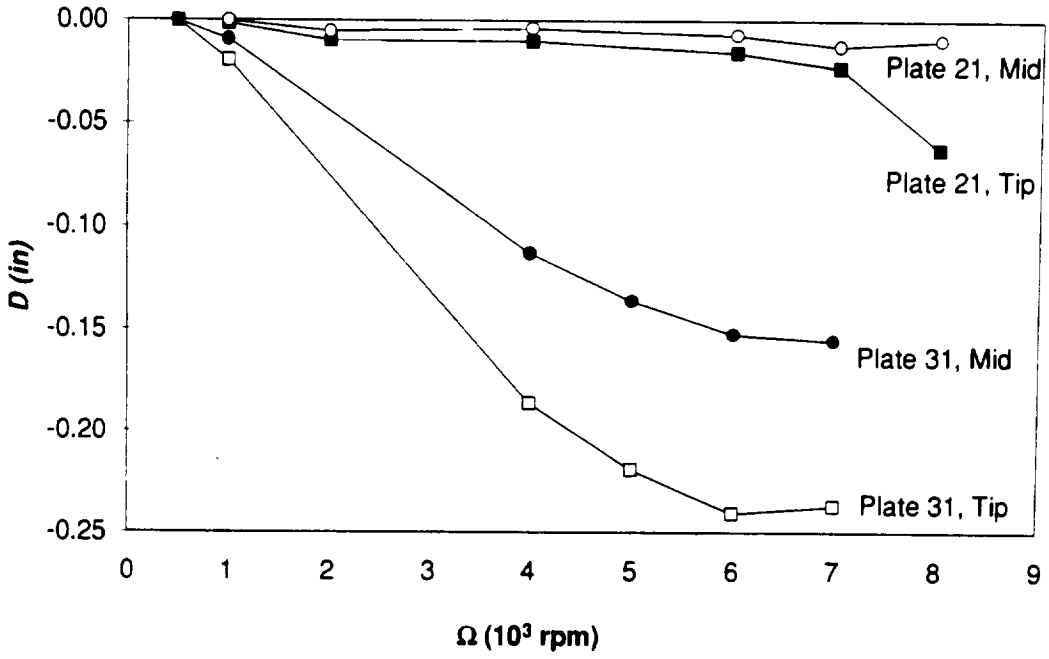

Figure 3.54: Deflection comparisons between Plates 21 and 31 for Configuration B.

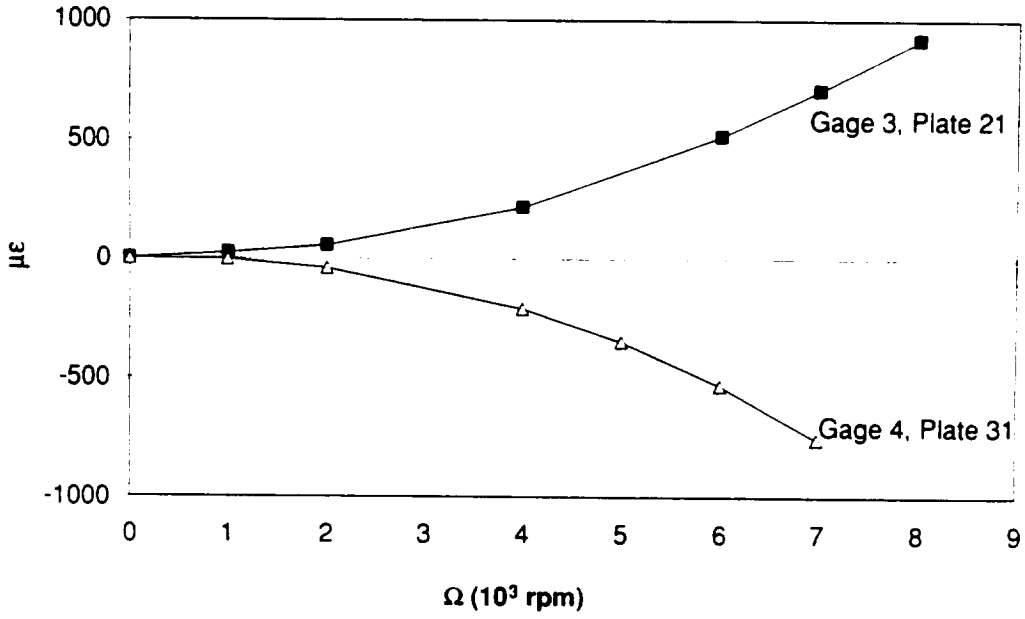

Figure 3.55: Torsion strain comparisons between Plates 21 and 31 for Configuration B.

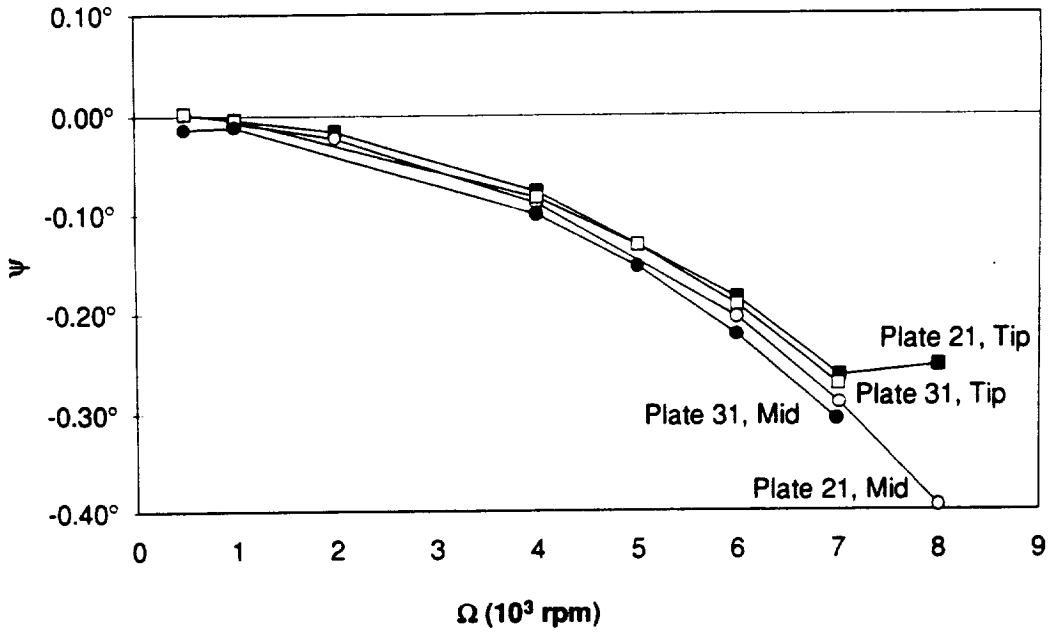

Figure 3.56: Twist comparisons between Plates 21 and 31 for Configuration B.

3.2.16 Plates 21 and 31, Configuration C

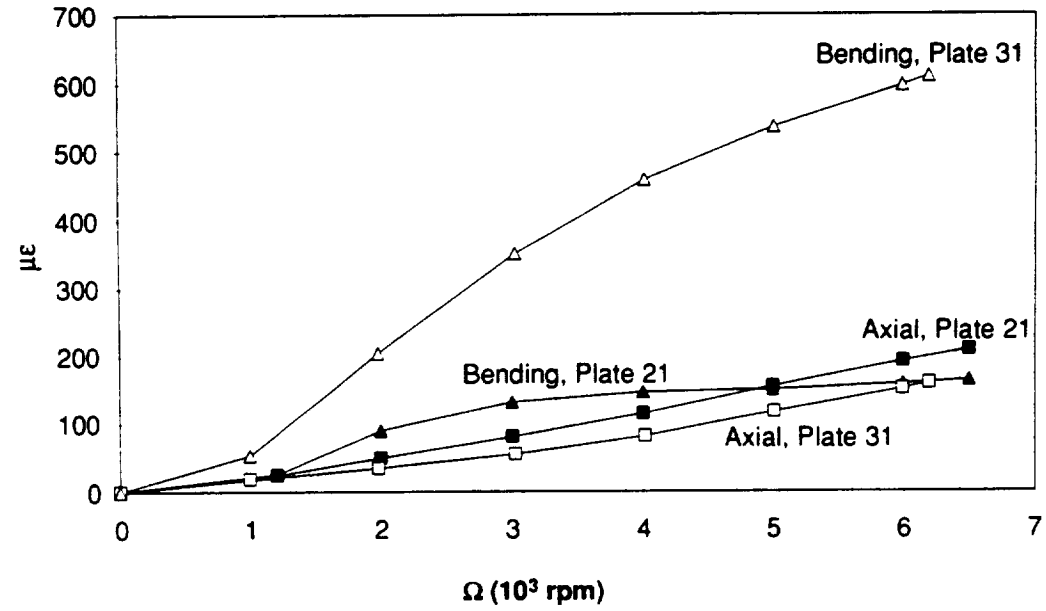

Figure 3.57: Axial and bending strain comparisons between Plates 21 and 31 for Configuration C.

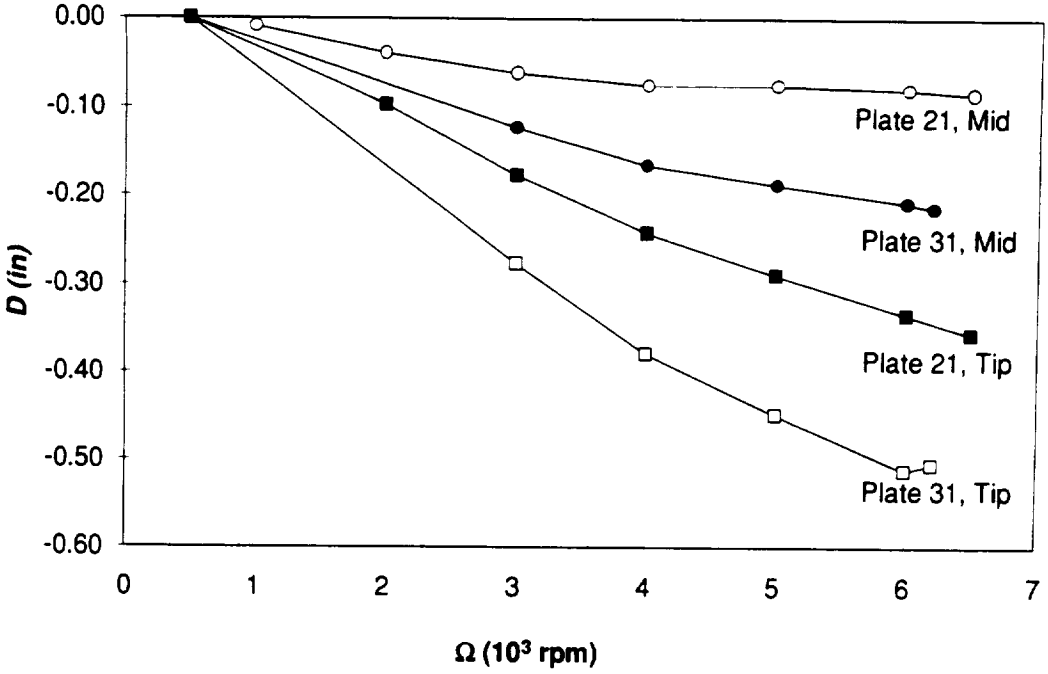

Figure 3.58: Deflection comparisons between Plates 21 and 31 for Configuration C.

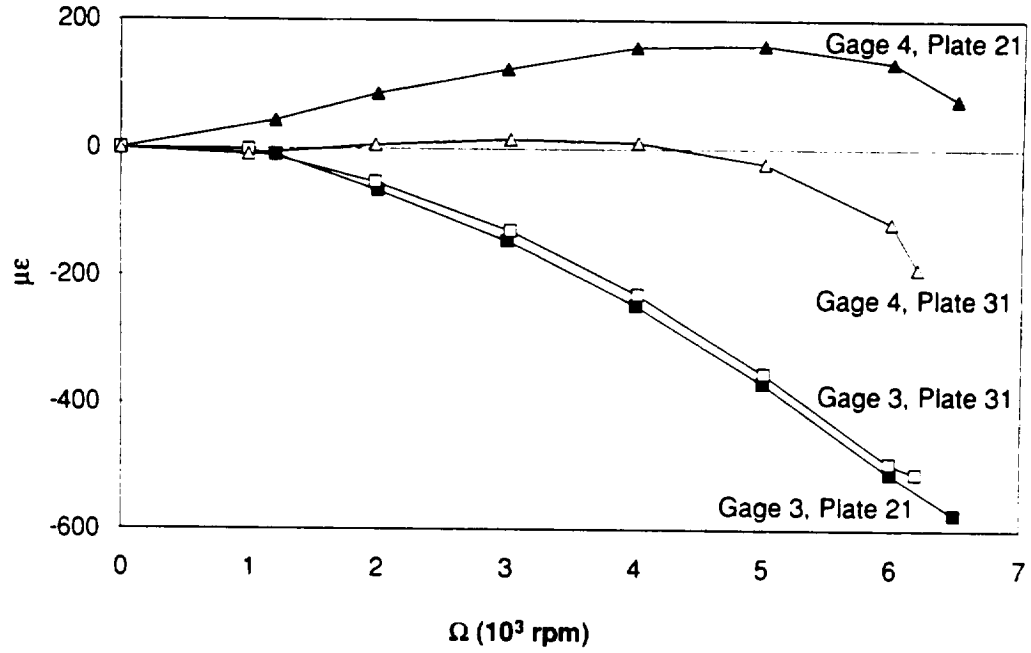

Figure 3.59: Torsion strain comparisons between Plates 21 and 31 for Configuration C.

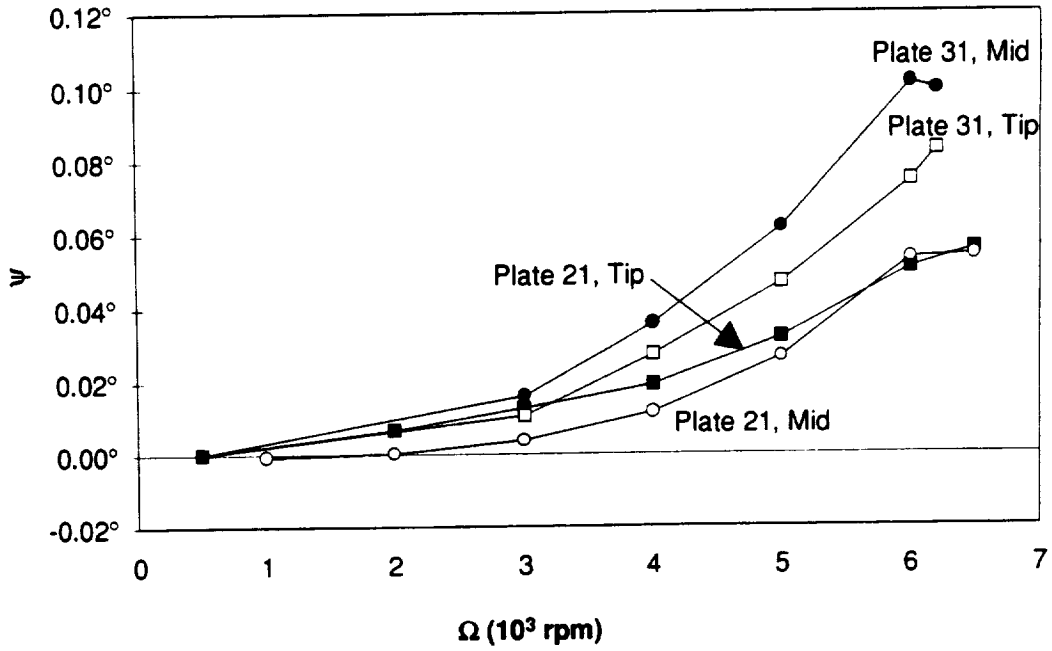

Figure 3.60: Twist comparisons between Plates 21 and 31 for Configuration C.

3.2.17 Plates 31 and 32, Configuration A

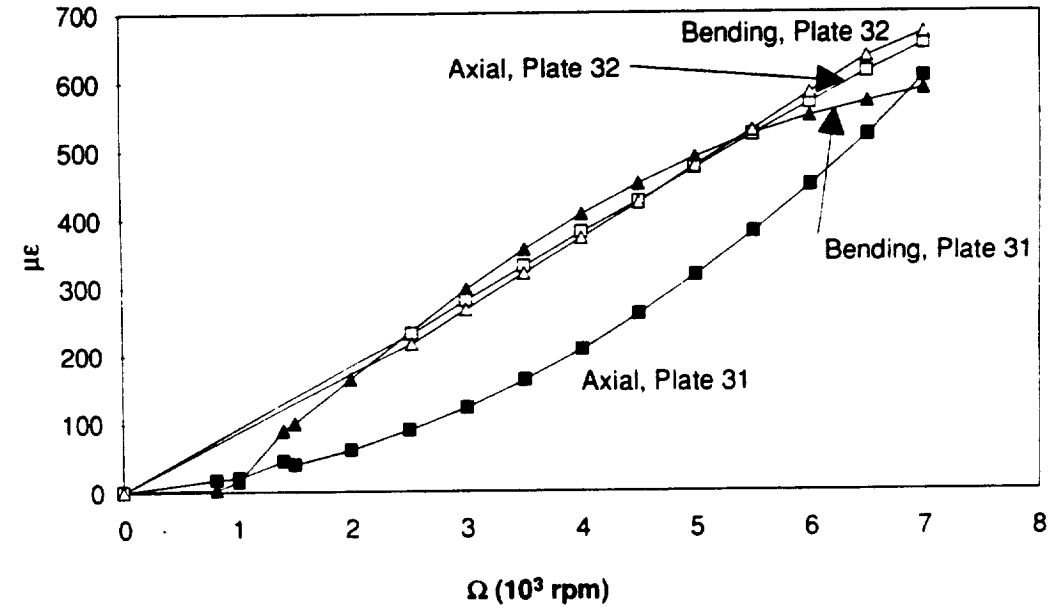

Figure 3.61: Axial and bending strain comparisons between Plates 31 and 32 for Configuration A.

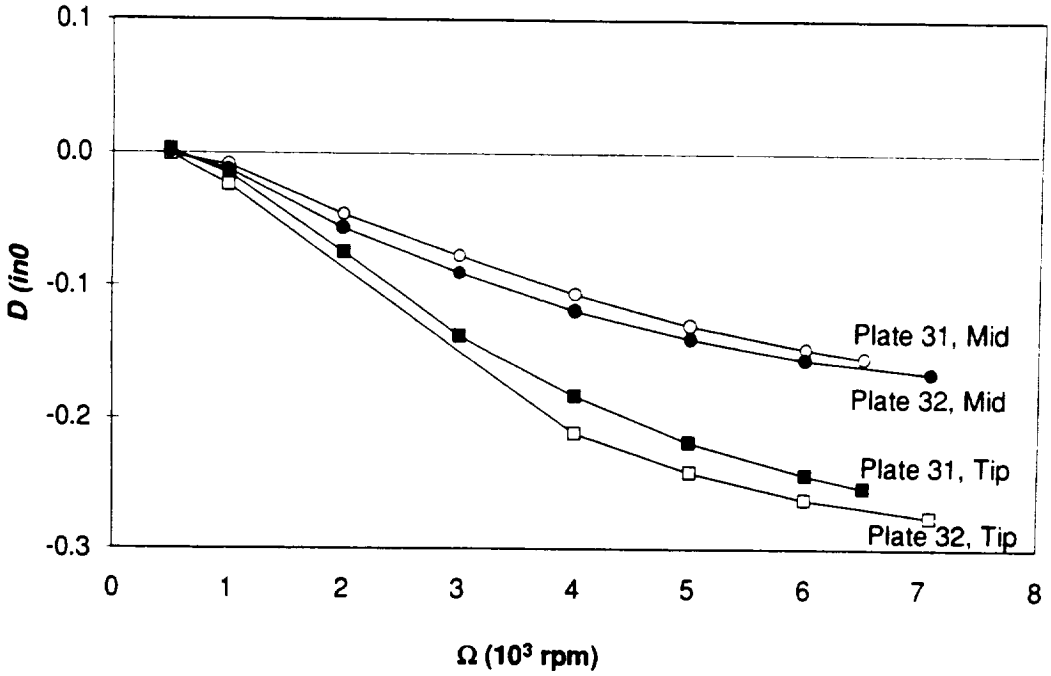

Figure 3.62: Deflection comparisons between Plates 31 and 32 for Configuration A.

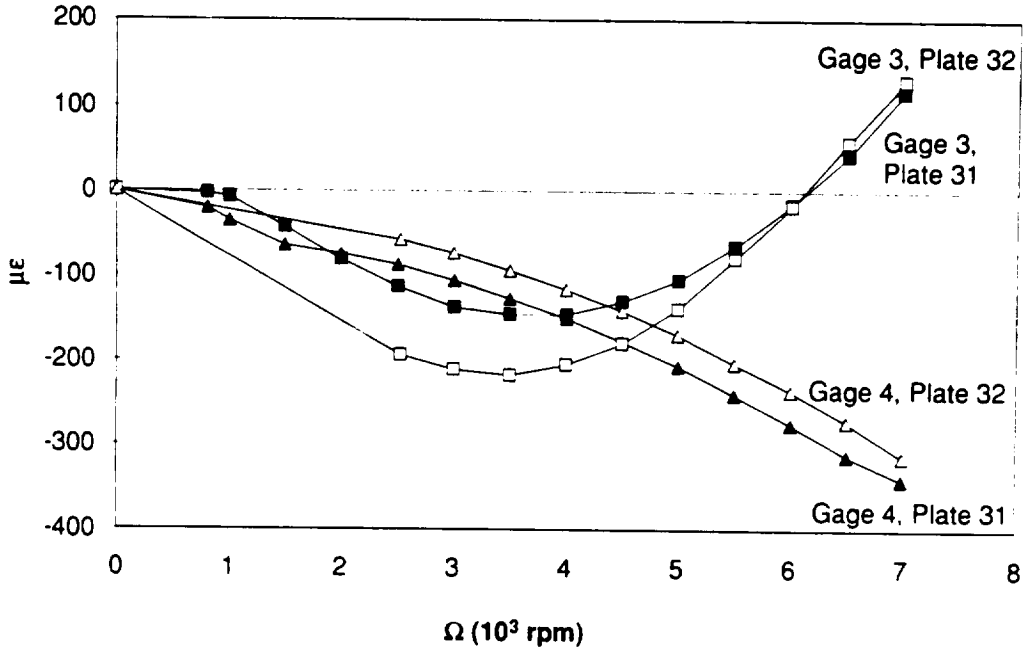

Figure 3.63: Torsion strain comparisons between Plates 31 and 32 for Configuration A.

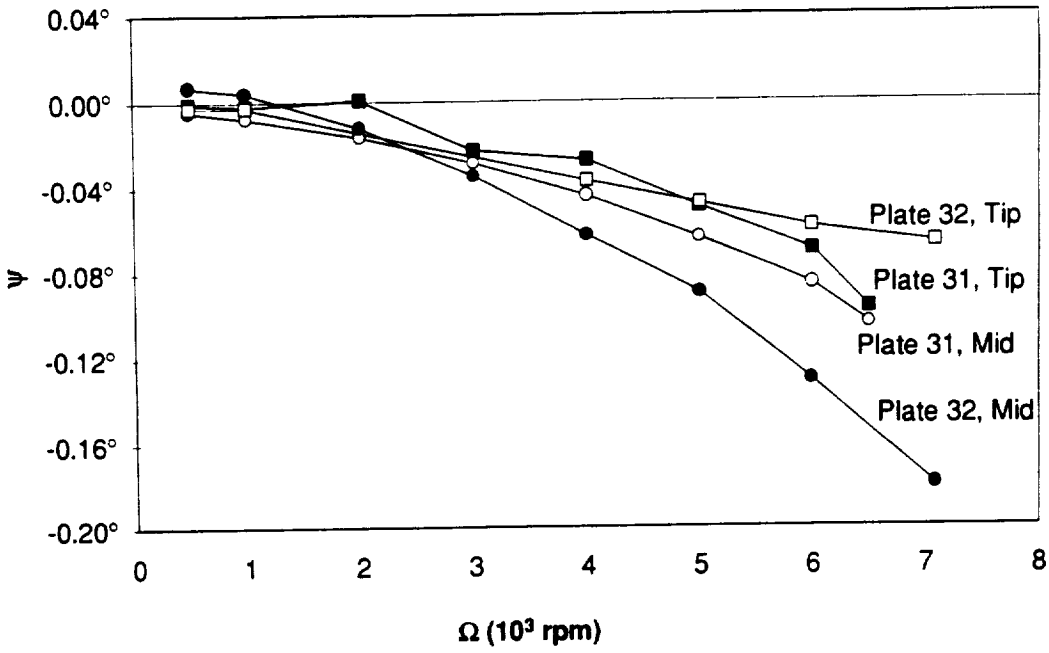

Figure 3.64: Twist comparisons between Plates 31 and 32 for Configuration A.

3.2.18 Plates 31 and 32, Configuration B

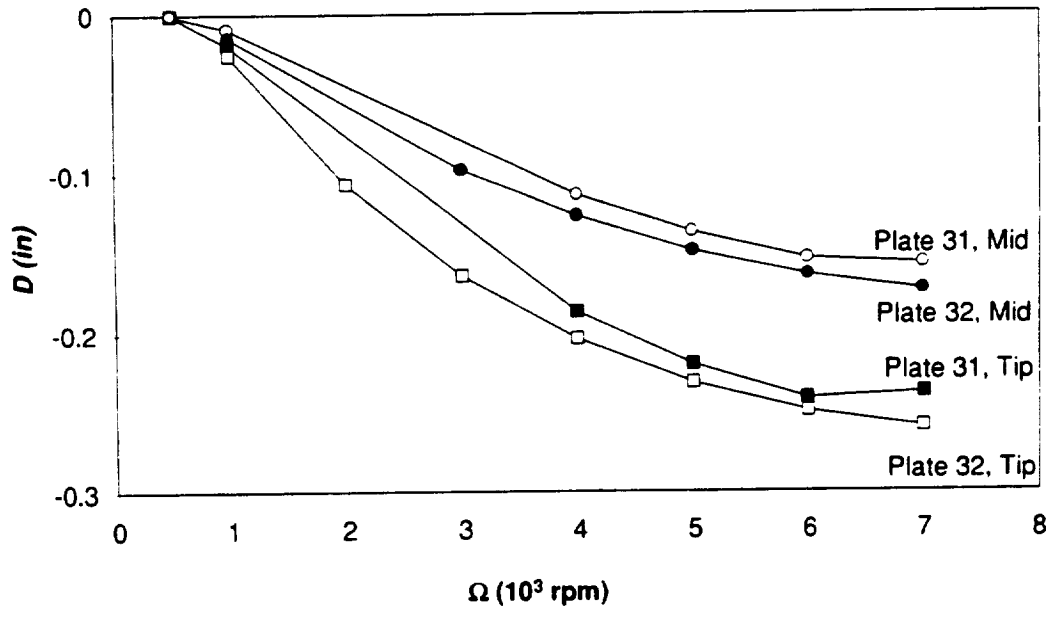

Figure 3.65: Deflection comparisons between Plates 31 and 32 for Configuration B.

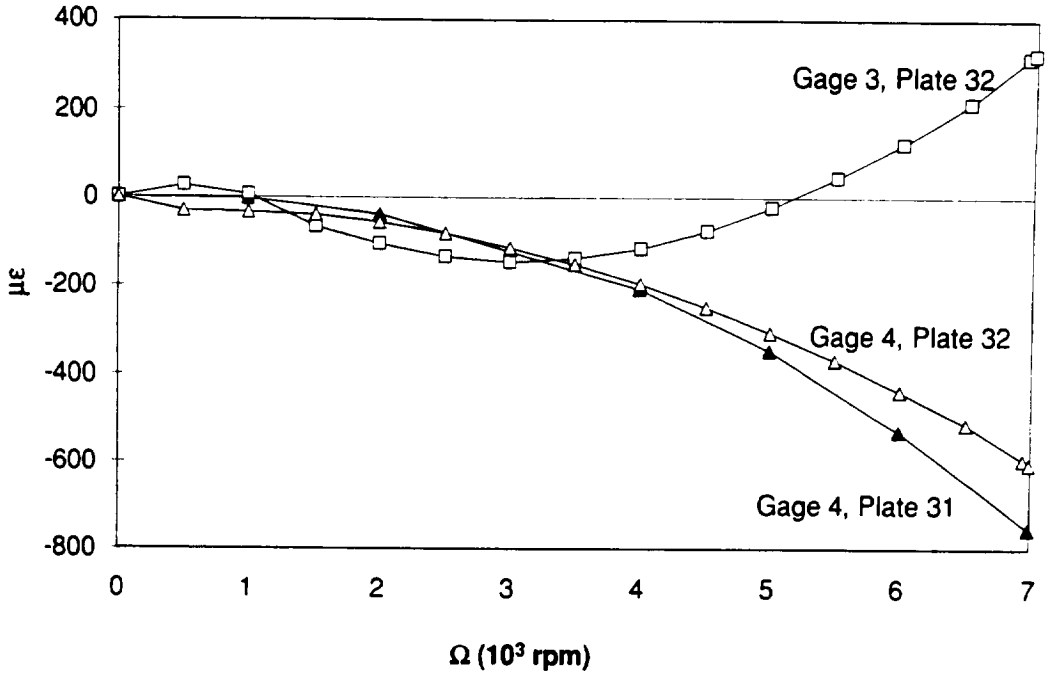

Figure 3.66: Torsion strain comparisons between Plates 31 and 32 for Configuration B.

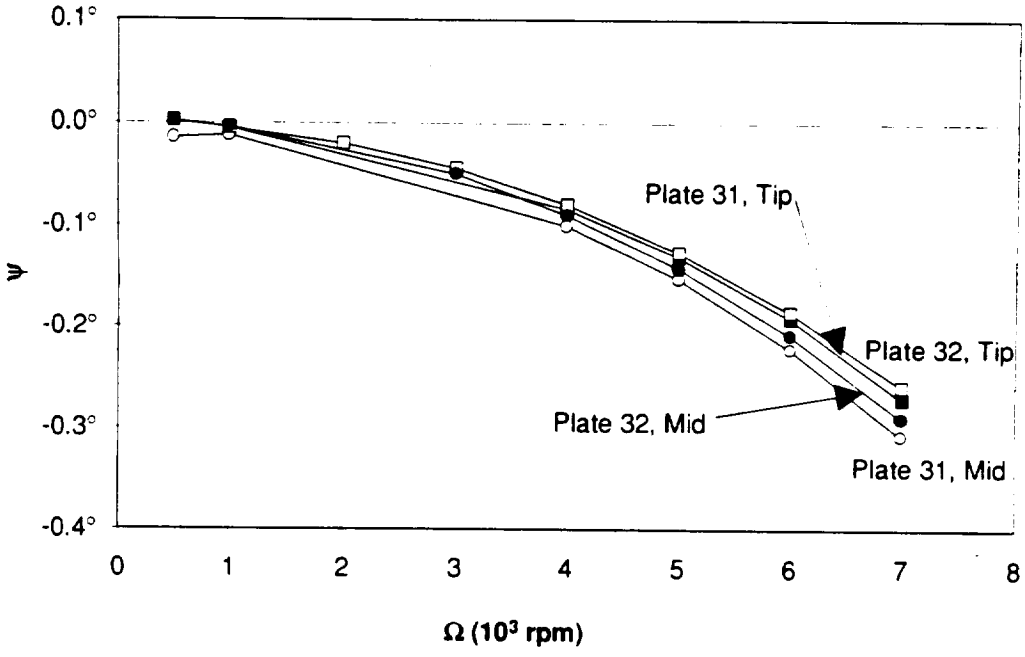

Figure 3.67: Twist comparisons between Plates 31 and 32 for Configuration B.

3.2.19 Plates 31 and 32, Configuration C

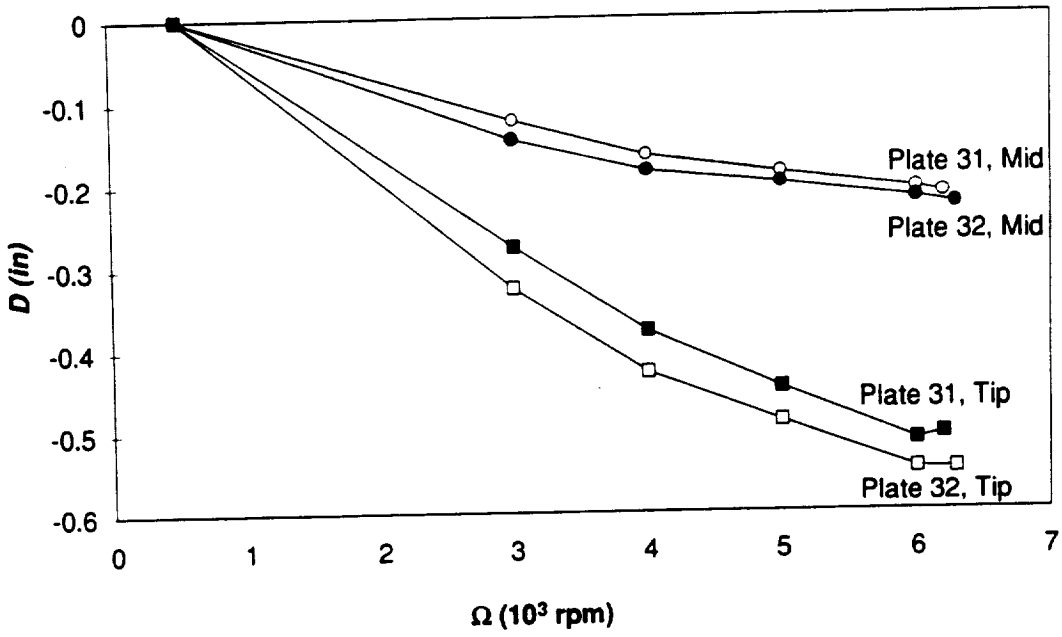

Figure 3.68: Deflection comparisons between Plates 31 and 32 for Configuration C.

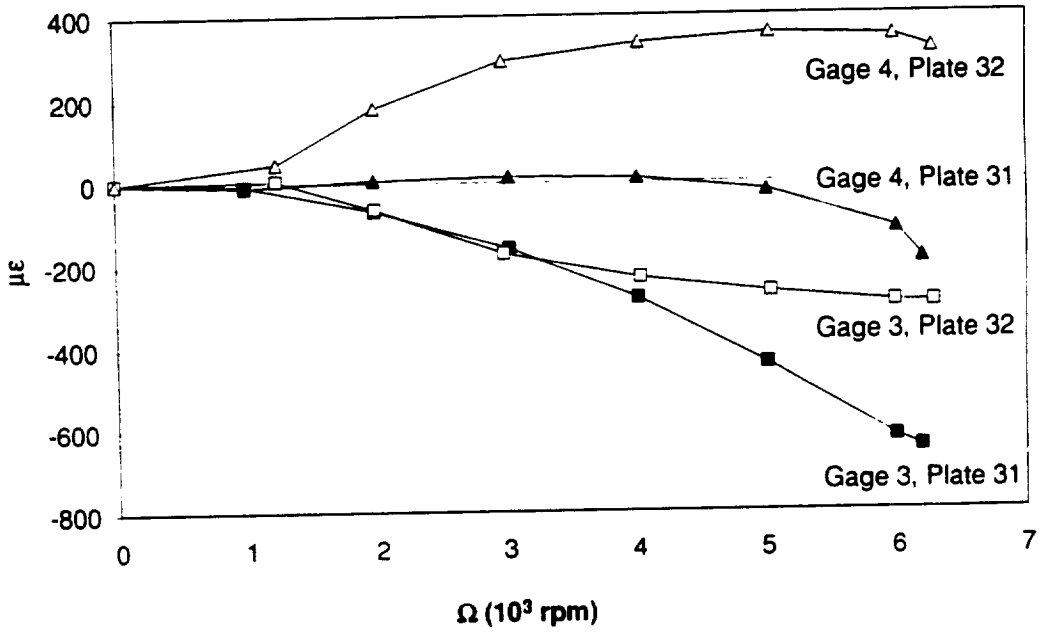

Figure 3.69: Torsion strain comparisons between Plates 31 and 32 for Configuration C.

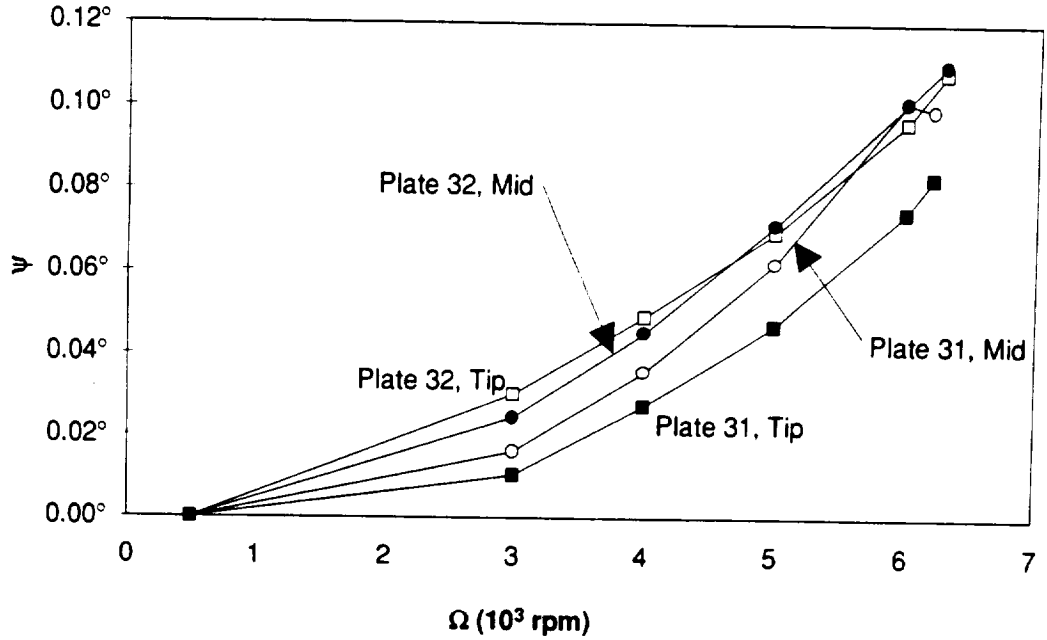

Figure 3.70: Twist comparisons between Plates 31 and 32 for Configuration C.

3.2.20 Plates 11 and 13, Configuration A

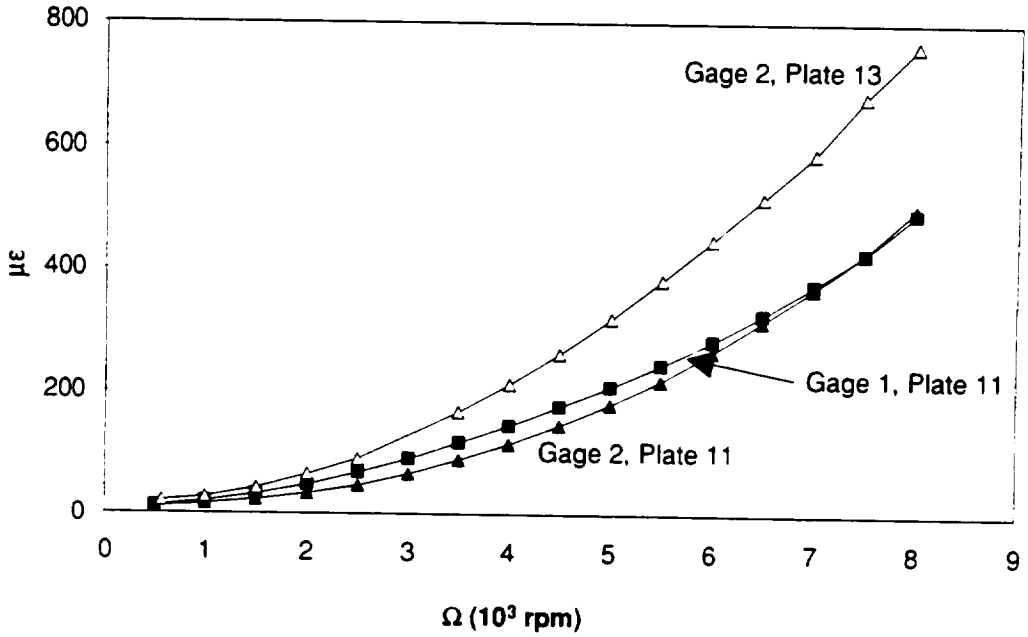

Figure 3.71: Strain comparisons between Plates 11 and 13 for Configuration A.

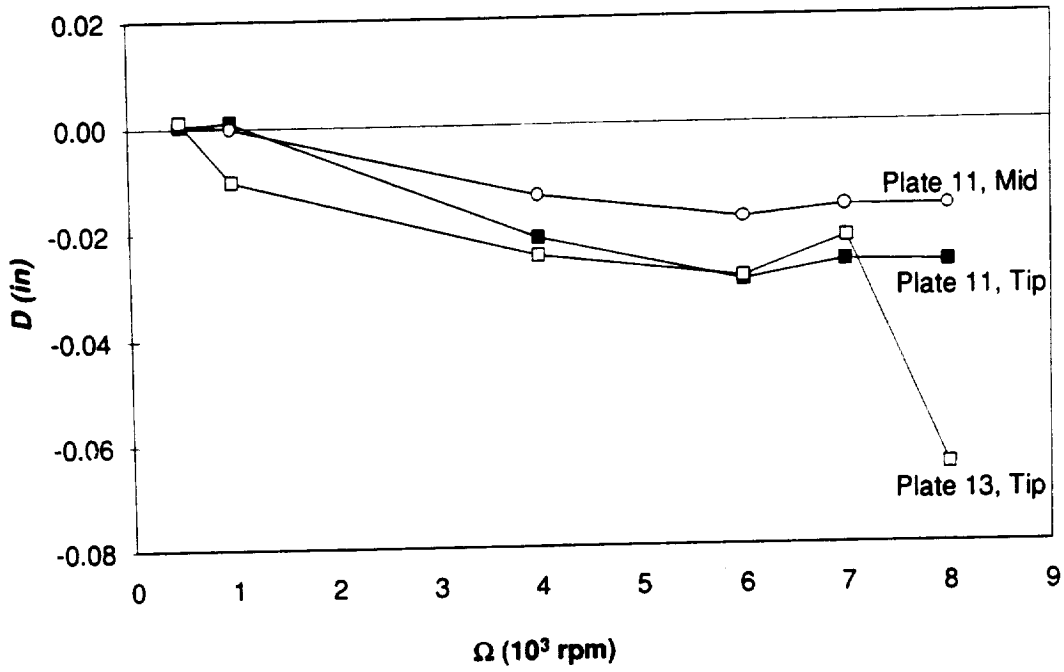

Figure 3.72: Deflection comparisons between Plates 11 and 13 for Configuration A.

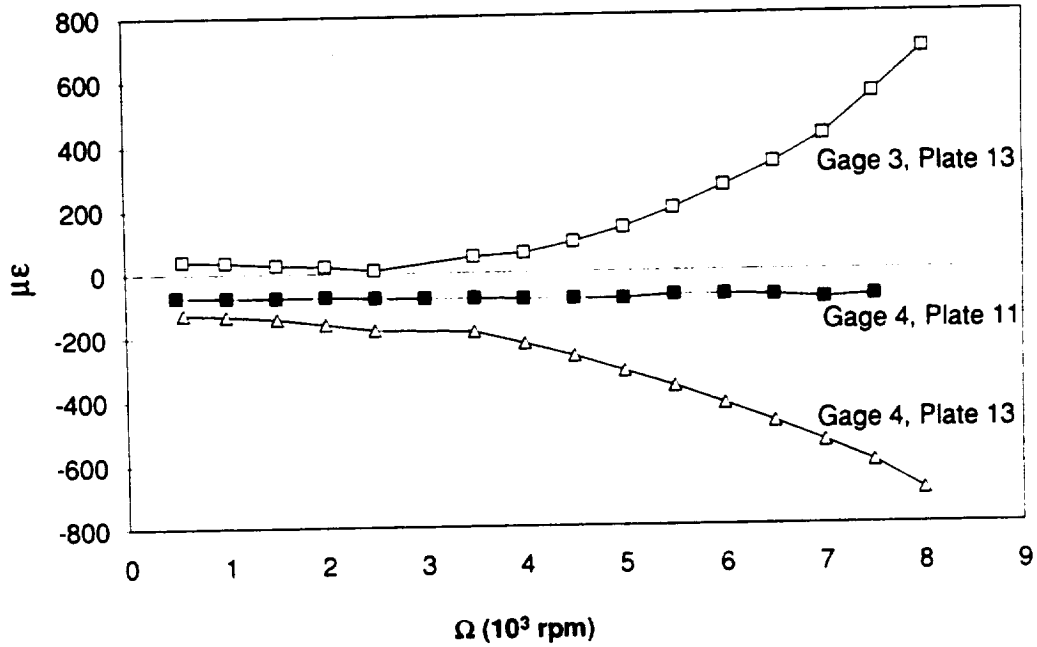

Figure 3.73: Torsion strain comparisons between Plates 11 and 13 for Configuration A.

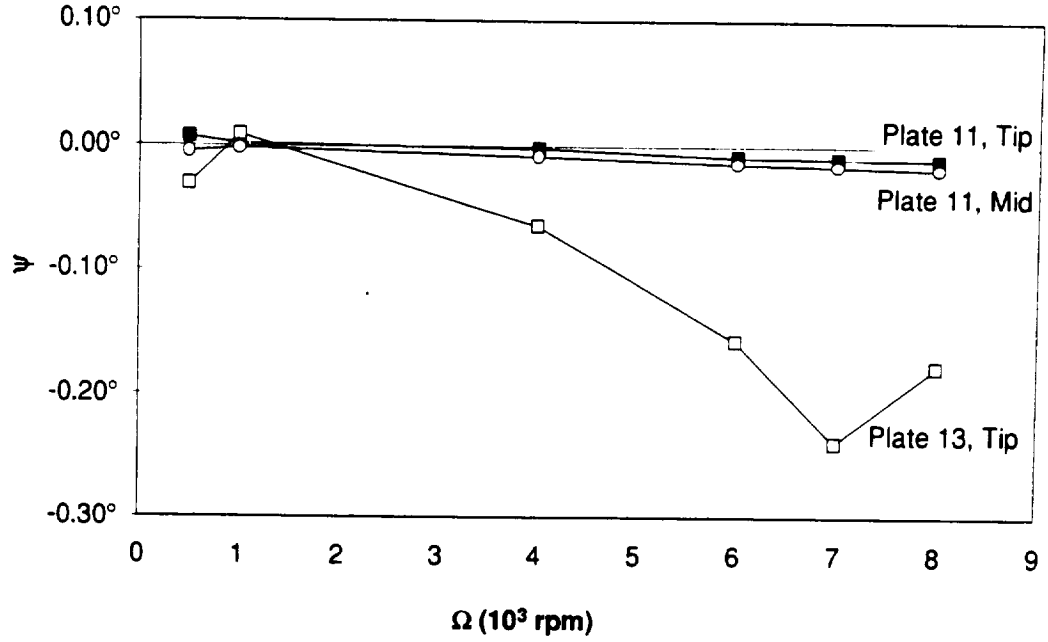

Figure 3.74: Twist comparisons between Plates 11 and 13 for Configuration A.

3.2.21 Plates 21 and 23*, Configuration A

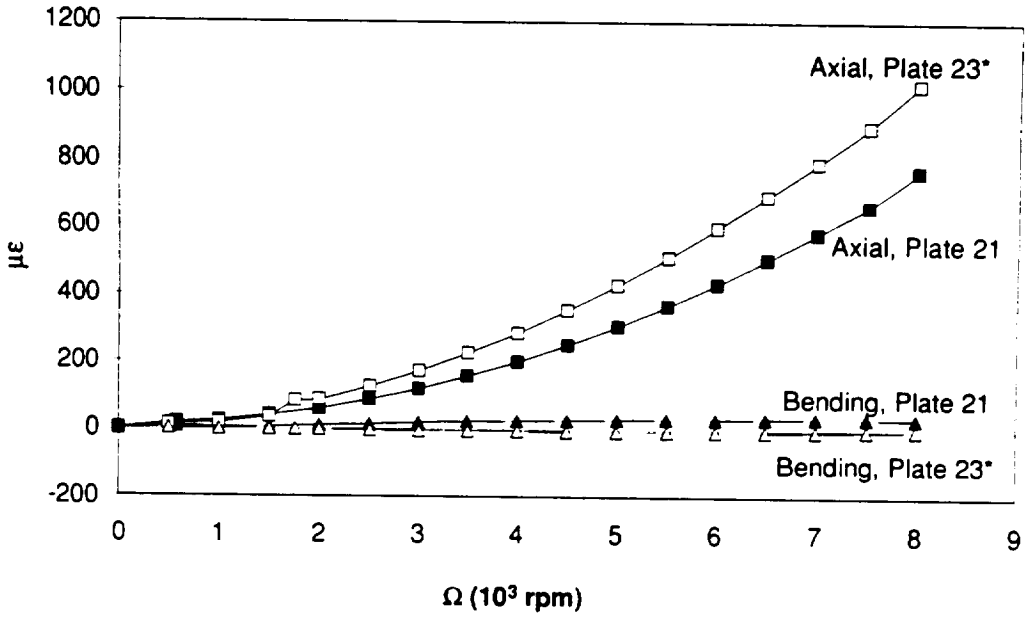

Figure 3.75: Axial and bending strain comparisons between Plates 21 and 23* for Configuration A.

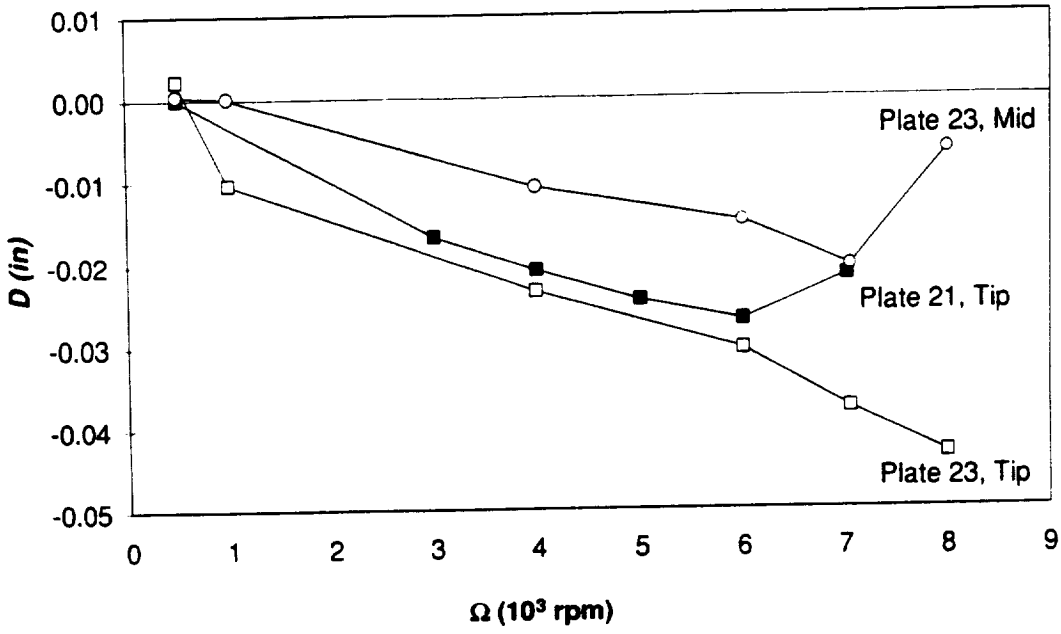

Figure 3.76: Deflection comparisons between Plates 21 and 23* for Configuration A.

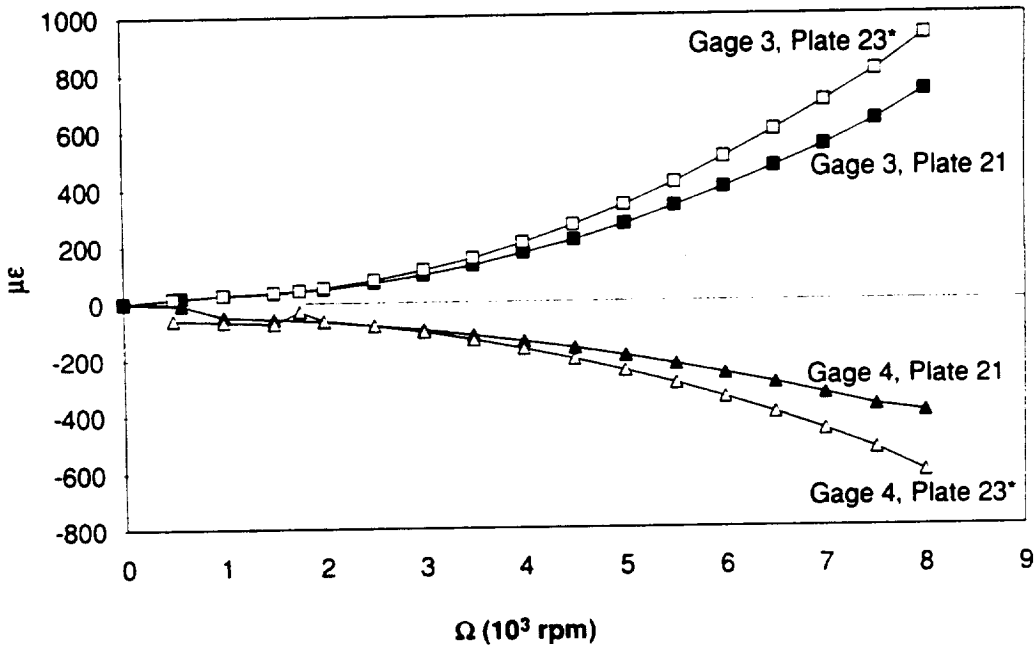

Figure 3.77: Torsion strain comparisons between Plates 21 and 23* for Configuration A.

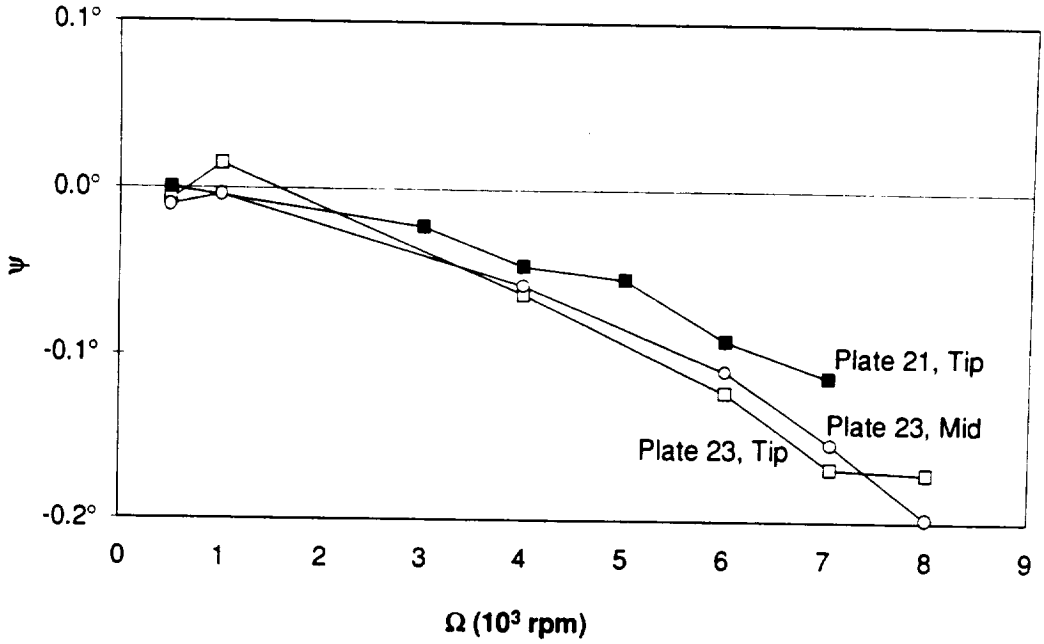

Figure 3.78: Twist comparisons between Plates 21 and 23* for Configuration A.

3.2.22 Plates 13 and 23*, Configuration A

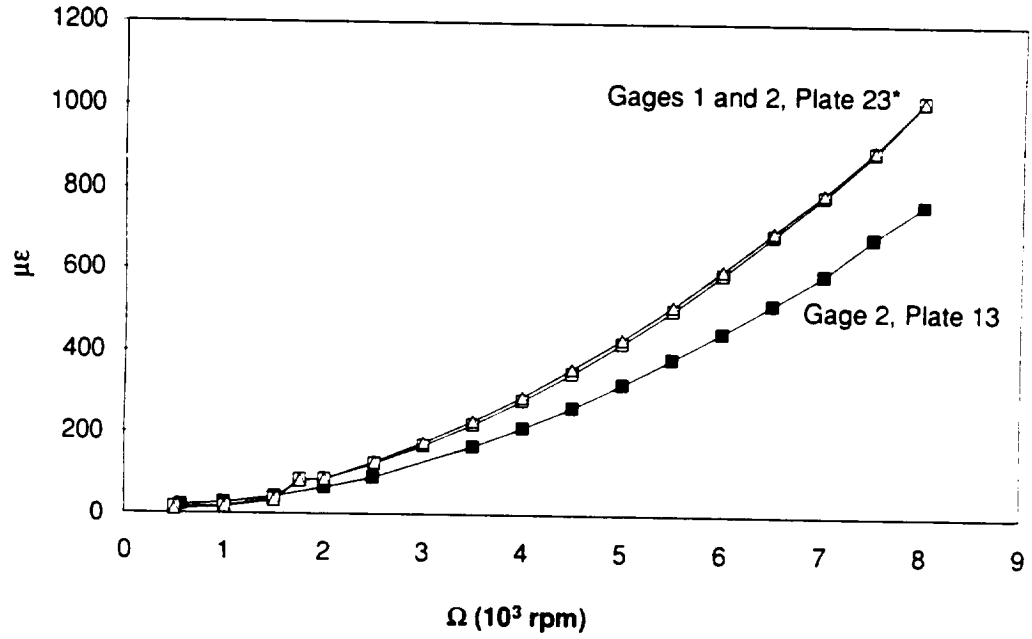

Figure 3.79: Strain comparisons between Plates 13 and 23* for Configuration A.

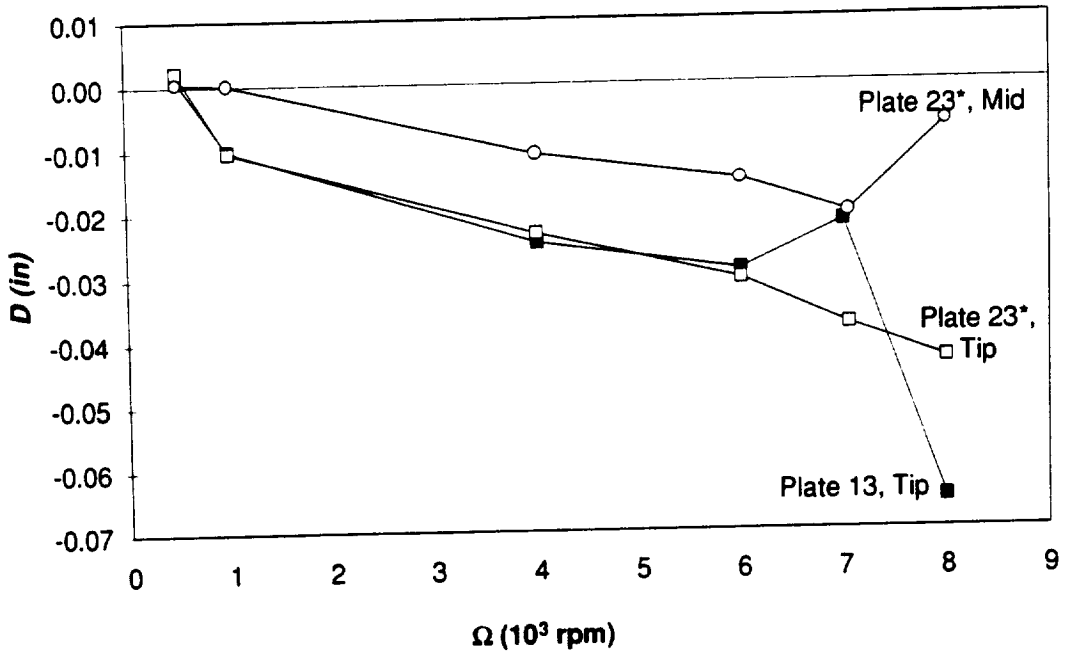

Figure 3.80: Deflection comparisons between Plates 13 and 23* for Configuration A.

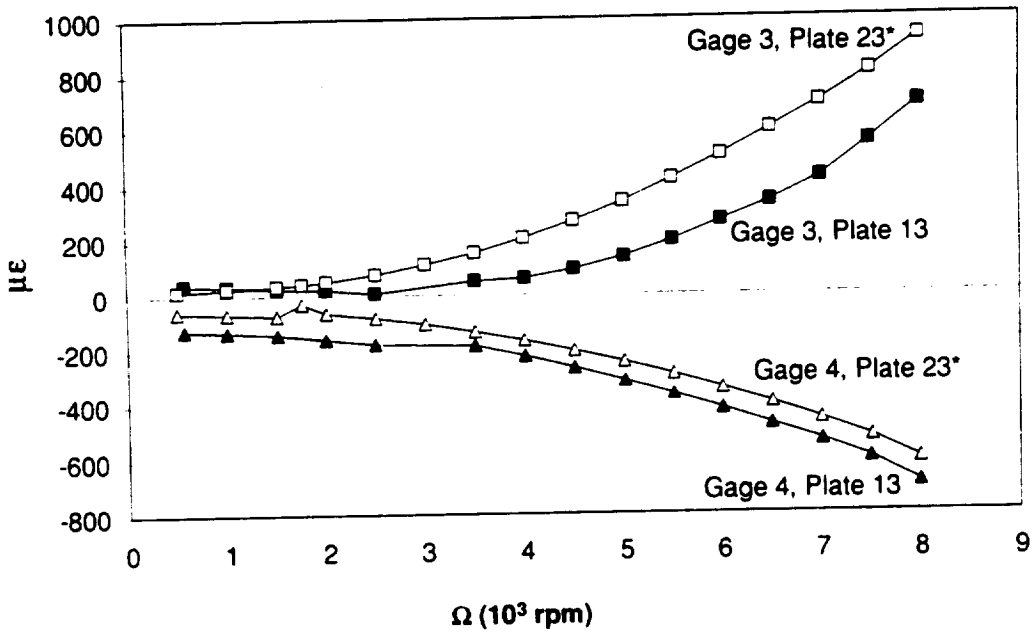

Figure 3.81: Torsion strain comparisons between Plates 13 and 23* for Configuration A.

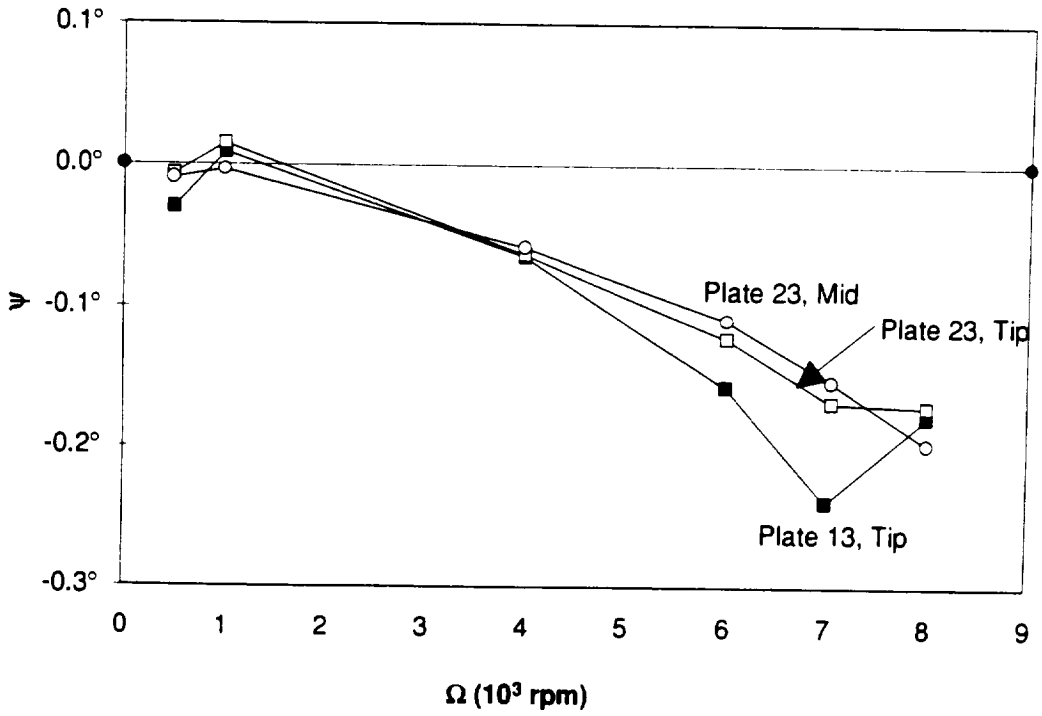

Figure 3.82: Twist comparisons between Plates 13 and 23* for Configuration A.

Chapter 4

Vibration Results and Discussion

This chapter presents and discusses the results of the experimental tests on the graphite/epoxy plates. The first section presents data from the non-rotating static displacements and strain results. The next two sections contain experimental data from the rotating steady-state strain and displacement tests. The fourth section presents the non-rotating vibration results from both the Aerospace Structures Laboratory (ASL) at the University of California San Diego and the NASA Lewis Research Center. The final section presents data from the rotating vibration tests. The purpose of these experiments is to investigate the static and dynamic properties of the spinning, pre-twisted, laminated composite plates. The coupled effects of the stacking sequence and geometry are examined, and for the rotating tests the effects of pitch and sweep are investigated.

4.1 Non-Rotating Vibrations

This section presents results from the non-rotating vibration tests conducted at the ASL and the Laser Holography Laboratory at the NASA Lewis Research Center. The modal tests seek to identify the natural frequencies, mode shapes, and damping of the cantilevered composite plates. The modal tests done at the Laser Holography Laboratory are unable to measure the damping but they do provide a full field view of the mode shapes. The tests at the ASL are able to measure damping and give a good view of the mode shape. Figure 4.1 is a physical description of the mode shapes of a cantilevered plate; the dashed lines are nodal lines [27].

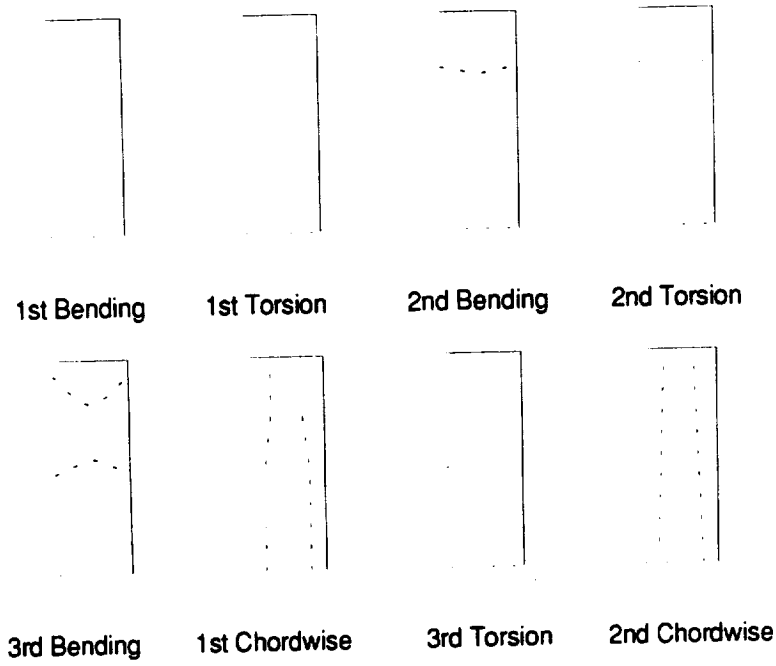

Figure 4.1: Mode shapes of a cantilevered plate. The nodal lines are represented by the dashed curves.

The next series of tables show how the natural frequencies vary with the ply lay-up and geometry. All of the results in Tables 4.1-4.6 are the average values from the measurements conducted at the ASL and the Laser Holography Laboratory for the two plates that comprise each set. The mean value is given by

$$\bar{x} = \frac{1}{N}\sum_{i=1}^{N} x_i \tag{4.1}$$

where N is the number of separate measurements and x_i is a single separate measurement of x [26]. The percent error is the standard deviation of the mean [26] and is given by

$$\sigma_x = \sqrt{\frac{1}{N(N-1)}\sum (x_i - \bar{x})^2}\,. \tag{4.2}$$

The differences in the measured values of the natural frequencies amongst each plate set come from the errors associated from the manufacturing process of the plates and the test setup. Errors from manufacturer arise from the lay-up process and the machining

of the samples. Both of these tasks are performed by hand and any small errors in the ply angles or geometry would cause differences in the measured results. Errors from the test setup arise from the slight differences in the clamping force at the cantilever end and the mass loading of the plate by the accelerometer for the tests conducted at the ASL. For the experiments conducted at the Laser Holography Laboratory, the possibility of the speaker being placed at a node is a source of error. The differences in the natural frequencies are never more than 2.3%.

Table 4.2 shows the effects of the ply lay-up and geometry on the 1st Bending natural frequency, and Figure 4.2 is a graph of the results for the two symmetric laminates. Previous experimental results for isotropic plates with c/t=20 and l/c=1 [8] have shown that the first bending frequency decreases with increasing twist. For the graphite/epoxy plates in this experiment (c/t=30 and l/c=3), the decrease in the first bending frequency is less pronounced. There is a 2% decrease in the first bending frequency from a flat plate to a pre-twisted one for the first lay-up (Table 4.1 and Figure 4.2). The pre-twist axis location has no measurable effect on this frequency and overall the geometry variations have a negligible effect on the first bending natural frequency for all three lay-ups.

There is a more significant effect on the first bending frequency due to the stacking sequence whereby the second lay-up is softer in bending than the first one (Table 4.1 and Figure 4.2). For the flat geometry the second lay-up is 25% softer than the first one and 22% softer for the pre-twisted one. This behavior is caused by the orientation of the plies where ply angles closest to $\theta = 0°$ would result in higher bending frequencies. In general, a lay-up with $\theta = 0°$ would yield the highest bending frequencies and $\theta = 90°$ would have the highest chordwise frequencies. The highest torsion frequencies would occur at some θ between 0° and 90°; the exact angle would depend on the aspect ratio of the plate.

For the third lay-up, the first bending mode is much higher for the pre-twisted plates than for the flat ones. This is because the zero angle plies on the outer surface of

the laminate causes the plate to be much stiffer in bending. Comparing the 1st Bending frequencies between the pre-twisted geometries of lay-ups 1 and 3, the first bending mode is 2.1% higher for the third lay-up.

Table 4.1: Ply lay-up and geometry effects on the 1st Bending natural frequency.

Lay-up / Geometry	1. $\theta = 22.5°$ (Hz)	2. $\theta = 45°$ (Hz)	3. $[(+22.5)_5/0_5]_A$ (Hz)
1. Flat	68.2 ± 0.5%	54.7 ± 0.6%	51.3 ± 0.6%
2. 30° Pre-Twist about the Mid-Chord	67.4 ± 1.3%	55.1 ± 0.8%	68.2 ± 1.9%*
3. 30° Pre-Twist about the Quarter-Chord	66.2 ± 0.6%	55.1 ± 1.2%	68.7 ± 2.3%*
4. 30° Pre-Twist about the Leading Edge	67.0 ± 0.8%	54.9 ± 0.6%	67.9 ± 2.3%*
For the first two lay-ups the stacking sequence is $[\pm\theta/0_2/-\theta/0_2/+\theta/0_2]_S$ *The lay-up for this plate is $[0_2/+22.5_2/0_2/+22.5_3/0]_A$			

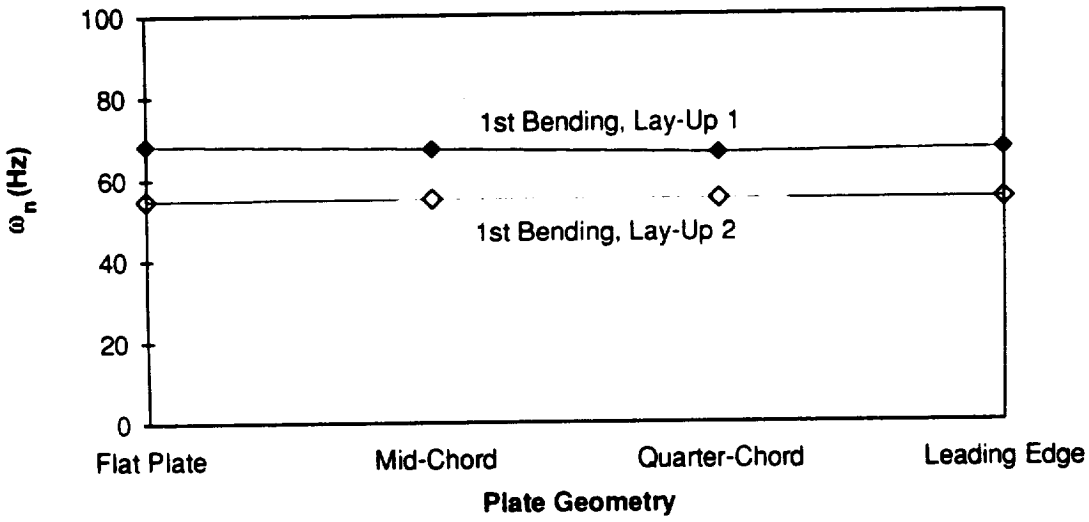

Figure 4.2: The first bending natural frequency for lay-ups 1 and 2.

Tables 4.2 and 4.3 list the 2nd Bending and 1st Torsion natural frequencies for the graphite/epoxy plates, respectively. Figure 4.3 is a graph of the 2nd Bending and 1st Torsion mode of the symmetric plates. The decrease in the 2nd Bending frequency due to

the pre-twist is more apparent for this mode than for the 1st Bending mode. For the two symmetric lay-ups the decrease in the second bending natural frequency upon the introduction of pre-twist is 15% for the first lay-up and 11% for the second one. Previous experimental results on isotropic plates for l/c=3 and c/t=20 show a 13% drop between a flat plate and 30° pre-twisted one [8]. The flat plate vibrates in a single plane for the bending modes; the introduction of pre-twist causes coupling between the extension, bending, and torsion modes that results in the decrease in the bending frequencies. The pre-twist axis location has an immeasurable effect on the 2nd Bending natural frequency for all three lay-ups.

Table 4.2: Ply lay-up and geometry effects on the 2nd Bending natural frequency.

Lay-up / Geometry	1. θ = 22.5° (Hz)	2. θ = 45° (Hz)	3. $[(+22.5)_5/0_5]_A$ (Hz)
1. Flat	424.2 ± 0.6%	336.8 ± 0.3%	313.7 ± 0.2%
2. 30° Pre-Twist about the Mid-Chord	360.2 ± 2.2%	300.3 ± 1.2%	361.1 ± 1.9%*
3. 30° Pre-Twist about the Quarter-Chord	358.3 ± 1.8%	299.1 ± 1.1%	365.7 ± 2.3%*
4. 30° Pre-Twist about the Leading Edge	366.0 ± 1.0%	300.8 ± 1.0%	363.3 ± 2.3%*
For the first two lay-ups the stacking sequence is $[\pm\theta/0_2/-\theta/0_2/+\theta/0_2]_S$ *The lay-up for this plate is $[0_2/+22.5_2/0_2/+22.5_3/0]_A$			

Table 4.3: Ply lay-up and geometry effects on the 1st Torsion natural frequency.

Lay-up / Geometry	1. θ = 22.5° (Hz)	2. θ = 45° (Hz)	3. $[(+22.5)_5/0_5]_A$ (Hz)
1. Flat	267.1 ± 0.5%	305.5 ± 0.4%	302.8 ± 0.3%
2. 30° Pre-Twist about the Mid-Chord	502.1 ± 1.7%	507.5 ± 0.5%	496.6 ± 1.3%*
3. 30° Pre-Twist about the Quarter-Chord	481.6 ± 1.2%	495.9 ± 0.5%	491.8 ± 1.3%*
4. 30° Pre-Twist about the Leading Edge	495.5 ± 0.3%	491.2 ± 0.4%	485.8 ± 1.3%*
For the first two lay-ups the stacking sequence is $[\pm\theta/0_2/-\theta/0_2/+\theta/0_2]_S$ *The lay-up for this plate is $[0_2/+22.5_2/0_2/+22.5_3/0]_A$			

For the 1st Torsion mode, there is a large increase in this natural frequency upon the introduction of pre-twist, 85% for $\theta = 22.5°$ and 63% for $\theta = 45°$. Experimental results for an isotropic plate with an aspect ratio (l/c) of 3 and a thickness ratio (c/t) of 20 show a 20% increase in the first torsion mode upon the introduction of a 30° pre-twist from a flat plate [8]. This behavior is caused by the extension-bending-torsion coupling for pre-twisted plates that causes a slight decrease in the bending modes and an increase in the torsion ones. This results in the switching of the second and third natural frequencies upon the introduction of pre-twist. For the flat plate, the first three modes are 1st Bending, 1st Torsion, and 2nd Bending, and for a plate with a 30° pre-twist the first three modes are 1st Bending, 2nd Bending, and 1st Torsion. This suggests an intermediate pre-twist angle between 0° and 30° where the 2nd Bending and 1st Torsion frequencies cross (Figure 4.3).

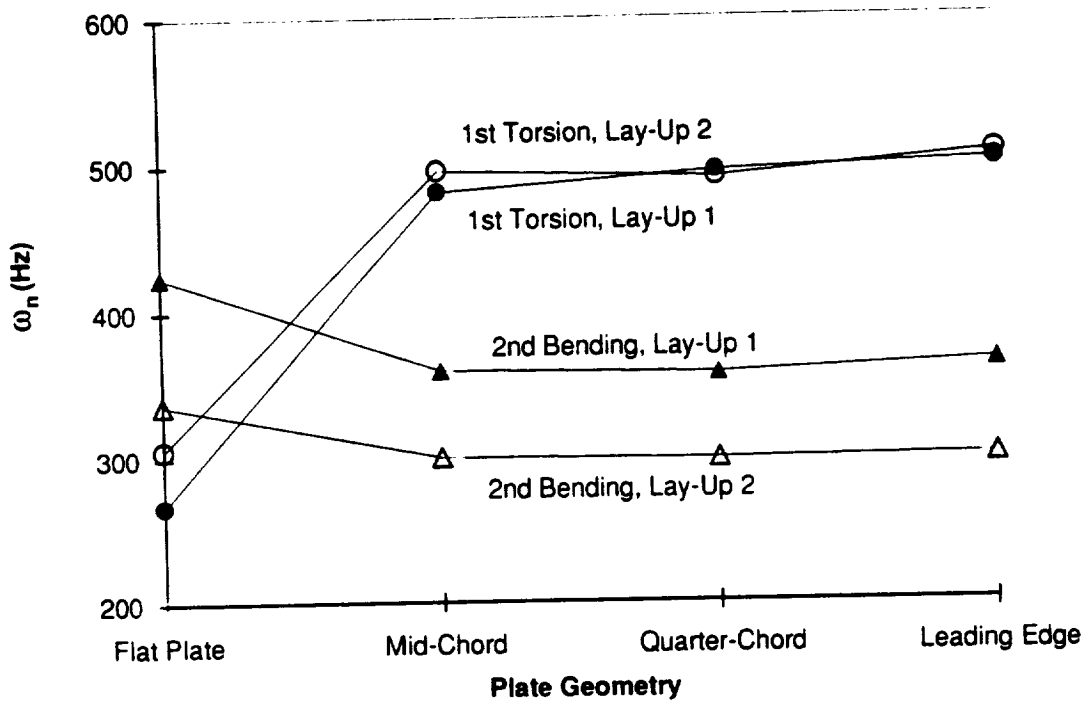

Figure 4.3: The second bending and first torsion natural frequencies for lay-ups 1 and 2.

For the pre-twisted geometries of lay-ups 2 and 3 the first torsion mode decreases as the pre-twist axis moves from the mid-chord to the leading edge. This implies that the bending-torsion coupling becomes less pronounced as the pre-twist axis moves from the mid-chord outward. If the pre-twist angle is kept constant and the axis is moved further and further out, then the plate begins to resemble a plate pre-bent about the root and the bending-torsion coupling decreases.

Comparing the lay-ups, the 2nd Bending mode is lower for the second lay-up than for the first one for all geometries, 21% lower for the flat plate and 17% for the pre-twisted ones (Table 4.2 and Figure 4.3). This difference is caused by the stacking sequence of the laminates where a θ closest to 0° would give the largest bending frequencies. For the flat and pre-twisted geometries of the third lay-up one can see that the placement of the 0° angle plies on the outer surfaces makes the plate significantly stiffer for the second bending mode. The pre-twist should serve to decrease the 2nd Bending mode such as in lay-ups 1 and 2 but the stacking sequence overwhelms this effect.

Looking at the differences between lay-ups 1 and 3, there exists only a 0.5% difference between the pre-twisted geometries. Given the fact that the 0° plies are on the outside for the third lay-up, it can be inferred that the asymmetry of the lay-up causes the plate to be softer in bending which suggests further bending-torsion coupling due to the lay-up.

Comparing the symmetric lay-ups, the 1st Torsion mode is lower for the first lay-up than for the second one for all geometries, 13% lower for the flat plate and only 1% lower for the pre-twisted ones (Table 4.3 and Figure 4.3). The lowest torsion modes should occur for either θ = 0° or 90° and the highest should be at around 45° depending on the aspect ratio. The small difference between the first torsion mode of the pre-twisted

plates of lay-ups 1 and 2 shows that a greater increase in torsional stiffness can be gained through the bending-torsion coupling due to the geometry rather than the lay-up.

For the third lay-up, the first torsion mode for the pre-twisted plates is much greater than the flat one. The lay-up for the pre-twisted plates should be torsionally softer than the one for the flat plate but the geometry coupling masks this behavior. Comparing 1st Torsion frequencies between the pre-twisted plates for lay-ups 1 and 3, one sees that the plates for lay-up are only 0.3% stiffer. One would expect that because lay-up 3 has 0° angle plies on the outer surfaces that it would be much more torsionally softer than it is. However, the asymmetry of the plate introduces extension-bending-torsion coupling that makes it softer in bending and stiffer torsionally.

A list of the 3rd Bending and 2nd Torsion natural frequencies for the composite plates are given in Tables 4.4 and 4.5, respectively. Figure 4.4 is a graph of the third bending and second torsion modes for the symmetric plates. For the two symmetric lay-ups there is a decrease in the third bending natural frequency upon the introduction of pre-twist, 8% for lay-up 1 and 2% for lay-up 2 (Table 4.4 and Figure 4.4). Again as in the second bending mode, this decrease is caused by the bending-torsion coupling that exists for pre-twisted plates. The pre-twist axis location has no measurable effect on the 3rd Bending natural frequency for all three lay-ups. For the 2nd Torsion mode there is a significant increase in the second torsion natural frequency upon the introduction of pre-twist due to the bending-torsion coupling; a 38% increase for lay-up 1 and a 39% increase for lay-up 2. As with the case with the second and third natural frequencies, the 4th and 5th modes of the flat and pre-twisted plates for the first lay-up have switched because of the coupling caused by the geometry. The switching does not occur for the second lay-up because the second torsion frequency is already higher than the 3rd Bending mode (Figure 4.4). For the second lay-up the 2nd Torsion frequency decreases as the pre-twist axis moves from the mid-chord to the leading edge. This is similar to the behavior exhibited

for the 1st Torsion mode where the geometry effects of the pre-twist are lessened as the pre-twist axis moves farther away from the mid-chord.

Table 4.4: Ply lay-up and geometry effects on the 3rd Bending natural frequency.

Lay-up / Geometry	1. $\theta = 22.5°$ (Hz)	2. $\theta = 45°$ (Hz)	3. $[(+22.5)_5/0_5]_A$ (Hz)
1. Flat	1180 ± 0.9%	932.8 ± 1.5%	881.1 ± 0.2%
2. 30° Pre-Twist about the Mid-Chord	1098 ± 1.0%	918.0 ± 0.4%	1103 ± 0.4%*
3. 30° Pre-Twist about the Quarter-Chord	1086 ± 0.7%	915.9 ± 0.4%	1104 ± 0.9%*
4. 30° Pre-Twist about the Leading Edge	1092 ± 0.3%	909.2 ± 0.1%	1101 ± 0.6%*
For the first two lay-ups the stacking sequence is $[\pm\theta/0_2/-\theta/0_2/+\theta/0_2]_S$ *The lay-up for this plate is $[0_2/+22.5_2/0_2/+22.5_3/0]_A$			

Table 4.5: Ply lay-up and geometry effects on the 2nd Torsion natural frequency.

Lay-up / Geometry	1. $\theta = 22.5°$ (Hz)	2. $\theta = 45°$ (Hz)	3. $[(+22.5)_5/0_5]_A$ (Hz)
1. Flat	878.9 ± 0.6%	967.5 ± 0.1%	919.5 ± 0.3%
2. 30° Pre-Twist about the Mid-Chord	1231 ± 1.4%	1371 ± 0.4%	1232 ± 1.0%*
3. 30° Pre-Twist about the Quarter-Chord	1194 ± 1.2%	1336 ± 0.6%	1236 ± 0.6%*
4. 30° Pre-Twist about the Leading Edge	1219 ± 0.2%	1330 ± 0.3%	1229 ± 0.2%*
For the first two lay-ups the stacking sequence is $[\pm\theta/0_2/-\theta/0_2/+\theta/0_2]_S$ *The lay-up for this plate is $[0_2/+22.5_2/0_2/+22.5_3/0]_A$			

Likewise as in the 2nd Bending mode, the 3rd Bending mode is higher for the first lay-up than for the second one for all geometries, 27% for the flat plate and 19% for the pre-twisted ones. This can also be attributed to the orientation of the fibers of the plate. Similarly as in the results for the second bending frequency, the zero angle plies on the outer surfaces in the pre-twisted plates for the third lay-up cause the third bending frequency to be significantly higher than the flat, asymmetric laminate. Again the decrease in the third bending mode of due to the pre-twist for the asymmetric lay-up is not evident

because of the lay-up difference masks this behavior. Compared to the natural frequencies of lay-up 1, the frequencies for the pre-twisted plates for lay-up 3 are only 1% higher. This shows that the asymmetry of the laminate does make the plate softer in bending despite the zero angle plies on the outer surfaces.

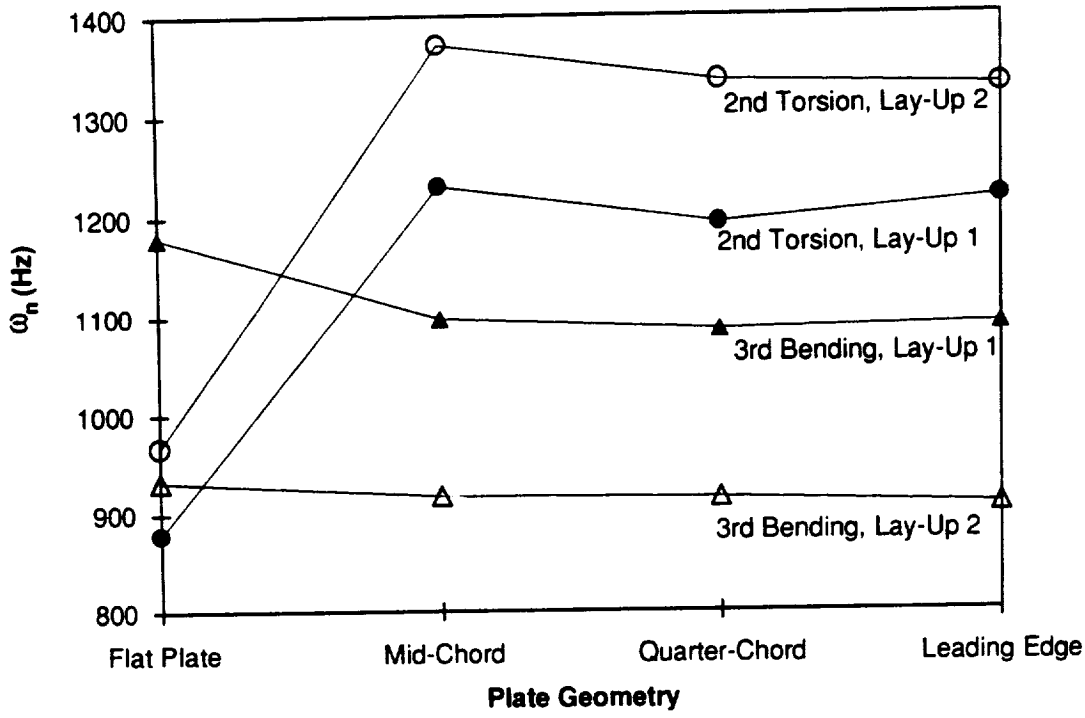

Figure 4.4: The third bending and second torsion natural frequencies for lay-ups 1 and 2.

Because of the ply orientation of the fibers, the second lay-up is softer for the 2nd Torsion mode, 9% softer for the flat plate and 10% for the pre-twisted ones. The effects on the second torsion natural frequency due to the geometry, however, are still greater than the ones caused by the lay-up. For the third lay-up, the zero angle plies on the outside surfaces for the pre-twisted plates should make these plates less stiff than the pre-twisted plates with the first lay-up. The material coupling caused by the asymmetry of the laminate, however, causes the pre-twisted, asymmetric plates to be stiffer.

Table 4.6 lists the 1st Chordwise natural frequencies for the graphite/epoxy plates, and Figure 4.5 depicts this mode versus the geometry for the symmetric lay-ups. For lay-up 1 there is a 1.7% decrease in the first chordwise natural frequency between the flat plate and the pre-twisted, mid-chord one. Comparing with the isotropic results from [8], there is also a 1.7% decrease in the 1st Chordwise frequency as the flat plate is pre-twisted 30° about the mid-chord. The chordwise motion is similar to the bending motion in the sense that no twisting is occurring, thus one would expect a decrease in the chordwise modes caused by the bending-torsion coupling of the pre-twist. As the pre-twist axis moves from the mid-chord to the leading edge the first chordwise frequency increases for the first lay-up. The increase causes the first chordwise mode for the pre-twisted, leading edge plate to be higher than the one for the flat plate. This behavior is not exemplified for the plates with the second lay-up, but is to a certain extent for the third one.

Comparing the frequencies of the two symmetric lay-ups, the 1st Chordwise natural frequency is 36% higher for the second lay-up than for the first for the pre-twisted geometries (Table 4.6 and Figure 4.5). The first chordwise mode for the flat plate with lay-up 2 is not found because it is so much higher than all the other modes. A ply angle with $\theta = 90°$ would give the highest chordwise frequencies; this explains why the frequencies for lay-up 2 are so much higher than the other lay-ups.

Table 4.6: Ply lay-up and geometry effects on the 1st Chordwise natural frequency.

Lay-up / Geometry	1. $\theta = 22.5°$ (Hz)	2. $\theta = 45°$ (Hz)	3. $[(+22.5)_5/0_5]_A$ (Hz)
1. Flat	1413 ± 0.9%	—	1305 ± 0.4%
2. 30° Pre-Twist about the Mid-Chord	1389 ± 1.8%	1917 ± 0.3%	1313 ± 0.8%
3. 30° Pre-Twist about the Quarter-Chord	1392 ± 0.8%	1918 ± 0.0%	1325 ± 0.8%
4. 30° Pre-Twist about the Leading Edge	1426 ± 0.0%	1904 ± 0.1%	—

For the first two lay-ups the stacking sequence is $[\pm\theta/0_2/-\theta/0_2/+\theta/0_2]_S$

*The lay-up for this plate is $[0_2/+22.5_2/0_2/+22.5_3/0]_A$

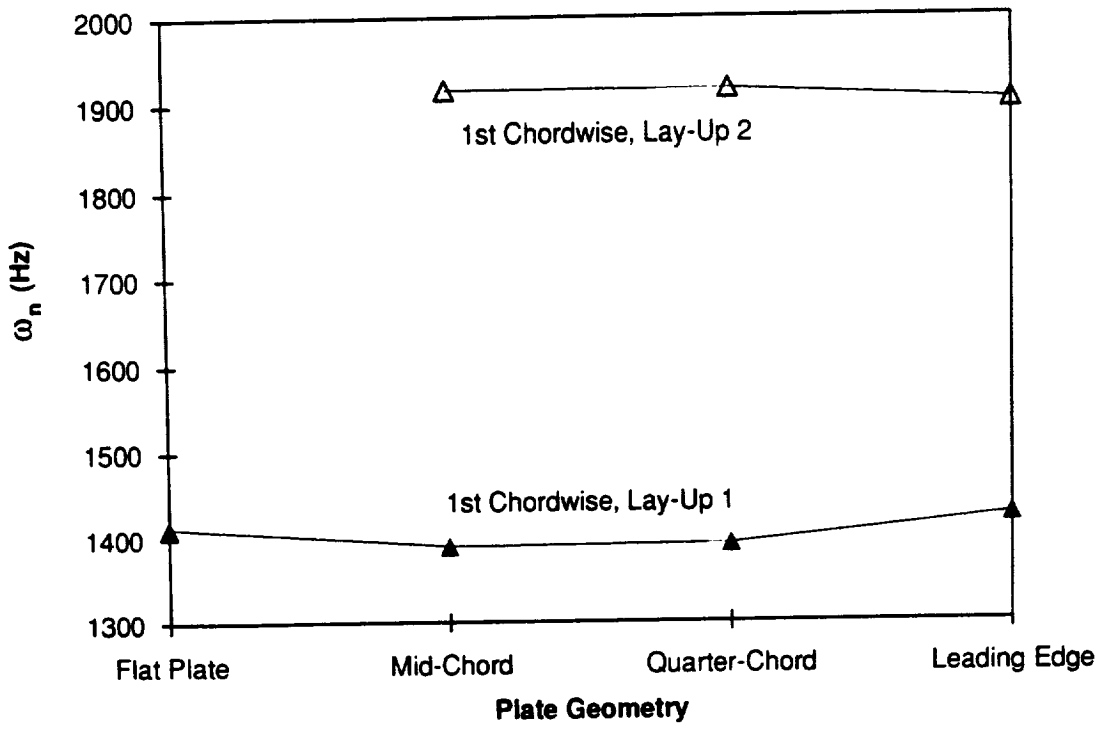

Figure 4.5: The first chordwise natural frequency for lay-ups 1 and 2.

Figures 4.6-4.8 depict the holographic images of the mode shapes for the flat plate with lay-up 1, the pre-twisted plate about the quarter-chord with lay-up 1, and the flat plate with the asymmetric lay-up $[+22.5_5/0_5]_A$. The results from Table 4.1 and Figure 4.2 show that there is very little discernible amount of bending-torsion coupling due to the pre-twist for the first mode and is more evident for the 2nd Bending and 1st Torsion frequencies. From Figures 4.6 and 4.7 one can see the effects of the coupling near the root of the plate on the 2nd Bending and 1st Torsion modes. The mode shape for the flat plate is more symmetric about the mid-chord of the plate than the pre-twisted one. From the same two sets of photographs the coupling effects on the 3rd Bending and 1st Chordwise modes are not as readily seen in the photographs but can be seen in the 2nd Torsion mode.

The comparison of Figures 4.6 and 4.8 (flat plates with symmetric lay-up 1 and asymmetric lay-up 3, respectively) examines the bending-torsion coupling of the asymmetric laminate. As in the discussion above with the flat and pre-twisted plates, there is no visible coupling of the mode shapes for the first bending natural frequency. The 2nd Bending and 1st Torsion modes are symmetric about the mid-chord for the flat, symmetric laminate (Figure 4.6). In the same modes for the asymmetric one the nodal area for the torsion mode aligns itself along the direction of the fibers, and for the second bending mode the nodal area is angled perpendicular to the fibers (Figure 4.8). For the asymmetric plate the coupling isn't evident in 2nd Torsion mode (Figure 4.8), but in the 3rd Bending mode the nodal areas are straighter and angled slightly towards the fibers. Finally, the 1st Chordwise mode for the flat, asymmetric plate shows that the left nodal area near the tip aligns itself along the direction of the fibers (Figure 4.8). The other right nodal area near the tip curves towards the right, perpendicular to the fibers.

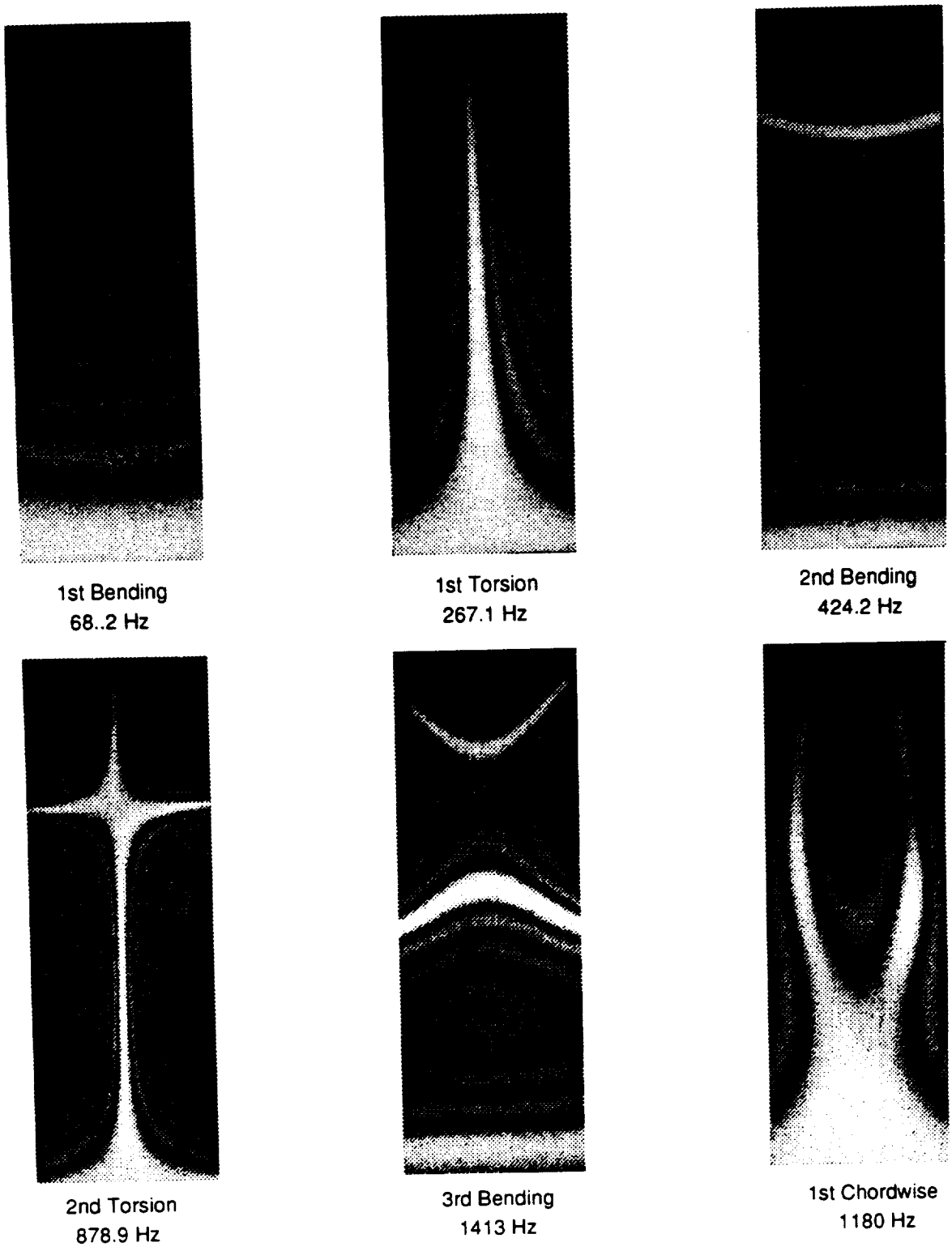

Figure 4.6: Photographs of the first six mode shapes for Plate 11.

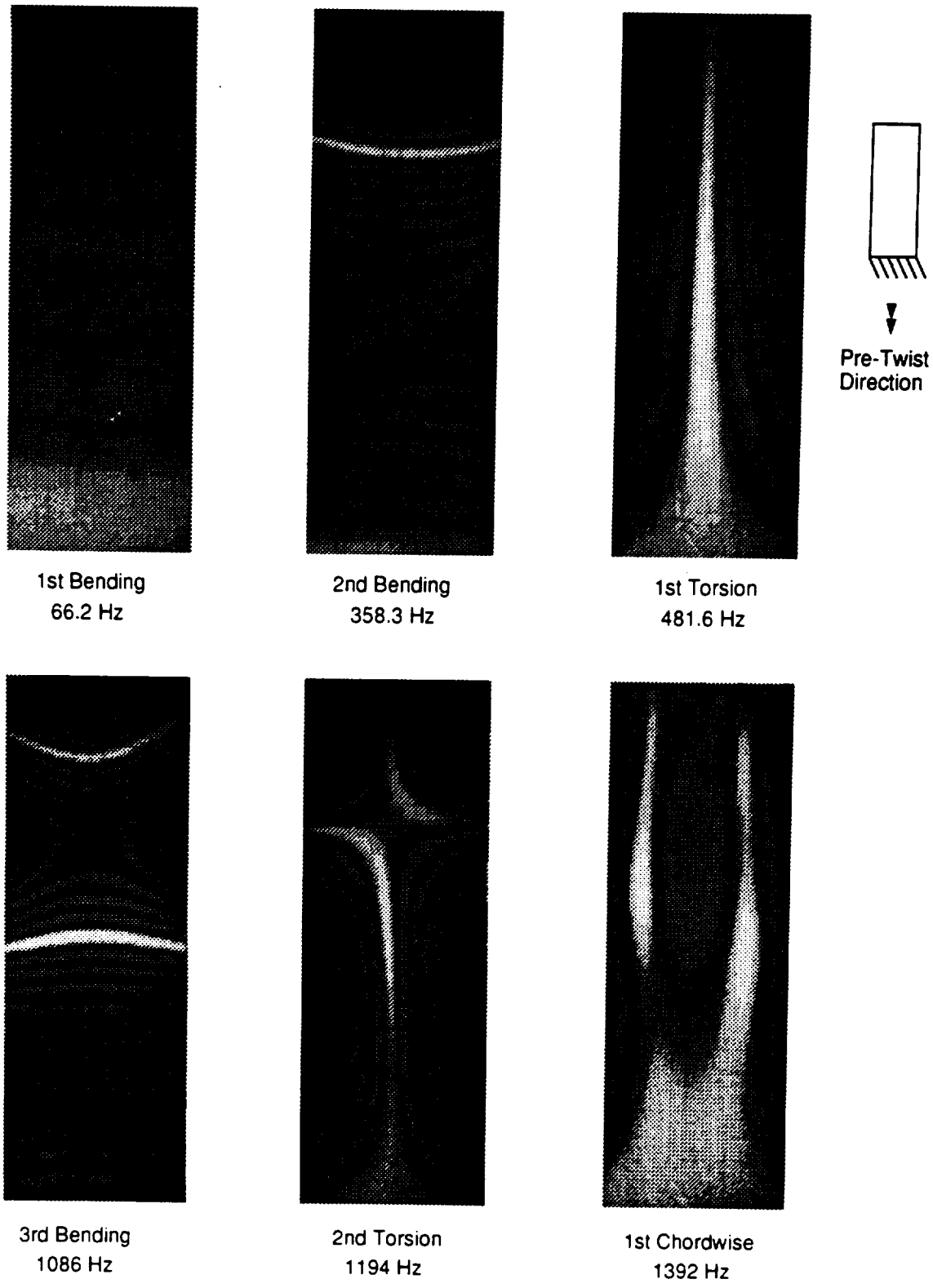

Figure 4.7: Photographs of the first six mode shapes for Plate 31.

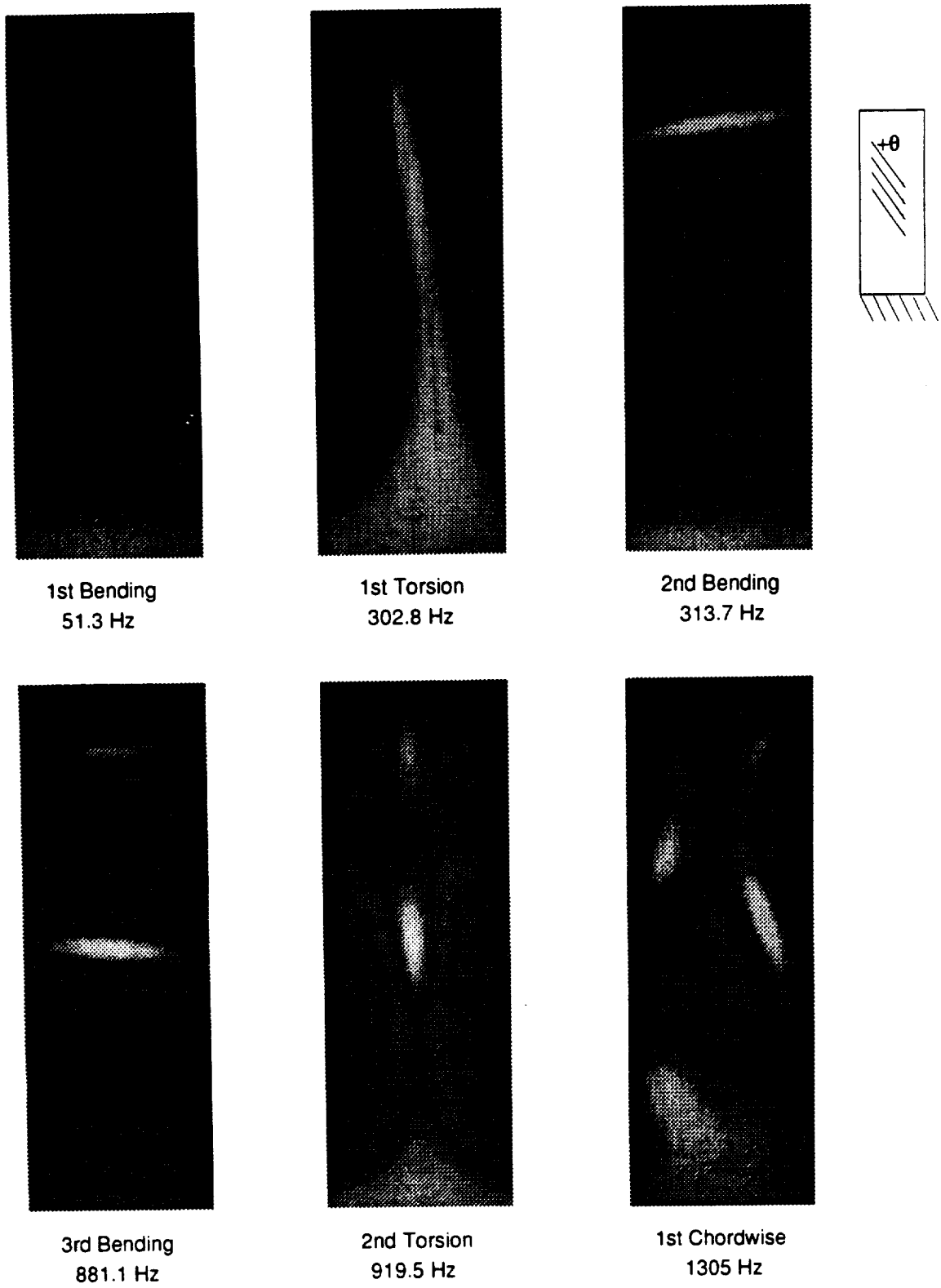

Figure 4.8: Photographs of the first six mode shapes for Plate 13.

4.2 Rotating Vibrations

This section presents results from the rotating vibration tests conducted at the Dynamic Spin Rig Facility at the NASA Lewis Research Center. The purpose of these tests is to examine the effects of the rotating forces on the vibration modes of the plates. Because of the time constraints only six of the twelve plate sets are tested–Plates 11, 21, 31, 32, 13, and 23 and in only one test configuration, $\beta_s = 0°$ (sweep) and $\beta_p = 90°$ (pitch). Tables 4.7-4.17 (pp. 136–139) lists the difference in the plate natural frequencies between the Dynamic Spin Rig at 0 rpm with the results obtained from the ASL and the Laser Holography Laboratory. The purpose of these tables is to document the effect of the spin rig setup on the natural frequencies. Figures 4.9-4.20 (pp. 141–146) depict graphs of the plate natural frequencies versus the rotational speed (ω vs. Ω) as well as graphs of the square of the natural frequency of the spinning plate versus the square of the rotational speed (ω^2 vs. Ω^2). The lines in the first set of graphs (ω vs. Ω) represent polynomial fits of the data to help the reader better visualize the trends. The tables and graphs for the individual plates are presented at the end of Section 4.2.6. The last section makes comparisons between all of the different plate sets.

In general, the square of the natural frequency of the plate is directly proportional to the stiffness of the plate

$$\omega^2 = c_1 K_N + c_2 K_R \tag{4.3}$$

where c_1 and c_2 are constants of proportionality and K_N and K_R are the non-rotating and rotating stiffnesses of the plate, respectively. At 0 rpm, the second term $c_2 K_R$ goes to zero for a non-spinning plate and $c_1 K_N$ goes to the ω_0, the natural frequency of the plate at 0 rpm. The rotating stiffness, K_R, is directly proportional to the centrifugal force, F_c, which is in turn directly proportional to the square of the rotational speed (Ω). Equation 4.3 becomes

$$\omega^2 = \omega_0^2 + S\Omega^2 \tag{4.4}$$

where S is commonly known as the Southwell coefficient and is a function of the pitch, sweep, natural frequency under consideration, and plate stiffness. In the following series of graphs (Figures 4.9-4.20) that plot ω^2 vs. Ω^2, a least squares analysis approach is used on the measured data to calculate the Southwell coefficient, S. From [26], the variables ω_0^2 and S can be calculated as

$$\omega_0^2 = \frac{\left[\sum(\Omega_i^2)^2\right]\left(\sum\omega_i^2\right) - \left(\sum\Omega_i^2\right)\left(\sum\Omega_i^2\omega_i^2\right)}{N\left[\sum(\Omega_i^2)^2\right] - \left(\sum\Omega_i^2\right)^2} \tag{4.5}$$

and

$$S = \frac{N\left(\sum\Omega_i^2\omega_i^2\right) - \left(\sum\Omega_i^2\right)\left(\sum\omega_i^2\right)}{N\left[\sum(\Omega_i^2)^2\right] - \left(\sum\Omega_i^2\right)^2}. \tag{4.6}$$

A linear correlation coefficient, r, indicates how well the data fits a straight line where a value of 1 or -1 means the data is perfectly linear and is given by

$$r = \frac{\sum\left(\Omega_i^2 - \overline{\Omega^2}\right)\left(\omega_i^2 - \overline{\omega^2}\right)}{\left[\sum\left(\Omega_i^2 - \overline{\Omega^2}\right)^2 \sum\left(\omega_i^2 - \overline{\omega^2}\right)^2\right]^{1/2}}. \tag{4.7}$$

The natural frequencies of the plates were measured and processed using strain gages and an 8 channel spectrum analyzer. The mode shapes were identified at 0 rpm and were tracked as the speed was increased. Modal tracking was difficult because extraneous peaks from the spinning assembly and a 60 Hz electrical noise and the harmonics from both would show up on the frequency spectrum. Because of the noisy frequency spectra and the amount of energy needed to excite the higher modes, only the first three natural

frequencies were tracked. An attempt, however, was made to try to identify the fourth and fifth modes of Plate 13; no other plates were tried because of the time limitations.

The next six sections present data associated with each individual plate set. The section afterwards summarizes the Southwell and linear correlation coefficients and discusses the vibrational behavior of the plates.

4.2.1 Flat Plate with $[\pm 22.5/0_2/-22.5/0_2/+22.5/0_2]_S$ Lay-Up

Table 4.7 (p. 136) lists the difference in the natural frequencies between the Dynamic Spin Rig at 0 rpm with the results obtained from the ASL and the Laser Holography Laboratory for Plate 11. The largest percent difference between the setup at the spin rig and the non-rotating vibration results is 2.6% for the 1st Bending mode. Table 4.8 is a list of the measured natural frequencies of Plate 11 at rotational speeds from 0 to 8000 rpm as well as the percent change in the natural frequency from 0 to 8000 rpm. As the rotational speed increases, there is a steady increase in the 1st Bending, 1st Torsion, and 2nd Bending natural frequencies, which is caused by the centrifugal stiffening of the plate. For the 1st Bending and 1st Torsion modes, the behavior is linear for ω^2 vs. Ω^2 in Figure 4.10 (p. 141). The linearity breaks down for the 2nd Bending mode because of the shear deformation effects.

4.2.2 Pre-Twisted Plate about the Mid-Chord with $[\pm 22.5/0_2/-22.5/0_2/+22.5/0_2]_S$ Lay-Up 1

Table 4.9 (p. 137) lists the difference in the natural frequencies between the Dynamic Spin Rig at 0 rpm with the results obtained from the ASL and the Laser Holography Laboratory for Plate 21. The largest percent difference between the setup at the spin rig and the non-rotating vibration results is -2.3% with the 2nd Bending mode. Table 4.10 lists the measured natural frequencies from 0 to 8000 rpm and the percent

increase from 0 to 8000 rpm. Figure 4.11 (p. 142) shows the first three natural frequencies as a function of the rotational speed. The first and second bending modes increase with the rotational speed while the first torsion mode decreases. The 2nd Bending and 1st Torsion modes cross one another at a speed just below 6750 rpm. Figure 4.12 is a plot of ω^2 vs. Ω^2 (Equation 4.4), and the squares of the measured results for the 1st Bending and 1st Torsion modes vary linearly with the square of the rotational speed. The second bending mode is the only mode to exhibit non-linear behavior with Equation 4.4.

4.2.3 Pre-Twisted Plate about the Quarter-Chord with $[\pm 22.5/0_2/-22.5/0_2/+22.5/0_2]_S$ Lay-Up

Table 4.11 (p. 137) lists the difference in the natural frequencies between the Dynamic Spin Rig at 0 rpm with the results obtained from the ASL and the Laser Holography Laboratory. The largest percent difference between the two is 3.8% at the 1st Torsion mode. Figure 4.13 (p. 143) shows the first three natural frequencies as a function of the rotational speed. The behavior is similar to that of the mid-chord plate in the previous section. The two bending modes increase with rotational speed while the first torsion mode decreases; the crossing occurs at a speed just above 6500 rpm. Figure 4.14 is a graph of the ω^2 vs. Ω^2 (Equation 4.4); and with the exception of the second bending mode, it is shown that the squares of ω and Ω vary linearly with each other.

4.2.4 Pre-Twisted Plate about the Quarter-Chord with $[\pm 45/0_2/-45/0_2/+45/0_2]_S$ Lay-Up

Table 4.13 (p. 138) lists the difference in the natural frequencies between the Dynamic Spin Rig at 0 rpm with the results obtained from the ASL and the Laser Holography Laboratory. The largest percent difference between the two is 0.9% at the

1st Torsion mode. Figure 4.15 (p. 144) shows the first three natural frequencies as a function of the rotational speed. The behavior is similar to the that of the other two pre-twisted plates presented so far. The first and second bending modes increase and the first torsion mode decreases with increasing rotational speed. The crossing of the 2nd Bending and 1st Torsion modes is not observed for this plate. This is because the lay-up makes the plate torsionally stiffer and softer in bending than plates with lay-up 1. Thus, the frequency crossing should occur at a higher rotational speed. Because this lay-up is centrifugally softer than the others, the maximum speed this plate is tested at is 7000 rpm. Figure 4.16 plots ω^2 vs. Ω^2 (Equation 4.4), and it can be seen that the square of the natural frequency varies linearly with the square of the rotational speed.

4.2.5 Flat Plate with $[+22.5_5/0_5]_A$ Lay-Up

This is the only plate set where an attempt at recording the first five rotating vibration modes was made. Table 4.15 (p. 139) lists the difference in the first five natural frequencies between the Dynamic Spin Rig at 0 rpm with the results obtained from the ASL and the Laser Holography Laboratory. The largest percent difference between the two is 2.8% for the 3rd Bending mode. Figure 4.17 (p. 145) shows the first five natural frequencies as a function of the rotational speed and all five modes increase with the rotational speed. Figure 4.18 shows a graph of ω^2 vs. Ω^2 (Equation 4.4) and all of the modes except for the third bending mode exhibit linear behavior.

4.2.6 Pre-Twisted Plate about the Mid-Chord with $[0_2/+22.5_2/0_2/+22.5_3/0]_A$ Lay-Up

Table 4.17 (p. 139) lists the difference in the first three natural frequencies between the Dynamic Spin Rig at 0 rpm with the results obtained from the ASL and the Laser Holography Laboratory. The largest percent difference between the two is -3.2%

for the 1st Bending mode. Figure 4.19 (p. 146) shows the first three natural frequencies as a function of the rotational speed. Like all the other pre-twisted plates, the first two bending modes increase and the first torsion mode decreases with increasing rotational speed. The 2nd Bending and 1st Torsion modes cross at a speed between 5500 and 6000 rpm. Figure 4.20 is a graph of ω^2 vs. Ω^2 (Equation 4.4), and it shows that the square of the natural frequency varies linearly with the square of the rotational speed for the first bending and torsion modes.

Table 4.7: Comparison of the natural frequency results from the ASL and Laser Holography Laboratory to the Dynamic Spin Rig Facility at 0 rpm for Plate 11.

Mode Shape	ASL and the Laser Holography Laboratory, (Hz)	Dynamic Spin Rig at 0 rpm, (Hz)	%difference with the ASL and Laser Holography Laboratory
1st Bending	68.2	70.0	2.6%
1st Torsion	267.1	271.5	1.6%
2nd Bending	424.2	428.0	0.9%

Table 4.8: Measured experimental natural frequencies from 0 to 8000 rpm for Plate 11.

Rotational Speed, (rpm)	1st Bending, (Hz)	1st Torsion, (Hz)	2nd Bending, (Hz)
0	70.0	271.5	428.0
1000	75.0	272.5	430.8
2000	87.0	277.5	443.5
3000	103.8	285.8	455.5
4000	123.5	296.5	467.0
5000	145.0	309.5	499.5
6000	167.0	325.0	529.5
7000	189.8	342.0	553.5
8000	212.5	360.0	623.0
%change from 0 → 8000	204%	32.6%	45.6%

Table 4.9: Comparison of the natural frequency results from the ASL and Laser Holography Laboratory to the Dynamic Spin Rig Facility at 0 rpm for Plate 21.

Mode Shape	ASL and the Laser Holography Laboratory (Hz)	Dynamic Spin Rig at 0 rpm (Hz)	%difference with the ASL and Laser Holography Laboratory
1st Bending	67.4	66.0	-2.1%
2nd Bending	360.2	352.0	-2.3%
1st Torsion	502.1	501.0	-0.2%

Table 4.10: Measured experimental natural frequencies from 0 to 8000 rpm for Plate 21.

Rotational Speed, (rpm)	1st Bending, (Hz)	2nd Bending, (Hz)	1st Torsion, (Hz)
0	65.5	352.0	501.0
1000	70.5	355.0	500.0
2000	82.8	354.0	497.0
2500	91.0	362.5	495.0
3000	100.0	367.0	493.0
3500	109.8	379.0	490.0
4000	120.0	388.5	488.5
5000	141.3	416.5	480.0
6000	163.3	443.5	467.0
6750	180.0	464.5	458.0
7000	185.8	472.5	457.0
7250	191.3	480.0	453.5
7500	197.0	487.0	451.0
8000	208.3	498.5	445.0
%change from 0 → 8000	218%	41.6%	-11.2%

Table 4.11: Comparison of the natural frequency results from the ASL and Laser Holography Laboratory to the Dynamic Spin Rig Facility at 0 rpm for Plate 31.

Mode Shape	ASL and the Laser Holography Laboratory (Hz)	Dynamic Spin Rig at 0 rpm (Hz)	%difference with the ASL and Laser Holography Laboratory
1st Bending	66.2	66.0	-0.3%
2nd Bending	358.3	347.3	-3.1%
1st Torsion	481.6	499.8	3.8%

Table 4.12: Measured experimental natural frequencies from 0 to 8000 rpm for Plate 31.

Rotational Speed, (rpm)	1st Bending, (Hz)	2nd Bending, (Hz)	1st Torsion, (Hz)
0	65.5	347.3	499.8
1000	70.5	352.5	500.0
2000	83.5	351.0	491.8
3000	104.0	368.5	486.0
4000	120.0	385.8	477.8
5000	141.3	416.8	471.0
6000	163.0	445.0	466.5
6250	168.8	454.3	461.5
6500	174.8	457.0	456.5
6750	180.3	468.0	453.0
7000	186.5	472.0	450.0
8000	208.3	500.5	440.5
%change from 0 → 8000	218%	44.1%	-11.9%

Table 4.13: Comparison of the natural frequency results from the ASL and Laser Holography Laboratory to the Dynamic Spin Rig Facility at 0 rpm for Plate 32.

Mode Shape	ASL and the Laser Holography Laboratory (Hz)	Dynamic Spin Rig at 0 rpm (Hz)	%difference with the ASL and Laser Holography Laboratory
1st Bending	55.1	55.0	-0.3%
2nd Bending	299.1	298.7	-0.1%
1st Torsion	495.9	500.4	0.9%

Table 4.14: Measured experimental natural frequencies from 0 to 7000 rpm for Plate 32.

Rotational Speed, (rpm)	1st Bending, (Hz)	2nd Bending, (Hz)	1st Torsion, (Hz)
0	55.0	299.0	500.5
1000	60.8	301.5	501.5
2000	75.0	317.0	499.0
3000	94.0	337.0	494.0
4000	115.0	357.0	487.0
5000	137.0	394.5	482.0
6000	160.0	418.0	476.0
7000	183.0	449.5	
%change from 0 → 7000	233%	50.3%	-4.9% (6000 rpm)

Table 4.15: Comparison of the natural frequency results from the ASL and Laser Holography Laboratory to the Dynamic Spin Rig Facility at 0 rpm for Plate 13.

Mode Shape	ASL and the Laser Holography Laboratory (Hz)	Dynamic Spin Rig at 0 rpm (Hz)	%difference with the ASL and Laser Holography Laboratory
1st Bending	51.3	52.0	1.4%
1st Torsion	302.8	300.5	-0.8%
2nd Bending	313.7	312.0	-0.5%
3rd Bending	881.1	905.9	2.8%
2nd Torsion	919.5	907.3	-1.3%

Table 4.16: Measured experimental natural frequencies from 0 to 8000 rpm for Plate 13.

Rotational Speed, (rpm)	1st Bending, (Hz)	1st Torsion, (Hz)	2nd Bending, (Hz)	3rd Bending, (Hz)	2nd Torsion, (Hz)
0	51.5	300.5	312.0	905.9	907.3
1000	57.5	302.0	318.5	–	915.8
2000	72.5	298.0	331.0	901.0	932.5
3000	92.5	301.5	357.5	907.0	958.5
4000	114.0	302.0	386.5	902.8	992.0
5000	136.5	306.8	426.0	908.0	1035.5
6000	159.5	315.5	466.5	914.3	1086.5
7000	183.5	327.3	507.5	927.3	1138.5
8000	206.5	341.3	544.0	942.5	1186.8
%change from 0 → 8000	301%	13.6%	74.4%	4.01%	30.8%

Table 4.17: Comparison of the natural frequency results from the ASL and Laser Holography Laboratory to the Dynamic Spin Rig Facility at 0 rpm for Plate 23*.

Mode Shape	ASL and the Laser Holography Laboratory (Hz)	Dynamic Spin Rig at 0 rpm (Hz)	%difference with the ASL and Laser Holography Laboratory
1st Bending	68.2	66.0	-3.2%
2nd Bending	361.1	352.3	-2.5%
1st Torsion	496.6	503.3	1.3%

Table 4.18: Measured experimental natural frequencies from 0 to 8000 rpm for Plate 23*.

Rotational Speed, (rpm)	1st Bending, (Hz)	1st Torsion, (Hz)	2nd Bending, (Hz)
0	65.5	352.3	503.3
1000	70.8	356.0	503.5
2000	82.8	355.8	495.0
3000	105.0	382.3	487.5
4000	120.0	405.8	474.5
5000	141.0	435.0	465.5
6000	163.0	467.0	455.5
7000	185.5	500.8	436.8
8000	208.0	527.5	418.0

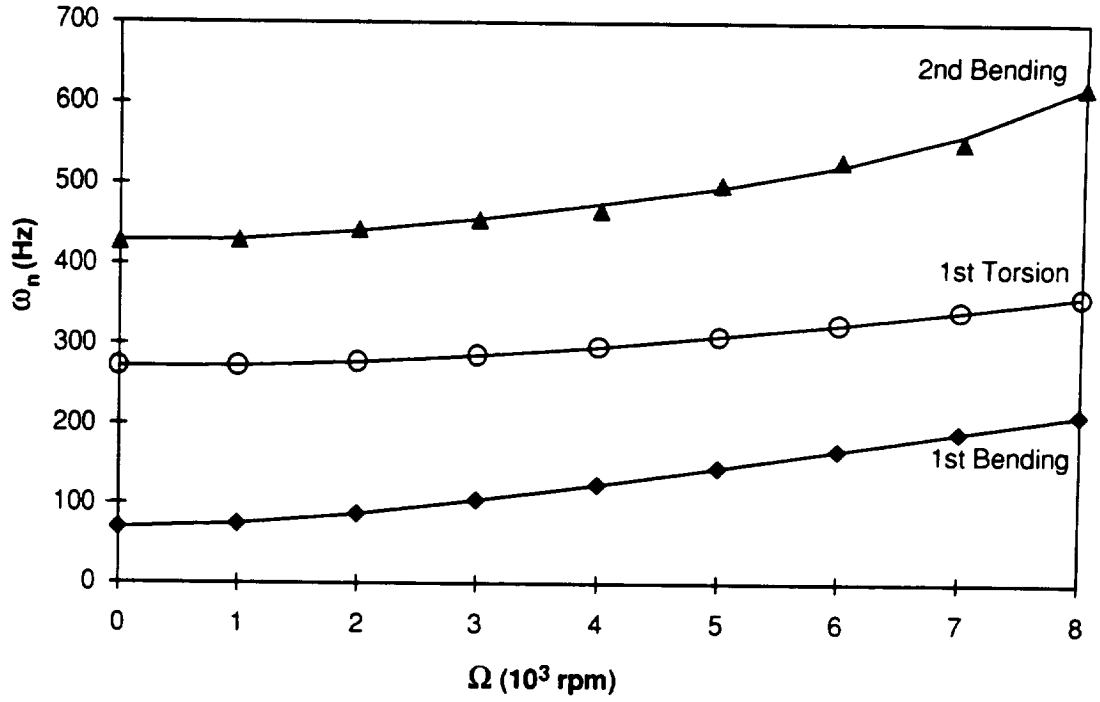

Figure 4.9: The measured natural frequencies vs. the rotational speed for Plate 11.

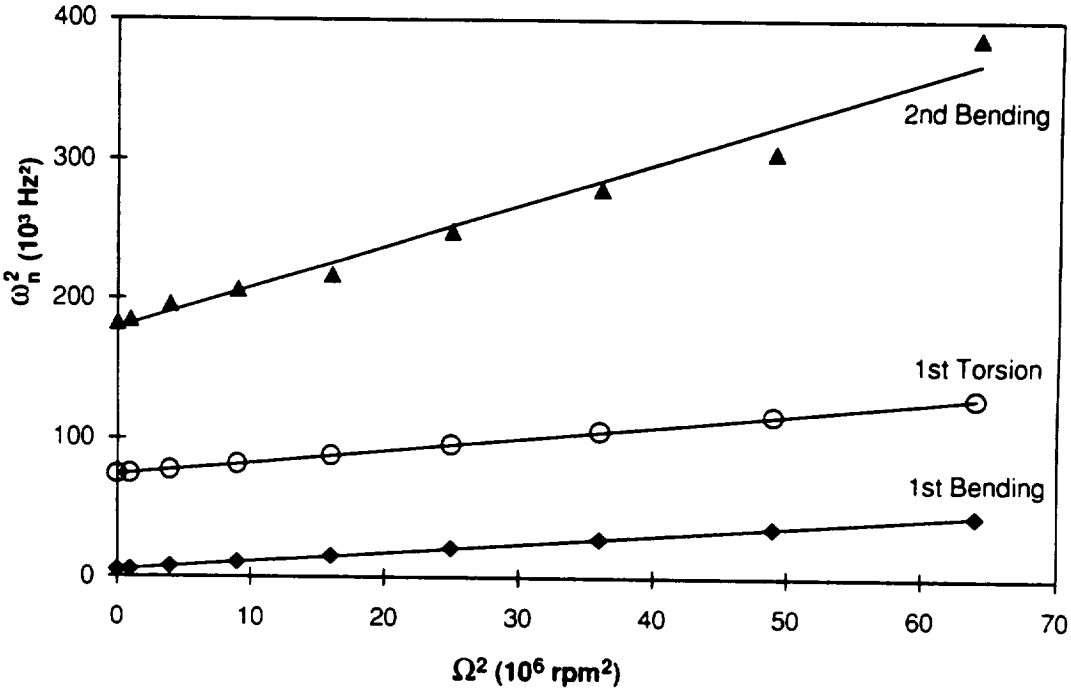

Figure 4.10: Least squares fit of the square of the natural frequency vs. the square of the rotational speed for Plate 11.

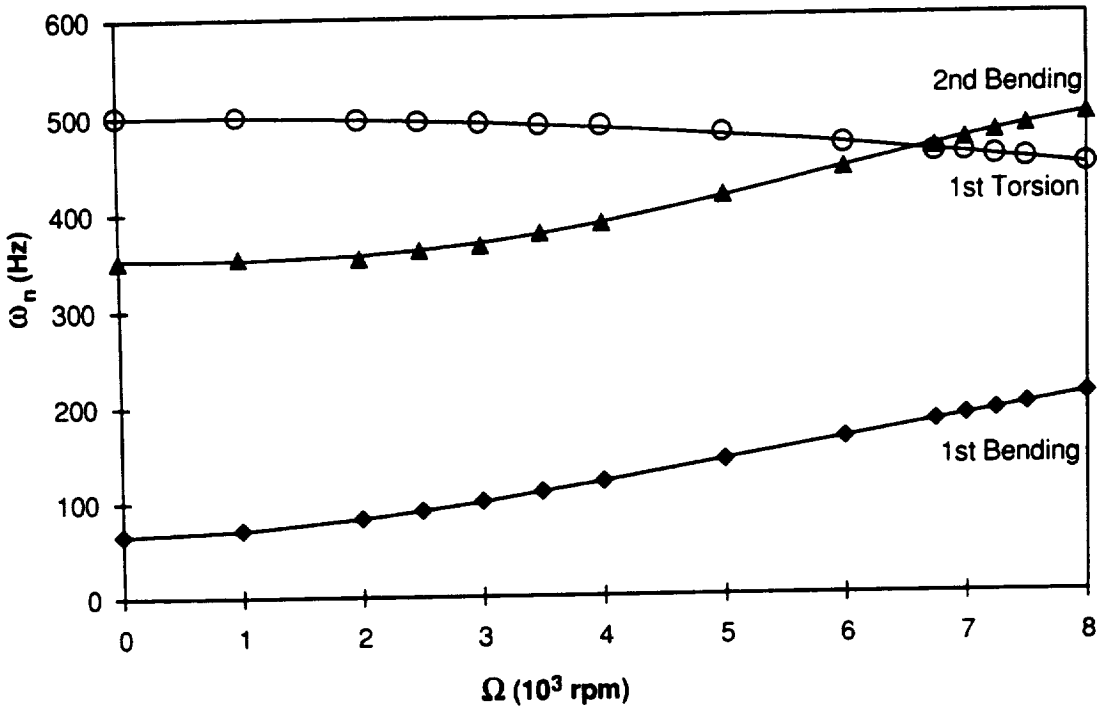

Figure 4.11: The measured natural frequencies vs. the rotational speed for Plate 21.

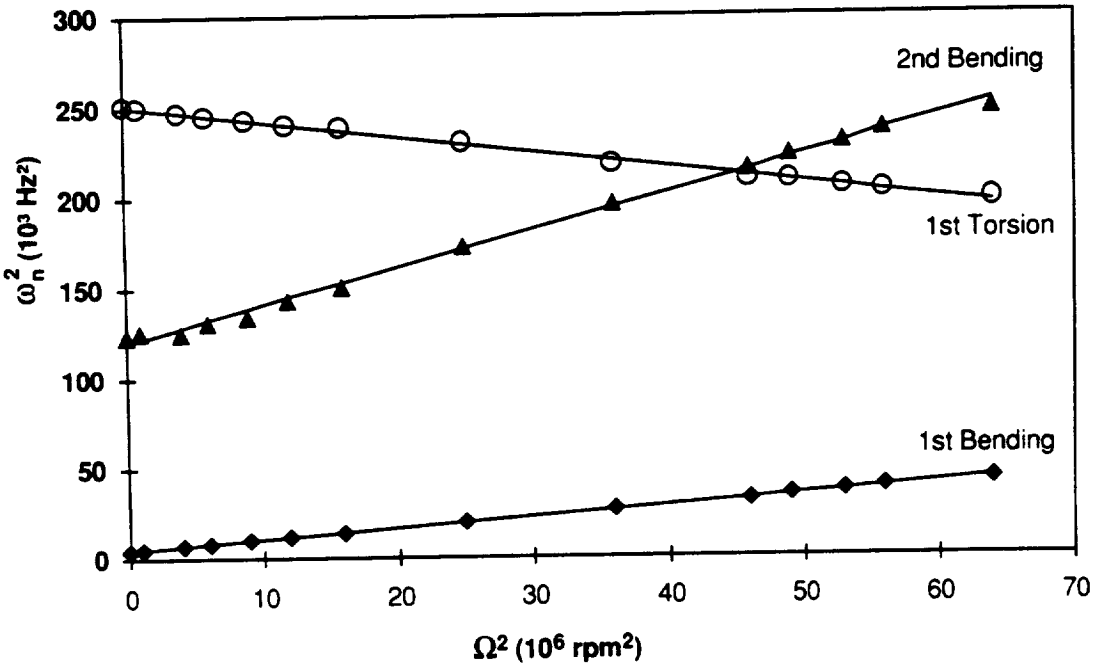

Figure 4.12: Least squares fit of the square of the natural frequency vs. the square of the rotational speed for Plate 21.

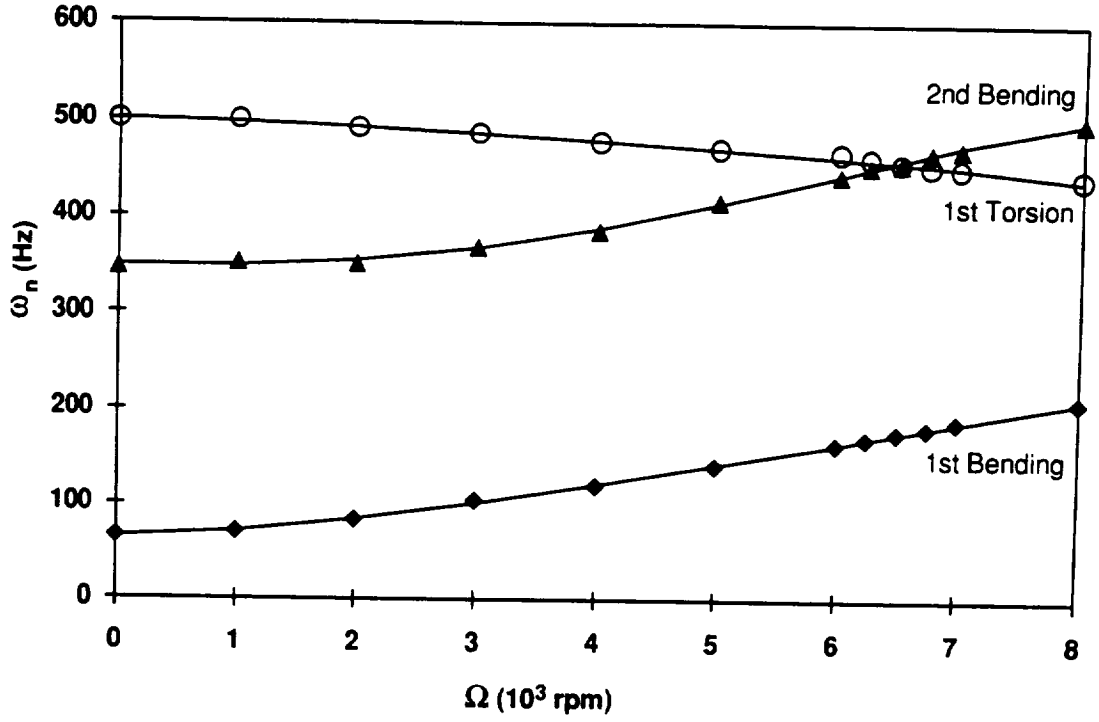

Figure 4.13: The measured natural frequencies vs. rotational speed for Plate 31.

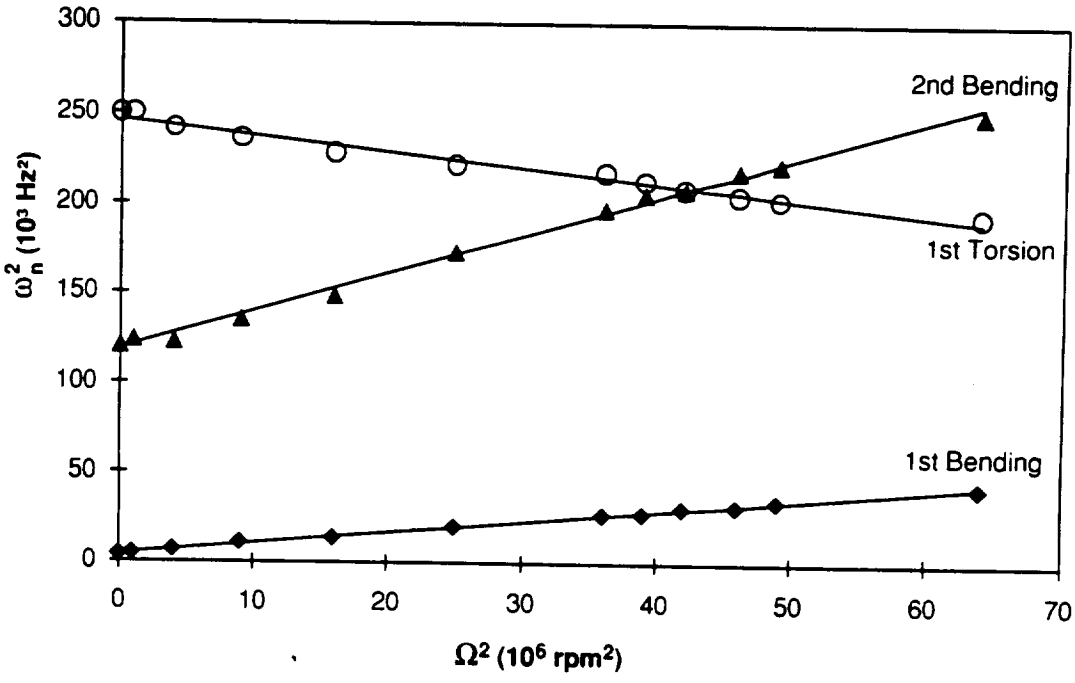

Figure 4.14: Least squares fit of the square of the natural frequency vs. the square of the rotational speed for Plate 31.

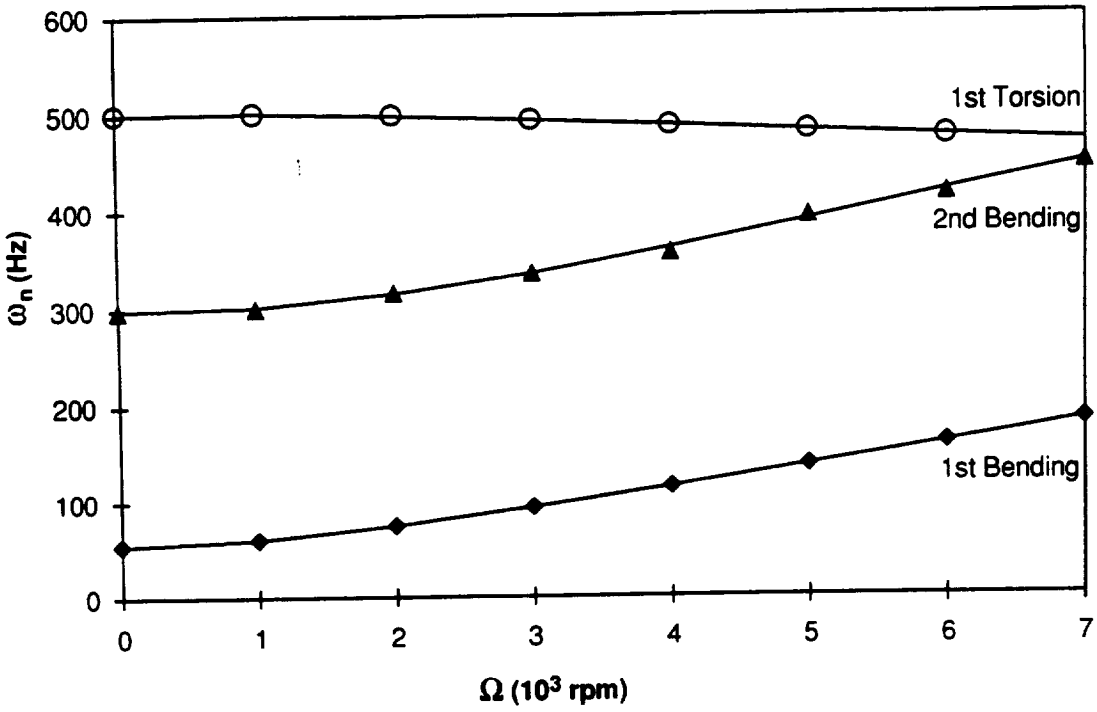

Figure 4.15: The natural frequency vs. ¹e rotational speed for Plate 32.

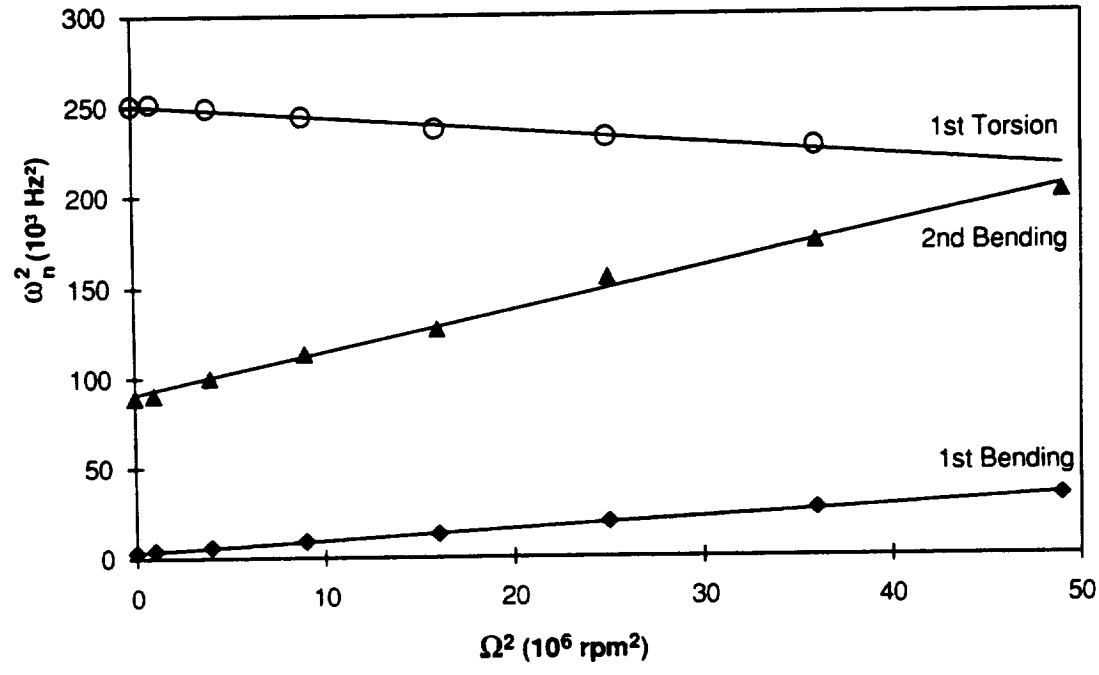

Figure 4.16: Least squares fit of the square of the natural frequency vs. the square of the rotational speed for Plate 32.

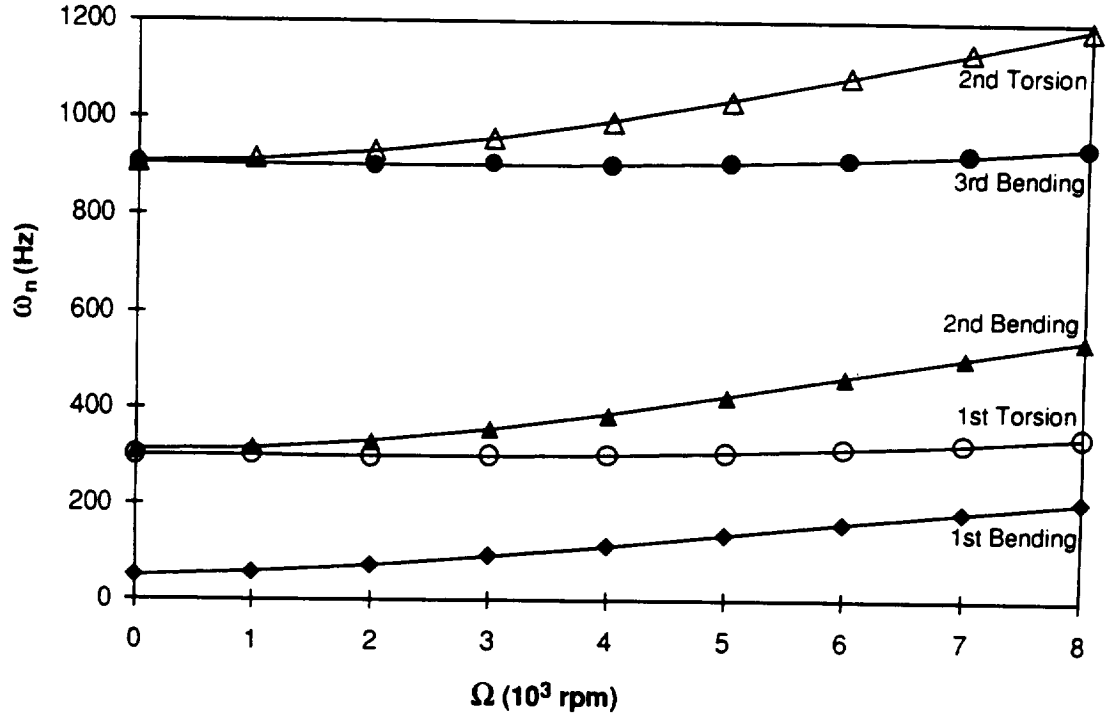

Figure 4.17: The natural frequency vs. the rotational speed for Plate 13.

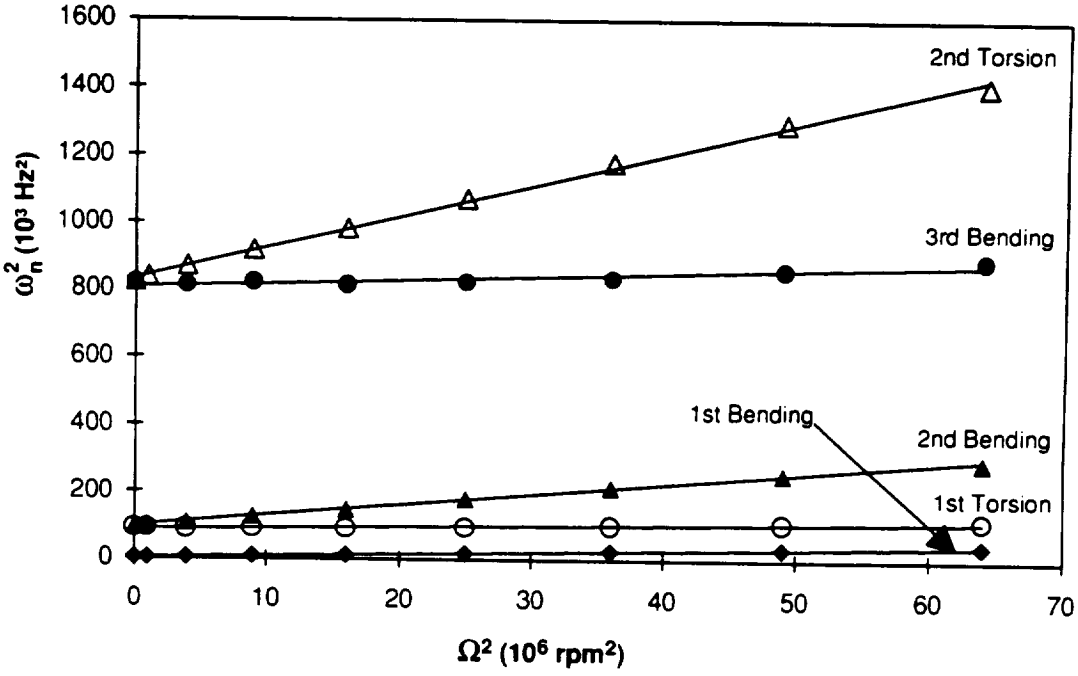

Figure 4.18: Least squares fit of the square of the natural frequency vs. the square of the rotational speed for Plate 13.

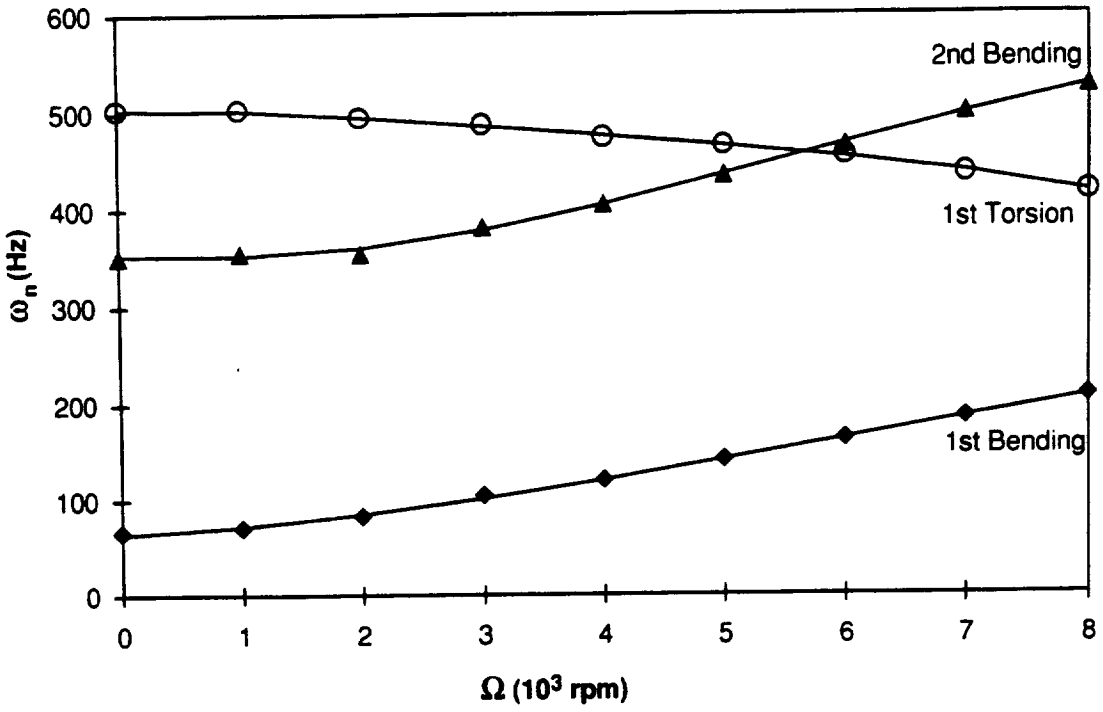

Figure 4.19: The natural frequency vs. the rotational speed for Plate 23*.

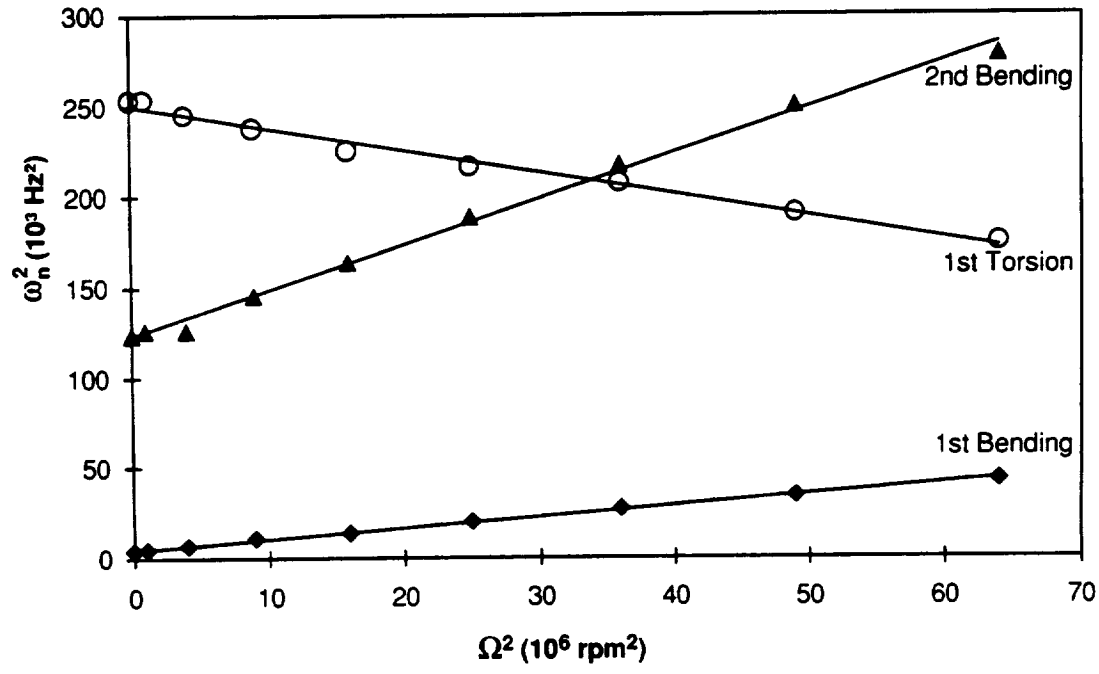

Figure 4.20: Least squares fit of the square of the natural frequency vs. the square of the rotational speed for Plate 23*.

4.2.7 Rotating Vibrations Comparisons and Discussions

This section presents a discussion and comparison study of the experimentally measured rotating vibration frequencies. The plates for the rotating vibration study are spun with pitch and sweep angles of $\beta_p = 90°$ and $\beta_s = 0°$, respectively. The tables and graphs for this section are presented at the end (pp. 151–154). Tables 4.19 and 4.20 (p. 151) summarizes the experimentally determined Southwell coefficients and the linear correlation coefficients, respectively, from the rotating plates. For the fundamental frequency, the correlation coefficient is 1.00 for all of the plates. The linearity of Equation (4.4) breaks down for the higher modes because of shear deformation effects.

The only type of vibratory behavior due to rotation that should be observed for the flat plates is an increase in the natural frequencies with increasing speed due to the centrifugal loading. This is observed experimentally for this plate set in Figure 4.9. The first comparison begins with the flat and pre-twisted, mid-chord plates with lay-up 1 (Plates 11 and 21). Figure 4.21 (p. 152) depicts the comparisons between the 1st Bending, 2nd Bending, and 1st Torsion frequencies between the two plates. The first bending mode rises with the rotational speed, and the flat plate frequencies are higher than the pre-twisted one. This is caused by the bending-torsion coupling of the pre-twisted geometry that raises the torsion frequencies and lowers the bending ones. Due to the geometry coupling, the centrifugal stiffening for the first bending mode is greater for the flat plate than the pre-twisted one.

The most obvious observation for the 1st Torsion mode is the fact that this frequency decreases with the rotational speed for the pre-twisted plate (Figure 4.21, p. 152). The bending-torsion coupling caused by the pre-twisted geometry causes the plate to be significantly stiffer in torsion at 0 rpm. Upon rotation the flat plate frequency for the 1st Torsion mode increases while the pre-twisted one decreases. The rates of increase and decrease can be quantified by the Southwell coefficients listed in Table 4.19,

and it can be seen that the coefficient decreases from 0.88 to -0.85 with a 30° pre-twist. This suggests the existence of an intermediate pre-twist angle that will cause the plate to have a constant 1st Torsion frequency with increasing speed. This assumes, however, that the Southwell equation (4.4) is true. It is shown that for the 2nd Bending mode the linear correlation coefficient, r^2, decreases (Table 4.20), which means the Southwell equation begins to break down because it does not take into account the shear deformation. The drop in the torsion frequency is attributed to the geometric untwisting of the plate. If the plate untwists completely to a flat plate, then the geometric coupling of the extension-bending-torsion behavior is eliminated. Thus, the torsion frequency may indeed begin to rise due to the centrifugal stiffening. Previous experimental results for a spinning, flat, steel plate with an aspect ratio (l/c) of 3 and a thickness ratio (c/t) of 20 show the 1st Torsion frequency to remain nearly constant with increasing speed [11, 14]. Similarly, for a 90° pre-twisted plate with an aspect ratio (l/c) of 2.175 and a thickness ratio (c/t) of 20, it is shown that the first four natural frequencies increase with the rotational speed [6]. The increase or decrease in the 1st Torsion frequency clearly depends on the pre-twist geometry and material properties.

For the 2nd Bending mode, the introduction of pre-twist for lay-up 1 causes a drop in the bending frequency at 0 rpm, and the frequency increases with the rotational speed. As can be seen from Figure 4.21 and the Southwell coefficients listed in Table 4.19, the curves for the flat and pre-twisted plate diverge at higher rotational speeds. Like the behavior for the 1st Torsion mode the Southwell coefficient decreases with pre-twist because of the extension-bending-torsion coupling. Further experimental or analytical studies of larger pre-twist angles are needed to see if the Southwell coefficient for the 2nd Bending mode can be made to go to zero or even negative.

The next comparison discusses the effect of the pre-twist axis location. As discussed in the results for the rotating, steady-state strains and displacement section, the

quarter-chord plate first deflects and bends as well as axially stretches with an increase in the rotational speed. This is important to remember because this type of behavior will affect the vibrational properties of the plate. Figure 4.22 (p. 152) is a plot of the first three natural frequencies versus the rotational speed for the mid-chord and quarter-chord plate with lay-up 1. The 1st Bending mode increases with rotational speed and there is very little difference between the two plates. The Southwell coefficient for both these plates is 0.61 for the two geometries.

For the 1st Torsion mode one can see that the frequency decreases with the rotational speed for both plates. From the non-rotating vibrations section the placing of the pre-twist axis farther away from the mid-chord lessens the effect of the bending-torsion coupling due to the pre-twist, and this leads to an increase in the bending modes and a decrease in the torsion ones. The experimental first torsion frequencies for the quarter-chord plate are lower than the mid-chord one (Figure 4.22), but the rate of decrease is higher for the quarter-chord, -0.85 for the mid-chord and -0.87 for the quarter-chord (Table 4.19). Similarly, the Southwell coefficients for the 2nd Bending mode are 2.07 and 2.13 for the mid-chord and quarter-chord plates, respectively. The absolute increase in the coefficients is due to the fact that the quarter-chord plate is also bending as well as axially extending with the increasing rotational speed.

Figure 4.23 (p. 153) compares the two symmetric lay-ups for the pre-twisted, quarter-chord plates. As noted in the non-rotating vibrations section, lay-up 2 is shown to have lower bending and higher torsion frequencies; this is also true for the rotating natural frequencies (Figure 4.23). The ply stacking sequence would also affect the Southwell coefficients. Lay-up 2 is shown to be stiffer in torsion than lay-up 1 and therefore should have a lower absolute Southwell coefficient for the torsion modes. Experimentally, the Southwell coefficients for the 1st Torsion mode are -0.87 and -0.72 for lay-ups 1 and 2, respectively. Similarly, lay-up 2 is also softer in bending than the first lay-up and so it

should have a higher absolute Southwell coefficient for the bending modes. For the 2nd Bending mode the experimentally measured values are 2.13 and 2.33 for lay-ups 1 and 2, respectively.

It is shown in the non-rotating vibration sections that the asymmetric lay-up also introduces extension-bending-torsion coupling that causes an increase in the torsion frequencies and a decrease in the bending ones. Furthermore, since the plates are under the influence of centrifugal forces, there is also extension-twist coupling for the asymmetric lay-up. The twisting of the flat, asymmetric plate under centrifugal loading will introduce further bending-torsion coupling causing the plate to be stiffer torsionally at higher speeds and softer in bending. Figure 4.24 (p. 153) is a graph of the first three natural frequencies for the flat plates with lay-ups 1 and 3. For the 1st Bending mode, the Southwell coefficient for both plates is 0.63 (Table 4.19). For the 1st Torsion mode, the natural frequency for the asymmetric lay-up 3 increases at a lower rate than the one for the symmetric lay-up, 0.40 for lay-up 3 versus 0.88 for lay-up 1 (Table 4.19). The twisting of the plate is causing bending-torsion coupling that causes the absolute decrease in the Southwell coefficient for the 1st Torsion mode of the asymmetric lay-up. Likewise, the Southwell coefficient for the 2nd Bending mode increases for the asymmetric lay-up, 2.96 for lay-up 1 to 3.17 for lay-up 3.

The final comparison is the effect the asymmetric laminate has on the pre-twisted plates. Before making any comparisons it must be remembered that the centrifugal axial forces on the plate cause it to untwist. Furthermore, the asymmetric stacking sequence has extension-twist coupling where the selection of the ply angle can cause the plate to twist clockwise or counter-clockwise. Therefore, a pre-twisted composite plate with an asymmetric lay-up can be fabricated to produce twisting at a faster or slower rate by having the ply related twist work with or against the geometric related untwist. The experimental results from the steady-state, rotating deflections show that the pre-twisted,

asymmetric laminate untwists more than the symmetric one. This implies reduced bending-torsion coupling at higher rotational speeds that leads to lower torsion frequencies and higher bending ones. Figure 4.25 (p. 154) is a graphical comparison of the first three natural frequencies for the pre-twisted plates about the mid-chord with lay-ups 1 and 3*. The figure shows that the asymmetric laminate does have lower 1st Torsion frequencies and a higher 2nd Bending one at the higher rotational speeds; there is no measurable difference between the 1st Bending mode. Furthermore, because the asymmetric plate untwists at a greater rate, the absolute Southwell coefficients for the asymmetric plate are greater for the asymmetric plate, -1.21 (asymmetric) versus -0.87 (symmetric) for the 1st Torsion mode and 2.52 (asymmetric) versus 2.13 (symmetric) for the 2nd Bending mode.

Table 4.19: The experimentally measured Southwell coefficients (S), $\left(10^3 \times Hz^2/rpm^2\right)$.

Mode	Plate Description					
	Plate 11	Plate 21	Plate 31	Plate 32	Plate 13	Plate 23*
1st Bending	0.63	0.61	0.61	0.62	0.63	0.61
First Torsion	0.88	-0.85	-0.87	-0.72	0.40	-1.21
2nd Bending	2.96	2.07	2.13	2.33	3.17	2.52
3rd Bending	–	–	–	–	1.08	–
2nd Torsion	–	–	–	–	9.26	–

Table 4.20: The linear correlation coefficients, r^2.

Mode	Plate Description					
	Plate 11	Plate 21	Plate 31	Plate 32	Plate 13	Plate 23*
1st Bending	1.00	1.00	1.00	1.00	1.00	1.00
First Torsion	1.00	1.00	0.98	0.98	0.92	0.99
2nd Bending	0.98	1.00	1.00	0.99	1.00	1.00
3rd Bending	–	–	–	–	0.87	–
2nd Torsion	–	–	–	–	1.00	–

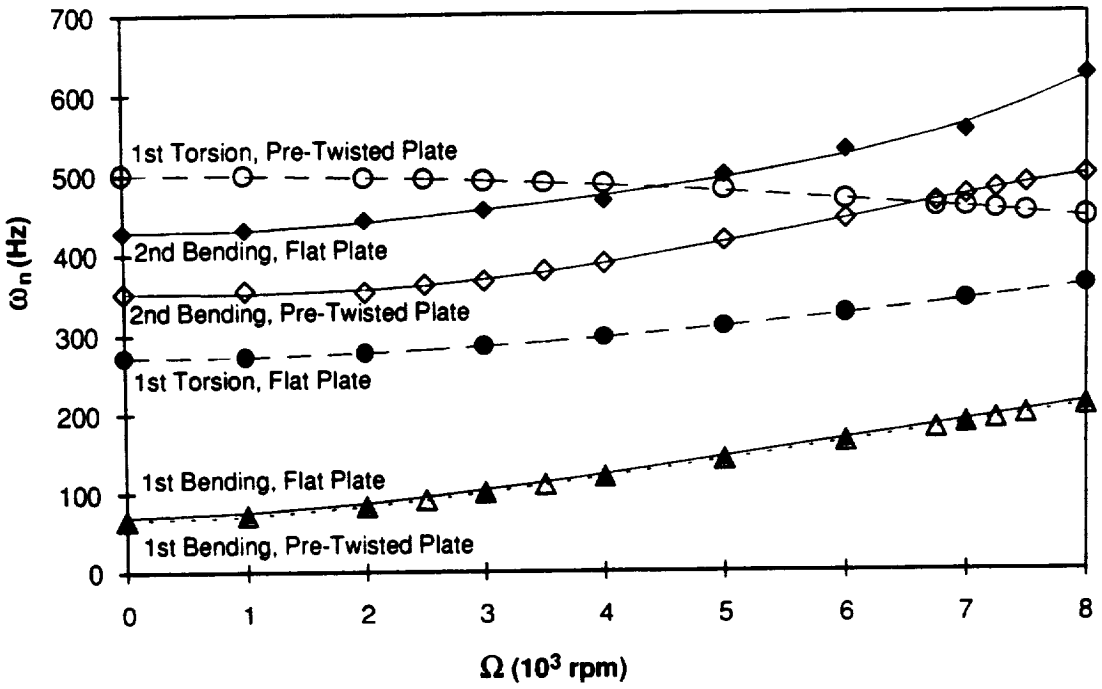

Figure 4.21: Geometry comparisons of the rotating vibration modes between Plates 11 and 21.

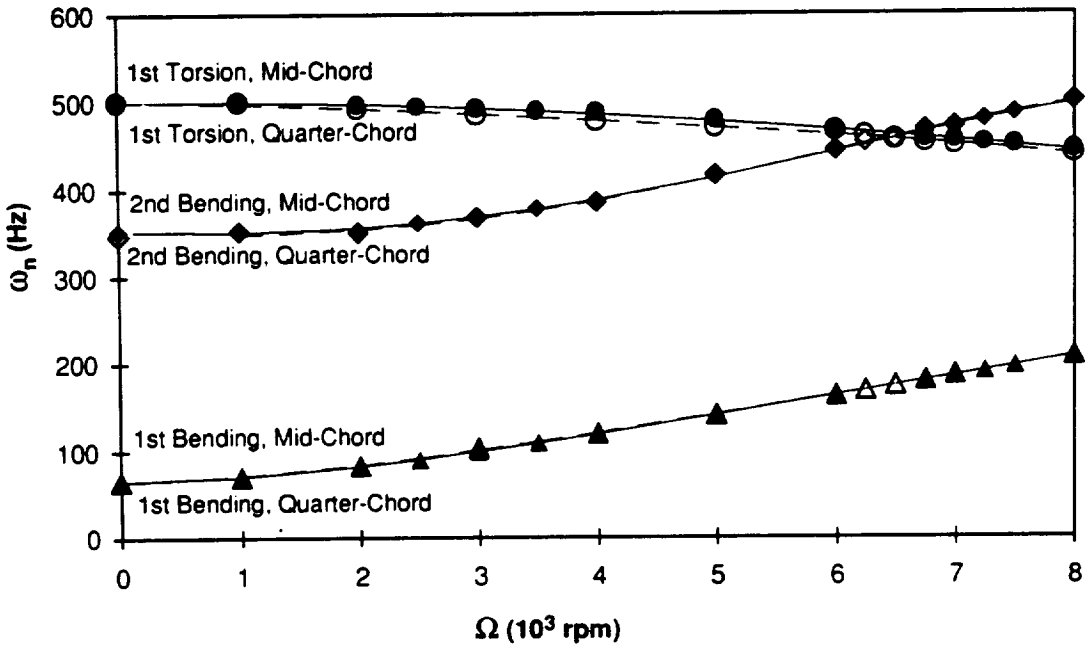

Figure 4.22: Geometry comparisons of the rotating vibration modes between Plates 21 and 31.

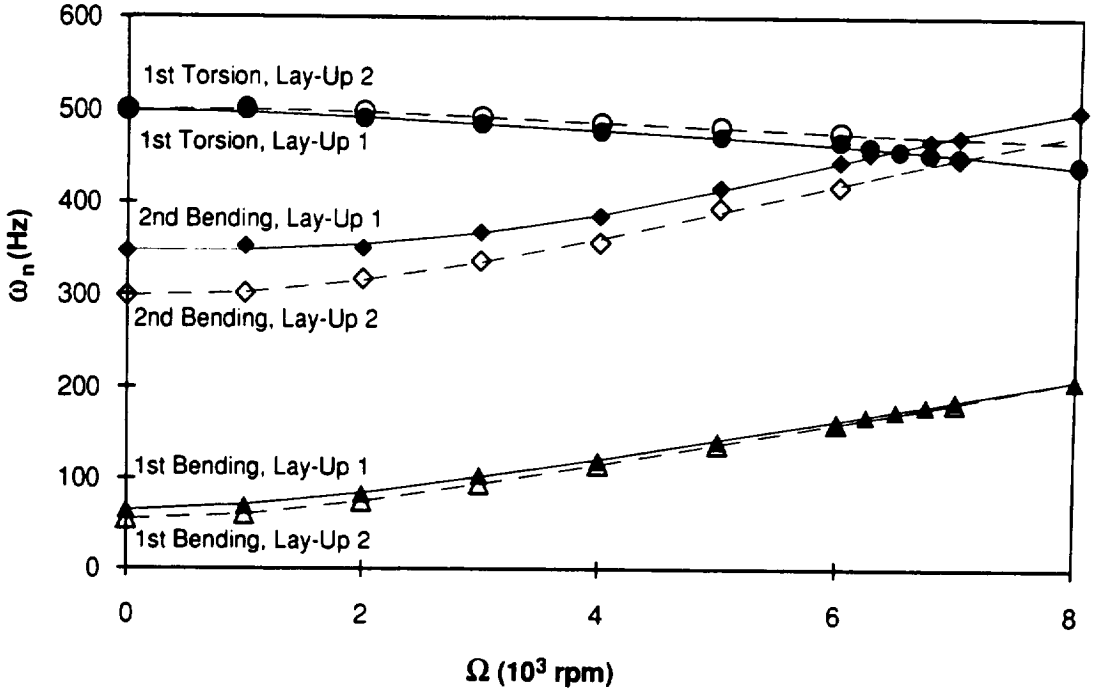

Figure 4.23: Lay-up comparisons of the rotating vibration modes between Plates 31 and 32.

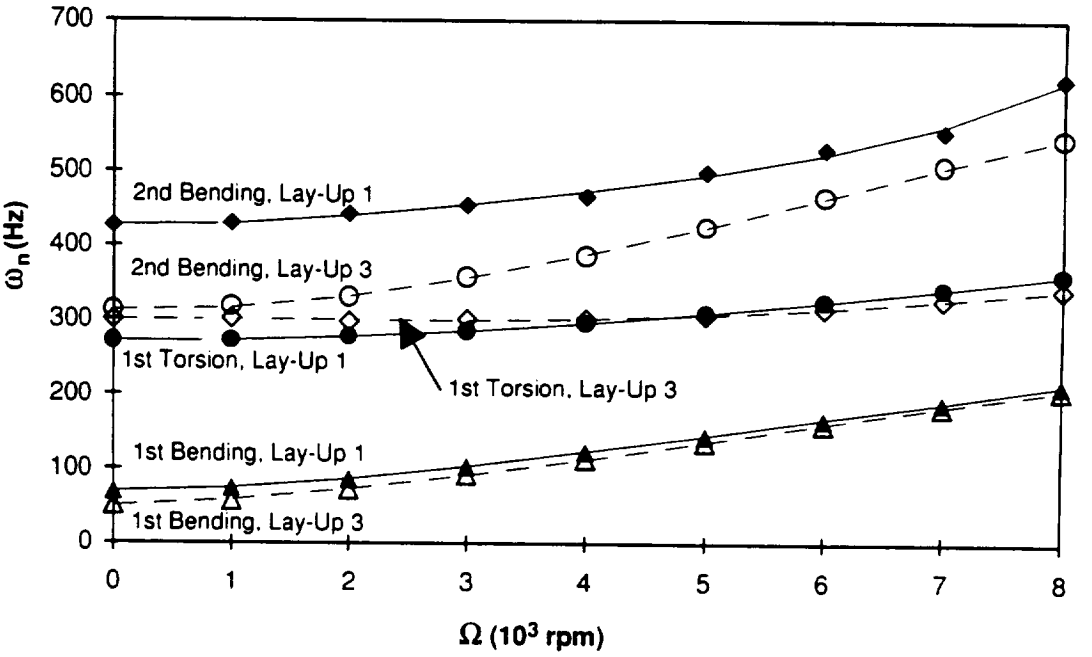

Figure 4.24: Lay-up comparisons of the rotating vibration modes between Plates 11 and 13.

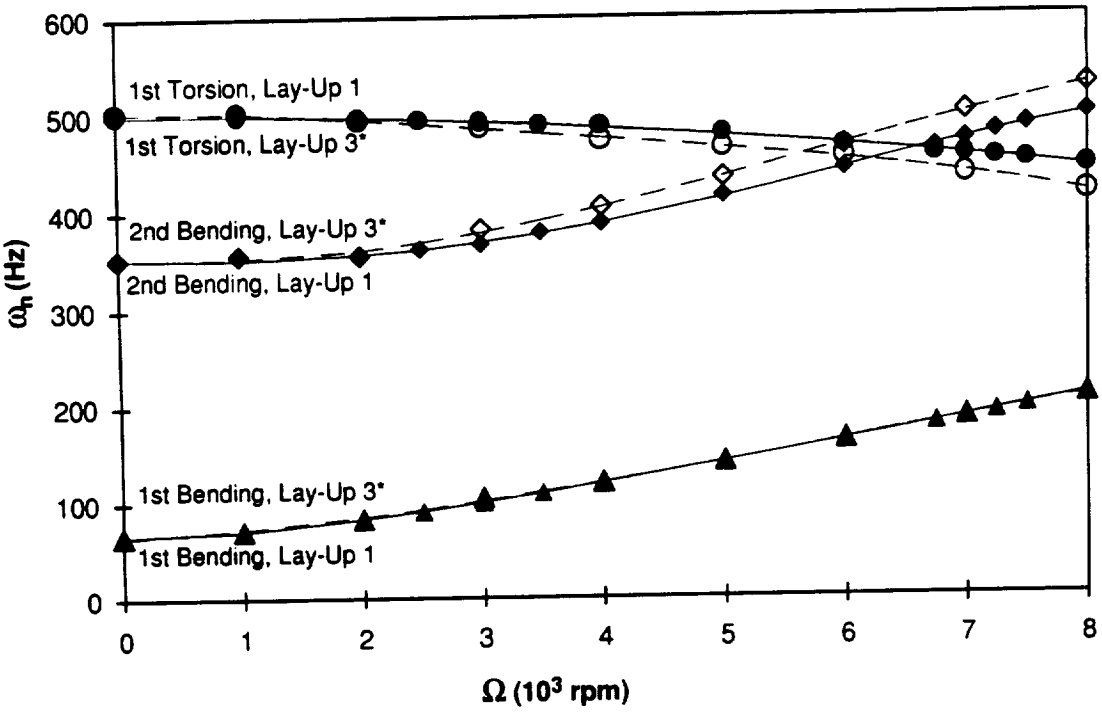

Figure 4.25: Lay-up comparison of the rotating vibration modes between Plates 21 and 23*.

Chapter 5

Conclusions

An extensive experimental database on the behavior of spinning, pre-twisted composite plates has been collected. Twelve graphite/epoxy plates were manufactured and tested. The plates embodied four different geometries (1 flat plate and 3 pre-twisted plate geometries) and three different lay-ups. Four tests were performed on the plates: (1) static displacement and strain; (2) rotating displacement and strain; (3) non-rotating modal tests; and (4) rotating vibration tests. The following sections summarize the results from the four tests.

5.1 Static Displacement and Strain

Three load cases were modeled on the finite element package I–DEAS: (1) a transverse load at the tip; (2) an axial load at the tip; and (3) and a bending-moment at the tip in the axial direction. Experimental tests were also performed on the plates and were summarized in Appendix B.

Transverse Load.

- The deflections due to the loading decrease as the flat plate is given an initial pre-twist, which is caused by the geometric coupling introduced by the pre-twisted geometry.
- The geometric coupling plays a larger role in the twist of the plate than the lay-up.
- As the pre-twist axis moves from the mid-chord to the leading edge, the deflections for all three materials increase and the twist decreases because of the location of the load relative to the pre-twist axis.

Axial Load.

- All of the pre-twisted plate geometries untwist due to the loading.
- There are non-zero deflections for the quarter-chord and leading edge geometries due to the geometric asymmetry.
- Only the flat plate with lay-up 3 has a non-zero twist caused by the extension-twist coupling of the asymmetric lay-up.

Torsion Moment.

- For the flat plate, only lay-up 1 is shown to have any deflections due to the moment, which is caused by the bend-twist coupling of the laminate.
- There is a large decrease in the twist as the plate goes from a flat to a pre-twisted plate, which is due to the geometric coupling that makes the pre-twisted plate torsionally stiffer.

5.2 Rotating Displacement and Strain

Six of the twelve plate sets were spin tested at the vacuum spin rig facility at the NASA Lewis Research Center. They were tested in three configurations to investigate the effects of pitch and sweep.

Configurations A and B: 0° and 30° pitch, 0° sweep.

- There is little difference in the plate behavior due to the pitch.
- In spite of the material extension-bend coupling of lay-up 1, there is little or no deflection for the flat and mid-chord plates.
- The centrifugal forces cause the pre-twisted plates to untwist.
- For the same lay-up, the extension-twist coupling causes the pre-twisted plates to undergo more axial straining than the flat plate.
- The geometric asymmetry of the quarter-chord geometry causes this plate to axially extend and deflect. The deflections level off at the higher rotational speeds.
- Lay-up 2, which has ±45° off-angle plies, is shown to have higher deflections and axial strains than lay-up 1, which has ±22.5° off-angle plies.

- The pre-twisted plate with the asymmetric stacking sequence is shown to work together to cause the plate to untwist due to the centrifugal loading. Another possible test would be to reverse the angles of the plies so that the material extension-twist coupling would resist the centrifugal untwisting.
- The asymmetric lay-up is shown to have higher axial straining than the symmetric lay-up because of the material extension-twist coupling. Adding pre-twist also works to increase the axial straining.

Configuration C: 0° pitch, 22.5° sweep.

- The centrifugal forces cause the pre-twisted plates to undergo large deflections and increased twisting. As the rotational speed increases, the axial extension of the plate that causes the untwisting to dominate, and the twisting due to the sweep angle levels off.
- The location of the quarter-chord axis causes the plates to deflect even more in this configuration. Because of the sweep configuration of the plate, a pre-twisted plate with a $\frac{3}{4}$–chord geometry would counteract the deflection caused by the sweep angle.

5.3 Non-Rotating Vibrations

Modal tests were conducted on all 12 plate sets using an impact hammer technique and laser holography. The following observations were made from the tests:

- The pre-twist and the pre-twist axis location have a negligible effect on the 1st Bending frequency.
- There is a decrease in the bending modes and an increase in the torsion modes upon the introduction of pre-twist. The 2nd Bending and 1st Torsion modes cross as the pre-twist angle increases, and likewise for the 3rd Bending and 2nd Torsion modes for lay-up 1. This is due to the extension-bend-twist coupling of the pre-twisted geometry.

- As the pre-twist axis moves from the mid-chord to the leading edge, the torsion frequencies decrease. This is because the effects of the geometry coupling caused by the pre-twist are lessened as the pre-twist axis moves farther away from the mid-chord.
- There is a small difference between the first torsion mode of the pre-twisted plates of lay-ups 1 and 2. This shows that a greater increase in torsional stiffness can be gained through the coupling due to the geometry rather than the lay-up.
- The asymmetric lay-up makes the plate softer in bending because of the material coupling.
- There is a decrease in the chordwise frequency as the plate is pre-twisted. As the pre-twist axis moves towards the leading edge the effect of the pre-twist decreases and the chordwise frequencies rise.
- Lay-up 2 is stiffer for the chordwise modes than lay-up 2 because of the fiber orientation.

5.4 Rotating Vibrations

Six of the twelve plate sets were spin tested at the Dynamic Spin Rig Facility.

- For the flat plate geometry, there is a rise in the first three natural frequencies with the rotational speed.
- The Southwell equation, which states a linear relationship between the square of the rotational speed and the square of the natural frequency, breaks down for the higher bending modes. This is because the equation does not take into account the shear deformation of the plate, which becomes more important at these frequencies.
- For the pre-twisted plates, the bending modes increase with the rotational speed while the 1st Torsion mode decreases. The 2nd Bending and 1st Torsion frequencies cross at a higher rotational speed. The behavior is attributed to the plate untwisting. The decrease in the torsion frequency is tempered by the

centrifugal stiffening. As the plate untwists the geometry coupling is reduced, which implies that the torsion frequency will level off at higher rotational speeds. Previous results on pre-twisted isotropic plates show an increase in the torsion frequency with the rotational speed, which clearly shows a dependence of the torsion frequency on the geometry and material coupling.

- For the pre-twisted plate with lay-up 2, the 1st Torsion and 2nd Bending modes converge towards one another, but no frequency crossing is observed for this plate. Both the lay-up and geometry serve to increase the frequency difference between the two modes.
- For a flat plate with an asymmetric laminate, the centrifugal loading causes the plate to twist. Both the geometry and material coupling cause the torsion frequencies to rise faster than the bending modes. This behavior is also observed for a pre-twisted plate. The asymmetric laminate, however, can be aligned such that it resists the twisting caused by the pre-twisted geometry.

Appendix A

Geometry Measurements

This Appendix presents the measurement results of the graphite/epoxy plates. Figure A.1 is a physical description of the geometry as well as labels for the strain gagtes. Tables A.1, A.2, and A.3 list the measured geometric parameters of all the plates with lay-ups 1, 2, and 3, respectively.

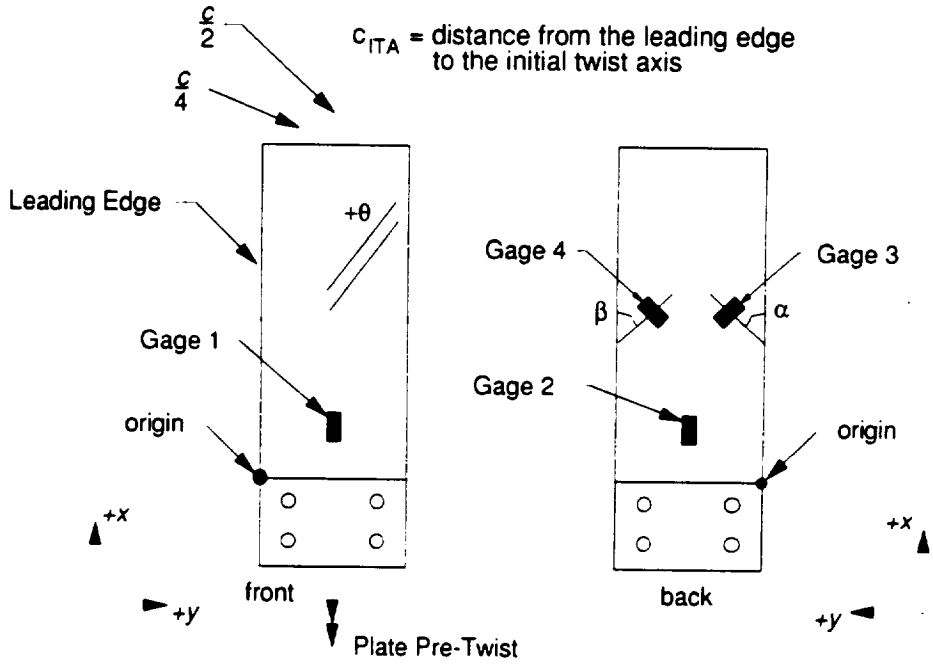

Figure A.1: Pre-twist geometry and strain gage locations.

Table A.1: Geometry measurements for plates with $[\pm 22.5/0_2/-22.5/0_2/+22.5/0_2]_S$.

Plate	Flat Plate		Mid-Chord		Quarter-Chord		Leading Edge	
	A	B	A	B	A	B	A	B
l (inch)	9.000	8.997	9.191	9.224	9.183	9.222	9.232	9.131
t (inch)	0.104	0.103	0.103	0.100	0.102	0.102	0.100	0.100
c_{root}	2.995	2.995	3.033	3.044	3.033	3.023	3.047	3.049
c_{tip}	2.995	2.995	2.984	3.008	3.018	3.032	3.003	2.992
ϕ (degrees)	0.000	0.000	30.41	30.13	29.23	29.55	29.53	29.61
$\frac{c_{ITA\ (root)}}{c}$	0.000	0.000	0.505	0.494	0.231	0.243	0.035	0.053
$\frac{c_{ITA\ (tip)}}{c}$	0.000	0.000	0.519	0.528	0.269	0.251	0.035	0.051

Table A.2: Geometry measurements for plates with $[\pm 45/0_2/-45/0_2/+45/0_2]_S$.

Plate	Flat Plate		Mid-Chord		Quarter-Chord		Leading Edge	
	A	B	A	B	A	B	A	B
l (inch)	8.998	9.000	9.175	9.135	9.162	9.200	9.201	9.221
t (inch)	0.100	0.100	0.100	0.100	0.102	0.102	0.100	0.100
c_{root}	2.997	2.997	3.030	3.026	3.057	3.033	3.040	3.043
c_{tip}	2.997	2.997	2.996	3.023	2.972	3.017	2.988	3.002
ϕ (degrees)	0.000	0.000	30.19	30.17	29.61	29.54	29.35	29.38
$\frac{c_{ITA\ (root)}}{c}$	0.000	0.000	0.474	0.472	0.242	0.247	0.062	0.066
$\frac{c_{ITA\ (tip)}}{c}$	0.000	0.000	0.502	0.505	0.293	0.279	0.066	0.069

Table A.3: Geometry measurements for plates with $[\pm 22.5_5/0_5]_A$.

Plate	Flat Plate		Mid-Chord*		Quarter-Chord*		Leading Edge*	
	A	B	A	B	A	B	A	B
l (inch)	9.046	8.998	9.171	9.150	9.154	9.151	9.154	9.166
t (inch)	0.099	0.098	0.104	0.102	0.103	0.103	0.100	0.100
c_{root}	3.038	3.028	3.058	3.040	3.058	3.062	3.042	3.042
c_{tip}	3.021	3.002	2.994	2.993	3.005	2.980	2.971	3.003
ϕ (degrees)	11.51	11.71	33.06	33.20	32.58	32.69	32.74	32.32
$\frac{c_{ITA\ (root)}}{c}$	0.510	0.489	0.477	0.476	0.298	0.272	0.084	0.064
$\frac{c_{ITA\ (tip)}}{c}$	0.510	0.489	0.477	0.476	0.298	0.272	0.084	0.064

*The lay-up for this plate is $[0_2/+22.5_2/0_2/+22.5_3/0]_A$

Table A.4: Strain gage locations for Plates 11, 21, and 31.

Plate	11A	11B	21A	21B	31A	31B
Gage 1						
x (inch)	0.9694	0.9463	0.9599	0.9285	0.9409	0.9659
y (inch)	1.4426	1.4572	1.4178	1.4822	1.4718	1.4745
Gage 2						
x (inch)	0.7848	0.9661	0.9727	0.9502	1.0435	0.9707
y (inch)	1.5452	1.4353	1.4214	1.4867	1.4597	1.4647
Gage 3						
x (inch)	4.4644	4.4566	4.4814	4.4255	4.5031	4.4828
y (inch)	0.7948	0.8033	0.7161	0.7363	0.6756	0.7336
α (degrees)	43.0	44.0	44.0	47.5	47.0	45.5
Gage 4						
x (inch)	4.4643	4.5062	4.4683	4.4282	4.5033	4.4571
y (inch)	2.0535	2.1318	2.2019	2.2031	2.1900	2.2063
β (degrees)	46.0	45.0	46.0	45.0	43.0	46.0

Table A.5: Strain gage locations for Plates 32, 13, and 23*.

Plate	32A	32B	13A	13B	23*A	23*B
Gage 1						
x (inch)	0.9760	0.9697	0.9663	0.9314	0.9861	0.9790
y (inch)	1.4287	1.4589	1.4444	1.4480	1.4525	1.4734
Gage 2						
x (inch)	1.0225	0.9536	0.9801	0.9636	0.9529	1.0407
y (inch)	1.4665	1.4879	1.4585	1.4576	1.4678	1.4491
Gage 3						
x (inch)	4.4890	4.4691	4.4561	4.4318	4.4136	4.4749
y (inch)	0.7811	0.8516	0.8338	0.8441	0.8313	0.8674
α (degrees)	44.0	45.0	44.0	46.0	45.5	47.5
Gage 4						
x (inch)	4.5157	4.4521	4.4439	4.4326	4.4214	4.4744
y (inch)	2.0185	2.0783	2.1104	2.0977	2.0659	2.0610
β (degrees)	46.0	46.5	46.0	47.0	45.0	45.0

Appendix B

Experimental Strain and Displacement Results

This Appendix lists the results from the experimental strain and displacement results. The measured data is compared with analytical models generated using the finite element package I-DEAS. Table B.1 is a summary of the plate descriptions and serial numbers from Chapter 2. The serial number is a two digit number followed by a letter where the first and second digits refer to the geometry type and lay-up, respectively.

Table B.1: Plate Serial Numbers. The first digit refers to the geometry and the second is the lay-up.

Geometry \ Lay-up	1. $\theta = 22.5°$	2. $\theta = 45°$	3. $[(+22.5)_5/\overline{0_5}]_A$
1. Flat	11	12	13
2. 30° Pre-Twist about the Mid-Chord	21	22	23*
3. 30° Pre-Twist about the Quarter-Chord	31	32	33*
4. 30° Pre-Twist about the Leading Edge	41	42	43*

For the first two lay-ups the stacking sequence is $[\pm\theta/0_2/-\theta/0_2/+\theta/0_2]_S$

*The lay-up for this plate is $[0_2/+22.5_2/0_2/+22.5_3/0]_A$

Aspect Ratio, $c/l = 3$
Thickness Ratio, $c/t = 30$

Figure B.1 shows the plate setup for the experiment. The displacements of points A and B due to a tip load at point A are measured. The deflection, D, and twist, ψ, are defined by equations B.1 and B.2 (Section 2.3.2)

$$D = \frac{z_A + z_B}{2} \tag{B.1}$$

and

$$\psi = \arcsin\left(\frac{z_A + z_B}{c}\right). \tag{B.2}$$

The strains are measured from strain gage 2 as shown in Figure B.1.

The mesh used for the analytical modeling has 49 nodes along the x-direction and 17 nodes along the y-direction. Three node linear, triangular elements were used with a total of 1536 elements used to model the plates (Figure B.2). A linear static analysis was used to solve for the strains and deflections; the results converged to less than 1% from the previous mesh.

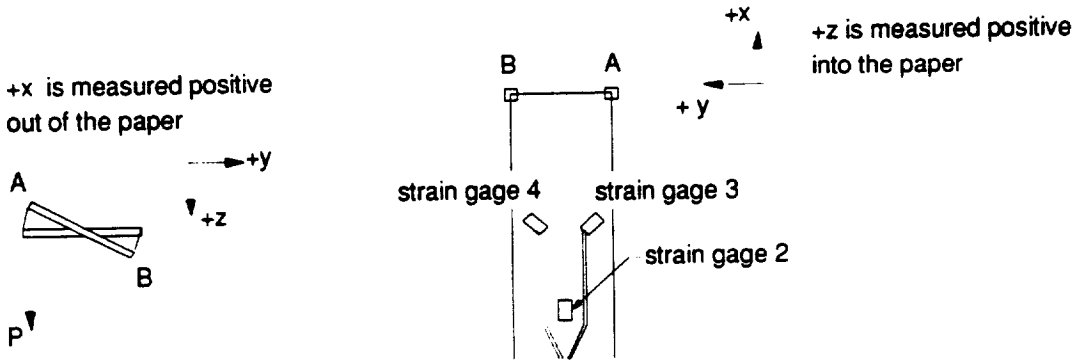

1. xyz-Deflections are measured at points A and B
2. The load. P. is applied at point A
3. The strain is recorded from strain gage 2.

Figure B.1: The experimental plate setup for the static strain and displacement tests.

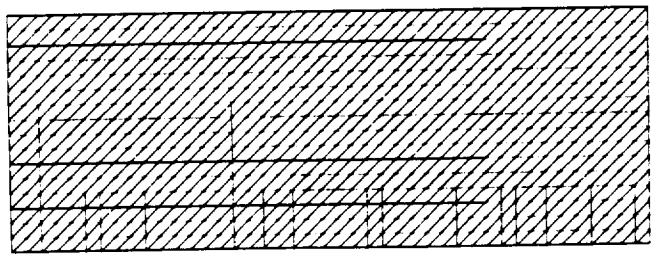

Figure B.2: The finite element mesh used for the analytical modeling on I-DEAS.

B.1 Error Analysis

The following section presents the error analysis for the measured strains and deflections. Suppose the independent quantities $i, \ldots, k$ and $u, \ldots, w$ are measured with their uncertainties $\delta i, \ldots, \delta k$ and $\delta u, \ldots, \delta w$ [26]. If the value q is computed as

$$q = i + \cdots + k - u + \cdots + w \tag{B.3}$$

and if the uncertainties are independent and random then the uncertainty in q is expressed as

$$\delta q = \sqrt{(\delta i)^2 + \cdots + (\delta k)^2 + (\delta u)^2 + \cdots + (\delta w)^2}\,. \tag{B.4}$$

If the value q is computed as

$$q = \frac{i \times \cdots \times k}{u \times \cdots \times w} \tag{B.5}$$

and if the uncertainties are independent and random then the fractional uncertainty in q is expressed as

$$\frac{\delta q}{|q|} = \sqrt{\left(\frac{\delta i}{|i|}\right)^2 + \cdots + \left(\frac{\delta k}{|k|}\right)^2 + \left(\frac{\delta u}{|u|}\right)^2 + \cdots + \left(\frac{\delta w}{|w|}\right)^2}\,. \tag{B.6}$$

In general, if the uncertainties in the measured values of $i, \ldots, k$ are independent and random, then the uncertainty for any function $q(i, \ldots, k)$ can be expressed as

$$\delta q = \sqrt{\left(\frac{\partial q}{\partial i}\delta i\right)^2 + \cdots + \left(\frac{\partial q}{\partial k}\delta k\right)^2} \tag{B.7}.$$

The strain is given by Equation (2.14) as $\varepsilon = \dfrac{a}{G_F(1+a)^2}\dfrac{\Delta V_{out}}{V_{in}}$ where $a = \dfrac{R_2}{R_1} = \dfrac{R_G}{R_3}$. From the engineering data sheet [28], the percent error for the resistances and gage factor, G_F, is ±0.3% and ±0.5%, respectively. The percent uncertainty for the voltages is 0.2%. Using Equation B.7 and the fact that a is never more than 10 for a

quarter bridge [17], the percent uncertainty for the term, $\frac{a}{(1+a)^2}$, is ±0.3%. From Equation (3.6) the percent uncertainty for the strain, ε, is $\delta\varepsilon = 0.9\%$.

The measurement error for the dial indicators on the milling machine is ±0.003 inches. From Equations (B.4), (B.7), and (B.1), the error for the deflection is ±0.002 inches. Using Equations (B.2) and (B.7), the error for the twist is

$$\delta\psi(\text{rad}) = \sqrt{\frac{(\delta z_A)^2 + (\delta z_B)^2 + \frac{(z_A + z_B)}{c^2}(\delta c)^2}{(z_A + z_B + c)(c - z_A - z_B)}} \qquad \text{(B.8)}.$$

B.2 Strain and Displacement Results

The following tables and graphs summarize the experimental and analytical results of the static displacement and strain tests for all plates. Plates 11, 21, 31, 32, 13, and 23* are the only plates instrumented with strain gages and these are the only plates where strain data comparisons are made. For the most part, the deflections for all of the plates are linear while the twist is not.

Table B.2: Experimental and analytical strain results for Plate 11.

Load, P (lbs)	Experimental (με)	I-DEAS (με)	%Error
0.0	0	0	0.0%
6.0	489	529	8.2%
10.4	830	913	10.0%
14.9	1174	1303	11.0%
19.2	1500	1681	12.1%
23.7	1834	2070	12.9%
28.1	2166	2459	13.5%

Table B.3: Experimental and analytical deflection results for Plate 11.

Load, P (lbs)	Experimental (in)	I-DEAS (in)	%Error
0.0	0.000	0.000	0.0%
6.0	0.302	0.320	6.1%
10.4	0.527	0.553	5.0%
14.9	0.752	0.789	5.0%
19.2	0.977	1.018	4.3%
23.7	1.174	1.253	6.8%
28.1	1.332	1.489	11.9%

Table B.4: Experimental and analytical twist results for Plate 11.

Load, P (lbs)	Experimental (degrees)	I-DEAS (degrees)	%Error
0.0	0.00	0.00	0.0%
6.0	1.68	1.69	0.3%
10.4	2.96	2.92	-1.4%
14.9	3.82	4.16	9.0%
19.2	4.84	5.37	11.0%
23.7	5.65	6.62	17.3%
28.1	8.39	7.87	-6.1%

Table B.5: Experimental and analytical strain results for Plate 21.

Load, P (lbs)	Experimental (με)	I-DEAS (με)	%Error
0.0	0	0	0.0%
6.0	545	558	2.4%
10.4	941	964	2.4%
14.9	1336	1375	2.9%
19.2	1720	1774	3.2%
23.7	2108	2184	3.6%
28.1	2484	2595	4.5%

Table B.6: Experimental and analytical deflection results for Plate 21.

Load, P (lbs)	Experimental (in)	I-DEAS (in)	%Error
0.0	0.000	0.000	0.0%
6.0	0.357	0.319	-10.6%
10.4	0.610	0.550	-9.7%
14.9	0.832	0.785	-5.6%
19.2	1.083	1.013	-6.4%
23.7	1.343	1.247	-7.1%
28.1	1.584	1.482	-6.4%

Table B.7: Experimental and analytical twist results for Plate 21.

Load, P (lbs)	Experimental (degrees)	I-DEAS (degrees)	%Error
0.0	0.00	0.00	0.0%
6.0	0.85	0.42	-49.8%
10.4	1.99	0.73	-63.1%
14.9	0.24	1.05	342.9%
19.2	1.71	1.35	-21.2%
23.7	2.28	1.66	-27.2%
28.1	3.72	1.97	-47.0%

Table B.8: Experimental and analytical strain results for Plate 31.

Load, P (lbs)	Experimental (με)	I-DEAS (με)	%Error
0.0	0	0	0.0%
6.0	560	538	-4.0%
10.4	955	928	-2.8%
14.9	1359	1324	-2.6%
19.2	1742	1709	-1.9%
23.7	2122	2103	-0.9%
28.1	2492	2499	0.3%

Table B.9: Experimental and analytical deflection results for Plate 31.

Load, P (lbs)	Experimental (in)	I-DEAS (in)	%Error
0.0	0.000	0.000	0.0%
6.0	0.339	0.311	-8.3%
10.4	0.586	0.536	-8.5%
14.9	0.893	0.765	-14.3%
19.2	1.141	0.987	-13.5%
23.7	1.390	1.215	-12.6%
28.1	1.642	1.443	-12.1%

Table B.10: Experimental and analytical twist results for Plate 31.

Load, P (lbs)	Experimental (degrees)	I-DEAS (degrees)	%Error
0.0	0.00	0.00	0.0%
6.0	-0.02	0.43	-2361.8%
10.4	1.20	0.75	-38.0%
14.9	-0.13	1.06	-896.0%
19.2	-0.32	1.37	-522.9%
23.7	0.99	1.69	70.2%
28.1	2.94	2.01	-31.7%

Table B.11: Experimental and analytical deflection results for Plate 41.

Load, P (lbs)	Experimental (in)	I-DEAS (in)	%Error
0.0	0.000	0.000	0.0%
6.0	0.359	0.334	-6.9%
10.4	0.615	0.576	-6.3%
14.9	0.877	0.823	-6.2%
19.2	1.118	1.061	-5.1%
23.7	1.372	1.306	-4.7%
28.1	1.616	1.552	-3.9%

Table B.12: Experimental and analytical twist results for Plate 41.

Load, P (lbs)	Experimental (degrees)	I-DEAS (degrees)	%Error
0.0	0.00	0.00	0.0%
6.0	0.44	0.47	7.2%
10.4	1.22	0.81	-33.5%
14.9	2.19	1.16	-47.2%
19.2	2.86	1.50	-47.8%
23.7	4.11	1.84	-55.2%
28.1	5.37	2.19	-59.3%

Table B.13: Experimental and analytical deflection results for Plate 22.

Load, P (lbs)	Experimental (in)	I-DEAS (in)	%Error
0.0	0.000	0.000	0.0%
6.0	0.536	0.488	-8.8%
10.4	0.924	0.843	-8.7%
14.9	1.303	1.203	-7.6%
19.2	1.655	1.552	-6.2%
23.7	2.003	1.911	-4.6%

Table B.14: Experimental and analytical twist results for Plate 22.

Load, P (lbs)	Experimental (degrees)	I-DEAS (degrees)	%Error
0.0	0.00	0.00	0.0%
6.0	0.59	0.38	-36.0%
10.4	1.36	0.65	-51.8%
14.9	2.35	0.93	-60.3%
19.2	3.37	1.21	-64.2%
23.7	4.50	1.48	-67.0%

Table B.15: Experimental and analytical strain results for Plate 32.

Load, P (lbs)	Experimental (με)	I-DEAS (με)	%Error
0.0	0	0	0.0%
6.0	775	799	3.1%
10.4	1322	1379	4.3%
14.9	1860	1968	5.8%
19.2	2362	2540	7.5%
23.7	2852	3126	9.6%

Table B.16: Experimental and analytical deflection results for Plate 32.

Load, P (lbs)	Experimental (in)	I-DEAS (in)	%Error
0.0	0.000	0.000	0.0%
6.0	0.515	0.480	-6.6%
10.4	0.885	0.829	-6.3%
14.9	1.242	1.183	-4.7%
19.2	1.584	1.527	-3.6%
23.7	1.918	1.880	-2.0%

Table B.17: Experimental and analytical twist results for Plate 32.

Load, P (lbs)	Experimental (degrees)	I-DEAS (degrees)	%Error
0.0	0.00	0.00	0.0%
6.0	0.37	0.40	7.7%
10.4	0.95	0.69	-27.9%
14.9	1.83	0.98	-46.4%
19.2	2.58	1.26	-51.1%
23.7	3.99	1.56	-61.0%

Table B.18: Experimental and analytical deflection results for Plate 42.

Load, P (lbs)	Experimental (in)	I-DEAS (in)	%Error
0.0	0.000	0.000	0.0%
6.0	0.525	0.507	-3.4%
10.4	0.898	0.875	-2.5%
14.9	1.265	1.249	-1.2%
19.2	1.605	1.611	0.4%
23.7	1.938	1.984	2.4%

Table B.19: Experimental and analytical twist results for Plate 42.

Load, P (lbs)	Experimental (degrees)	I-DEAS (degrees)	%Error
0.0	0.00	0.00	0.0%
6.0	0.77	0.41	-46.7%
10.4	1.38	0.71	-48.9%
14.9	2.47	1.01	-59.3%
19.2	3.20	1.30	-59.4%
23.7	4.40	1.60	-63.6%

Table B.20: Experimental and analytical strain results for Plate 13.

Load, P (lbs)	Experimental (με)	I-DEAS (με)	%Error
0.0	0	0	0.0%
6.0	999	1016	1.7%
10.4	1725	1754	1.7%
14.9	2460	2503	1.8%
19.2	3165	3229	2.0%

Table B.21: Experimental and analytical deflection results for Plate 13.

Load, P (lbs)	Experimental (in)	I-DEAS (in)	%Error
0.0	0.000	0.000	0.0%
6.0	0.636	0.590	-7.1%
10.4	1.095	1.019	-6.9%
14.9	1.546	1.454	-5.9%
19.2	1.981	1.876	-5.3%

Table B.22: Experimental and analytical twist results for Plate 13.

Load, P (lbs)	Experimental (degrees)	I-DEAS (degrees)	%Error
0.0	0.00	0.00	0.0%
6.0	1.63	1.39	-14.8%
10.4	2.53	2.39	-5.4%
14.9	4.12	3.42	-17.1%
19.2	5.66	4.41	-22.0%

Table B.23: Experimental and analytical strain results for Plate 23*.

Load, P (lbs)	Experimental (με)	I-DEAS (με)	%Error
0.0	0	0	0.0%
6.0	628	573	-8.7%
10.4	1070	990	-7.5%
14.9	1532	1413	-7.8%
19.2	1960	1823	-7.0%
23.7	2400	2244	-6.5%
28.1	2830	2666	-5.8%

Table B.24: Experimental and analytical deflection results for Plate 23*.

Load, P (lbs)	Experimental (in)	I-DEAS (in)	%Error
0.0	0.000	0.000	0.0%
6.0	0.354	0.321	-9.2%
10.4	0.600	0.555	-7.5%
14.9	0.870	0.792	-9.0%
19.2	1.115	1.021	-8.4%
23.7	1.373	1.257	-8.4%
28.1	1.625	1.494	-8.0%

Table B.25: Experimental and analytical twist results for Plate 23°.

Load, P (lbs)	Experimental (degrees)	I-DEAS (degrees)	%Error
0.0	0.00	0.00	0.0%
6.0	0.70	0.44	-37.3%
10.4	1.57	0.75	-51.9%
14.9	2.02	1.08	-46.6%
19.2	2.91	1.39	-52.2%
23.7	3.96	1.71	-56.8%
28.1	5.18	2.03	-60.8%

Table B.26: Experimental and analytical deflection results for Plate 33°.

Load, P (lbs)	Experimental (in)	I-DEAS (in)	%Error
0.0	0.000	0.000	0.0%
6.0	0.295	0.338	14.6%
10.4	0.497	0.583	17.2%
14.9	0.715	0.831	16.4%
19.2	0.915	1.073	17.3%
23.7	1.137	1.321	16.1%
28.1	1.332	1.569	17.8%

Table B.27: Experimental and analytical twist results for Plate 33°.

Load, P (lbs)	Experimental (degrees)	I-DEAS (degrees)	%Error
0.0	0.00	0.00	0.0%
6.0	0.44	0.47	7.1%
10.4	1.49	0.81	-45.5%
14.9	2.01	1.16	-42.2%
19.2	2.97	1.50	-49.5%
23.7	4.14	1.85	-55.4%
28.1	4.93	2.19	-55.5%

Table B.28: Experimental and analytical deflection results for Plate 43*.

Load, P (lbs)	Experimental (in)	I-DEAS (in)	%Error
0.0	0.000	0.000	0.0%
6.0	0.355	0.603	69.9%
10.4	0.605	1.041	72.2%
14.9	0.863	1.485	72.2%
19.2	1.104	1.916	73.7%
23.7	1.350	2.359	74.8%
28.1	1.603	2.803	74.9%

Table B.29: Experimental and analytical twist results for Plate 43*.

Load, P (lbs)	Experimental (degrees)	I-DEAS (degrees)	%Error
0.0	0.00	0.00	0.0%
6.0	0.89	0.45	-49.0%
10.4	1.64	0.78	-52.4%
14.9	2.22	1.11	-49.8%
19.2	3.03	1.44	-52.5%
23.7	3.96	1.77	-55.3%
28.1	4.89	2.10	-56.9%

Plate 11

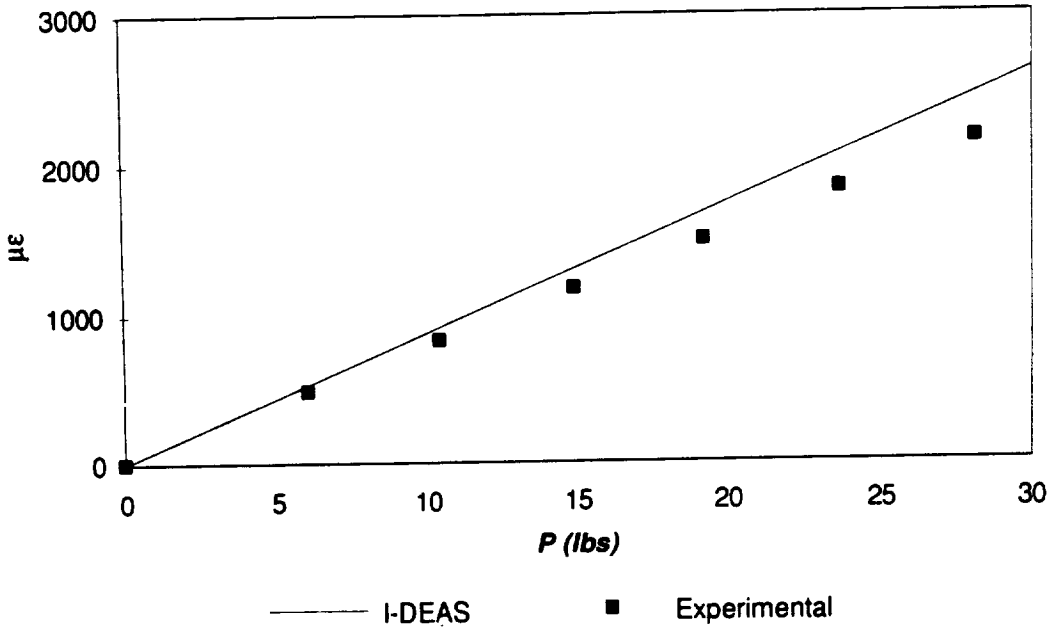

Figure B.3: Experimental and analytical strain results for Plate 11.

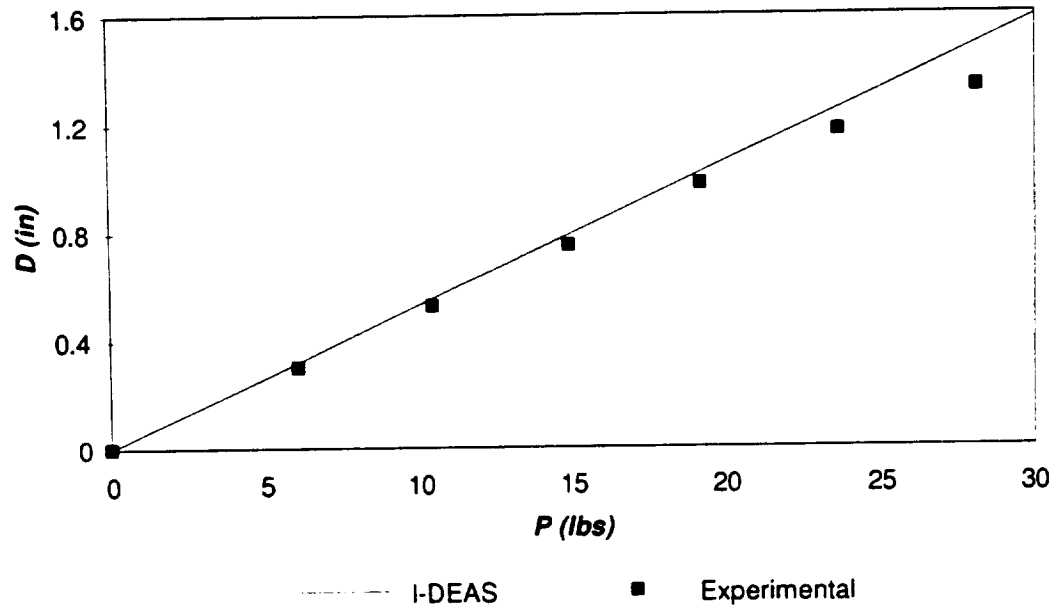

Figure B.4: Experimental and analytical deflection results for Plate 11.

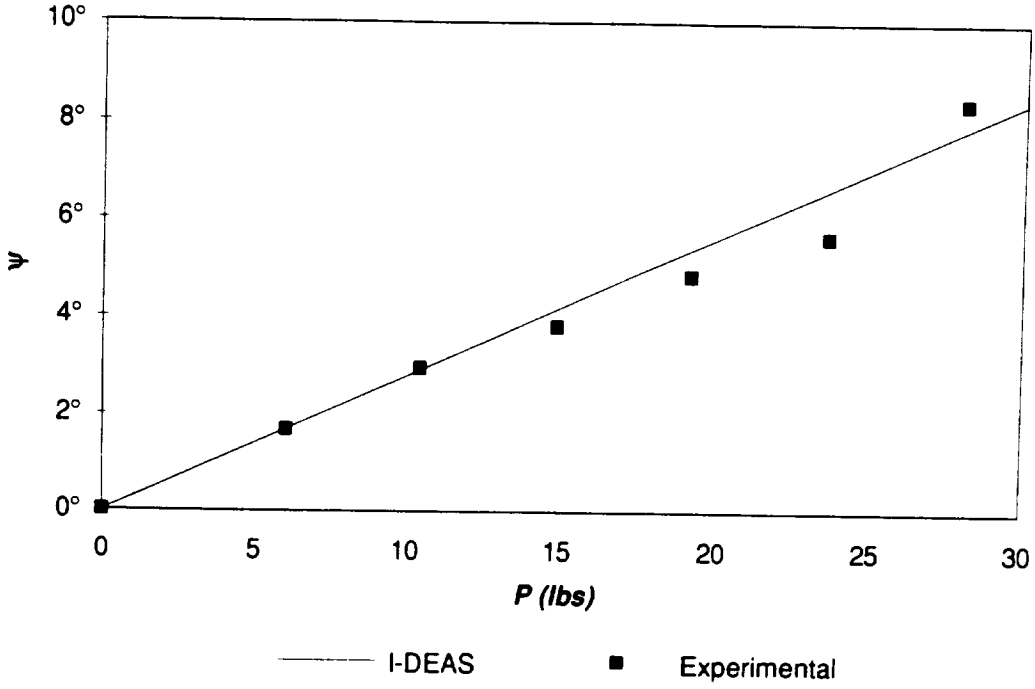

Figure B.5: Experimental and analytical twist results for Plate 11.

Plate 21

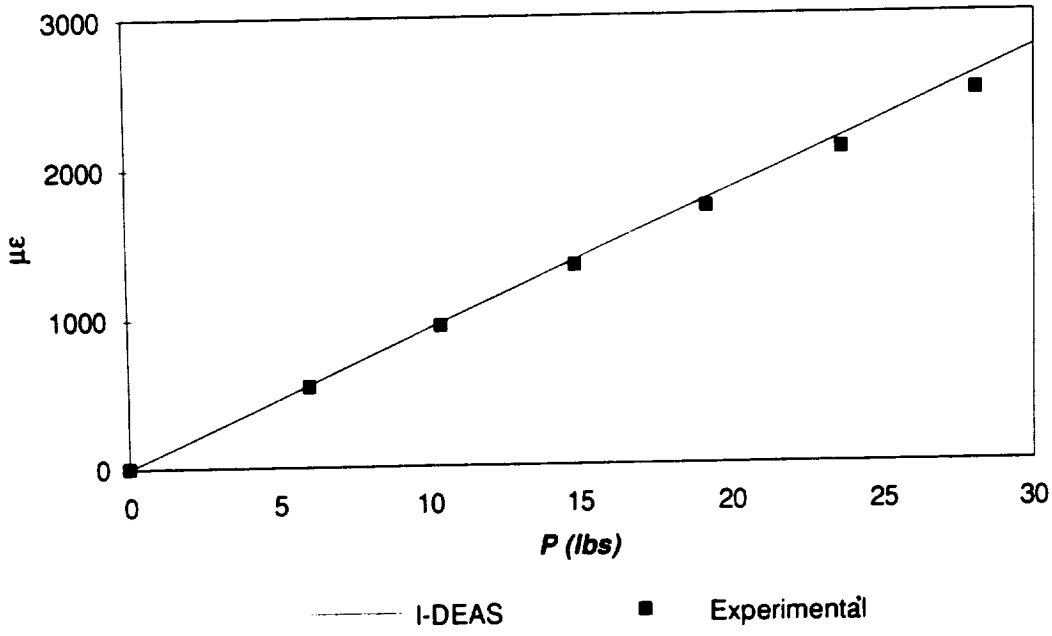

Figure B.6: Experimental and analytical strain results for Plate 21.

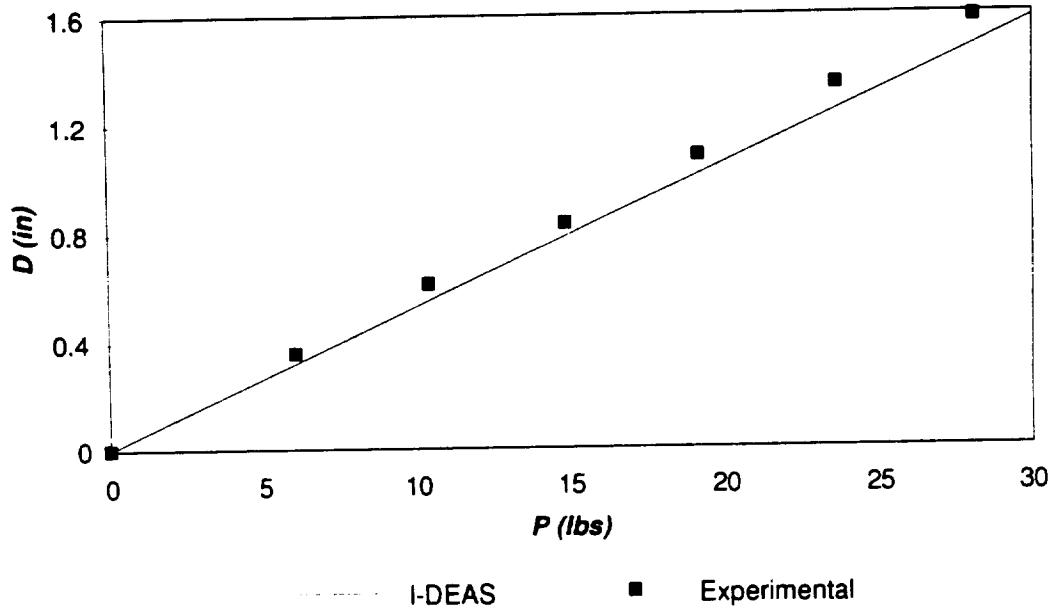

Figure B.7: Experimental and analytical deflection results for Plate 21.

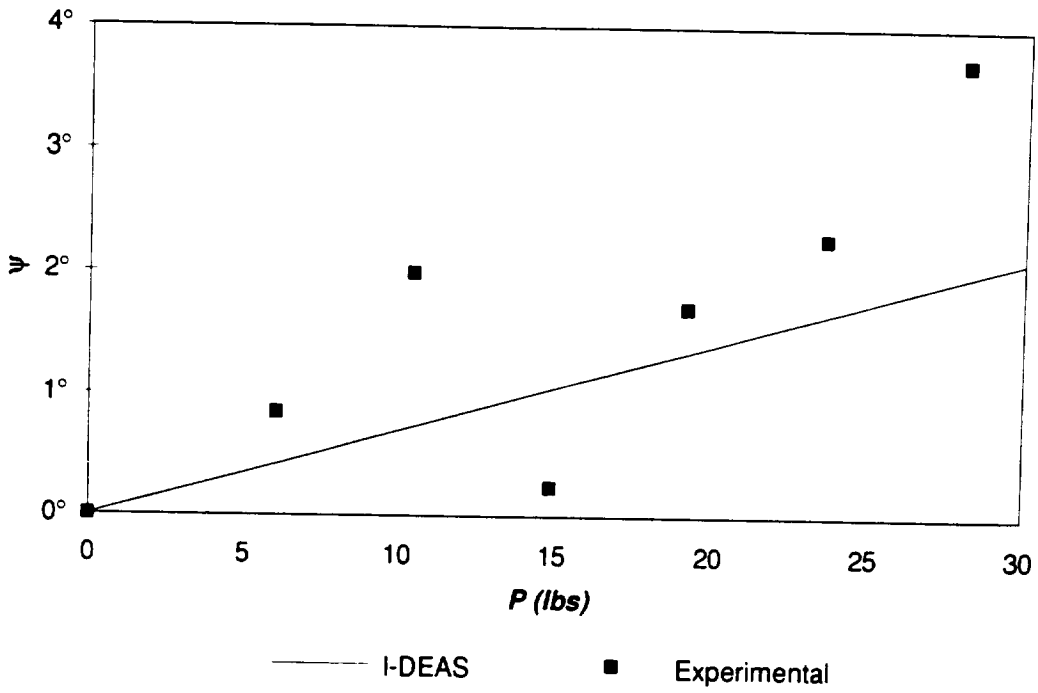

Figure B.8: Experimental and analytical twist results for Plate 21.

Plate 31

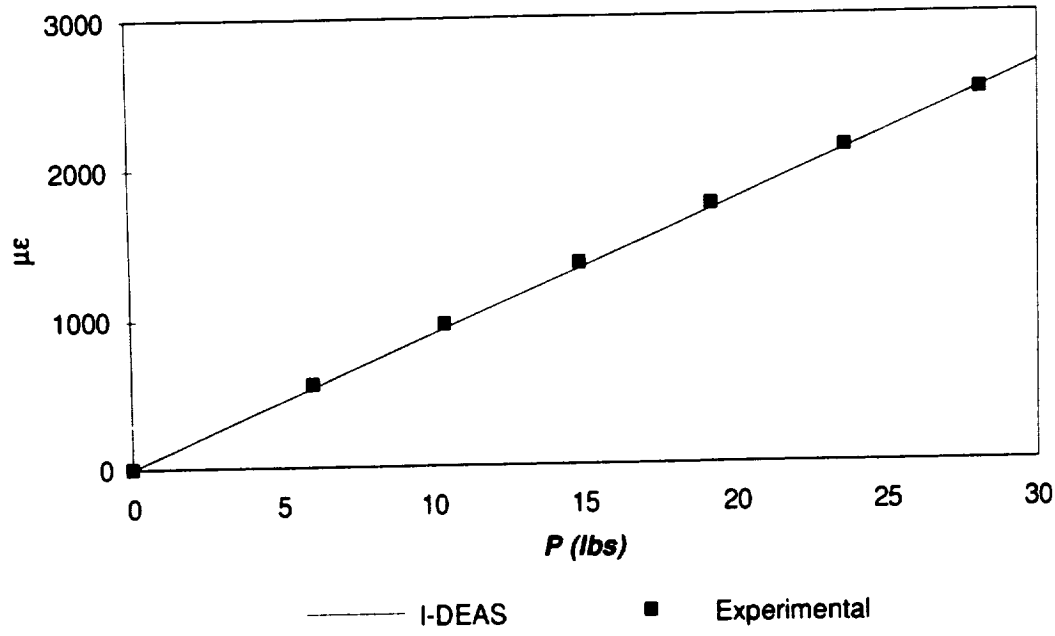

Figure B.9: Experimental and analytical strain results for Plate 31.

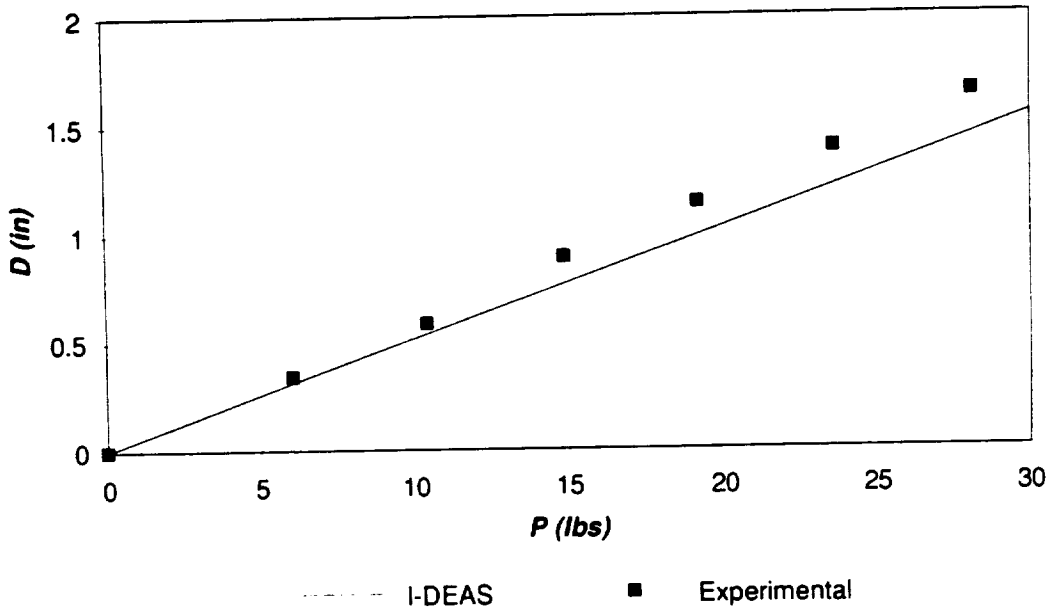

Figure B.10: Experimental and analytical deflection results for Plate 31.

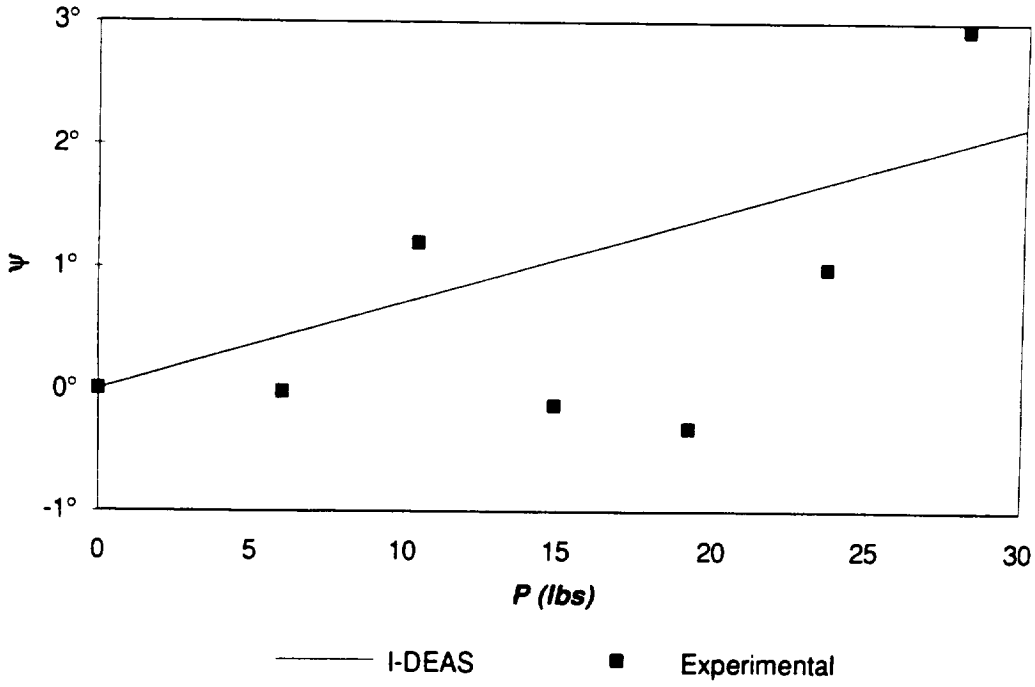

Figure B.11: Experimental and analytical twist results for Plate 31.

Plate 41

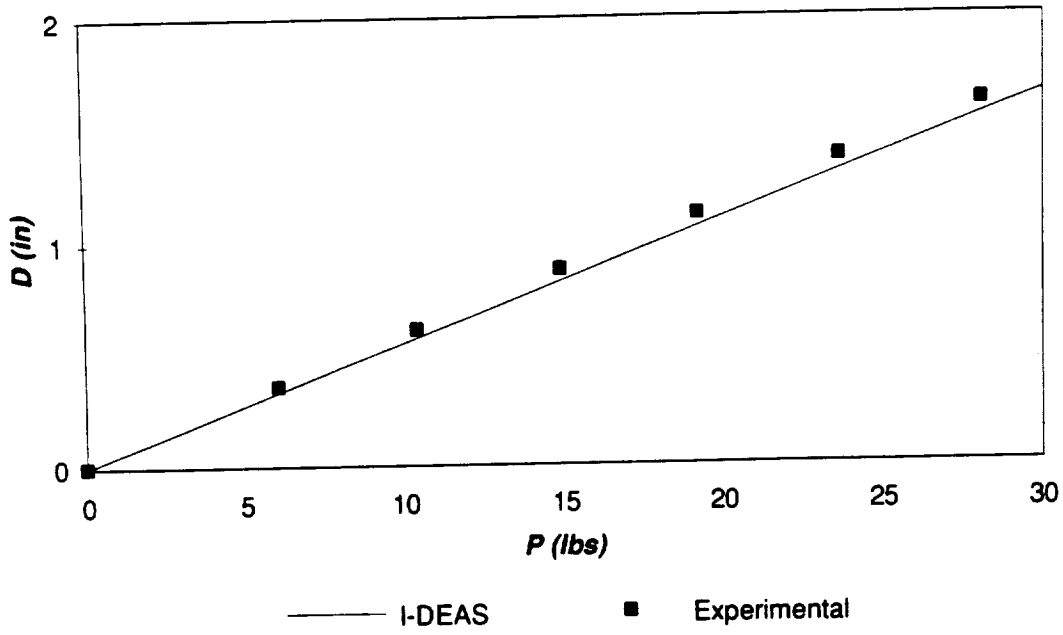

Figure B.12: Experimental and analytical deflection results for Plate 41.

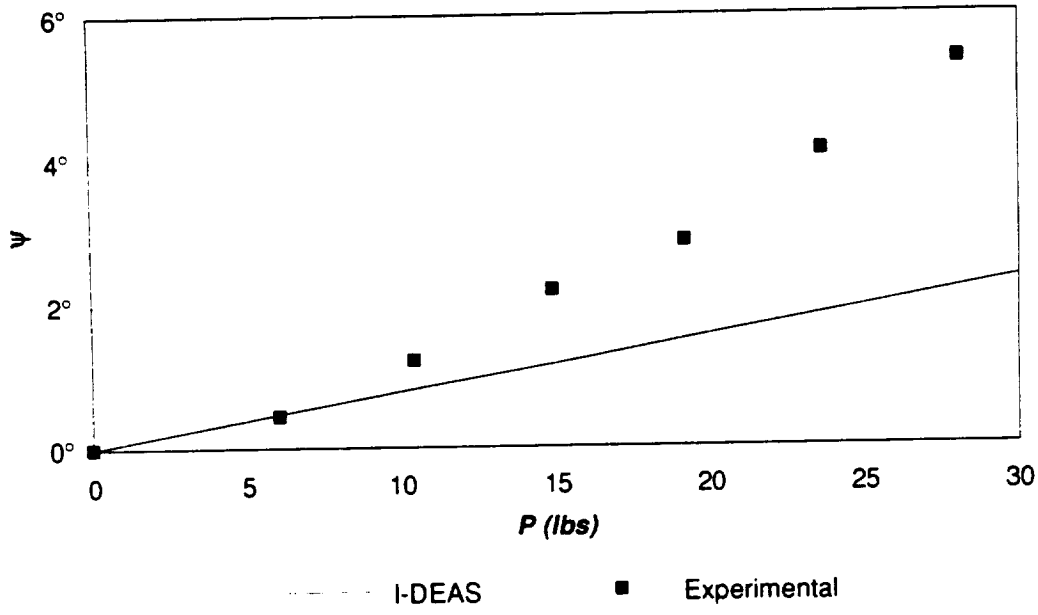

Figure B.13: Experimental and analytical twist results for Plate 41.

Plate 22

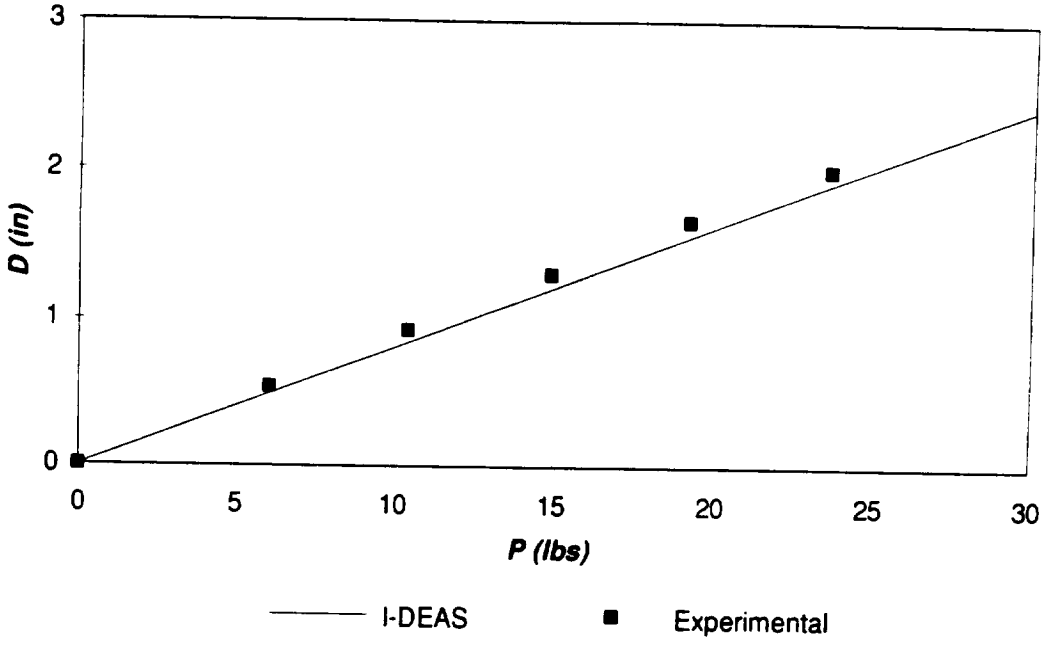

Figure B.14: Experimental and analytical deflection results for Plate 22.

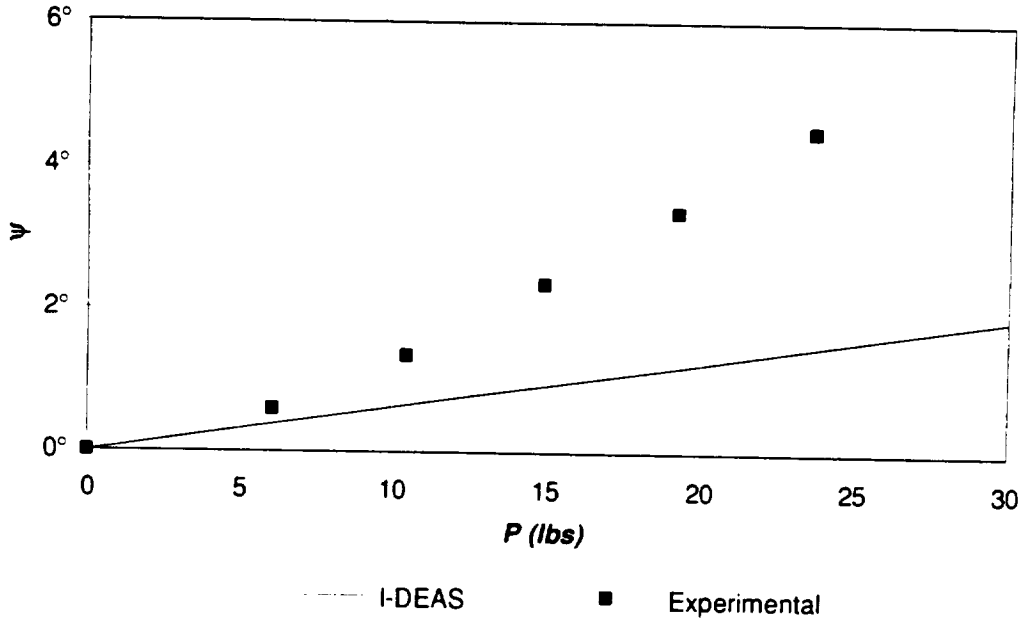

Figure B.15: Experimental and analytical twist results for Plate 22.

Plate 32

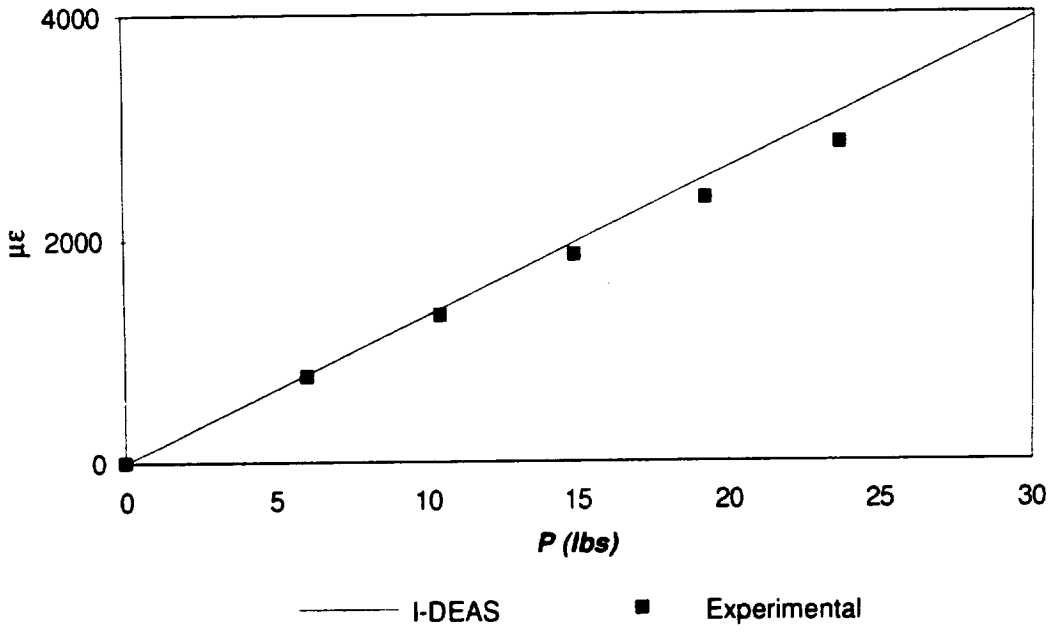

Figure B.16: Experimental and analytical strain results for Plate 32.

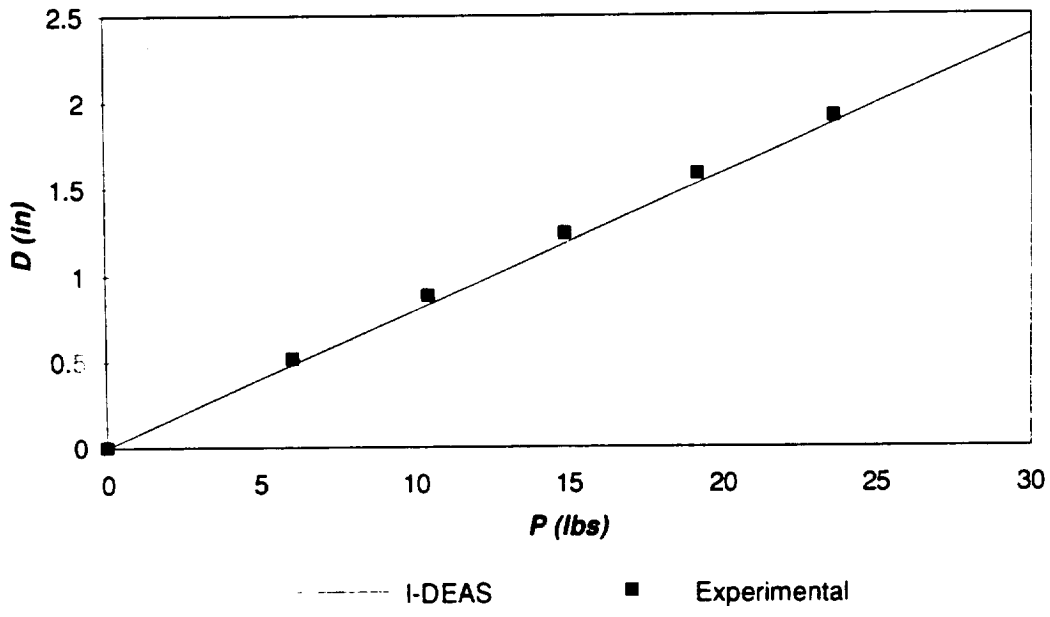

Figure B.17: Experimental and analytical deflection results for Plate 32.

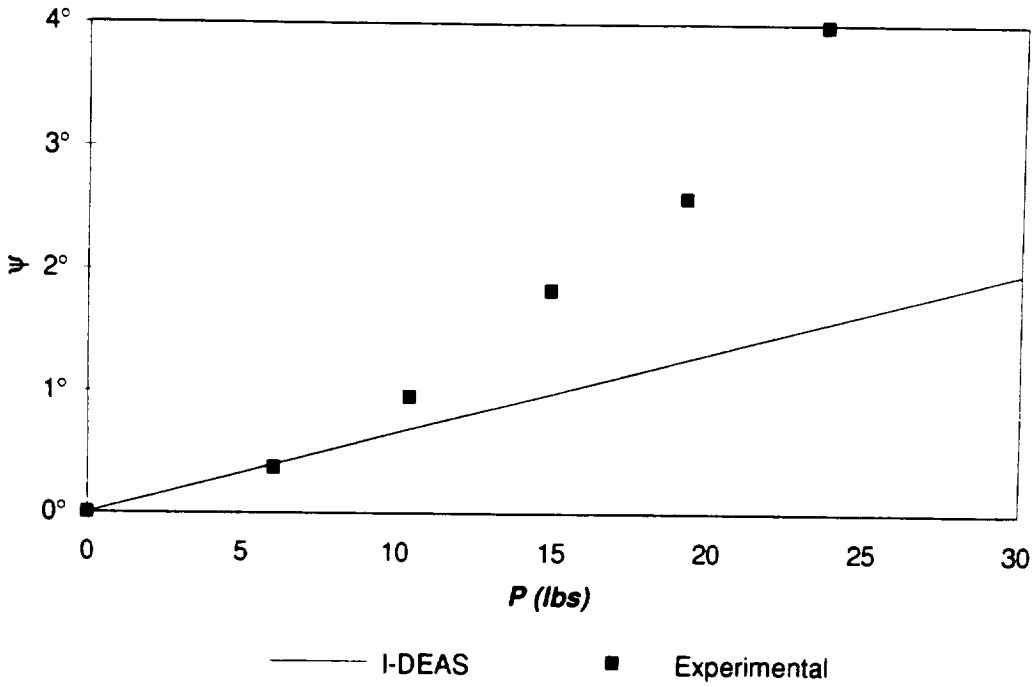

Figure B.18: Experimental and analytical twist results for Plate 32.

Plate 42

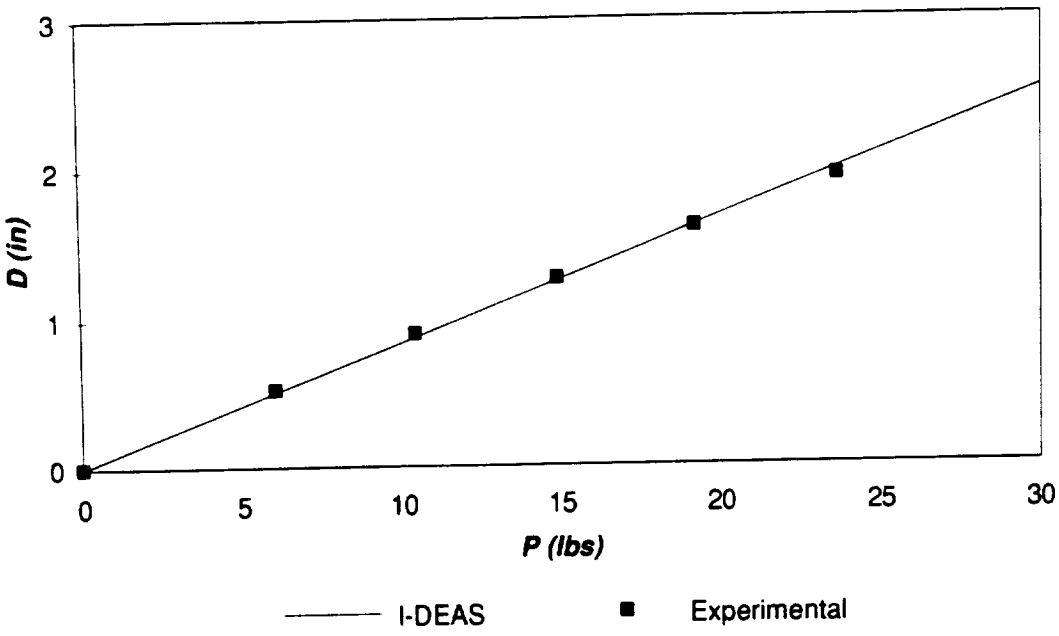

Figure B.19: Experimental and analytical deflection results for Plate 42.

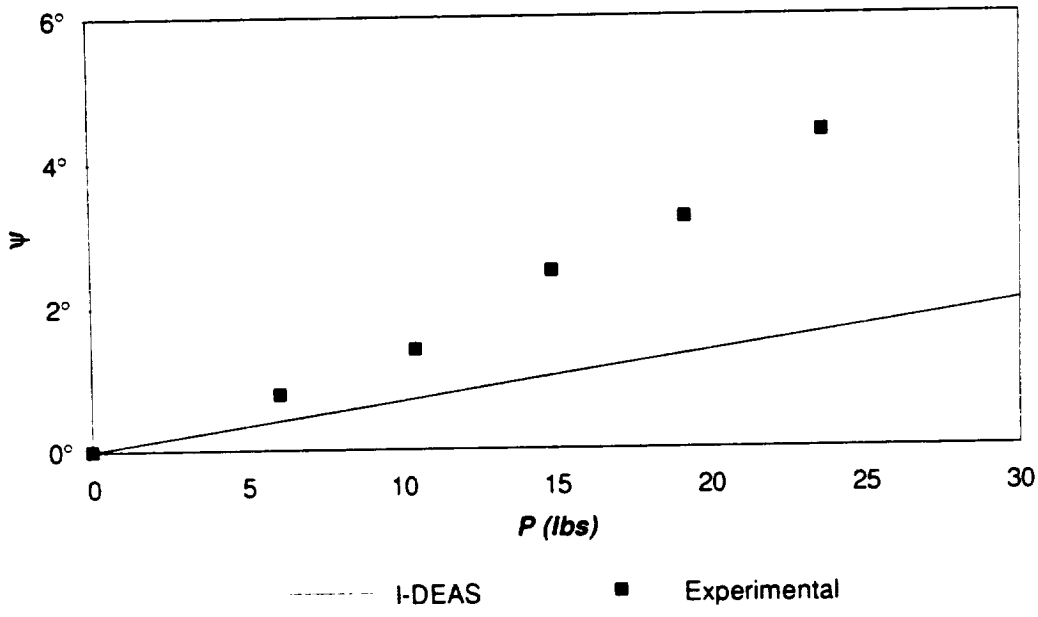

Figure B.20: Experimental and analytical twist results for Plate 42.

Plate 13

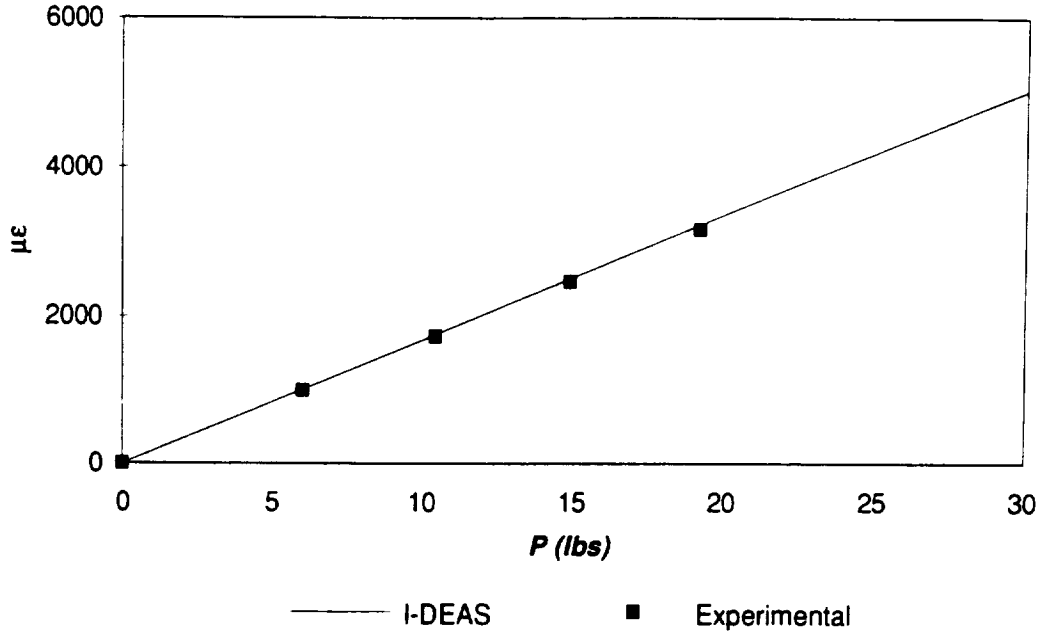

Figure B.21: Experimental strain results for Plate 13.

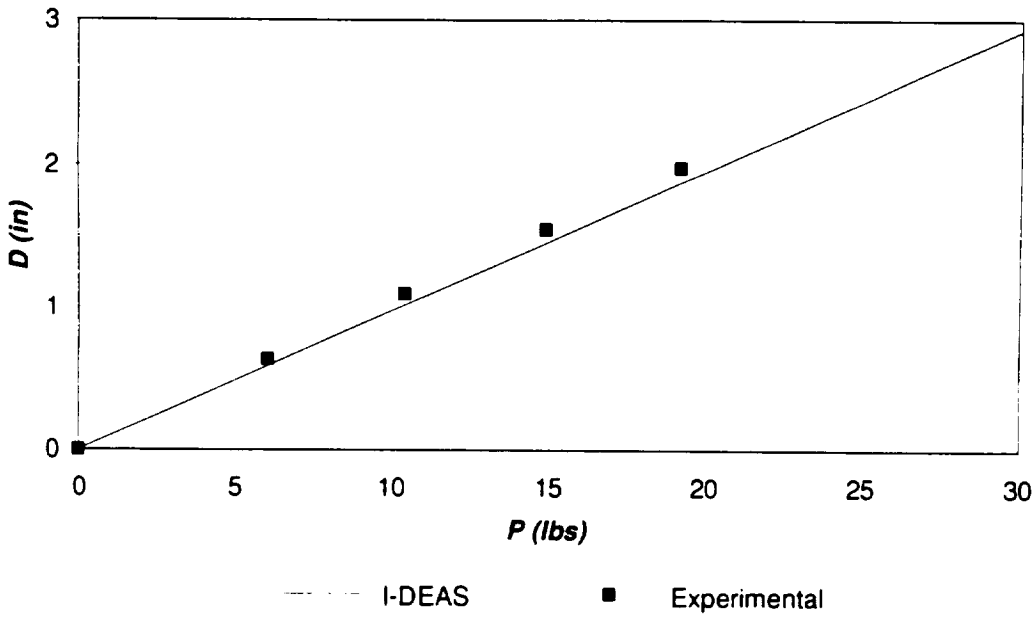

Figure B.22: Experimental and analytical deflection results for Plate 13.

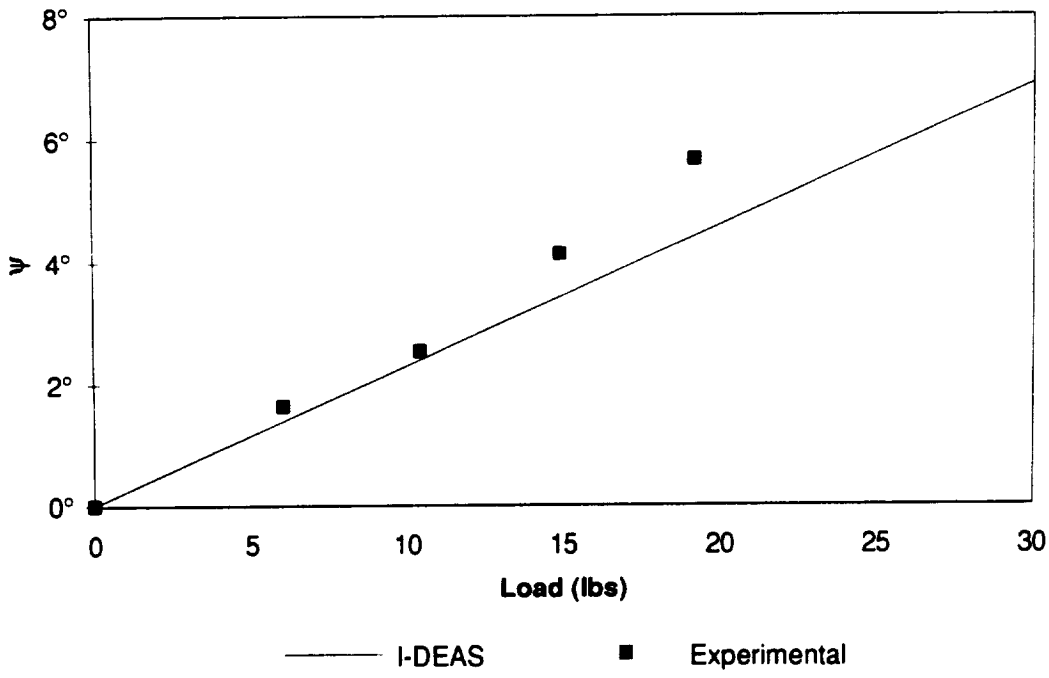

Figure B.23: Experimental and analytical twist results for Plate 13.

Plate 23*

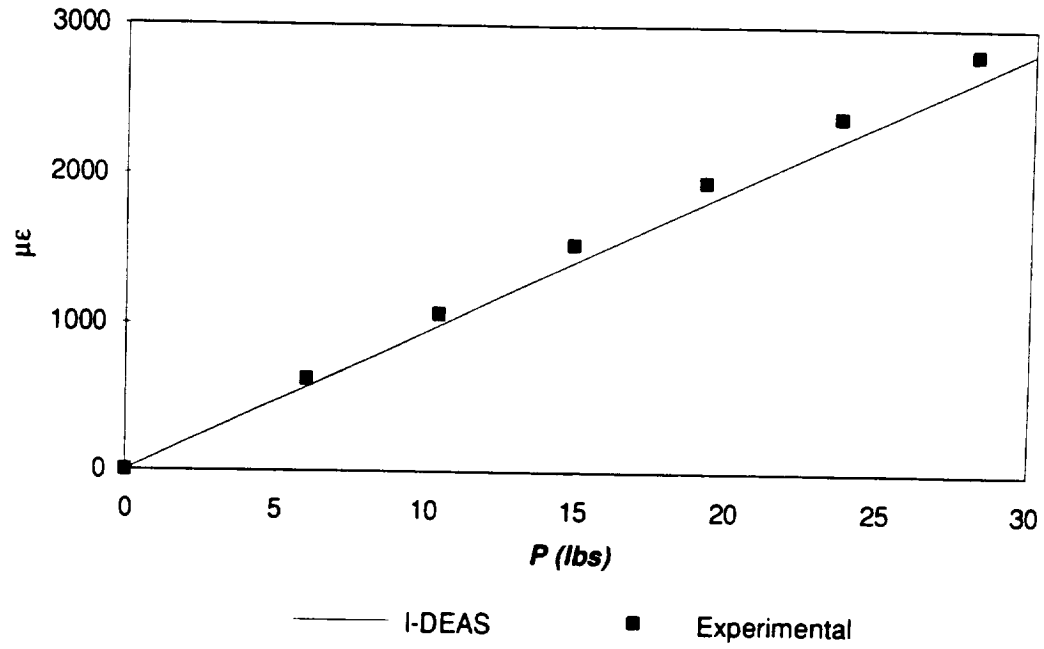

Figure B.24: Experimental strain results for Plate 23*.

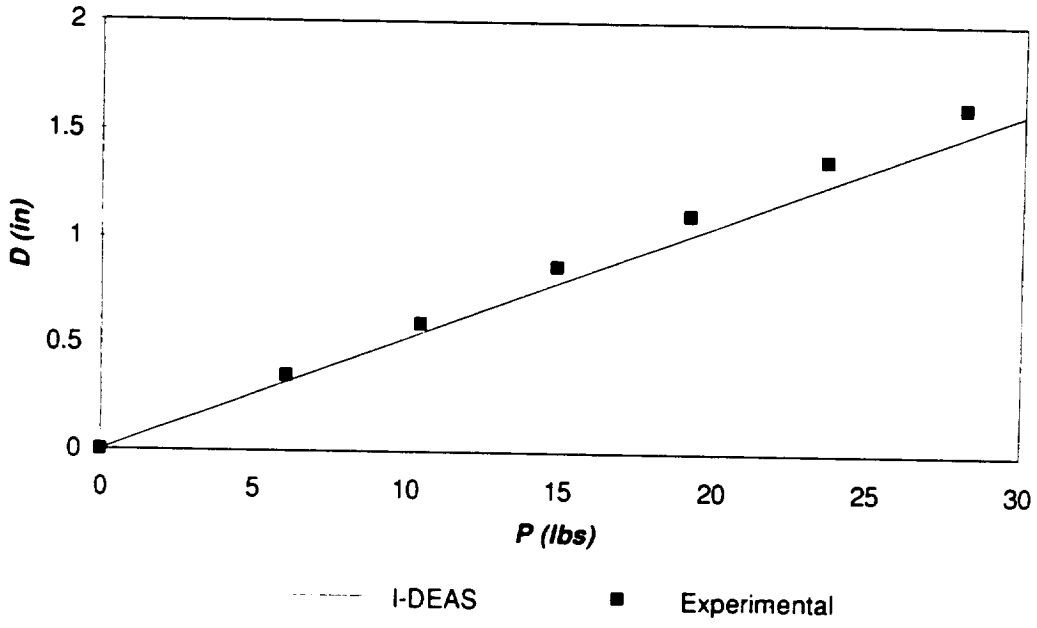

Figure B.25 : Experimental and analytical strain results for Plate 23*.

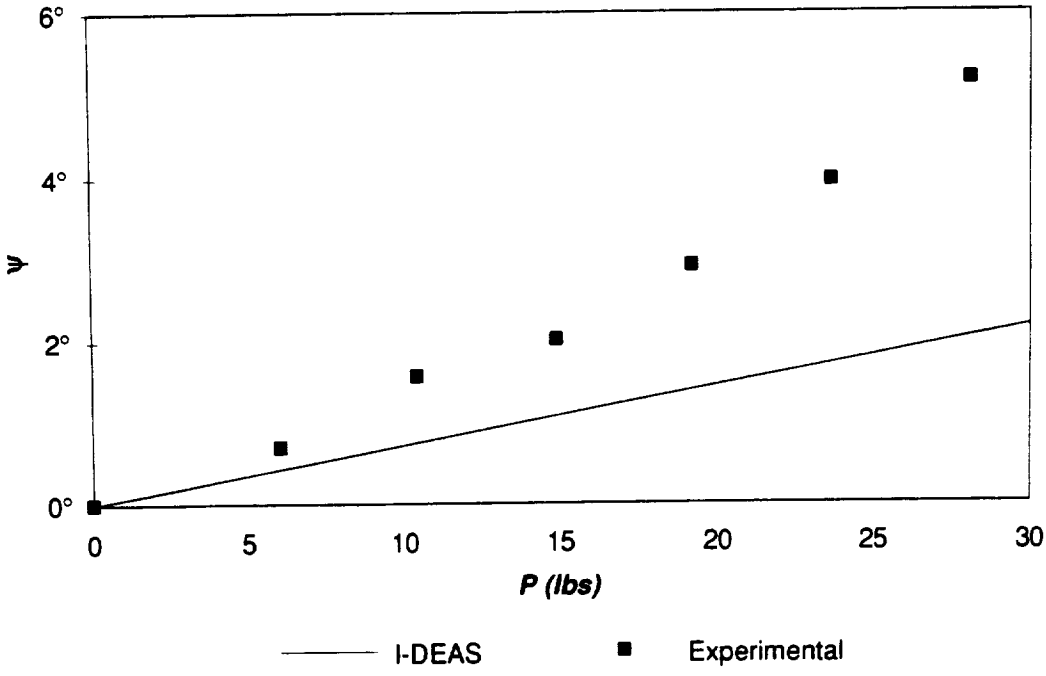

Figure B.26: Experimental and analytical twist results for Plate 23*.

Plate 33*

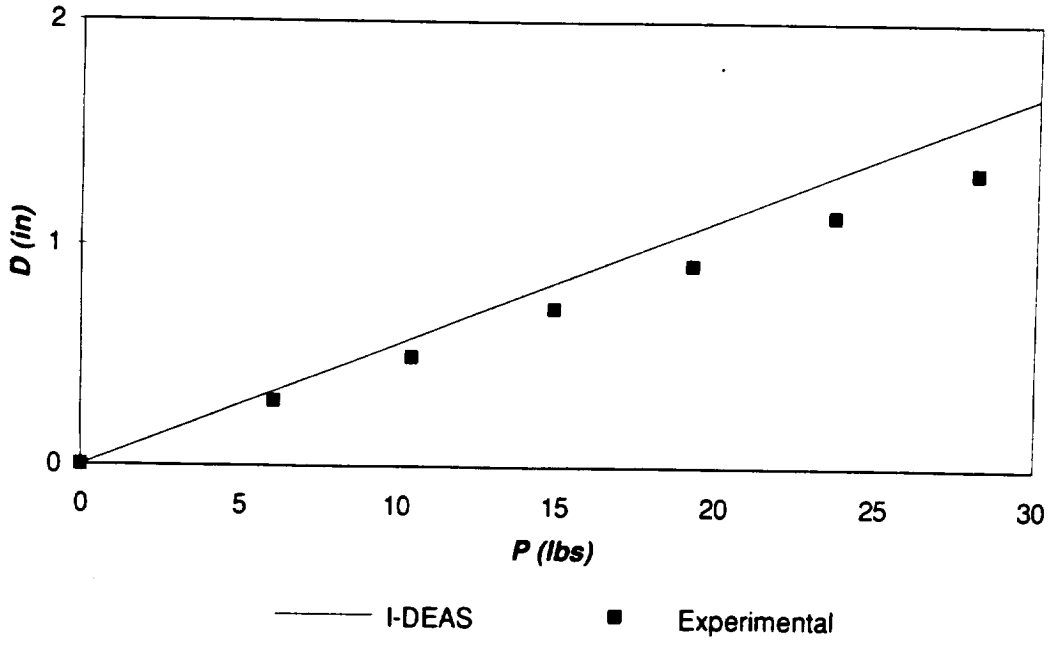

Figure B.27: Experimental and analytical deflection results for Plate 33*.

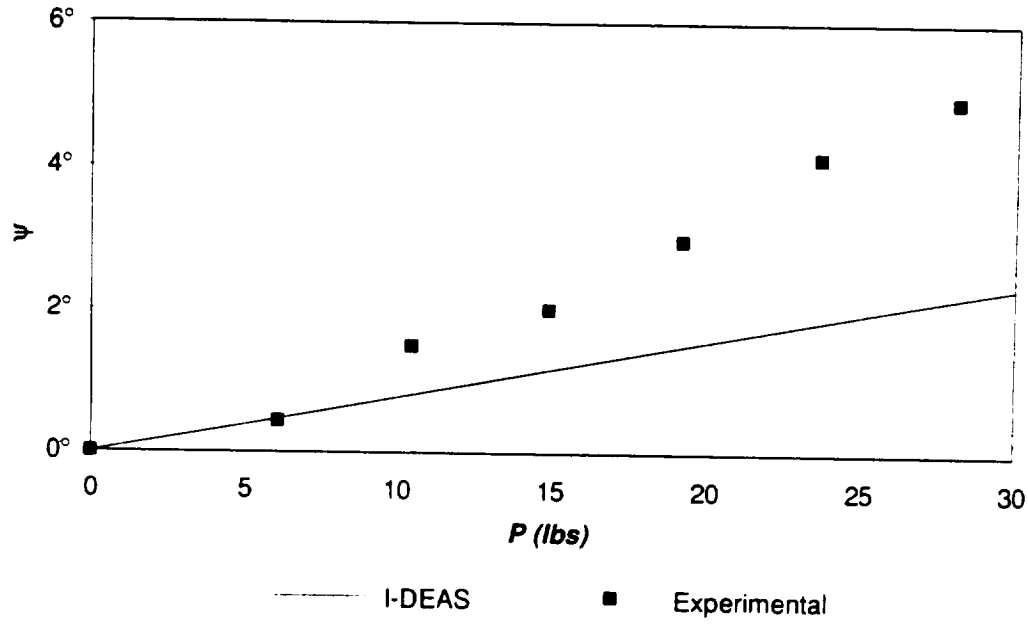

Figure B.28: Experimental and analytical twist results for Plate 33*.

Plate 43*

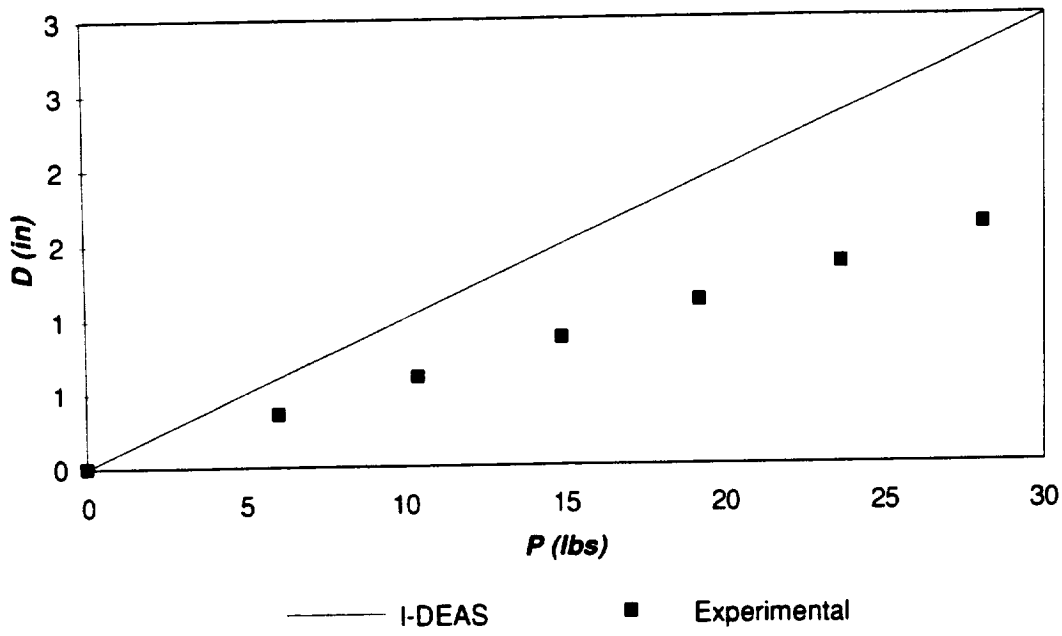

Figure B.29: Experimental and analytical deflection results for Plate 43*.

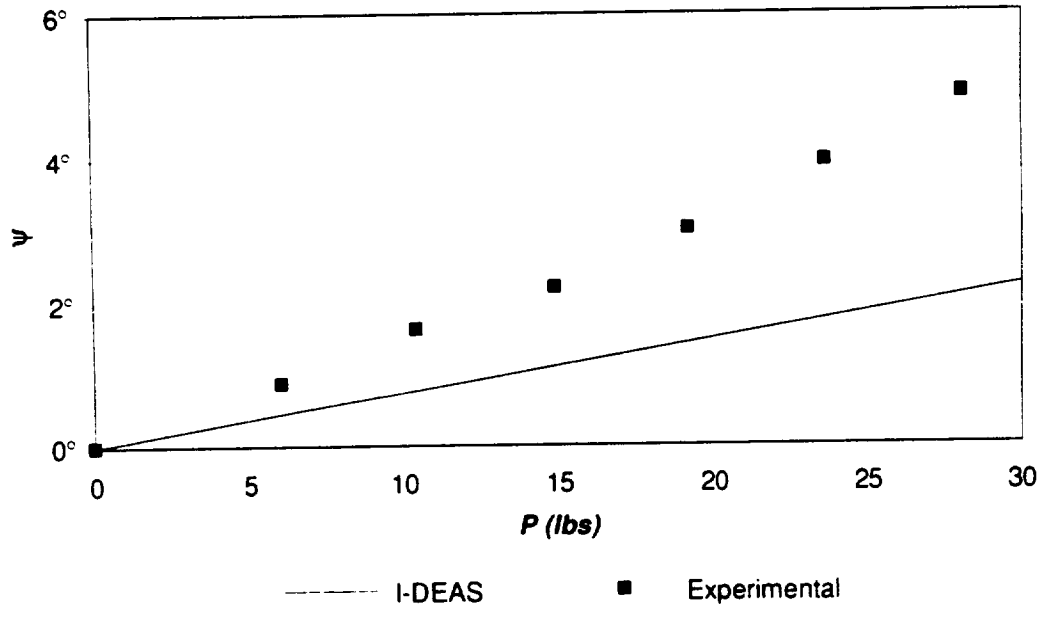

Figure B.30: Experimental and analytical twist results for Plate 43*.

References

1. Whitlow, J. B., Jr., and G. K. Sievers, "Fuel Savings Potential of NASA Advanced Turboprop Program," *NASA TM-83736*, September 1984.

2. Harlamert, W. B., and R. Edinger, "Composite Prop Blades are Quieter, Lighter," *Automotive Engineering*, No. 4, Vol. 87, pp. 67–70, April 1979.

3. Carnegie, W., "Vibrations of Pre-Twisted Cantilever Blading," *Proceedings of the Institution of Mechanical Engineers*, Vol. 176, pp. 315–322, 1962.

4. Dawson, B., N. G. Ghosh, and W. Carnegie, "Effect of Slenderness Ratio on the Natural Frequencies of Pre-Twisted Cantilever Beams of Uniform Rectangular Cross–Section," *Journal of Mechanical Engineering Science*, Vol. 13, pp. 51–59, 1971.

5. MacBain, J. C., "Vibratory Behavior of Twisted Cantilevered Plates," *Journal of Aircraft*, Vol. 12, pp. 343–349, 1978.

6. Nagamatsu, A., and S. Michimura, "Vibration of Blade of Rotating Impeller," *Theoretical and Applied Mechanics*, Vol. 26, pp. 327–338, 1978.

7. Leissa, A. W., J. C. MacBain, and R. E. Kielb, "Vibrations of Twisted Cantilevered Plates-Summary of Previous and Current Studies," *Journal of Sound and Vibration*, Vol. 96, No. 2, pp. 159-173, 1984.

8. MacBain, J. C., R. E. Kielb, and A. W. Leissa, "Vibrations of Twisted Cantilever Plates–Experimental Investigation," *Journal of Engineering for Gas Turbines and Power*, Vol. 107, pp. 187-196, 1985.

9. Kielb, R. E., A. W. Leissa, and J. C. MacBain, "Vibrations of Twisted Cantilever Plates–A Comparison of Theoretical Results," *International Journal for Numerical Methods in Engineering*, Vol. 21, pp. 1365-1380, 1985.

10. Kielb, R. E., A. W. Leissa, J. C. MacBain, and K. S. Carney, "Joint Research Effort on the Vibrations of Twisted Plates," *NASA RP-1150*, September, 1985.

11. Brown, G. V., R. E. Kielb, E. H. Meyn, R. E. Morris, and S. J. Posta, "Lewis Research Center Spin Rig and Its Use in Vibration Analysis of Rotating Systems," *NASA TP-2304*, 1984.

12. Crawley, E. F., "The Natural Modes of Graphite/Epoxy Cantilever Plates and Shells," *Journal of Composite Materials*, Vol. 13, pp. 195–205, July 1979.

13. Jensen, D. W., E. F. Crawley, and J. Dugundji, "Vibration of Cantilevered Graphite/Epoxy Plates with Bending-Torsion Coupling," *Journal of Reinforced Plastics and Composites*, Vol. 1, pp. 254–269, July 1982.

14. Ramamurti, V., and R. Kielb, "Natural Frequencies of Twisted Rotating Plates," *Journal of Sound and Vibration*, Vol. 97, pp. 429-449, 1985.

15. Jones, R. M., *Mechanics of Composite Materials*, Hemisphere Publishing Corporation, New York, pp. 90-97, 1975.

16. Ewins, D. J., *Modal Testing Theory and Practice*, New York, John Wiley & Sons, 1984.

17. Murray, W. M., and W. R. Miller, *The Bonded Electrical Resistance Strain Gage*, New York, Oxford University Press, 1992.

18. "Optimizing Strain Gage Excitation Levels," TN-502, Measurements Group, Inc., P. O. 27777, Raleigh, NC 276111, 1983.

19. "Temperature-Induced Apparent Strain and Gage Factor Variation in Strain Gages," TN-504, Measurements Group, Inc., P. O. 27777, Raleigh, NC 27611, 1983.

20. Powell, R. L., and K. A. Stetson, "Interferometric Vibration Analysis by Wavefront Reconstruction," *Journal of the Optical Society of America*, Vol. 55, pp. 1593-1598, December, 1965.

21. Monahan, M. A., and K. Bromley, "Vibration Analysis by Holographic Interferometry," *Journal of the Acoustical Society of America*, Vol. 44, pp. 1225-1231, January, 1968.

22. Collier, R. F., C. B. Burckhardt, and L. H. Lin, *Optical Holography*, New York, Academic Press, 1971.

23. Kurkov, A. P., "Optical Measurement of Propeller Blade Deflections," *NASA TP-2841*, 1988

24. Kurkov, A. P., "Optical Measurement of Unducted Fan Blade Deflections," *Journal of Turbomachinery*, Vol. 112, pp. 751-758, October, 1990.

25. Kurkov, A. P., and O. Mehmed, "Optical Measurement of Unducted Fan Flutter," *NASA TM-103825*, 1991.

26. Taylor, J. R., *An Introduction to Error Analysis: The Study of Uncertainties in Physical Measurements*, Mill Valley, University Science Books, 1982.

27. Leissa, A. W., *Vibration Of Plates*, NASA SP-160, 1969.

28. "Engineering Data Sheet for CEA-00-062UW-350 Strain Gage," Batch No. S101190, Measurements Group, Inc., P. O. 27777, Raleigh, NC 27611, 1991.